Investigation of a Tubular Linear Transverse Flux Machine for Use with a Free-Piston Engine

Junnan Wang

A thesis submitted for the degree of Doctor of Philosophy

Newcastle University 2017-09-20

School of Electrical and Electronic Engineering

Abstract –This thesis explores different topologies of permanent magnet linear electric machines for use with a renewable engine – Free-Piston Engine. By comparing their performances, it aims to prove that a new linear modulate pole (transverse flux) machine can be the best overall topology.

Five candidate topologies including longitudinal flux and transverse flux types are presented and simulated by finite element analysis method in MagNet software. The designer optimises each topology with the same effort and strategy by using an advanced algorithm in OptiNet software. The transverse flux and flux switching topology are detailed compared with different optimisation strategies to investigate machine performances.

The designer performs an advanced design study on the modulated pole machine to simplify the manufacturing process, reduce building cost and improve output performance. The process includes the tooth combination design, the single tooth winding design and the lamination design.

The designer expands the insight of the final designed modulated pole machine. The force production and power factor derivation are performed theoretically and numerically. The numerical solution is compared to the simulation result for validation.

Detailed mechanical design for the final designed modulate pole machine is performed consisting of: the shaft strength investigation, the stator assembly strategy, the winding assembly and drive linear actuator selection.

The designer tests the final build modulate pole machine in both static and dynamic conditions. Static tests include cogging force test and DC test. Dynamic tests include EMF test and short circuit current test. All results are compared with simulations for machine quality check.

The thesis demonstrates that the tubular transverse flux machine is manufacturable and fulfil the requirements of a Free-Piston Engine.

Acknowledgements – I would first like to show my heartfelt gratefulness to my supervisor Dr Nick Baker for his guidance during this project and most of all for being able to put up with me. I would also like to thank Dr YaoDong Wang and Prof. Tony Roskilly for their support and concern, especially during my first-year study.

I would also like to thank the various support staff of Newcastle University for their help on my machine prototype build and assemble; particular thanks go to Chris Manning and Samuel Burn from the mechanical workshop.

Finally, I would like to thank my family for supporting me through university in the first place and my girlfriend Miru for tolerating the four years of study at university without complaining.

Table of Contents

List of Figures

List of Tables

Chapter 1. Introduction

1.1 The Project Background of Free-Piston Engine and Linear Electric Machine

The number of vehicles powered by internal combustion engines (except pure electric vehicles) is increasing for recent decades. On the other hand, the fossil fuels used for vehicles are decreasing. Moreover, the increasing emissions standards push automotive companies to design and manufacture less polluting and higher fuel efficient vehicles [1]. As a result, vehicle manufacturers have an increasing interest in alternative engine configurations [2]. The Free-Piston Engine is one such configuration.

Pescara first introduced the Free-Piston Engine concept in the 1920s [3], he patented his Free-Piston Engine as an air compressor. From then on, many companies in the world, such as the French SIGMA, Junkers [4] in Germany and Ford Motor Company in the USA have been designing and developing different Free-Piston Engines used as air compressors or gas generators. In the 1960s the development of Free-Piston Engines technology was abandoned because it was viewed as not viable commercially [5]. In recent years, the Free-Piston Engine concept again stimulated interest among research groups for many technologies. The primary research orientations of Free-Piston Engine are hydraulic and generators. A Free-Piston Engine Generator (FPEG) is a machine with linear motion as the primary motion, which drives a linear generator to generate electric power. Some researches have been carried out in this area due to its simplicity. In 1991, Joseph E. Kos got the patent for his linear generator [6]. This patent described a single cylinder, which with a spring rebound device to store the energy. This model is the rudiment of the FPEG. University of Malaysia [7] studied the operation rule of a single FPEG, which was a two-stroke and spark-ignited engine with air-spring as the rebound device, under a variety of compression ratios and heat additions. It has been revealed that by increasing heat addition, the velocity and stroke length of slider-piston will increase; by increasing compression ratio, the velocity of the slider piston increases, but the stroke length remains constant. What is more, the Free-Piston Engine should be well suited for homogeneous charge compression ignition (HCCI) operation due to its low ignition timing control requirements, as has been proposed by some authors [8] [9]. The FPEG is currently under investigation by many research institutions all over the world, a topology of the FPEG announced by Toyota in 2014 [10] [11] is as shown in figure 1.1. The engine consists of a two-stroke combustion chamber, a linear generator and a gas spring chamber. The piston is moved by the combustion chamber, thereby converting the kinetic energy to the electrical energy. Instead of two opposed combustion chambers, Toyota selects to use a gas spring chamber for returning the piston for the subsequent combustion event. The burned gas

is scavenged out through exhaust valves mounted on the cylinder head of the combustion chamber, and the fresh air is brought in through the scavenging port at the side wall of the cylinder liner. The gas spring chamber is used to store part of the kinetic energy from the combustion chamber side and apply to the return stroke. Along with this reciprocating motion the magnetic translator could react with the stator coils to produce the electrical energy and works as a linear generator.

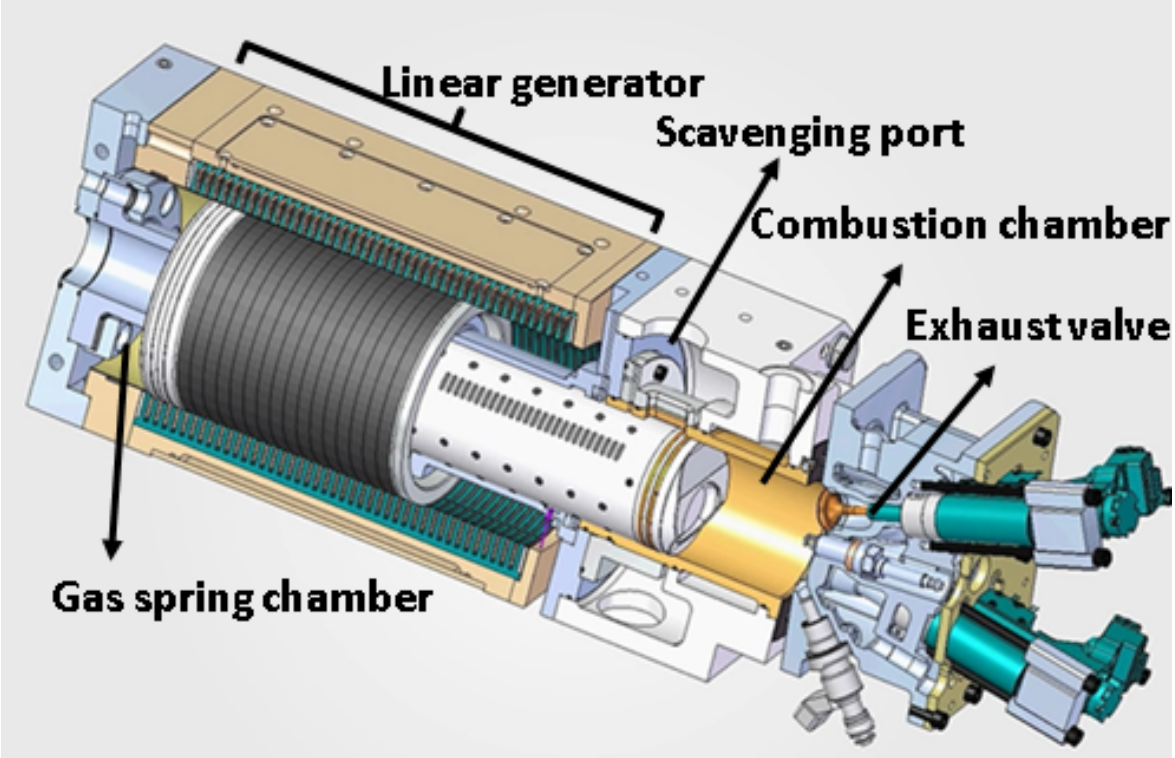

Figure 1.1 Toyota announced Free-piston Engine in 2014 [10] [11]

Before the advent of linear machines, rotary machines provided a solution to produce linear motion. Ball and screw, belt and pulley and other rotary solutions have been employed to convert rotary motion into translational. However, compared to a direct linear machine, these solutions are less precise and display backlash error. While using linear machines, the mechanical load is directly coupled with the translator without external gearing, namely almost no friction within the process [12] [13]. Linear machines have the same operating principles as rotary machines. The concept is simple: cut the rotary motor radially and lay it flat. In a linear machine, the air gap is usually more significant than that of a rotary motor, and the stator is shorter concerning the translator causing end effect. The leading technologies for linear machines are permanent magnet synchronous, induction and switched reluctance machines [14]. A simple linear machine is composed of a stationary track (often laid with permanent magnets) and a translator (with current). Both components are making relative

motion due to the interaction of electromagnetic field. In practice, these two roles can be switched [15], i.e. force holding the magnets and stationary track encompassing the current coil. The stroke length, in any case, increases by elongating the translator concerning the stator. Permanent Magnet Linear Synchronous Machines (PMLSMs) are used in various industrial applications when high dynamic performance is required, e.g. assembly lines, robots, CNC machine and high-speed trains [16]. Wherever efficiency and throughput are meant to be increased for translation motion, linear machines can be a better alternative to rotary ones.

Linear machines have been intensively developed since 1970 as the market of the linear machine is ever expanding with research going on in diverse applications such as Maglev, Ropeless Elevator, Aircraft and Shuttle launch, Tugging containers and Wave Energy [17]. The combination with internal combustion engine has been developed in recent years. When designing a PMLSM, it either can be distinguished by the motor and generator aspects or machine configuration and power electronic control configuration aspects. In this project, the designer would focus more on the topology design. Simulation works can assume the machine is either a motor or a generator model regarding the setup of the phase current, whereas tests will only focus on the machine force capability and EMF due to the lack of control system and power converters.

1.2 Voltage Source and Current Source for Synchronous Motor Design

The synchronous motor is an AC machine which only develops torque when the rotor speed synchronised with the stator armature field speed. The main magnetic field in the synchronous machine may be produced by dc currents or permanent magnets on the rotor. Machine torque is produced by the phase difference (load angle) between two magnetic fields. Three phase synchronous generator is responsible for about 99% of all bulk electricity generation and most embedded generation schemes due to the high efficiency and the ability to supply real and reactive power independently [18].

The torque is produced by misalignment of the rotor and stator field which can be classified by using voltage source or current source. For a voltage source, the torque varies with load angle δ in a sinusoidal manner. Considering a synchronous machine connected to a rotating source such as a DC drive machine, with a shaft rotating at synchronous speed and fed by a constant frequency three phase supply. If there is no friction and bearing loss within the system, then the two fields will be aligned, and no resultant torque produced. By applying a load torque on DC drive machine, then two fields will start to lose alignment (i.e. δ start to

increase). For a non-salient motor with load increasing to a certain level δ will achieve 90º and reach synchronous machine peak capacity, and further increasing on load will push the synchronous motor to synchronisation loss. Corresponding torque equation includes machine saliency shown below in equation. 1-1 where V is the voltage magnitude of the power source, E_f is machine back EMF which is dependently related to machine dimensions and working speed, X_d and X_q are related to machine saliency, ω_s is the synchronous speed.

$$T = \frac{VE_f}{X_d \omega_s} \sin\delta + \frac{V^2}{2\omega_s} \sin 2\delta \left(\frac{X_d - X_q}{X_q X_d}\right) \tag{1-1}$$

Since current controlled power electronic converters have become more commonplace, it has become attractive to use a current source to express the torque. The equation for torque production with a current source is shown in equation. 1-2 where I is the stator armature current, β is the phase angle between phase current and EMF. In this case, if ignoring machine saliency, magnetic torque can reach peak value by aligning current in phase with EMF. What is more, by using full controlled current source for a variable speed synchronous machine, field weakening can also be applied to either reduce the terminal voltage requirement or extend the machine to higher working speed.

$$T = \frac{E_f I}{\omega_s} \cos\beta + \frac{I^2}{2\omega_s} \sin 2\beta \left(X_d - X_q\right) \tag{1-2}$$

For the PMLSM it can be regarded as cutting the rotary permanent magnet machine and transfer into the flat or tubular configuration. However different from the rotary version, due to the stroke restriction, there is no steady state for PMLSM or in other words translator speed is varied with a reciprocating motion. Moreover, when the PMLSM is working with a Free-Piston Engine, the first step is acting like a motor to drive engine chamber to required compress ratio. Thus it is more realistic to design a PMLSM with a set of current sources.

1.3 Longitudinal Flux Machine and Transverse Flux Machine

According to the plane direction of the magnetic flux relative to the motion direction, electric machines can be categorised into longitudinal flux machines (LFMs) or transverse flux machine (TFMs) [19]. In a flat version of linear PM LFMs like that shown in figure 1.2 below is a counterpart of the conventional rotary machine with distributed winding configuration and full pole pitched radial surface mounted magnets. The active area is parallel to the translator motion direction as well as the flux loop plane. Instead of torque, the thrust force is produced by the interaction of the armature winding field and permanent magnets field. Compared to the rotary topology this linear LFM shows disadvantage on translator material,

in other words, there is a waste of translator core back steel and magnets materials due to the overhang length based on the required stroke length of the application. Apart from the cogging force, as the stator is not circular around the translator an additional fringing detent force is expected as a drawback of conventional linear LFMs [20] for this a lot researches have been done to minimise the detent force such as: adopting a suitable stator length, chamfering, fractional slot to pole ratio or choosing other magnets orientation etc.

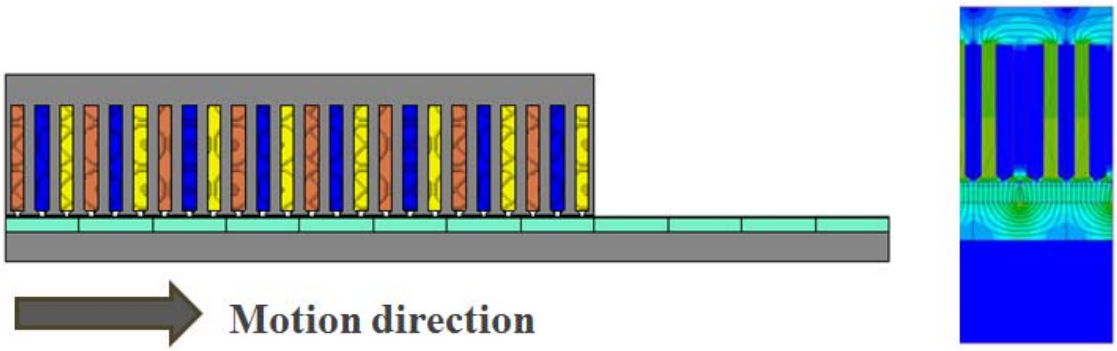

Figure 1.2 A flat version of linear LFMs

For above linear LFMs topology, the force can not only be performed from equation. 1-2 but also expressed in equation. 1-3 regarding the machine size based on the three orthogonal components of Lorentz's law. A is the armature current MMF/ stator active length defined as electrical loading in Arms. B is the peak fundamental air gap flux density defined as magnetic loading in Wb/mm^2. l is the stator depth or effective winding length in m. P is the pole pair numbers. τ is the pole pitch in m and Ψ is the phase angle as the same in equation. 1-2.

$$F = \frac{\sqrt{2}}{2} A B_{gmax} l P \tau \cos \Psi \tag{1-3}$$

From physical aspect in LFMs A and B share the same space in LFMs, namely for fixed machine overall size and fixed translator dimensions wider tooth width not only contribute to higher peak flux density but also reduces space for coils thus reducing the MMF. Since then a trade-off between A and B is inevitable when designing an LFM. In nowadays, most industrial and domestic applications are using LFMs due to its comprehensive design technology and easy manufacture.

TFM is a competitive machine topology due to their high torque density. Most of this is due to TFM breaking the tradition of A and B confliction [21]. In figure 1.3, two early flat versions of linear PM TFMs are presented where for either of them the flux loop plane is perpendicular to the translator motion direction, the tooth width can be independently varied

without influencing the armature current MMF, thus for a particularly active area, change on pole numbers will not drop the machine capability to place coils. However, a known weakness is its low power factor. As reported in [22], a reaction rail mounted magnet transverse machine typically can achieve a power factor of 0.35, whereas a flux-concentrated machine can reach 0.53.

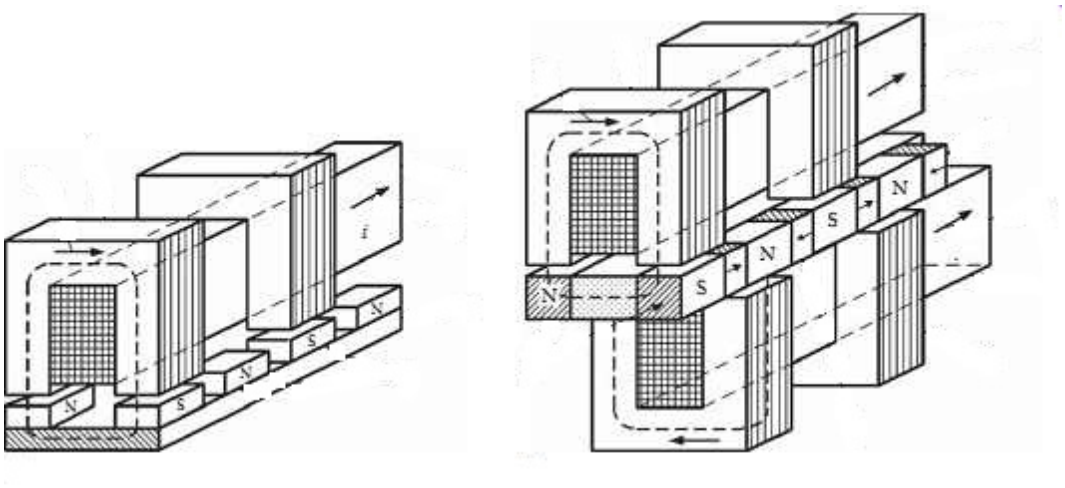

Figure 1.3 Flat version of linear TFMs [36]

Different from conventional LFMs which are featured by different magnet orientations [23], TFMs' family possesses more diverse topologies, and they usually are more complicated to manufacture. For rotary form, TFMs are often proposed for dense torque application like electric vehicles [24] [25]. Linear TFMs have been studied for wave energy [26] and Free-Piston Engine [27] [28]. Rotary topologies have been presented which use soft magnetic composites, laminations or a combination for manufacturing.

1.4 Objectives and Overview of This Thesis

In this project, five nominated machine topologies (3 LFMs and 2 TFMs) will be discussed based on the literature review investigation in Chapter 2. Simulation results will be compared in Chapter 3 to determine the final topology to build in the lab with improved building strategy in Chapter 4. Meanwhile, numerical solution will be investigated to validate the simulation results for the final topology in Chapter 5. Detailed mechanical design and test results comparison will be presented in Chapter 6 and7, at the end conclusions will be listed in Chapter 8 and lead the research to the next stage—plug into the application system. By finishing this research either the insight of machine design or the innovative design will be practised, the linear machine topology will be thoroughly discussed and ready to collaborate with renewable energy engine technology Free-Piston Engine to face the environmentally friendly future.

Chapter 2. Literature review

2.1 Introduction

In this Chapter, the designer will review related literature including developments of soft/ hard magnetic material, early linear machine topologies, the developed history of conventional permanent magnet machines, transverse flux machines and flux switching machines. Ideas of the selection of machine core material, magnet material and nominated machine topologies are based on the literature review. Some machine assembles methods will also be introduced in this section to raise a material hybrid concept. Finally, with the revision of fundamental knowledge of machine designs, a clear research thinking will be drawn.

2.2 Soft Magnetic Materials and SMC

Soft magnetic materials are widely used in electric and electronic devices due to their low coercivity, high flux permeability and ease of magnetisation and demagnetisation. They can be defined by a hysteresis curve (figure 2.1 for example) when the material coercivity is lower than 100A/m then it can be classified as soft magnetic material [29].

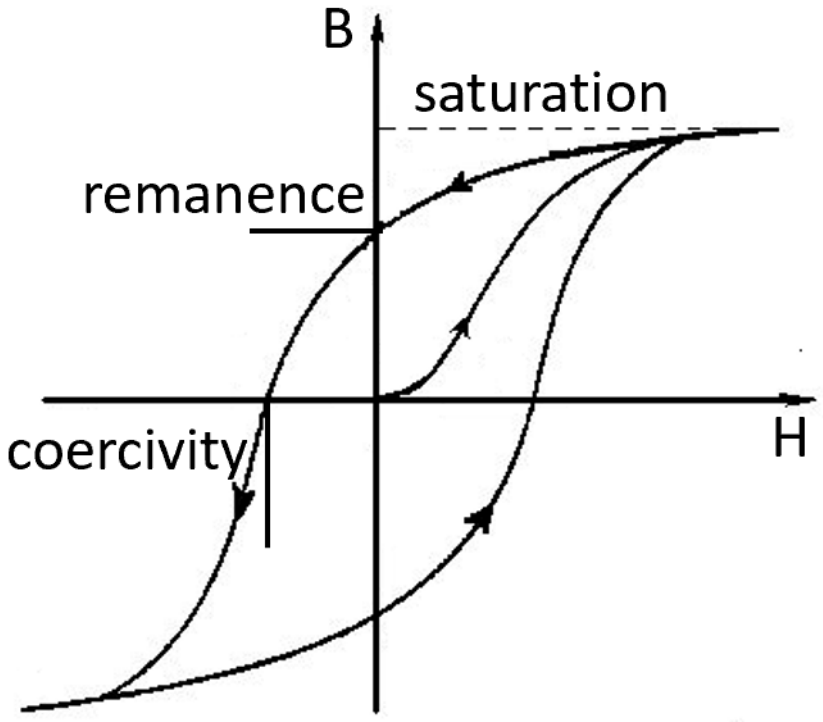

Figure 2.1 Hysteresis curve example

Conventional soft magnetic materials and their characteristics are in table 2.1, for any sized electric machine the most common used soft magnetic material is Fe-Si alloy or silicon steel lamination since this material has a low coercivity and high flux permeability. A high silicon

content can further increase the resistance of the material thus reduce the eddy current loss. In this project, the translator and stator steel material used in the simulation are M270-35A5 where the detailed *B*/*H* curve and loss characteristic are in figure 2.2.

Iron and low carbon steel	High magnetic saturation, low cost, easy manufacture; low electrical resistivity thus high eddy current loss; generally applied to static applications like electromagnetic core, relay.
Fe-Si alloy	Consistent magnetism, low thermal conductivity, high electric resistivity and flux permeability; higher silicon content could cause magnetic saturation reducing and high brittleness; generally served as lamination and favourably used in AC devices like an electric machine, transformer.
Fe-Al alloy	The good soft magnetic property, high flux permeability, high electric resistivity, high rigidity; brittle; customarily applied small sized transformer, magnetron.
Fe-Si-Al alloy	High levels of rigidity, magnetic saturation, flux permeability and electric resistivity; hard manufacture; mainly used in audio and video magnetic head.
Ni-Fe alloy (permalloy)	High flux permeability, constant permeable, high plasticity, sensitive to stress; used in pulse transformer, inductor iron core.
Iron cobalt alloy	High magnetic saturation; low electric resistivity; used in the small-sized electric machine, small sized transformer.
Soft magnetic ferrite	High electric resistivity, low cost; low magnetic saturation; widely used in inductive devices and transformer.

Table 2.1 Soft magnetic material list

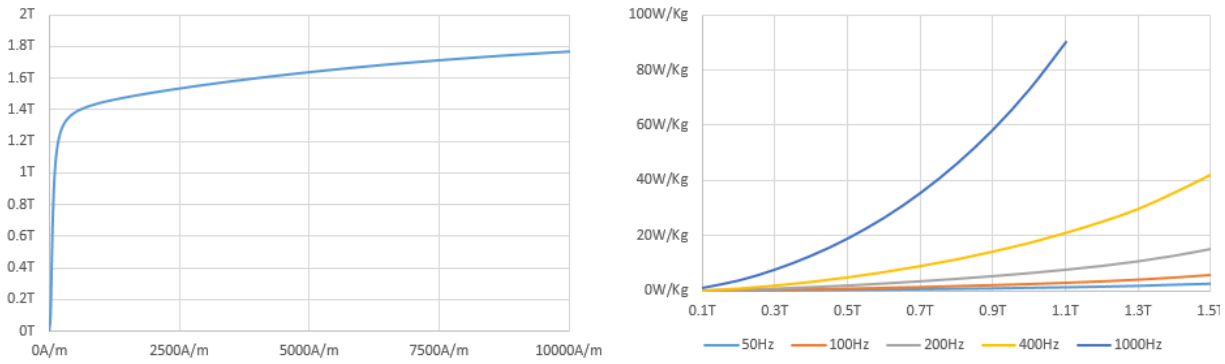

Figure 2.2 Simulation applied soft magnetic material characteristics

Soft magnetic composite (SMC) is an advanced processing technique which is as ferromagnetic powder particles surrounded by an electrically insulating film. The unique advantages include: three-dimensional (3D) isotropic ferromagnetic behaviour, low eddy current from any direction of magnetic flux as illustrated in figure 2.3, relatively low total core loss at high frequency, flexible machine design, lower weight (circa 7500 kg/m^3 and 7650 kg/m^3 for lamination steel). The main drawback is the high cost due to complicated manufacturing, SMC is typically manufactured by conventional permanent magnet compaction combined with new techniques such as two-step compaction, warm compaction, multi-step and magnetic annealing followed by a heat treatment at relatively low temperature. [30]. Moreover, the isotropic property of SMC also bring some mechanical challenge during post-processing, as it is natural to breakdown SMC part with micro-cracks between adjacent particles when too high pressure is applied thus the overall permeability of the part will be reduced. In this project, the building of machine will use SMC on the translator and lamination on the stator with a material hybrid concept which will be detailed discussed in Chapter 6.

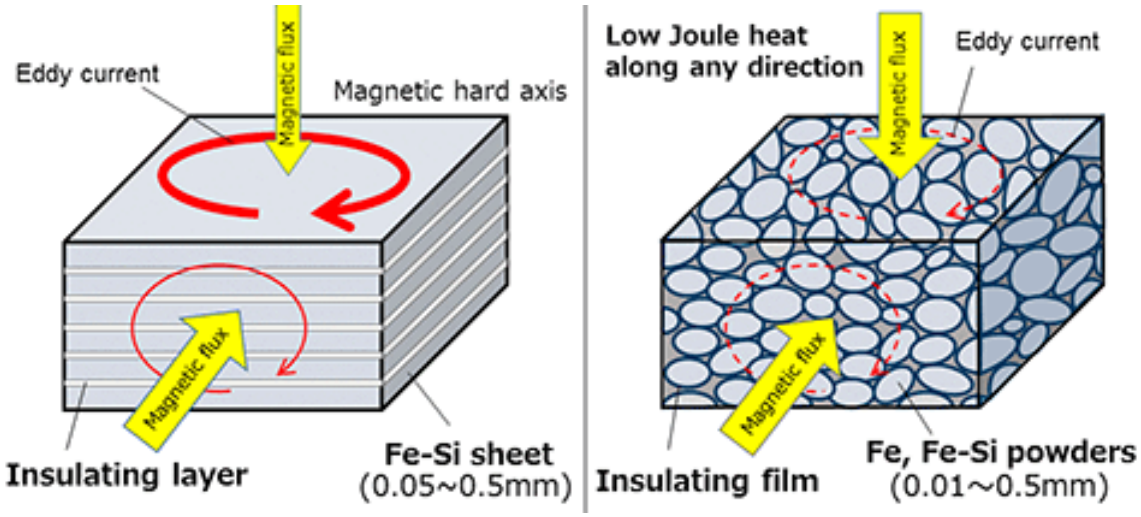

Figure 2.3 Lamination and SMC structure [30]

2.3 Hard magnetic materials

Hard magnetic materials or hard magnets, also referred to permanent magnets can retain magnetism after being magnetised. Contrary to soft magnetic materials these materials have an intrinsic coercivity of higher than 10kA/m [31]. The method making a permanent magnet is to place a hard magnetic material in a very high magnetising field, as long as field source removed, high remanent flux density will remain in the material like shown in figure 2.1. If the permanent magnet is ideally shorted (conducted by a material with infinite permeability), then a magnetic flux will flow in the closed loop with the remanent flux density. For above

case, if remove the permanent magnet, then an equivalent *MMF* with value $H_m l_m$ is required to maintain any flux in the loop as Ampere's Law; if there is an air gap isolating the closed loop, then a H_g field will be produced in the gap which results in a smaller flux density appears in the air gap.

Four common hard magnetic materials are used to form permanent magnets in conventional electric applications as alnico, hard ferrite, SmCo type and NdFeB type: alnico is the first type of hard magnetic material developed in the early 1930s also named as alnico alloy, this material typically is composed of iron, cobalt, nickel, aluminium, copper and titanium. When it comes to 1956 the energy produced by this material can achieve 80kJ/m^3; hard ferrite is the next advance material that developed in the 1950s also regarded as ceramic magnets, this material is ferromagnetic and considering the proportion of iron within the material has very low remanence circa 0.4T and 250kA/m coercivity. Such low performance causes the production only achieve 40kJ/m^3. In 1967 $SmCo_5$ was discovered and became the first commercial rare-earth (RE) and transition metal (TM) and had an energy of 40kJ/m^3, later in 1969 the energy improved to 160kJ/m^3 and 240kJ/m^3 in 1976 as Sm_2Co_{17}. NdFeB type is the most advanced hard magnetic material being developing since 1984 by General Motors in the USA and simultaneously by Sumitomo Special Metals in Japan. NdFeB type is made of neodymium, iron and boron and up to today NdFeB type has the most prominent family member and can achieve 450kJ/m^3 [31]. Detailed magnetisation characteristics of these four materials are in figure 2.4 with their advantages and disadvantages listed in table 2.2.

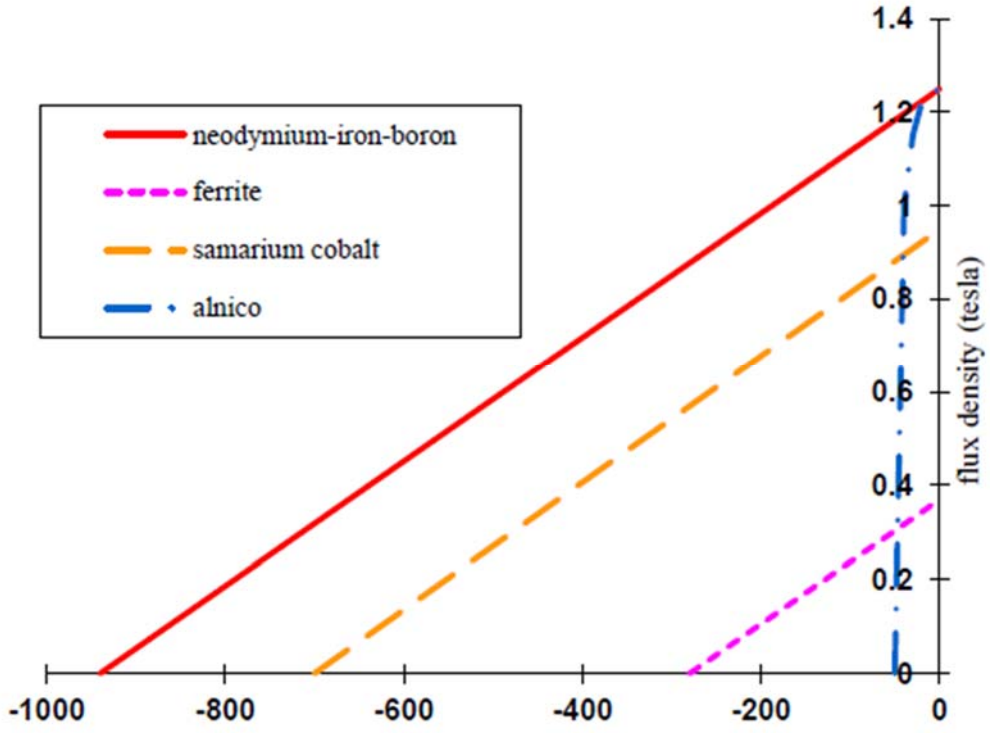

Figure 2.4 Typical permanent magnet characteristics [89]

	Advantages	**Disadvantages**
Alnico	Low cost, high remanence	Low coercivity easy demagnetised – now rarely used
Hard ferrite	Low cost	Low remanence and coercivity
SmCo type	High remanence and coercivity, good thermostability	High cost
NdFeB type	Very high remanence and coercivity	Low operating temperature (max 100-200oC)

Table 2.2 Major features of different materials [89]

2.4 Early Linear Electric Machine Topologies

The very first linear machine can be traced back to work done by Charles Wheatstone at King's College London between 1841 and 1845 [32] [33]. Figure 2.5 illustrates the system stator topology that a steel cylinder can be attracted to a row of dc-fed magnets which are switched on in turn. The working principle is like a linear reluctance machine (LRM) however this model has been pointed out too inefficient to be practical.

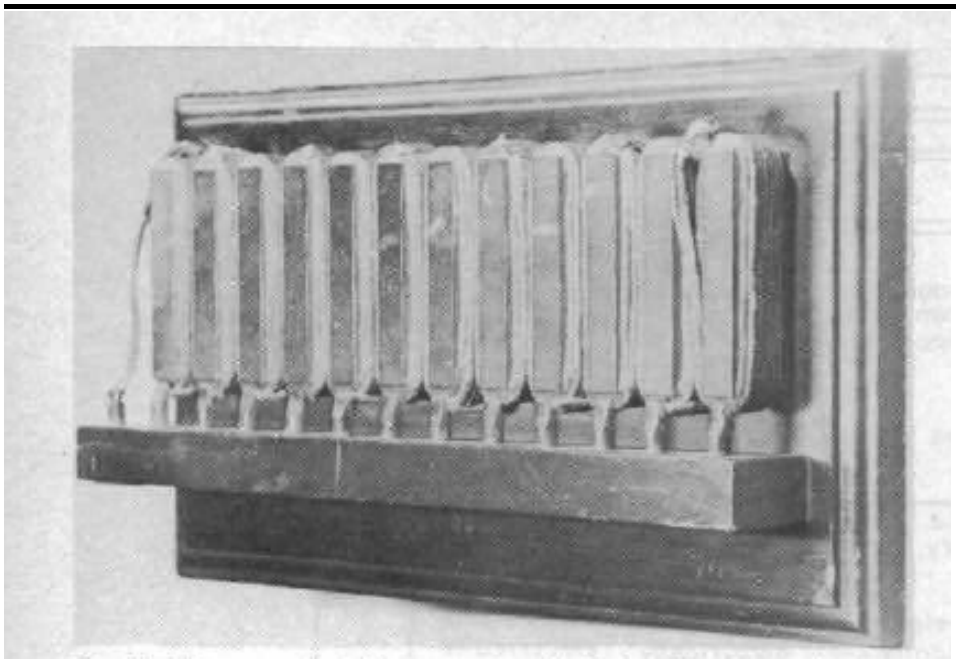

Figure 2.5 The very first linear machine [32]

Later in 1905, Alfred Zehden patented his linear induction machine (LIM) as a possible prototype as shown in figure 2.6 [34]. This machine was designed for driving trains or lifts. This type of topology can be regarded as the counterpart of conventional rotary induction machine where the primary side consists of a magnetic core with a three-phase winding, and secondary side may be a mental or three phase winding wound around a magnetic core. When a three-phase supply is connected to the primary side winding a flux wave travels along the primary core will be generated, then a current could be induced on the secondary conductor which cause the interaction with the flux wave thus to produce thrust. Later in 1950 Eric Laithwaite of Manchester University [35] developed the first full-size working model as a single sided version which the magnetic repulsion forces the conductor away from the stator, levitating it, and carrying it along in the direction of the moving magnetic field. It is also named as a magnetic river [36], and since then linear motors are often used in maglev propulsion.

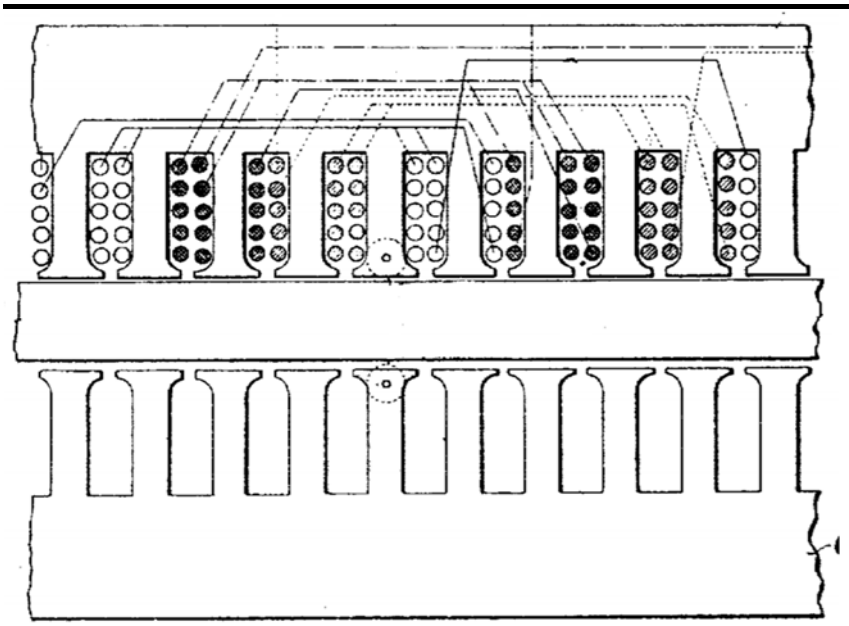

Figure 2.6 The first induction linear machine topology [34]

For many years the LIM played a dominant role. However, when it comes to 1990s since the improvement in power electronics and permanent magnet materials, the permanent linear magnet synchronous machine (PMLSM) became preferred for some applications [33]. To 1999 Jacek F. Gieras concluded Linear Synchronous machine (LSM) topologies could be classified according to whether they are flat or tubular, single sided or double sided, slotted or slotless, iron-cored or air cored and transverse flux or longitudinal flux. For linear permanent magnet synchronous machines, they can be simply classified as PMs mounted on the reaction rail or PMs mounted on the armature [37]. For early topologies they are more like imitating rotary counterparts, like shown in figure 2.7 are two most conventional topologies of the reaction rail mounted PMs type, where they share the same slotted armature iron core structure on stators, translators have different magnet orientations and different yoke materials (soft magnetic for (a) and non-magnetic for (b)) [38].

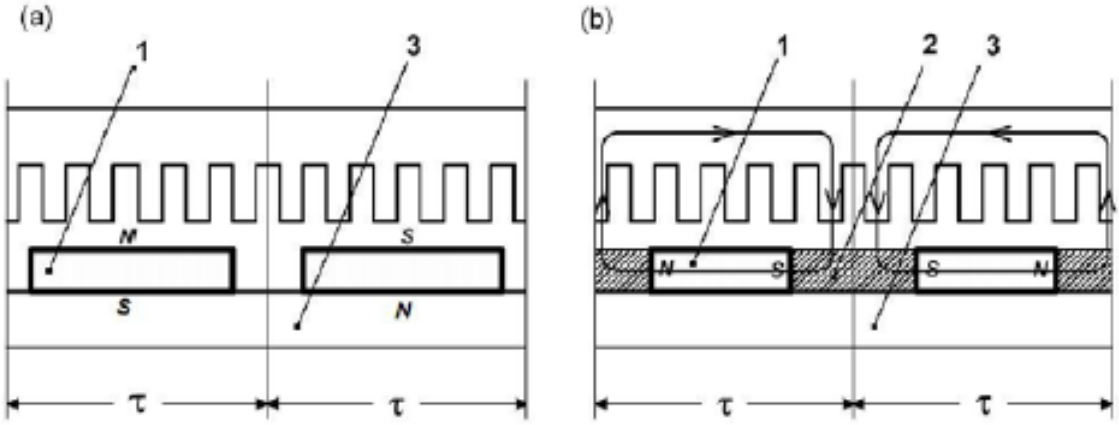

Figure 2.7 Single sided topology with (a) surface PMs (b) buried PMs. 1-PM, 2-mild steel core, 3-yoke. [38]

The Halbach array of PMs is also applied to PMLSMs, permanent magnets in this configuration can excite stronger sinusoidal flux density than that in conventional configuration [39]. In this case, it is even possible to form strong field flux without using the soft magnetic yoke and armature iron core as shown in figure 2.8. Damper winding or cage concept of the rotary machine also has a counterpart applied in PMLSMs, in figure 2.9 by using an aluminium shield or solid steel pole shoes not only the speed oscillation can be damped but also reduce the backward travelling magnetic field. Early concept of skewing which used to deal with the thrust ripple is also copied from rotary topologies by directly misaligning PMs in one segment or more as shown in figure 2.10.

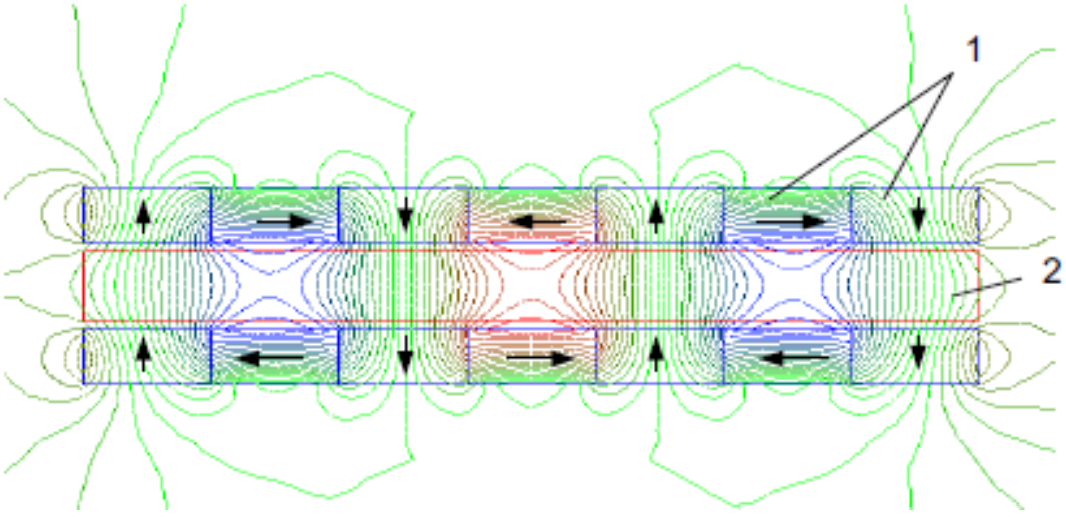

Figure 2.8 Double-sided topology with Halbach array of PMs. 1- PMs, 2-coreless armature winding. [39]

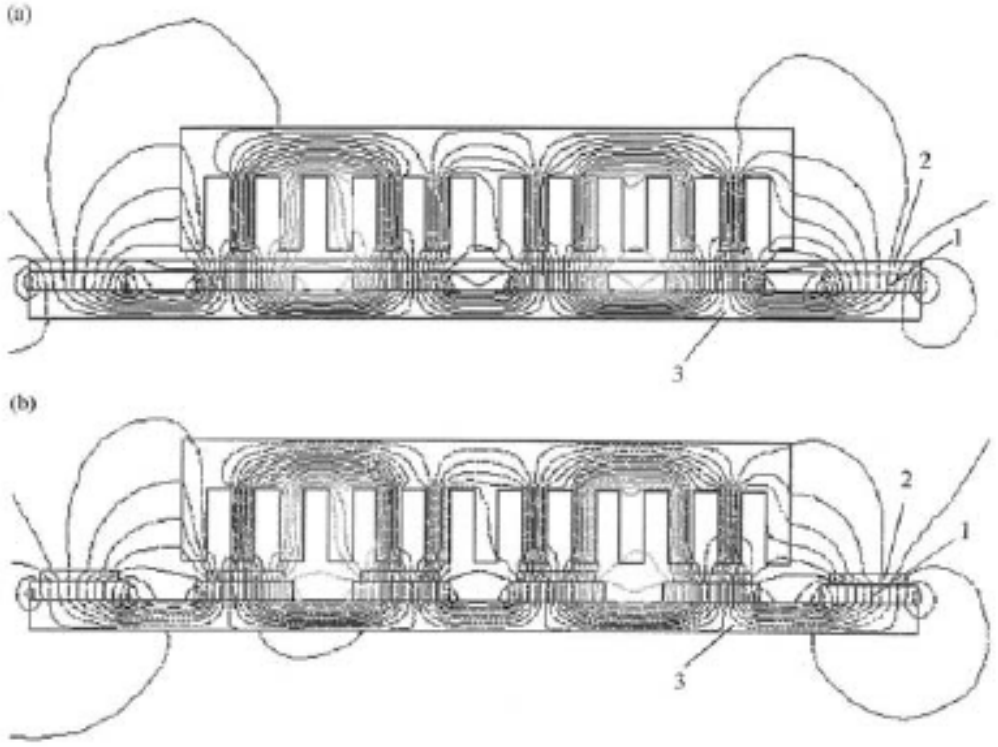

Figure 2.9 Dampers for surface mounted PMLSMs (a) aluminium shield, (b) solid steel pole shoes. 1-PM, 2-damper, 3-yoke. [39]

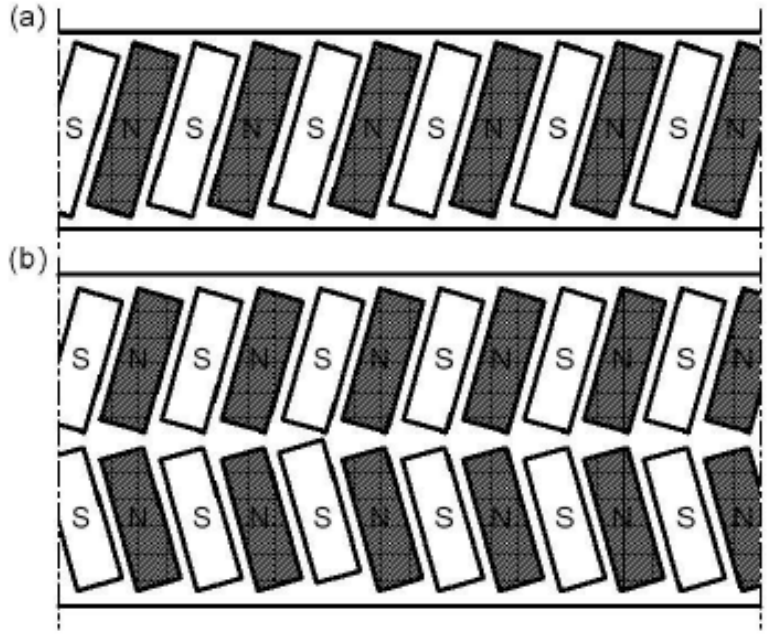

Figure 2.10 Skewed PMs in flat PMLSM (a) one segment (b) two segments. [39]

Compared to the rotary topology, the linear counterpart's moving part is not enclosed by the stator, since then more complicated structure – double sided is developed to take advantages of using yoke materials. In figure 2.11 are two possible topologies: moving magnets and moving armature where (a) can better use yoke materials on the translator and (b) can better

use those on the armature. The linear slotless topology can also be extended to double sided as shown in figure 2.12.

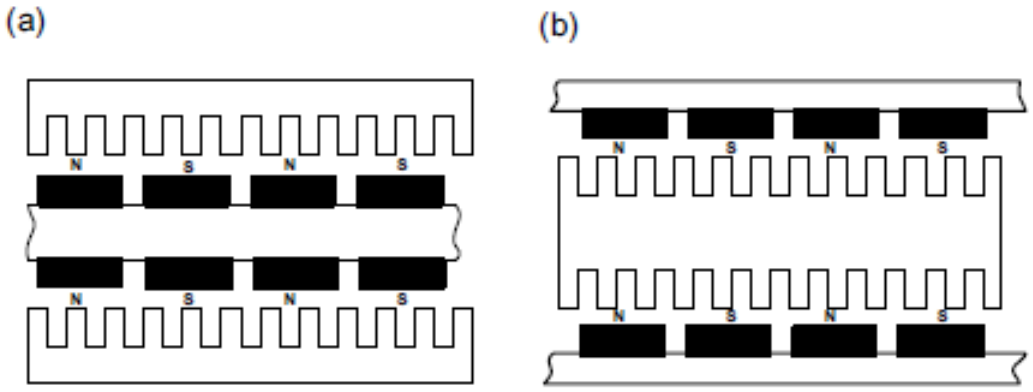

Figure 2.11 Double sided flat PMLSMs (a) moving magnets, (b) moving armature. [39]

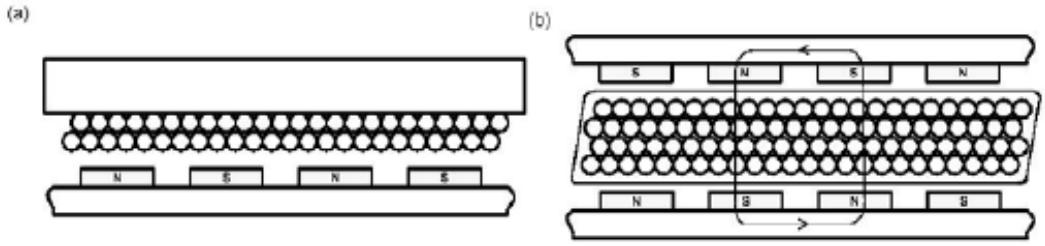

Figure 2.12 Flat slotless PMLSMs (a) single-sided, (b) double-sided. [39]

The complexity of PMLSMs can even go further by rolling a flat topology and turn into a tubular topology (figure 2.13). This feature can theoretically offset the attraction force between stator and translator, and integrate all machine parts includes stator, translator, bearing, position sensors and power electronics into a single metal cylinder [40]. Transverse flux machine can be classified into the reaction rail mounted PMs type too, as an example shown in figure 1.3.

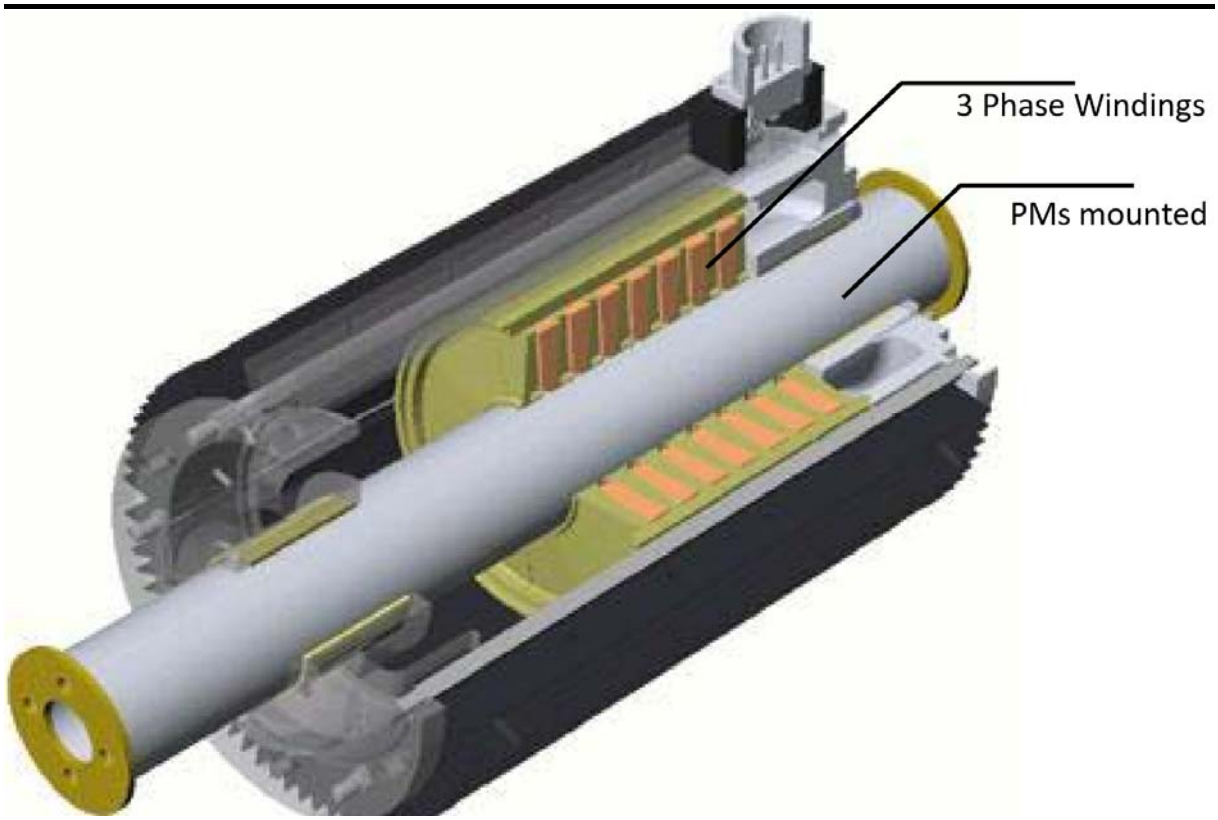

Figure 2.13 Tubular PMLSM (reaction rail mounted PMs) [40]

The armature mounted PMs type machine topology is a cheaper solution which aims to save the permanent magnet usage on the overhang length of the longer reaction rail. Such a linear machine is also called the homopolar, flux switching or flux reversal topology. In figure 2.14 is a homopolar PMLSM developed in the early 1990s [41] where the stator consists of the armature stack and the polyphase winding which are enclosed by a U shaped yoke. Two sets of permanent magnets are inserted between the armature stack and the U shape yoke with same polarities. Thus armature and excitation are bound together on the short stator. The translator is made of solid magnetic cubes (shown in black) and non-magnetic solid cubes (white). Armature PMs and magnetic solid cube produce EMF, and thrust is produced by the armature field and the salient pole reluctance. A further simplified single sided topology of this model as shown in figure 2.15.

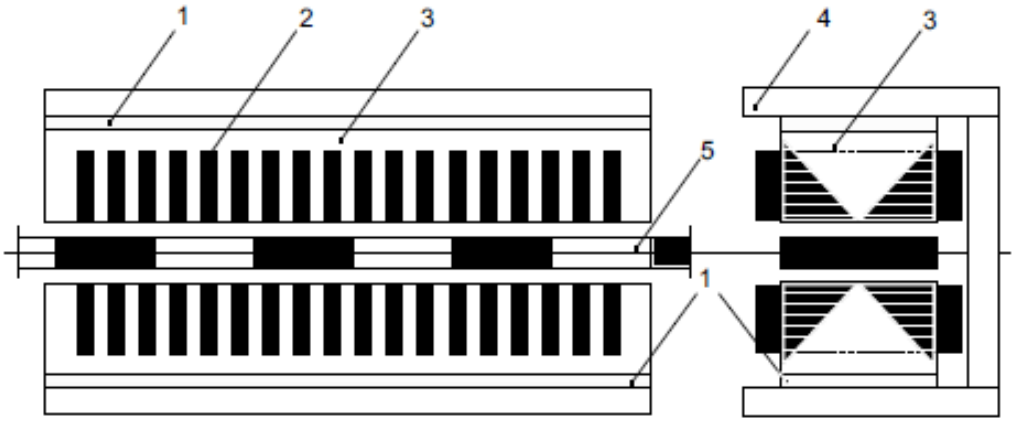

Figure 2.14 Double-sided homopolar PMLSM with armature mounted PMs. 1- PM, 2- armature winding, 3- armature stack, 4- yoke, 5- non-magnetic reaction rail. [41]

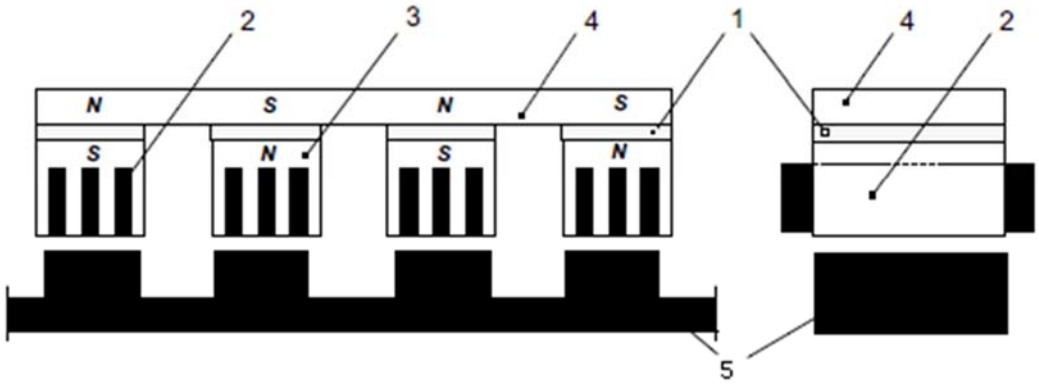

Figure 2.15 Single sided homopolar PMLSM with armature mounted PMS. 1- PM, 2- armature winding, 3-armature stack, 4-yoke, 5- magnetic reaction rail [41]

LSMs with electromagnetic excitation topology or superconducting excitation topology also exist where PMs in PMLSMs are replaced by dc excitation winding or coreless superconducting electromagnets. Topologies are presented in figure 2.16 and figure 2.17. For both topologies: brushes, contact bars and inductive power transfer system [42] are required to deliver excitation DC to the reaction rail. This concept was inherited from rotary topology, and the use of dc excitation could larger the machine size and reaction rail complexity. Since then there is a trade-off between the cost of permanent magnets and dc excitation when deciding to choose electromagnetic excitation or magnet excitation. However, when working with the Free-Piston Engine, the reaction rail (the translator) required to be as simple as possible, as a result, electromagnetic and superconducting excitation topologies will not be considered in this project. What is more, linear variable reluctance machines [43], linear stepping machines [44] and switching reluctance machine [45] are also options from early linear electric machine topologies concepts, but due to the low thrust capability [37], very few

researchers would apply these topologies to the Free-Piston Engine. Since then the designer only considers PMLSM with conventional reaction rail mounted PMs topology(RRPM), transverse flux topology(TFM) and flux switching topology(FS) for detailed design.

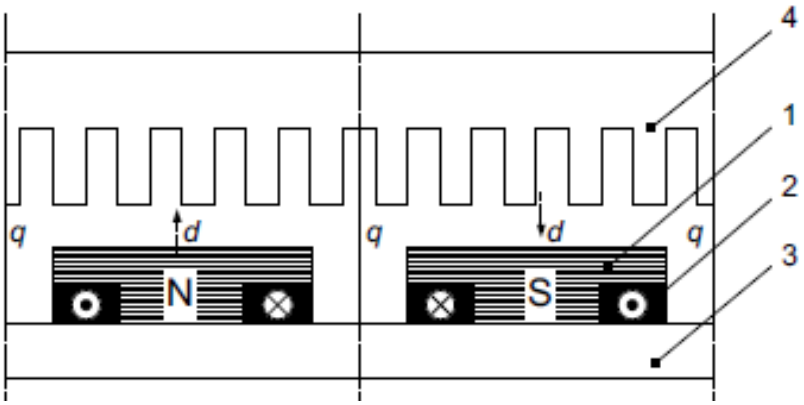

Figure 2.16 Electromagnetic excitation topology of LSM. 1- salient pole, 2- dc excitation winding, 3- yoke, 4- armature stator. [42]

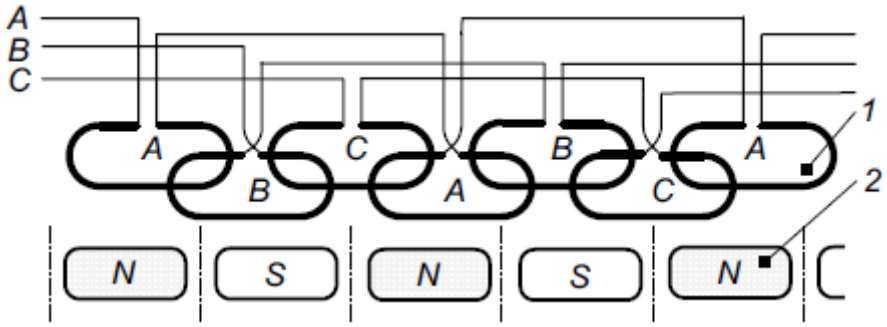

Figure 2.17 Three-phase air core LSM with superconducting excitation. 1- armature winding, 2-superconducting excitation winding. [42]

2.5 Developments of Conventional Reaction Rail Mounted Permanent Magnet Topologies

Among various linear machine configurations, the tubular topology with permanent magnet excitation has some distinctive features like high thrust density, zero net attraction force and excellent servo characteristics [33]. In [46] J Wang gives a general framework for the analysis and design of the tubular linear conventional reaction rail mounted permanent magnet machine in 1999. Topologies include (a) radially, (b) axially and (c) multipole Halbach magnetised magnets orientations as presented in figure 2.18. Corresponding numerical solutions (2D analysis on extracting the effective radial flux density profile in armature region) are well formed by referring magnets' coercivity, materials' permeability and dimensions for all these three topologies. The thrust and EMF can be calculated based on the flux density

profile and the armature radial flux density can be estimated in the same way based on the fundamental *MMF* thus to calculate the phase inductance and power factor [47].

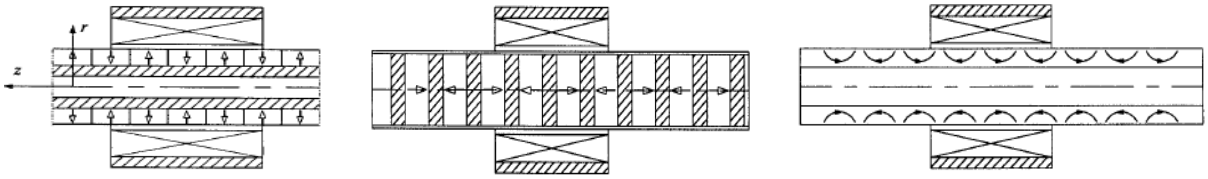

(a) (b) (c)

Figure 2.18 Typical tubular linear PM machine topologies [46]

Later in 2004 J Wang gave a detailed numerical analysis of slotted armature permanent magnet machines based on different armature winding topologies [48]. In figure 2.19: (a) brushless dc or single tooth winding with two coils per pole pair per phase, (b) full pitched synchronous ac winding with one slot per pole per phase, (c) short pitched synchronous ac winding with two slots per pole per phase and (d) synchronous ac winding with one slot per pole pair per phase. By applying Carter coefficient [49] and dimensions, radial air gap field distribution can be estimated thus the phase flux linkage, EMF and the thrust.

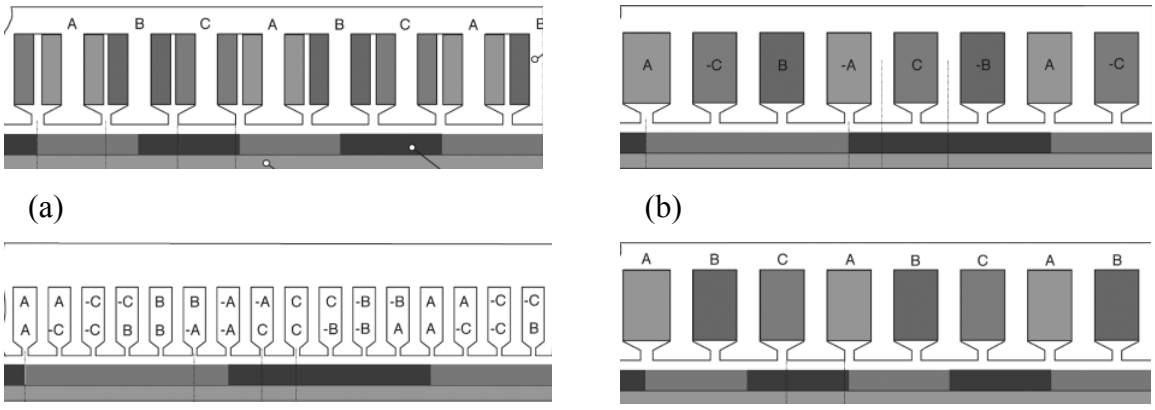

(a) (b)

(c) (d)

Figure 2.19 Different armature winding topologies [48]

The presence of permanent magnets and their interaction with the shorter slotted stator results in a cogging force, which manifests the translator in the tendency of the armature slot align in a position with minimum magnetic energy. J Wang gave two strategies to minimise aforementioned cogging force. In [50] the study is based on the work done in [49] (which already successfully related topologies' dimensions to the output cogging force), the result shows optimising armature core length can effectively reduce the cogging force. In [51] a more conventional way as skewing (a) or stepping (b) armature end face is used (figure 2.20), the principle of these strategies is more like that in rotary topologies, by skewing stator with the angle of slot pitch or short pitch this angle the cogging can theoretically drop to zero.

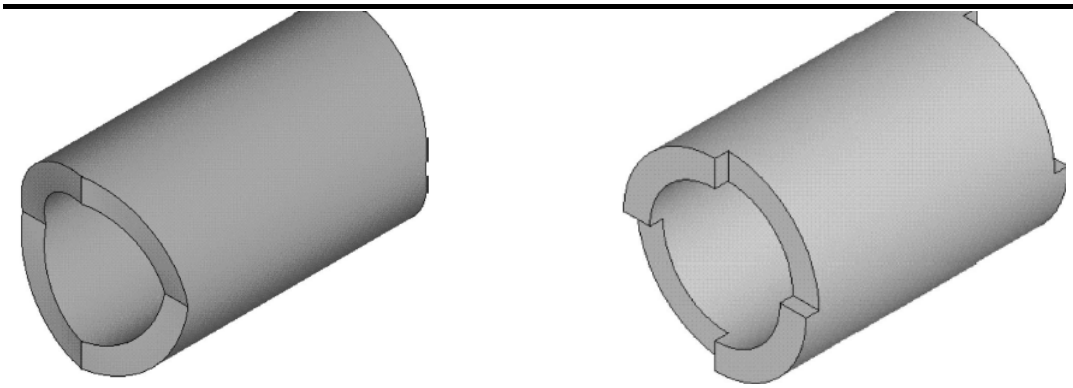

(a). Skewing (b). Stepping

Figure 2.20 Skewing and stepping strategies for cogging force reduction [51]

In 2007 again J Wang performed a permanent magnet machine for work with the Free-piston Engine as shown in figure 2.21. Different from topologies above, this topology has three phase, nine slots/ ten poles and quasi-Halbach magnet array [52]. With such armature topology the cogging force is initially small, and with such translator topology, the moving part mass can achieve minimum. The designer will use this stator topology with different translator magnets arrays to compare with the other two alternatives (transverse flux and flux switching machines) in Chapter 3.

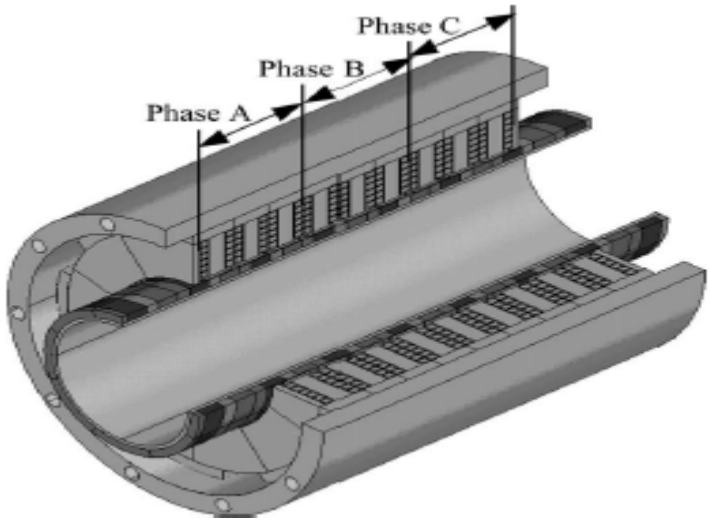

Figure 2.21 Schematic of 3-phase, 9-slot/10-pole, tubular PM machine with quasi-Halbach magnetised armature [52]

2.6 Developments of Transverse Flux Machine (TFM) Topologies

The concept of the TFM was firstly invented by Weh in 1986 [53] because of its high thrust density. The magnetic flux loop of conventional machines shows two dimensional (2D) feature, due to the stator tooth and winding are coupled on the same plane thus this mutual restriction makes its hard to increase the thrust density fundamentally. TFM can

simultaneously offer longitudinal and transverse magnetic flux direction as a three dimensional (3D) magnetic flux loop. Thus the tooth structure can be made as perpendicular to the winding space. Sizes of stator tooth and winding can, therefore, be chosen arbitrarily in some manner which can decouple the magnetic and electric loading, thus achieve possibility to increase the thrust density.

TFM is a promising topology [54] and has the following advantages compared to conventional longitudinal flux machine (TFM): 1. 3D magnetic flux characteristic achieves the decoupling of electric and magnetic loading namely high thrust density; 2. High designing flexibility on machine topologies, when all other parameters are constant the thrust output is proportional to the pole pair number; 3. Easy armature winding configuration. Independence between phases causes high fault tolerance in phase-deficient operation which can increase the system reliability [55]. In other words, three identical phases can be placed with 120 electrical degrees to form a three-phase topology, and each phase works individually without flux interference to the other two phases. Drawbacks of high flux leakage and low power factor are mentioned in Chapter 1. What is more, the complexity of machine topology also force up the building cost. TFM is a developing machine topology and flexible to design, so far TFM can be classified into four types depending on the magnet excitation conditions: reaction rail mounted magnet, flux-concentrated, armature mounted magnet (flux switching and flux reversal) and reluctance topologies [54] [56].

In figure 1.3 are single and double-sided reaction rail mounted magnet topologies, for this type, magnets are mounted on the reaction rail (translator) with opposite polarity to the adjacent pole, the stator iron cores are distributed along the translator with a pole pitch distance. For single-sided topology a severe drawback is the low use rate of translator magnets namely only half magnets contribute to the no-load peak flux linkage, double-sided topology can overcome this problem in some manner but the resulting complex structure could drag down the mechanical robustness and increase the building cost. In the linear machine topology with the tubular structure, it is fundamentally not possible to form a double-sided topology, [57] [58] present a novel tubular linear TFM topology (figure 2.22). For this topology the winding can be wounded around a single teeth stack length or the total active length, magnets can be arranged radially, axially or with Halbach array, but anyhow low magnet use rate is unchangeable.

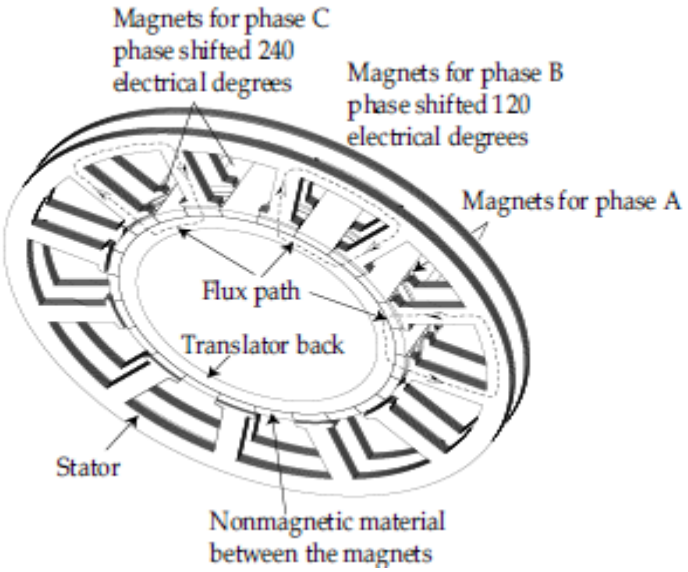

Figure 2.22 A novel tubular linear TFM use for Free-Piston Engine [58]

The flux-concentrate seems to be the most popular topology at present due to its high use rate of magnets. Figure 2.23 is a typical structure of the flux-concentrate topology discussed in [59], for each pole pair the interleaved stator tooth conducted both magnets to form a closed flux loop as no-load flux, ignoring the flux leakage the use rate of the magnet could achieve 100%. For this topology, the air gap flux density is fundamentally high, but since the flux loop contains all 3D directions thus expensive SMC material is required to build the machine, also the complex structure is another difficulty need to consider.

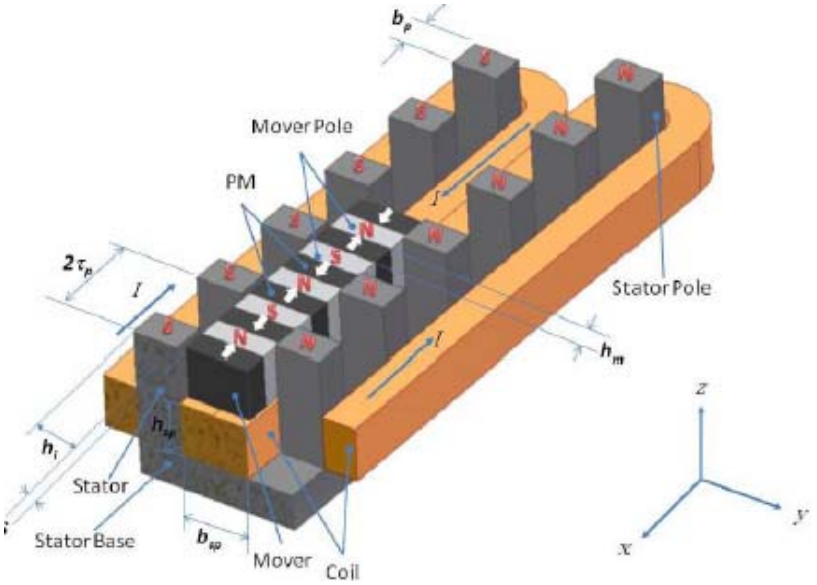

Figure 2.23 A typical linear TFM topology use for Free-piton Engine [59]

In 2012 an outer rotor three phase TFM was designed in Newcastle University [60], in figure 2.24 is a pole pair structure for a single phase topology. It is a flux-concentrate type topology

also named as modulated pole machine (MPM), the no-load flux loop is well explained with labelled arrows: flux is concentrated from two magnet poles (1) then conducted through (2)-(5) finally closed to (1). Two different stator topologies are investigated: separated phases model and combined phases model as shown in figure 2.25, it is reported that the combined model can achieve 10% improvement on fundamental EMF as well as torque output.

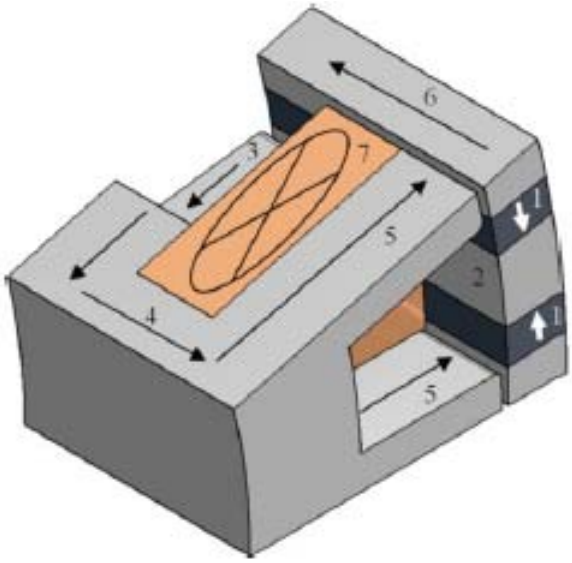

Figure 2.24 one pole pair structure for MPM topology [60]

(a). separated phases (b). combined phases

Figure 2.25 two models of three-phase MPM [60]

The material hybrid concept is used in this topology to form a fully 3D flux path as illustrated in figure 2.26 [61]. Conventional silicon steel stator laminations are used to supply radial flux path, SMC material is used in the rotor (sandwiched by magnet poles) and auxiliary core back (encircle the whole stator) to supply axial and transverse flux path. The designer will perform a linear MPM topology based on this study to compare with other two alternatives (permanent magnets and flux switching machines) in Chapter 3.

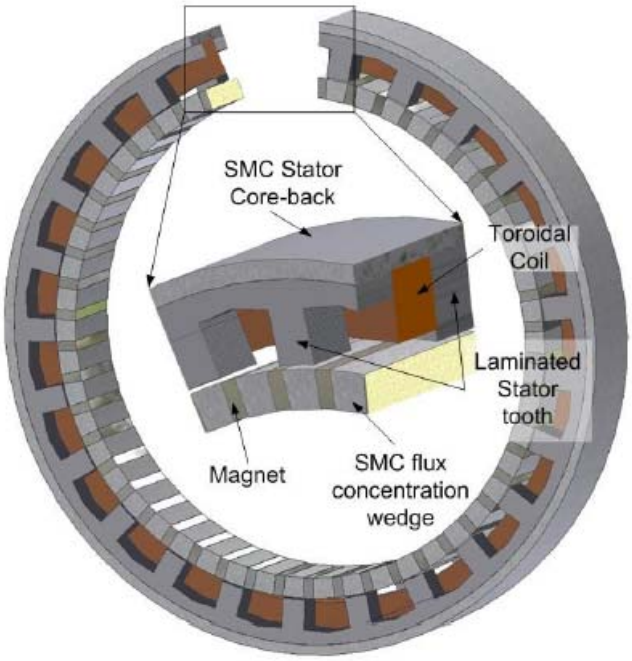

Figure 2.26 Material hybrid concept in MPM [61]

The armature mounted magnet topology is based on the reaction rail mounted magnet topology namely move the magnet to the stator side and lean the translator with a pole pitch. For this topology, the machine structure is relatively simple and easy for manufacturing, but the additional magnet requirement makes this topology not popular among the research community [54]. One topology example from [62] is shown in figure 2.27 where the flux leakage as shown in the blue loop will increase the magnet material used to achieve required thrust. This topology is also regarded as the flux switching machine topology with transverse flux characteristics.

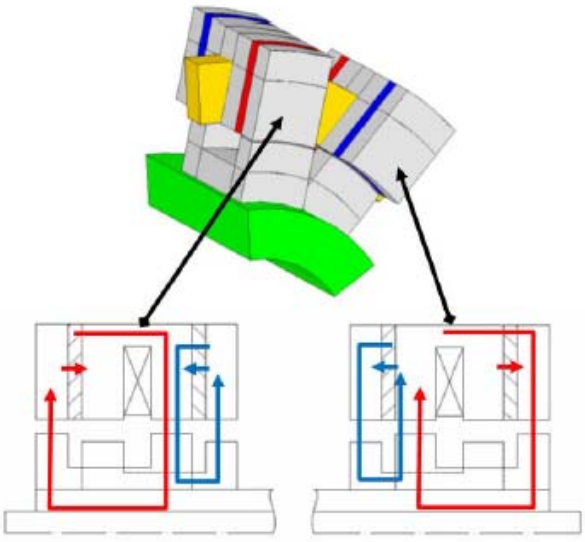

Figure 2.27 An example of armature mounted magnet TFM [62]

If taking the magnet in flux-concentrate or armature mounted magnet TFM away from the stator, by applying armature current, the thrust still can be produced; the complete machine is named as reluctance TFMs (figure 2.28). The same as the conventional switch reluctance machine working principle: the flux always follows the path with minimum reluctance, if applying the current to the stator then the rotor will be forced to align to the stator tooth [63]. The reluctance TFM produced thrust direction has nothing to do with the winding current direction, rotating direction is determined by the phase switch sequence, the simple structure, low cost and easy control make this topology applicative for some occasion, but the low thrust density constrains its development.

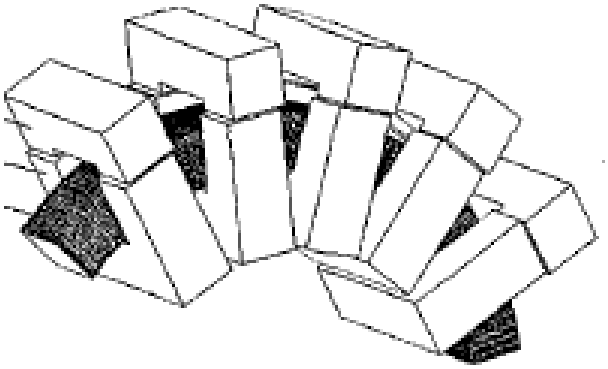

Figure 2.28 a reluctance TFM topology example [63]

For all above four types of TFM topologies, reaction rail mounted TFM and reluctance TFM show simple structure but low thrust density compared to flux-concentrate TFM. So far flux-concentrate TFM shows far more advantages (thrust density and power density) compared to the other three as the most promising TFM topology [54]. With the improvement of manufacturing process level, it has the most application development prospect.

2.7 Developments of Armature Mounted Permanent Magnet Topologies

One decent topology of the armature mounted permanent magnet topologies is the flux switching topology (FS). The concept of the FS topology was introduced in [64] (1955). In figure 2.29 are schematic diagrams for a rotary single phase topology with two different rotor positions. If define at position ‘a’ the coil flux linkage is at peak value, then position ‘b’ is when the coil is at negative peak value, this peak-peak spans a 180 electric angle. Namely, when the salient rotor spans 90 mechanical angles, the armature EMF spans 180 electric angles. In a conventional synchronous machine, such rotor structure means a two pole machine and should have the same electric angle as the mechanical angle. Thus in FS, for each pole pair the rotor need only one salient tooth then a simple and robust rotor structure can be achieved.

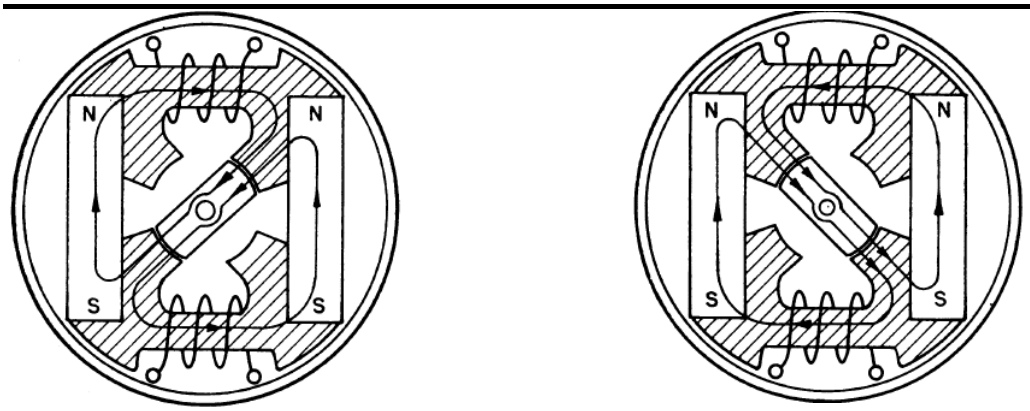

'a' position 'b' position

Figure 2.29 Schematic diagrams with a pole pitch difference [64]

To achieve a three-phase topology, fractional slot/pole pair combination need to be applied to the FS topology. From 1997 to 2008 combinations of 12/10 and 12/14 combinations were pointed out that can achieve a possible three-phase topology with good performance [65]-[68]. 6/5 and 6/7 are also feasible to form a balanced three-phase [69] but with a highly attractive force due to the unbalanced magnetic force of attraction. Thus it is necessary to double this combination to offset this force [70]. In fact combinations of 6/5 and 6/7 are sufficient in tubular linear FS version as the attractive force is naturally offset by the tubular feature. Similar to those in figure 2.19, possible winding configurations for above linear FS (FS) combinations are in figure 2.30 with their winding vector analysis in figure 2.31 [71].

Since the electric span is 360 degree between two adjacent translator teeth, thus the slot span is 300 electric degree for 6/5 and 420 electrical degrees for 6/7 combinations. An example to analyse the winding vector in double layer winding phase A with 6/5 combination: firstly assuming A1 is at 0 degrees then A2, A3, A4 are at 300 degrees, 900 degrees and 1200 degree which are equivalent to 0, 300, 180, and 120 degrees. Secondly, by considering the magnet polarity (if polarity changes electric angle + 180 degrees), the electric angles for A1, A2, A3 and A4 are 0, 480, 360, and 120 (equivalent to 0, 120, 0, and 120). Finally, by considering the winding polarity (+ 180 degrees if polarity changes), the angles then be updated to 0, 300, 0, 300 (as shown in figure 2.31). As a result double layer and single layer winding shall have a 60 electric degree short pitch angle which will discount the output with a 0.866 winding factor, monopolar winding can achieve one winding factor but may require for complicated winding installation process [71].

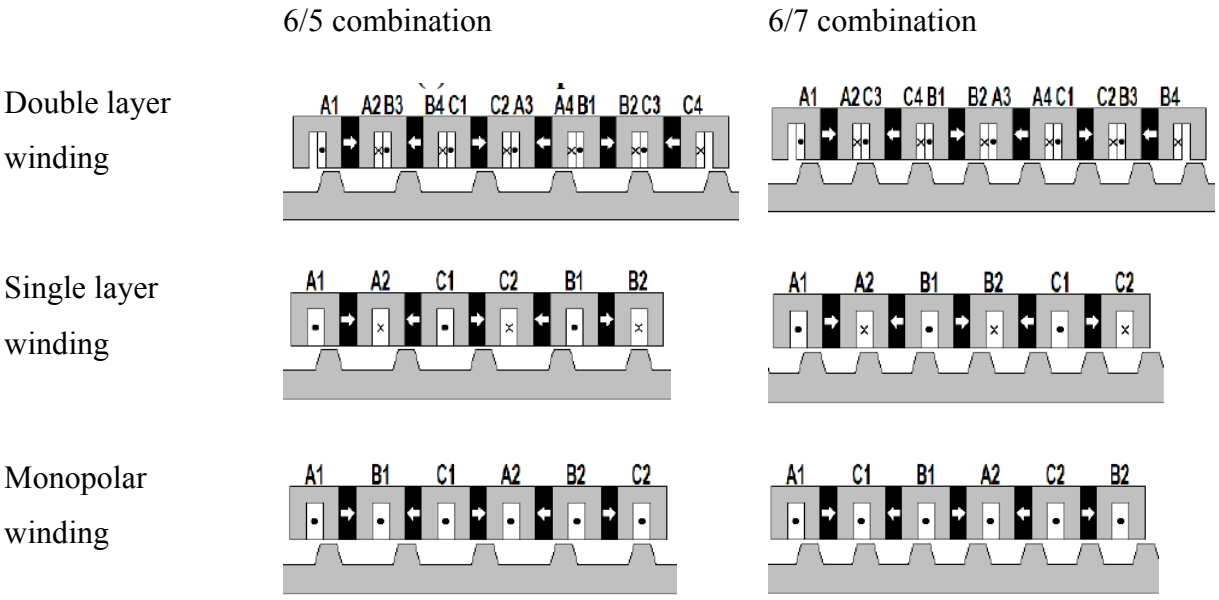

Figure 2.30 Winding configurations [71]

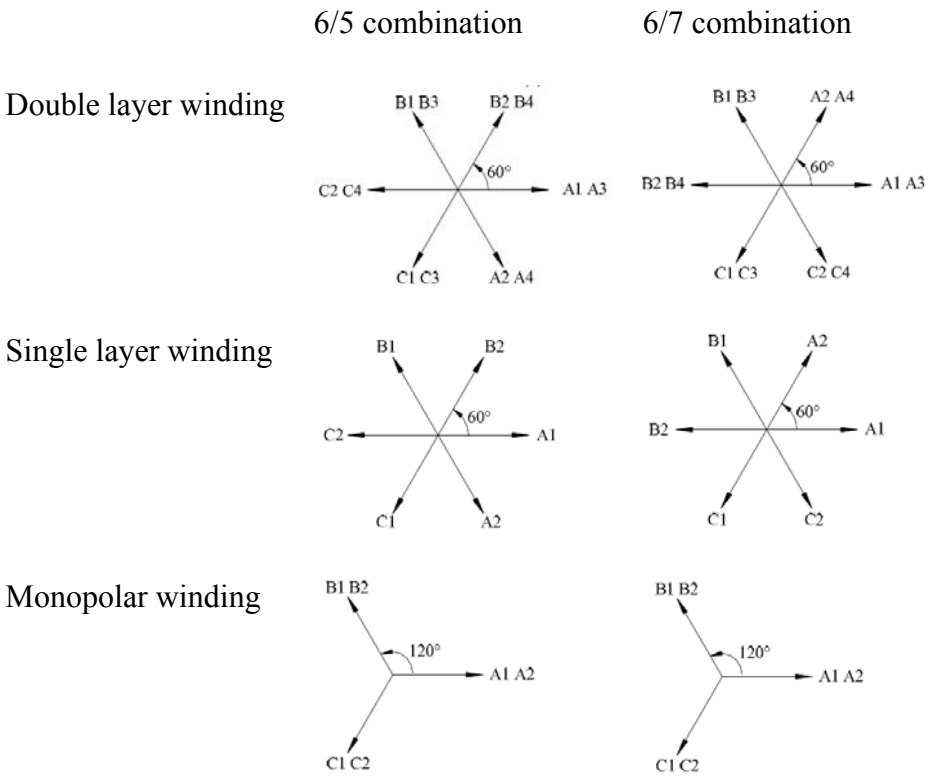

Figure 2.31 Winding vectors [71]

Another armature mounted magnet topology also named as linear Vernier machines [72] are in figure 2.32, which share similar working principle as topologies above but with magnets adhered on the surface of stator tooth (working as flux reversal topology). For this type of topologies due to a large number of poles and bulky machine size, it shows advantages of low

speed and high thrust direct drive application as railway traction and waves energy conversion. (but not favourable to use with Free-Piston Engine). [72] reports that topology with one piece stator (in figure 2.32(a)) can achieve better thrust capability and lower cogging thrust.

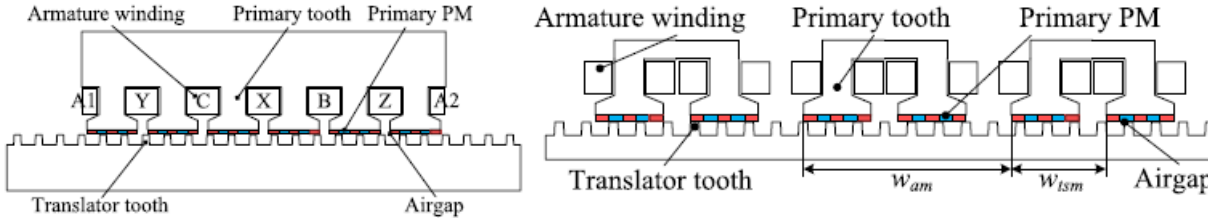

(a). one piece stator topology (b). hybrid topology

Figure 2.32 Linear vernier machine topologies [72]

For all above topologies belong to longitudinal flux machine (LFM) family, which are currently popular among the research community. The TFM family also have flux switching type topologies, an interesting topology [73] based on that in figure 2.27 is presented in figure 2.33 with main no load flux path sketched in wireframe diagram. Since it inherits the feature of TFM, the winding arrangement is not a concern to form a three-phase topology. It is reported that by using this topology, the mechanical installation can be much simplified with only about 30% torque /magnet density loss compared to the MPM topology. The designer will perform a linear version of this topology as FS to validate this conclusion in linear topology and compared to other alternatives (RRPMs and MPM) in Chapter 3.

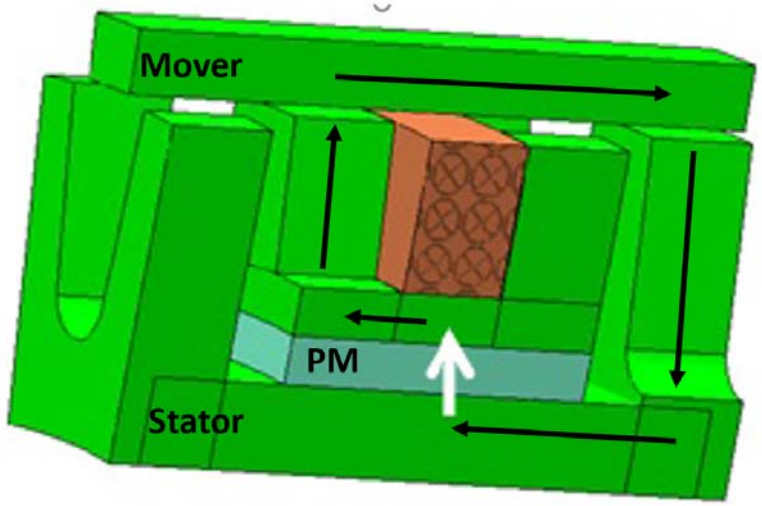

Figure 2.33 An novel FS topology with TFM characteristic [73]

2.8 Fundamentals of Electromagnetism and Use in Electric Machine Design

Fundamental electromagnetic parameters include voltage V, current I, magnetic flux φ, magnetic motive force F (or MMF), magnetic flux density B and magnetic strength H and

their relations are as shown in figure 2.34. Two important laws are: Faraday's law illustrates that varying magnetic flux can produce voltage and Ampere's law explains that electric current and vice versa can generate magnetic fields. Depending on the conducting material a certain magnetic field can produce a certain level of magnetic flux density in a nonlinear trend. If applied dimensions for this material with a closed loop then electric current can produce a flux flowing in this loop in a nonlinear trend, the ratio of the current to the flux shows the material's magnetic conductivity which also named as reluctance. The electric conductivity of the material is defined as resistance which is the ratio of voltage and current as Ohm's law.

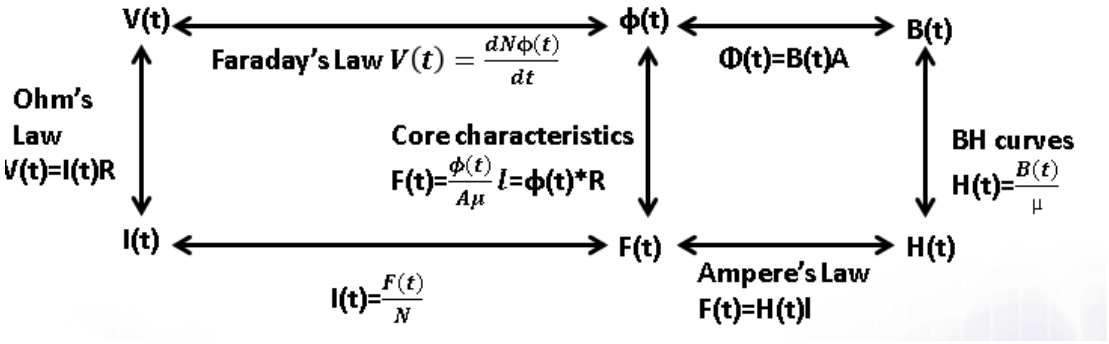

Figure 2.34 Fundamental electromagnetic parameters' relations

Between 1861 and 1862 James Clerk Maxwell published the early form of Maxwell's equations and first proposed that light has an electromagnetic phenomenon [74]. Maxwell's equations are a set of equations (simplified integrally formed equations in space area are as shown in equation. 2-1 to equation. 2-4) that together with the Lorentz force law based on the fundamental electromagnetism, classical optics, and electric circuits. They underpin all electric, optical and radio technologies, including power generation, electric motors, transformer, wireless communication. Thanks to these equations and their related theories, modern electric and electronic engineering can achieve a fast development.

$$\oiint_S E \cdot ds = \frac{Q}{\varepsilon_0} \tag{2-1}$$

E is the electric field strength, Q is net charge number, ε_0 is the vacuum permittivity. This equation is also known as Gauss's law, which illustrates the relations between the electric flux and charge number. Namely in vacuum space for a closed surface, by counting the number of the electric flux then the net charge number inside this surface can be calculated. In other words, the electric flux must flow from a positive charge and ends at a negative charge. The voltage difference is defined as the work done by per unit charge against the electric field as $dV = \frac{dW}{q} = Edl$.

$$\oiint_S B \cdot ds = 0 \tag{2-2}$$

B is the magnetic flux density. This equation is also known as Gauss's law for magnetism, which illustrates the characteristic of a dipole or as a 'magnetic unit'. The magnetic flux must starts from the N pole of a magnet unit and return to the S pole of it. Even breaking the magnet unit into pieces, each piece still contains N and S pole (or that the magnetic field is a solenoidal vector field from current). Thus if a closed surface is surrounding a magnet unit, then the magnetic flux exiting it must equal to that entering it. Similar to equation. 2-2, for a closed loop of the magnetic circuit$\int H\, dl = 0$.

$$\oint_l E \cdot dl = -\frac{d\Phi_B}{dt} \tag{2-3}$$

Φ_B is the flux linkage. This equation is Faraday's law, which illustrates how the magnetic field generates an electric field. Namely when the magnetic flux is varying by time, then a voltage can be produced in the open circuit conductor.

$$\oint_l B \cdot dl = \mu_0 I + \mu_0 \varepsilon_0 \frac{d\Phi_E}{d_t} \tag{2-4}$$

μ_0 is the vacuum permeability, I is current, Φ_E is the electric flux. This equation is Ampere's law with Maxwell's addition, which illustrates that the magnetic field can be produced by not only the current but also the varying electric field. Although Ampere's law illustrates the relationship between current and magnetic flux strength, however with Maxwell's addition, it proves the reversibility of Faraday's law. Also by using Ampere's law, the value of current can be calculated which used to substitute magnet.

The design of the electric machine is based on above equations and their related theories: for example, the topology design is related to equation. 2-2 and the magnetic circuit; the EMF is calculated based on equation. 2-3; the Ampere's law part in equation. 2-4 can be used to transfer magnet excitation to current excitation. Other parameters include the thrust/torque is calculated based on the Lorentz force law; the self/mutual/ armature inductance is calculated based on the reluctance network; the power factor is calculated depending on the EMF, inductance and excited condition (phase angle).

In electric machine design, the most critical performance is the torque or thrust depending on whether it is rotary or linear topology. If using a current source, depending on parameters in figure 2.34 and the Lorentz force law, the size and torque/ thrust can be related as shown in equation. 2-5 for rotary topology and equation. 2-6 for linear topology.

$$T = Fr = BILr$$

$$= \int_0^{2\pi} B \sin\theta \sqrt{2} A \sin(\theta + \psi) \div 3 \times 2\pi r l_a \, r \times 1.5 d\theta$$

$$= \sqrt{2} B A V_{rotor} \cos\psi \quad (2\text{-}5)$$

$$F = BIL$$

$$= \int_0^{2\pi} B \sin\theta \sqrt{2} A \sin(\theta + \psi) \div 3 \times 2P\tau l_c \times 1.5 \, d\theta$$

$$= \frac{\sqrt{2}}{2} B A S_{translator} \cos\psi \quad (2\text{-}6)$$

B is the peak air gap flux density as magnetic loading; A is the rms total MMF divide by rotor outer circumference length in equation. 2-5 and divide by translator active length in equation. 2-6; $\sqrt{2}$ is the factor that transferring the rms to the peak; 3 is three phases; l_a is the stack length, and r is the outer rotor radius for rotary topology; P is the pole pair number, τ is the pole pitch distance, l_c is the translator width for linear topology; 1.5 is the vector sum factor for three-phase machine, ψ is the phase angle. Thus it can be found that rotary machine torque is proportional to the rotor volume and linear machine thrust is proportional to the translator active surface area. BA is also regarded as shear stress which used to evaluate loading conditions.

The power factor reflects the loading condition too and indirectly influence the machine efficiency, which related to the EMF, armature current and armature inductance. As shown in figure 2.35 is a general phasor diagram of the synchronous machine when $\psi$is 0. Equation. 2-7 and equation. 2-8give details of the phasor diagram vector, where I_q is the armature phase current, X_q is the armature reactance, n is phase turns, w_s is the synchronous angle speed, R is the equivalent reluctance, $\hat{\phi}$ is the phase peak flux, f is the electric frequency of armature current, K_w is the winding factor, σ is the load angle and V is the phase terminal voltage.

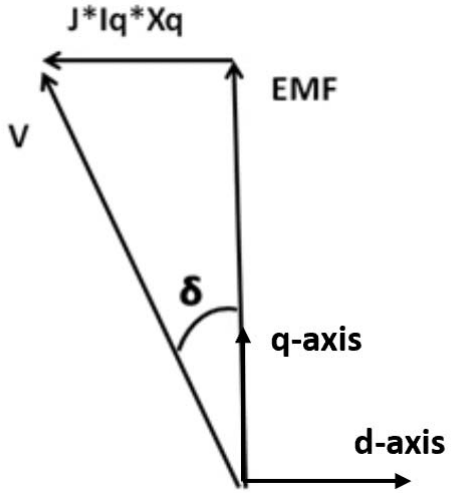

Figure 2.35 Phasor diagram

$$I_q X_q = \frac{MMF_{rms}}{n} \omega_s \frac{n^2}{R} = \frac{MMF_{rms} \times n \times \omega_s}{R} \tag{2-7}$$

$$EMF_{rms} = \frac{2\pi}{\sqrt{2}} n \hat{\phi} f K_w \tag{2-8}$$

The losses associated with the electric machine can generally be classified into four types:

- The copper loss which is produced in the winding coils, the value can be determined based on Ohm's law once the current waveform is known. Effects such as skin and proximity effect must be considered in large or high-frequency machines.
- The iron loss (eddy current loss and hysteresis loss) is related to both the flux density and supply frequency of the machine. Where the eddy current is produced based on Faraday's law that applied in the magnetic iron core of the machine and PM materials, hysteresis is related to the magnetic material property as shown in Fig, 2-1.
- The stray loss due to the leakage filed which is similar to the eddy current loss but produced in the core of the machine and other solid conducting components. This loss is tough to predict and is generally in design calculations empirically based on previous experiences.
- The friction and windage losses which are related to the mechanical aspect.

Typically when dealing with a low-speed machine, the copper loss is regarded as the central loss that used to estimate the machine efficiency, and for the high-speed machine, the iron loss must be taken into consideration. Stray loss and friction loss usually can be ignored when

it comes to design a small sized machine. The designer will only take copper and iron loss into estimation in the simulation study in Chapter 3 and 4.

2.9 Finite Element Analysis and MagNet Software

The finite element analysis (FEA) is a method which uses the mathematical approximation to simulate the real physical system. Namely simplifying a big complicated system to a lot of small, simple units, then calculate the approximate solution for each unit and combine all results to derive an approximation for the original system. FEA can achieve high accuracy and is an effective method for engineering analysis. Finite elements are discrete units that can represent the actual continuous domain when they are combined. The concept of finite elements can be traced back to centuries ago such as using a polygon to approximate the circumference of a cycle. In the early stage, FEA is regarded as matrix approximation method which used to calculate the structural strength of the aircraft, its convenience and effectiveness cause a keen interest of the researchers. After few decades' efforts, with the rapid development and popularisation of computer technology, the finite element method has rapidly expanded from the analysis of structural engineering strength analysis to almost all the fields of science and technology. Since FEA contains typically enormous calculated quantity thus the use of the software is inevitable, MagNet is one such software that using FEA to work on electromagnetic problems.

MagNet is an advanced software that currently available for modelling electromagnetic devices on a personal computer. It provides a virtual laboratory in which the user can create models from magnetic materials and coils, view displays in the form of field plots and graphs, and get numerical values for quantities such as flux linkage and force. A MagNet user needs only an elementary knowledge of magnetic concepts to model existing devices, modify designs and test new ideas. MagNet is designed as a full 3D modelling tool for solving electromagnetic problems that can involve static magnetic field, varying time fields, eddy currents and dynamic conditions with the motion. Also, MagNet offers the option of 2D modelling with a substantial saving in computing resources and solving time. A feature of MagNet is the use of latest methods of solving the field equations and calculating quantities such as force and torque. To get reliable results, the user needs to make the trade-off between running speed and accuracy, however in 2D simulation results could be obtained very rapidly but in 3D simulation, it could take considerable time to get accurate results. In this project, the designer will perform 2D modelling to the RRPMs' topologies since their magnetic field shows a longitudinal feature. As for MPM and FS, 3D modelling will be applied to simulate fully 3D magnetic field in the machine.

2.10 Summary

From the literature review above, material and electromagnetic fundamentals based on the machine have been reviewed. Permanent magnet electric machine type has been selected from early linear topologies for the target machine design. Through widely investigated permanent magnet machine topologies, histories from three main topology types (conventional reaction rail mounted permanent magnet, TFM and armature mounted permanent magnet) have been nominated. From the most recent studies, three featured topologies of above types have been targeted and decided to move on in this research.

To sum up, there will have mainly three machine topologies (RRPMs, MPM and FS) be compared based on both their static and dynamic performances. Force, power factor, efficiency and components' mass will be treated as essential factors of the machine performances. Both simulation and numerical solutions will be performed, where simulations will proceed in finite element analysis software, and numerical solutions will be performed from machine fundamentals. Chapter 3 will discuss detailed comparisons of all three main topologies.

Chapter 3. Comparison of Reaction Rail Mounted Magnets, Modulated Pole and Flux Switching Machines

3.1 Introduction

In this Chapter three main machine topologies will be investigated: reaction rail mounted permanent magnets with nine stator slots to ten pole combination (RRPM), transverse flux with modulated pole structure (MPM) and flux switching type (FS). Topologies' dimensions will be optimised by using the optimisation tool OptiNet, and output performance will be compared in finite element analysis tool MagNet. Detailed analysis on MPM and FS will be performed with different optimising strategies and improved tooth structure. Influences of different pole pair numbers and different active length to stroke length ratios will be expanded. As a result, MPM will be selected for later mechanical structure design due to its high efficiency, high flux loading and high power factor.

3.2 Machine Topologies

Three machine topologies are nominated to investigate as permanent magnet machine (RRPM), modulated pole machine (MPM) and flux switching machine (FS). All three types use magnets to supply the main field, the advantage of using magnets is mainly to reduce mechanical difficulty such as minimising machine volume, allowing higher machine air gap, simplifying translator structure. The concomitant drawback is the high cost of the magnet material.

RRPM is one of the LFMs' family member with magnets mounted on the longer translator as shown in figure 3.1 below. However different from that in figure 1.3, RRPM using a fractional slot per pole modular permanent magnet machine topology, which is reported as the most appropriate topology for working with a Free-Piston Engine [75]. It is composed of a three-phase, nine slot /ten pole combination an equipped with a modular stator winding in which coils of each phase are disposed of adjacent to each other. This topology would result in a high winding factor (close to 0.946 where 0.985 of the short pitch factor and 0.960 of the distributed factor) and virtually zero cogging force on the armature slotting without the need of skewing [75]. In fact, eight poles topology shares the same winding factor as ten poles topology and less pole number could achieve less electrical frequency at the same working speed thus lower iron loss. However, the designer finds out ten poles topology could achieve the best overall performance of MPM in later studies. For a fair comparison, the designer decides to use ten poles for all machine topologies' design.

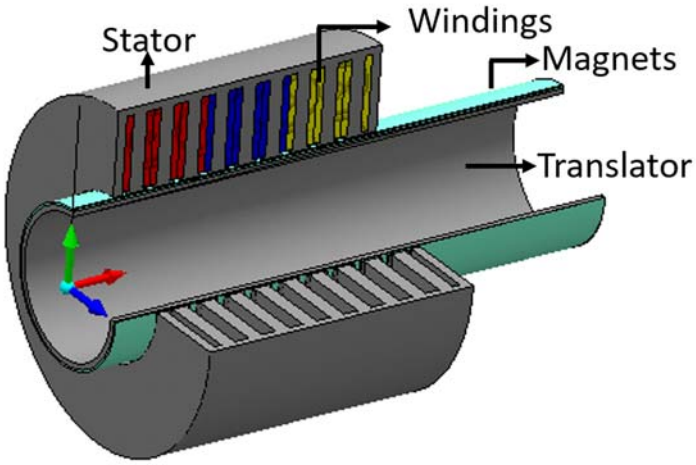

Figure 3.1 Permanent magnet machine topology

There are three magnet orientations for RRPMs: radial, axial and quasi-Halbach array. Quasi-Halbach magnetised magnets comprising radial and axial magnet in each pole pair to form a substantially sinusoidal distributed air gap flux density. As reported in [75] Quasi-Halbach magnet array can essentially provide a return path for radial flux hence the flux in translator core back is relatively small compared to that in the air gap. As a result, less soft magnetic or even non-magnetic material can be used to construct translator core back, thereby to minimise the moving part mass. As reported in [76] 2.85 kg for the quasi-Halbach array, 4 kg for radial array and 4.8 kg for the axial array. More detailed comparison among these three magnet orientations will be unfolded in later sections.

MPM belongs to the family of TFMs with magnets axially mounted on the longer translator separated by iron pole pieces, which acts as a flux concentrator. Three phase windings are evenly distributed on the stator with the same direction as moving direction. With this topology, the phase EMF unbalance issue could be removed since all three phase windings are surrounded with the same set of iron teeth and cover 120 mechanical degrees around the circumference of the translator (figure 3.2). From [76] this MPM topology can achieve less copper loading (21% of quasi- Hallbach RRPM without considering end windings). However the translator and total machine mass require double of those in quasi- Halbach RRPM.

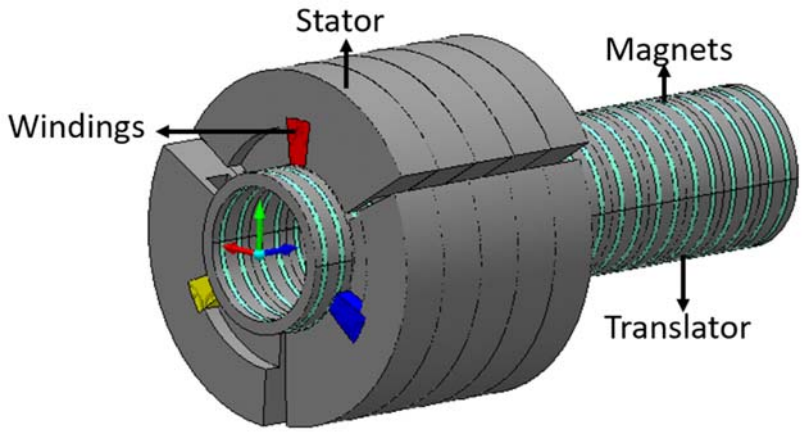

Figure 3.2 Modulated pole machine topology

For both RRPMs and MPM, magnets mounted on the translator resulting a problem that machine only use half the magnets at any time, with the other half not interacting with the stator. To tackle this, FS is nominated for investigation based on TFM topology. As shown in figure 3.3 FS has only one piece of magnet energised in outwards radial direction mounted on a single phase stator. The translator consists of isolated iron pole pieces which align to each stator pole, a rotating counterpart is discussed in [77]. FS shows potential to save the magnet material usage in concept however due to the high flux leakage factor FS then being excluded from target Free-piston Engine application [78] [79].

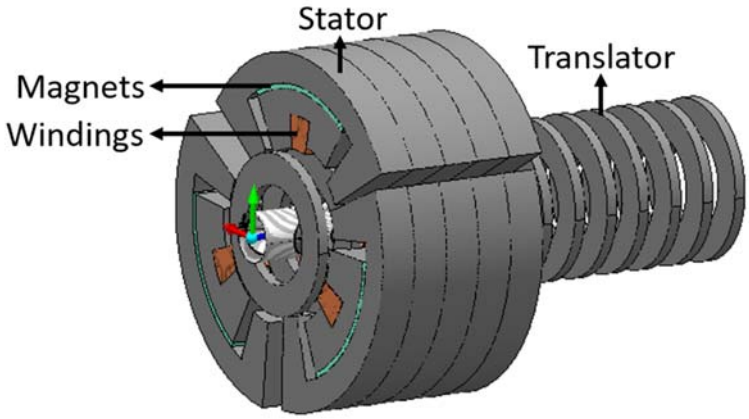

Figure 3.3 Flus switching machine topology

All these three topologies are nominated through the literature review of related research areas about linear machine design. Detailed comparisons of their performance will be expanded in later sections, and MPM will show superior performance among the other two topologies.

3.3 Finite Element Analysis Modelling

Based on machine dimensions, input power source and motion source, MagNet can simulate electric performance including no load and armature current flux field by using finite element analysis modelling. Based on fields profile it becomes possible to calculate output parameters including flux linkage, voltage, force, loss. Shown in figure 3.4 is an example of the RRPM with radial magnet array (RRPMR) topology and its flux plot at this position. With armature winding open circuited, the central (blue) phase is enclosed by equivalent zero field flux, namely the no-load flux linkage is zero. When applying motion to the translator, a continuous flux linkage profile will be produced in the blue phase as shown in figure 3.5(a) and its corresponding voltage profile (EMF) is as shown in figure 3.5(b), where the voltage waveform is the gradient of the flux linkage waveform. The other two phases have similar EMF waveform with 120 electric degrees difference as shown in figure 3.6(a). EMF waveforms have harmonic distortion which causes waveforms different from a pure sinusoidal shape. In figure 3.6(b) is the harmonics spectrum corresponding to phase blue.

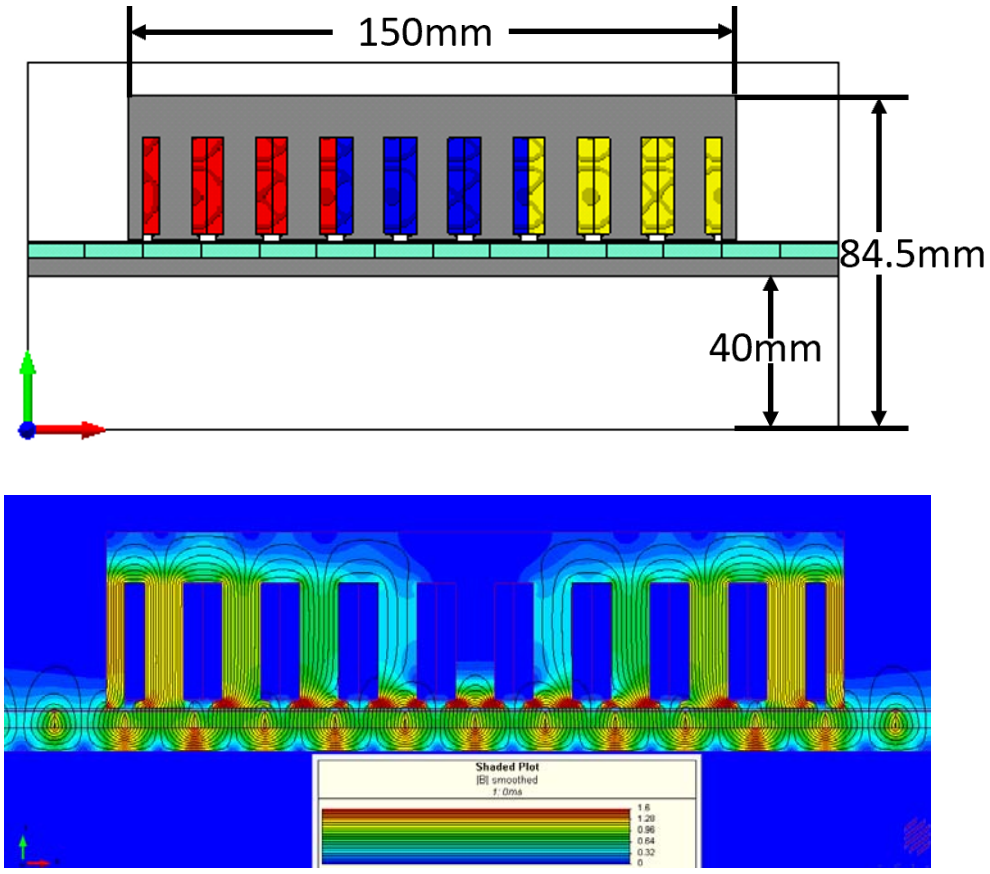

Figure 3.4 An example of radial RRPM topology and its flux plot

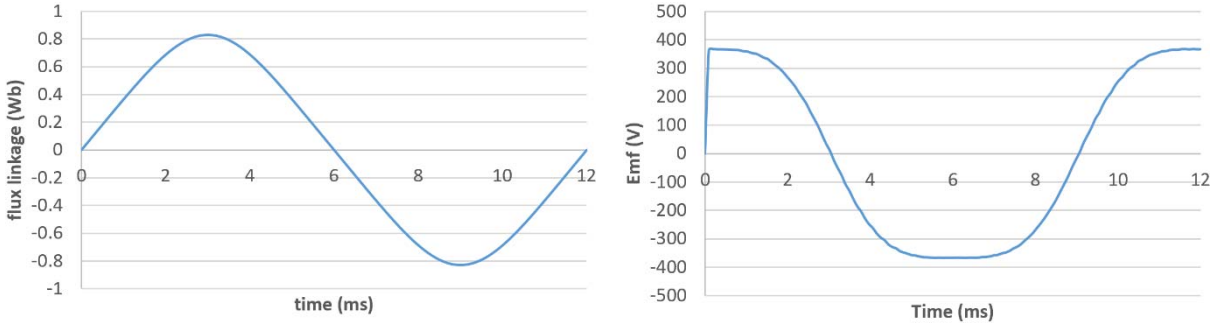

a b

Figure 3.5 Motion produced flux linkage and EMF

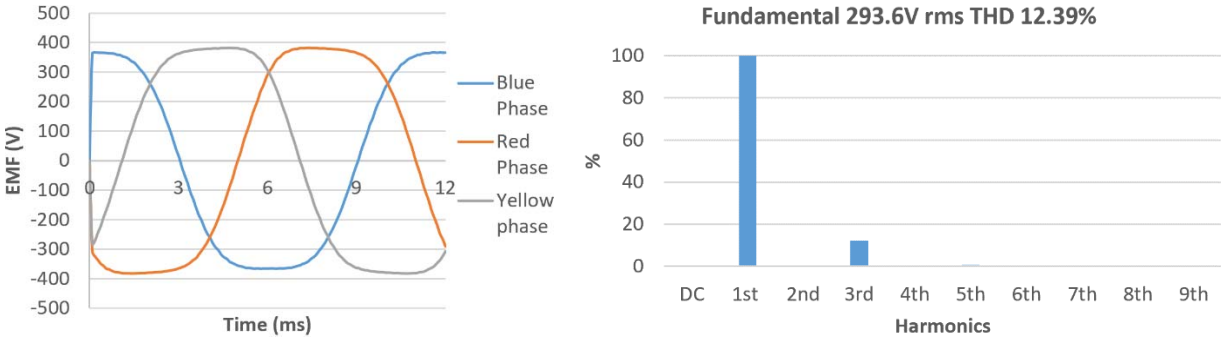

a b

Figure 3.6 Three-phase EMF and blue phase harmonics content

When sinusoidal armature currents are applied to phase windings as shown in figure 3.7, the produced force is as shown in figure 3.8. In figure 3.7 it can be seen that phase current is set to be in phase with EMF waveforms in figure 3.6, in other words, the phase angle β is zero as in equation. 1-2, and in this case the magnetic force can achieve the maximum. The force profile in figure 3.8 contains the cogging force waveform (red) and the magnetic force waveform (blue) along with a pole pair pitch. The cogging force oscillates around zero which is produced by the interaction between tooth and magnets. The magnetic force is a combination function of all three phases which is similar to the rectification theory, each phase can produce a force close to a sinusoidal shape, and the sum of all three phases will result in a constant force with ripples on it. The force waveform is the most critical output parameter of a machine. MagNet can simulate the force output based on air gap flux density and armature current profiles while motion or position constraints are applied. It means that an estimation of output force can be simulated in either dynamic or static solution. In this section, all results are extracted from the dynamic solution however in next section the optimisation will use static solution to minimise the simulated points thus shorten the computation time.

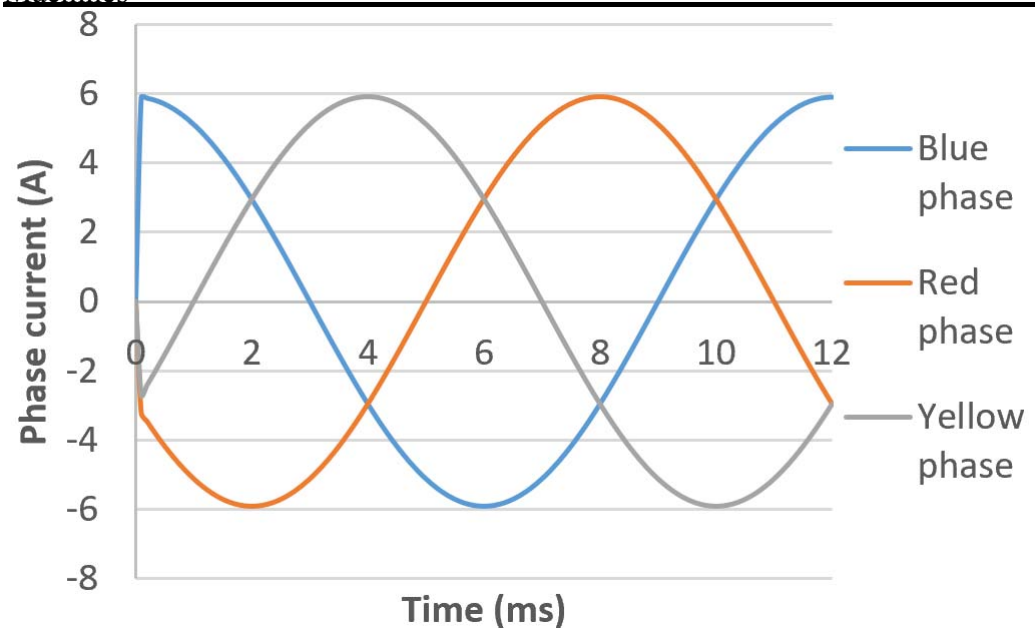

Figure 3.7 Currents waveform

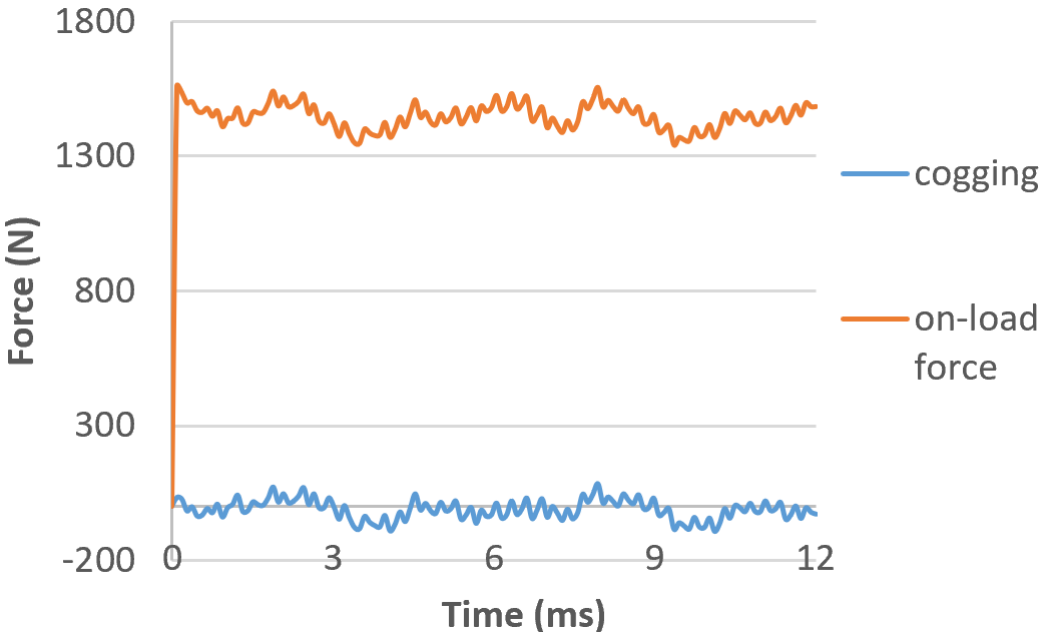

Figure 3.8 The force profile

MagNet can extract the airgap flux density profile, and figure 3.9 is the air gap flux density waveform of the blue phase. The average value of this flux density and the corresponding phase MMF can be used to estimate the produced force of blue phase by applying Lorentz's law. Figure 3.10 is the average flux density profile of the blue phase for a pole pair pitch. Based on this profile, phase current and total coil length the force produced can be calculated. All three phases produced force, and their sum is in figure 3.11 which show the consistency of the simulation result.

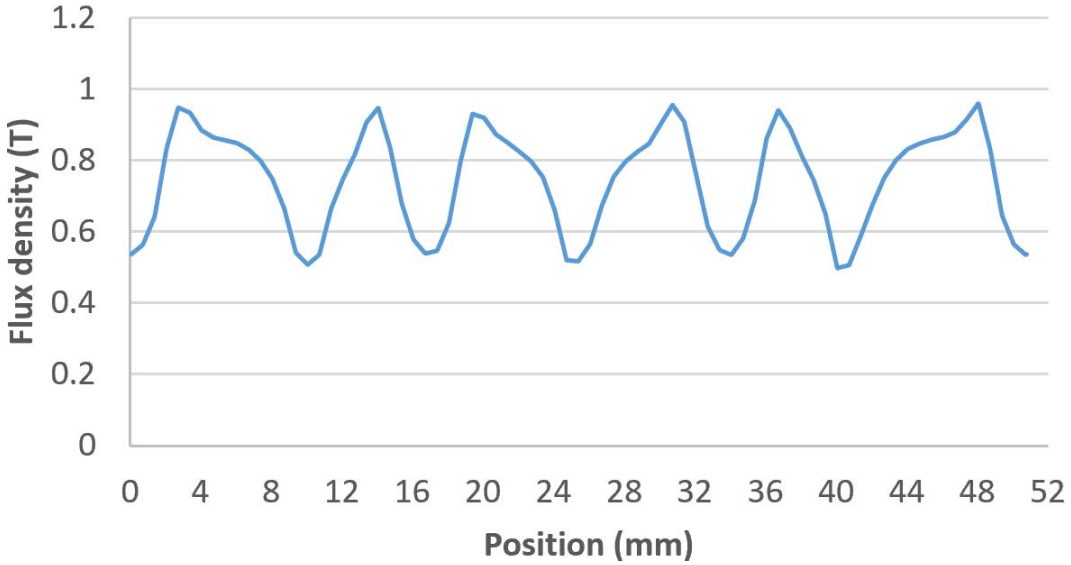

Figure 3.9 An example of no-load air gap flux density for phase blue

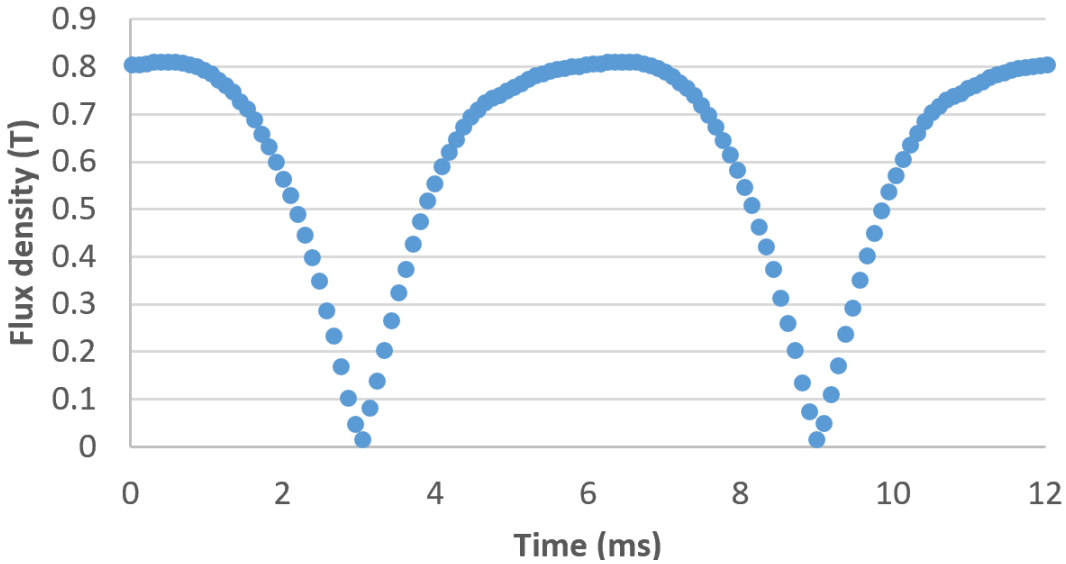

Figure 3.10 Air gap flux density profile of phase blue along with a pole pair pitch

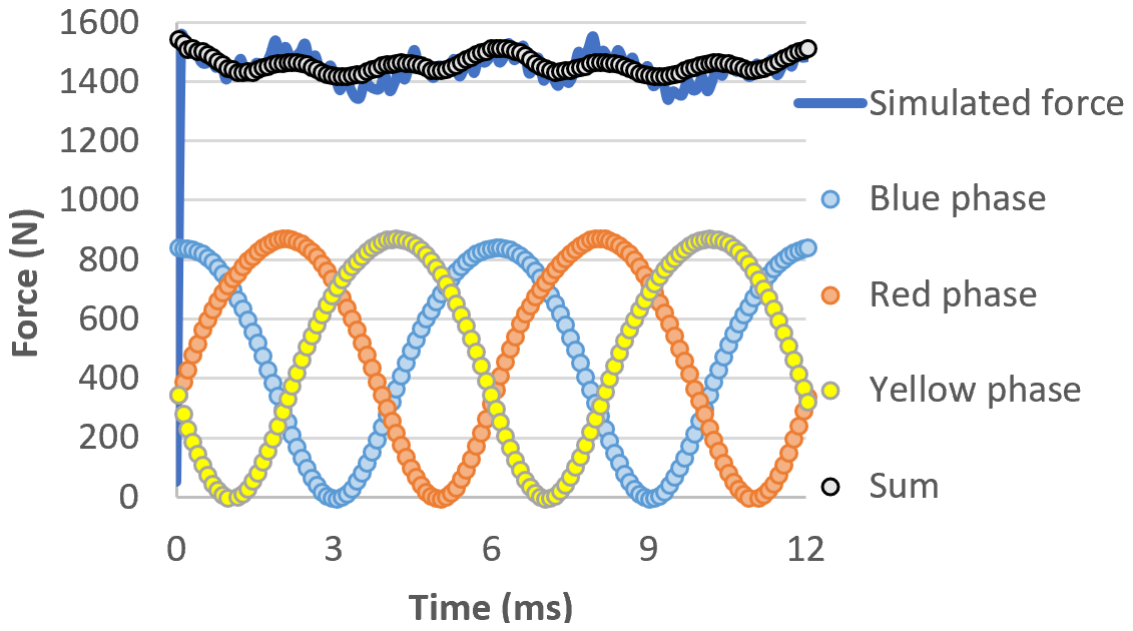

Figure 3.11 Phase calculated force and simulated force comparison

The power factor is a critical output parameter. For the machine working at high power factor, the synchronous reactance is small. Namely, the short circuit ratio (SCR) is high. High SCR contributes to high working stability and better voltage regulation capability. For the above study case, since the current is set in phase to the EMF as shown in figure 2.35, high power factor directly causes terminal voltage close to the EMF value. Thus for the desired working speed, the terminal voltage requirement is lower compared with that in a low power factor machine (or high power factor machine can achieve higher working speed when terminal voltage is limited).

MagNet can simulate the armature current flux linkage thus the phase inductance after setting the coil turns. In this simulation, the assumed turns per phase is 106 (assumed the winding fill factor is 100% and assumed each coil cross-section area is $1mm^2$). By combining phase inductance with the electrical angular speed, the phase current and EMF, the power factor can be calculated. Figure 3.12 is the phase inductance profile calculated from phase flux linkage and armature current where the phase peak flux linkage is 0.642Wb based on 106 turns and phase current is 5.9A which equals to the current density. The power factor is calculated through equation. 3-1.

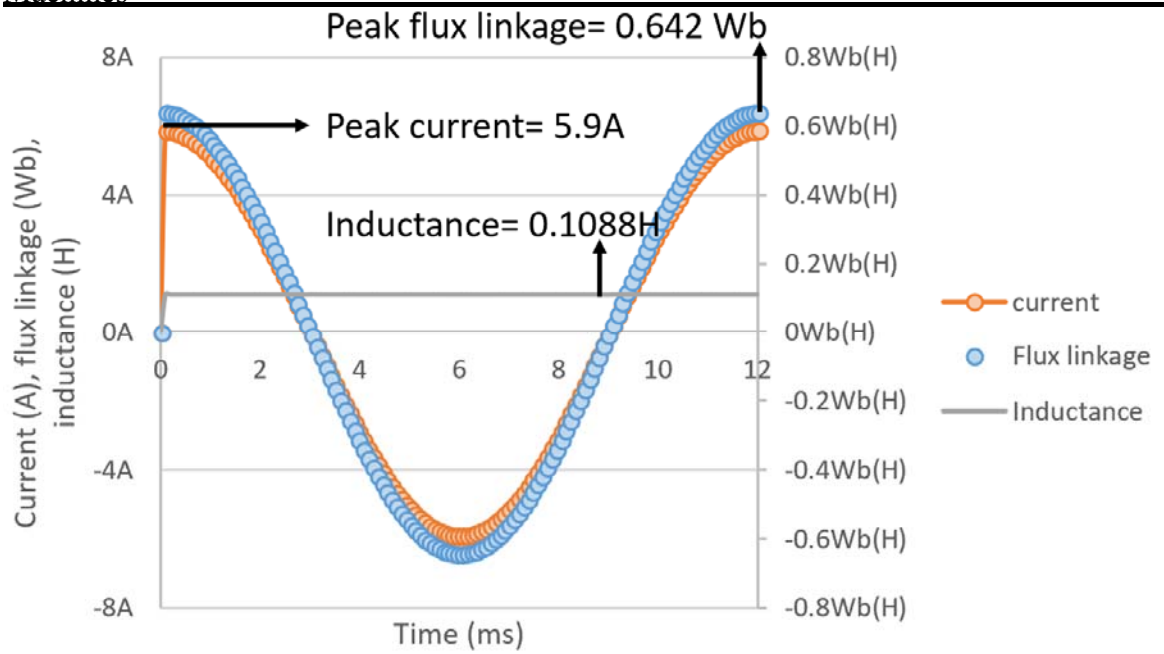

Figure 3.12 Phase blue inductance

$$PF = \cos\tan^{-1}\frac{I_{peak}\times\omega_e\times L}{EMF_{peak}} = \cos\tan^{-1}\frac{5.9A\times523.6rad/s\times0.1088H}{415} \approx 0.78 \qquad (3\text{-}1)$$

Another critical parameter is the machine loss: armature copper loss can either be manually calculated based on coil dimensions or directly extracted from MagNet. Figure 3.13 shows half slot winding copper loss waveform of the blue phase (one-sixth of a single phase); laminations and magnets' iron loss are in table 3.1. MagNet can also estimate every single component's mass and volume which are useful in following sections.

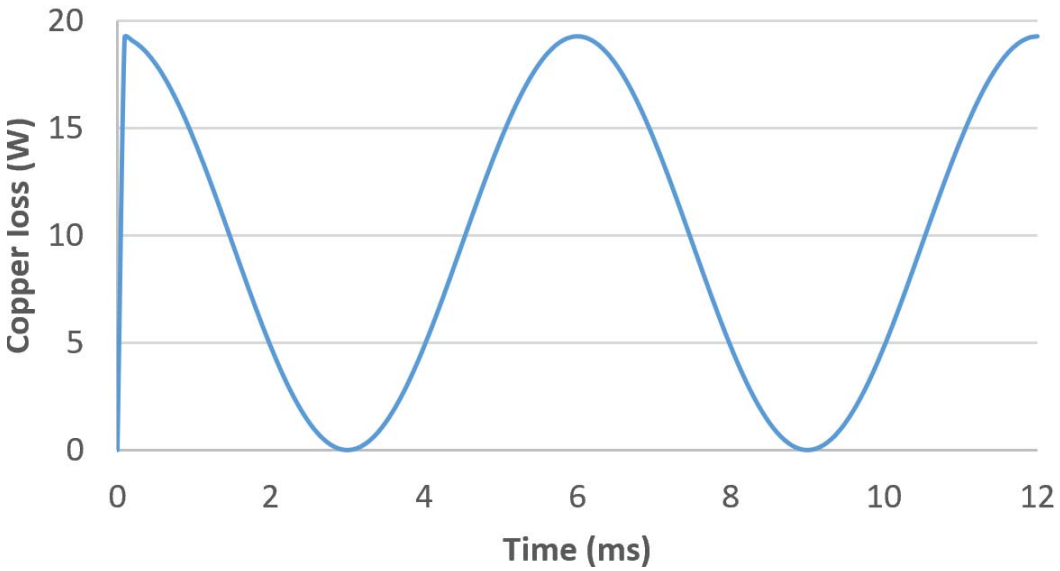

Figure 3.13 1/6 Phase blue copper loss

Time-Averaged	Hysteresis Loss (W)	Eddy Current Loss (W)
Translator Lams	1.020018	0.187838
Stator Lams	25.86779	6.265603
Magnets	--	12.19805

Table 3.1 Example RRPMR iron loss

3.4 Optimisation of Machine Topologies

Example results presented in the previous section are from optimised RRPMR topology, other optimised topologies including RRPMA, RRPMH, MPM and FS will be presented and compared in the next section. Each topology requires to be optimised with the same target and effort which is hard to achieve manually. In this project, software OptiNet is used to perform relatively equitable optimisations for all five topologies, an optimisation example (RRPMR) will be detailed presented in this section.

3.4.1 Optimisation software

OptiNet is an automated design optimisation tool which coupled with MagNet. It uses advanced and efficient algorithms based on stochastic evolutionary search (EA) to find optimal values for different design variables within specified constraints. Machine dimensions must be parameterised and then varied by the algorithm. Compared to the initial output, better output corresponding dimension will replace the original dimension until the optimum performance obtained. Meanwhile, all dimensions which cannot reach constraints or the output is worse than the previous result will be filtered.

3.4.2 Objective Function, Constraints and Design Variables

In this study, the optimisation objectives for all topologies are minimising the phase MMF on the stator, which aims to better the machine power factor and efficiency. Constraints include achieving force no less than 1500N and translator mass no more than 6 kg, which is inherited from the Free-piston Engine mechanical requirements as listed in table 3.2.

Stroke	152.4mm
Translator mass (constraint 1)	$\leq$ 6kg
Operation	Two-stroke
Nominal compression ratio	15: 1
Average speed	2.54m/s (8.3Hz)
Boost force (constraint 2)	1500N

Table 3.2 Mechanical constraints

Figure 3.14, figure 3.15 and figure 3.16 visually illustrate design variables for RRPMs, MPM and FS:

- For RRPMs, they share the same dimensional parameters where magnet factor (*m_f*) is the ratio of magnet pitch to pole pitch. *t_cbR* and *t_cbS* indicate the core back depth of the translator and stator. RRPMA's translator iron cores are separated by the magnet pieces which depend on the magnet factor thus there is no data on *t_cbR*. *t_m* is the magnet depth, however, in RRPMA *t_m* represents both the depth of magnet and iron core's height. Slot height (*s_h*) and slot width (*s_w*) indicate the slot (or tooth) size.
- As for MPM, slot factor (*sl_f*) indicates the ratio of the slot span angle to one phase span angle. Stator factor (*s_f*) indicates the ratio of the tooth pitch to a pole pitch. *t_m* indicates both the magnet depth and translator iron core back depth. Translator factor (*t_f*) indicates the ratio of the magnet pitch to pole pitch. *s_h* is the slot height, and *t-cb* is the stator core back depth.
- Regarding FS, *t_m* indicates the magnet depth. *t_md* and *t_mu* are the core depth beneath and above the magnet. *s_h* is the slot height, *sl_f* is the ratio of slot span angle to one phase span angle. *a_f* indicates the ratio of air gap span angle to one phase span angle subtract the slot span angle. *t_t* is the translator thickness, *s_f* share the same meaning as that in MPM, *t_f* means the translator iron core depth.

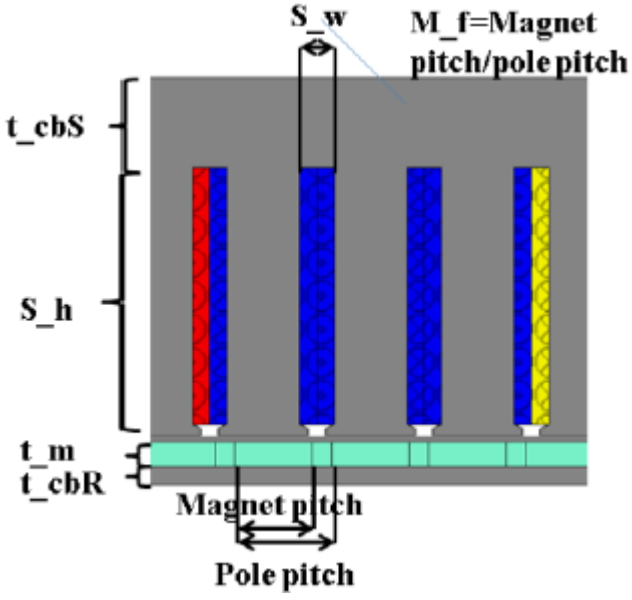

Figure 3.14 RRPMs schematic with parameters' specification

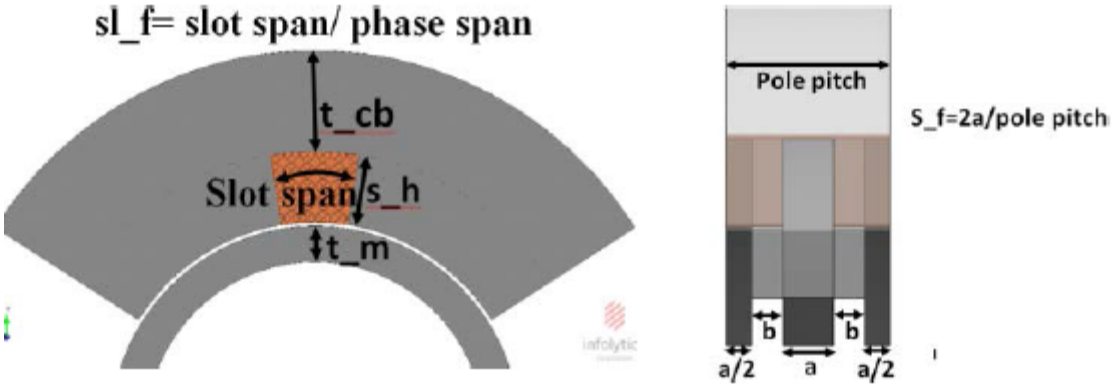

Figure 3.15 MPM schematic with parameters' specification

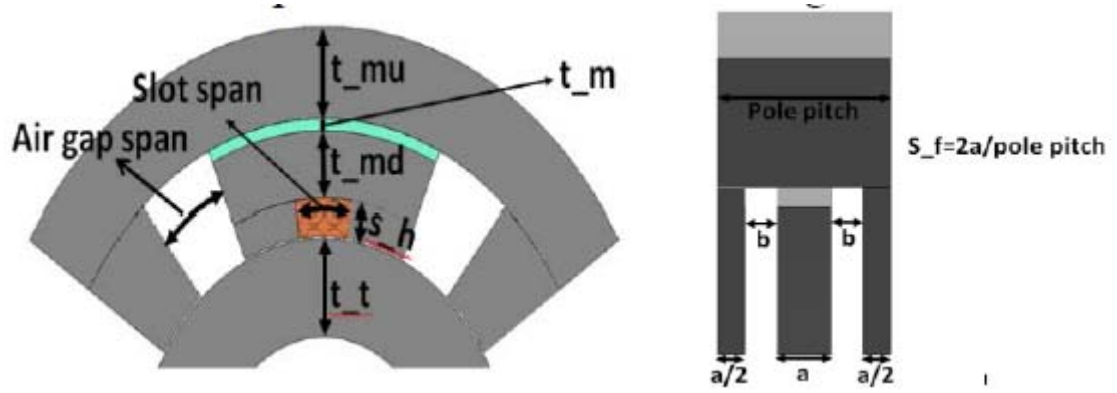

Figure 3.16 FS schematic with parameters' specification

3.4.3 Static Solution and Optimisation Result

OptiNet is set to use static solution from MagNet to optimise each topology. In static solution, there is no motion applied to the model. Thus no results related to motion could be calculated including voltage, loss, power factor and efficiency. However, force, MMF and component's mass can be extracted. The concept of the static solution is as shown in figure 3.17, by applying the correct MMF for each phase an approximate force can be obtained which close to the average force in dynamic solution.

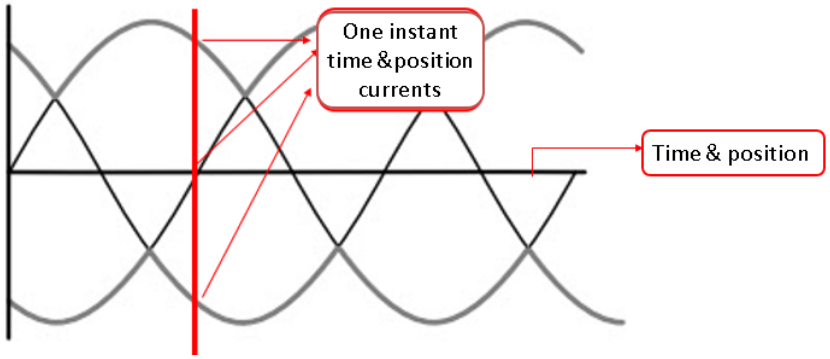

Figure 3.17 Static solution concept

An example of the optimisation of RRPMR is as shown in table 3.3, which shows initial parameters' definitions, variation ranges and precisions. There are two constants (air gap length and shaft diameter which are set to reduce variables); six variables which are related to the topology dimensions; *J* is the current density as the seventh variable which can combine slot area and work as a function of the phase MMF. Table 3.4 gives detailed data history interface. After 76 steps of optimisation, variables, objective and constraints finally converge to the optimum condition. Compared to the initial outputs, the required phase MMF drops by 20% without exceeding any constraint. Other topologies' optimisation results and full dynamic output performance will be presented and compared in the next section as early-stage results and analysis.

Dimension	Type	Initial	Minimum	Maximum	Step	unit
AG	Constant	1	--	--	--	mm
Shaft	Constant	80	--	--	--	mm
m_f	Variable	0.2	0	1	0.05	--
t_cbR	Variable	6.8	1	10	0.1	mm
t_m	Variable	2	1	10	0.1	mm
J	Variable	4.7	1	7	0.1	A/mm^2
s_h	Variable	41.5	15	50	0.5	mm
s_w	Variable	8	0	16	0.5	mm
t_cbS	Variable	19	1	50	0.5	mm

Table 3.3 OptiNet setting interface

ID	m_f	t_cbR	t_m	J	s_h	s_w	t_cbS	Ob_1	Co_1	Co_2
Unit								A	N	kg
1	0.2	6.8	2	4.7	41.5	8	19	780	1452	5.7
4	0.1	2	2.7	5.4	32	11.5	18	994	1539	2.75
8	0.1	4.8	2.8	6.5	35.5	8.5	33.5	980	2001	4.88
29	0	5.5	3.3	5.5	28.5	10	17.5	784	1678	5.61
65	0	5.2	3.3	5.6	25.5	9	14	643	1508	5.72
71	0	5.4	3.4	5.8	25.5	8.5	11	629	1518	5.93
77	0	5.1	3.4	5.9	25	8.5	11	627	1509	5.70
117	Convergence reached									

Table 3.4 Optimisation data history for RRPMR

3.5 Early Stage Results and Analysis

All five topologies optimisation results (initial and final) are as listed in table 3.5, table 3.6 and table 3.7, which show an effective optimisation can be achieved by using OptiNet.

3.5.1 Results of RRPMs

After optimising topologies dimensions RRPMA, RRPMR, RRPMH and MPM can achieve 47%, 20%, 56% and 29% reductions on the phase MMF without exceeding any constraint. All three optimised topologies of RRPMs are seen to be compliant with the required specification with nearly the same phase MMF. However, for RRPMH optimised results show an advantage on the translator mass (20% less).

RRPMA										
ID	**m_f**	**t_cbR**	**t_m**	**J**	**s_h**	**s_w**	**t_cbS**	**Ob_1**	**Co_1**	**Co_2**
unit	mm							A	N	kg
0	0.2	-	7.2	7	35.5	10	4	7452	1570	4.80
97	0.35	-	8.1	5	43.5	6.4	5.9	3924	1510	5.43
RRPMR										
0	0.2	6.8	2	4.7	41.5	8	19	4681	1452	5.70
76	0	5.1	3.4	5.9	25	8.5	11	3756	1509	5.70
RRPMH										
0	0.1	3.2	1.3	7	43.5	8.5	4.36	7764	1659	2.85
72	0.2	2.8	3.9	5.2	40	5.5	14	3432	1501	4.38

Table 3.5 RRPMs optimisation results

3.5.2 Results of MPM

For MPM optimised results, they show an advantage on the phase MMF (33% less than the smallest of that in RRPMs). However due to the topology of MPM is entirely different. Thus the copper loss estimation requires consideration of the coil length per turn which will be expanded in dynamic results later and combined with iron losses to estimate the efficiency.

ID	**sl_f**	**J**	**s_f**	**t_m**	**t_f**	**s_h**	**t_cb**	**Ob_1**	**Co_1**	**Co_2**
unit				mm		mm		A	N	kg
0	0.13	7	0.3	9	0.25	27.5	28.5	3213	1386	5.82
89	0.21	5	0.3	8.75	0.5	18.5	40.5	2296	1503	5.59

Table 3.6 MPM optimisation results

3.5.3 Results of FS

An unexpected result in FS optimisation shows that for FS with the applied optimisation routine, neither of the two constraints can be fulfilled. Namely, if the translator mass must be no more than 6 kg, the force can only reach 525N. In this case, a further optimisation routine is taken to explore if FS can save magnet material usage at the expense of a larger translator mass. The new optimisation removes the translator mass limit and also change to the objective of minimising the magnet usage. Results are as shown in table 3.8 where s_ indicates the shaft radius. It shows that not only the force increases to the required value but also save 40% magnet usage.

ID	**t_m**	**t_md**	**t_mu**	**s_h**	**s_f**	**a_f**	**t_t**	**sl_f**	**t_f**	**J**	**Ob_1**	**Co_1**	**Co_2**
unit	mm						mm				A	N	kg
0	14	20	20	20	0.1	0.45	20	0.2	0.8	7	1995	525	5.86
179	16	37	34	49	0.1	0.41	29	0.17	0.71	7	6506	1291	8.22

Table 3.7 FS optimisation results

ID	**t_m**	**t_md**	**t_mu**	**s_h**	**s_f**	**a_f**	**t_t**	**s_**	**sl_f**	**t_f**	**J**	**Ob_1**	**Co_1**
unit		mm					mm					kg	N
0	14	20	20	20	0.1	0.45	20	40	0.2	0.8	7	5.18	525
96	6.1	33	45	18	0.13	0.34	48	73	0.38	0.65	7	3.10	1508

Table 3.8 FS optimisation results with new routine

3.5.4 Static Results Comparison

More detailed results of five topologies (FS with two optimisation routines) are in table 3.9. All results are extracted from OptiNet and MagNet with the static solver.

Equation. 2-6 can be simplified conceptually as equation. 3-1, for better comparison between longitudinal and transverse flux machine equation. 3-1 can be further unified into equation. 3-2, where flux loading is flux produced in single turn per coil length. From table 3.9 MPM requires the minimum MMF and coil length to achieve the force requirement. Assuming the fill factor and winding diameter are the same, then the MPM can achieve the minimum copper loss. Flux loading per unit magnet is the no-load flux produced by a unit magnet which indicates the magnet use efficiency. MPM shows a significant advantage on this parameter. The phase MMF produced flux can cause flux saturation in the machine iron core, although the optimisation routine of minimising MMF makes this unlikely, by comparing parameter ‘constant’ in table 3.9, MPM and RRPMs show similar armature conditions (not saturated).

As for FS due to the translator mass constraint, the force requirement cannot be fulfilled. Even lifting this constraint to achieve required force but more permanent magnet usage (13% more than MPM even no magnet is on the stroke length in FS). What is more, a large translator mass is revealed (3.8 times larger than MPM). Thus it can conclude from static results that FS is not fit to the target Free-Piston Engine and cannot save magnet usage.

Topologies	**RRPMs**			**MPM**	**FS**	
	RRPMA	RRPMR	RRPMH		Achieve mass objective	Achieve force objective
MMF (A)	3924	3762	3432	2296	1995	4305
Force (N)	1511	1509	1501	1503	525	1508
Translator mass (kg)	5.43	5.72	4.38	5.60	5.86	22.17
Magnet mass (kg)	1.86	2.24	2.52	2.75	5.18	3.10
Force per unit magnet (N/kg)	812	673	596	547	101	486
Total mass (kg)	23.28	19.06	23.38	35.02	42.96	52.58
Coil length per turn (mm)	277	278	270	152.4	152.4	152.4
Flux loading (μWb/mm)	4.79	4.68	5.36	14.34	10.63	8.52
Flux loading per unit magnet (μWb/(mm*kg))	2.58	2.09	2.13	5.21	1.81	2.75
Constant (N/(A*Wb))	288	306	302	300	162	270

Table 3.9 Static results comparison

$$Force = constant \times electric\ loading \times magnetic\ loading \times active\ area \quad (3\text{-}1)$$

$$Force = constant \times MMF \times flux\ loading \times coil\ length \quad (3\text{-}2)$$

3.5.5 Dynamic Results Comparison

To calculate the iron loss and hence the efficiency, it is necessary to perform dynamic simulations. In the dynamic solution, the winding diameter is assumed to be 1 mm with 50% fill factor. RRPMs and MPM optimised topologies will be discussed, EMF and harmonics results are presented in figure 3.18, efficiency and power factor results are presented in table 3.10. MPM shows an advantage on the efficiency and RRPMR shows an advantage on the power factor. Designing an MPM with high power factor is a direct result of the decision to optimise based on a low MMF requirement. Using this optimisation routine hence removes one of the traditional barriers to the transverse flux machine topology. The MPM gives the highest efficiency by quite some margin, again directly resulting from the low MMF design. In this section only one optimisation routine is mainly used to optimise MPM and FS on dimensions, topologies are fundamentally unchanged, in next section alternative optimisation strategies and different tooth shapes will be detailed discussed.

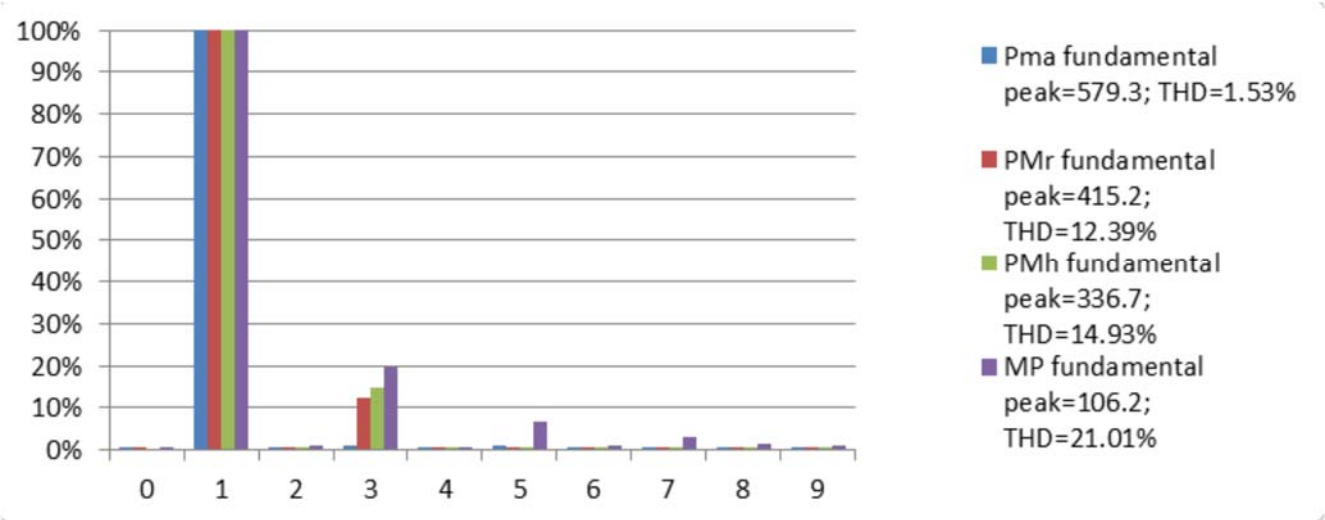

Figure 3.18 EMF and harmonics analysis

Topologies	**RRPMs**			**MPM**
	RRPMA	**RRPMR**	**RRPMH**	
Copper loss (W)	150	178	142	90
Iron loss (W)	77	45	61	14
Efficiency (%)	94	94.5	94.9	97.3
Power factor	0.62	0.78	0.61	0.62

Table 3.10 Efficiency and power factor profile

3.6 Further Comparison of MPM and FS

In this section, more detailed comparisons between MPM and FS will be performed to investigate the potential of transverse flux and flux switching topologies (MPM and FS).

3.6.1 New Optimisation Routines and New Topology

Two objective functions are applied in the optimisation: minimising electrical loading and minimising magnetic mass. What's more two alternative tooth shapes (rectangular and trapezoidal tooth like shown in figure 3.19) will be compared. Again stroke length is 152.4mm which equals to the machine active length, shaft diameter and air gap are constants as 80mm and 1mm. In transverse flux machine if the active length and the air gap are both constants, then the pole pair number could make a central role to determine the armature current flux linkage thus the output force. An example of the effect of pole pair number to the output force profile is in figure 3.20. The force is linear up until around three pole pairs then leakage flux starts to dominate. Chapter 5 will explore a detailed analysis in numerical solution.

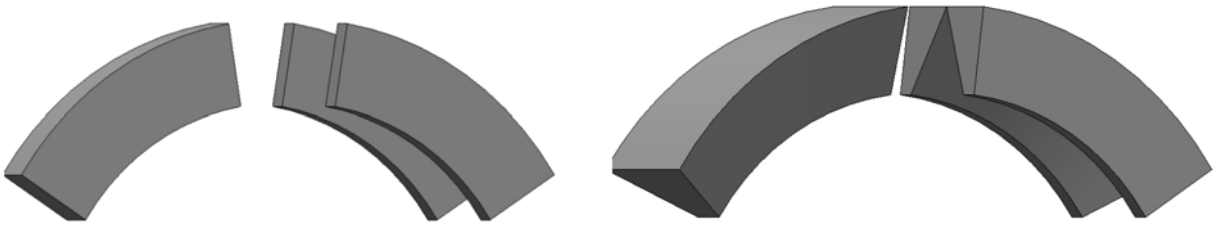

a. Rectangular tooth b. Trapezoidal tooth

Figure 3.19 Two alternative tooth shapes

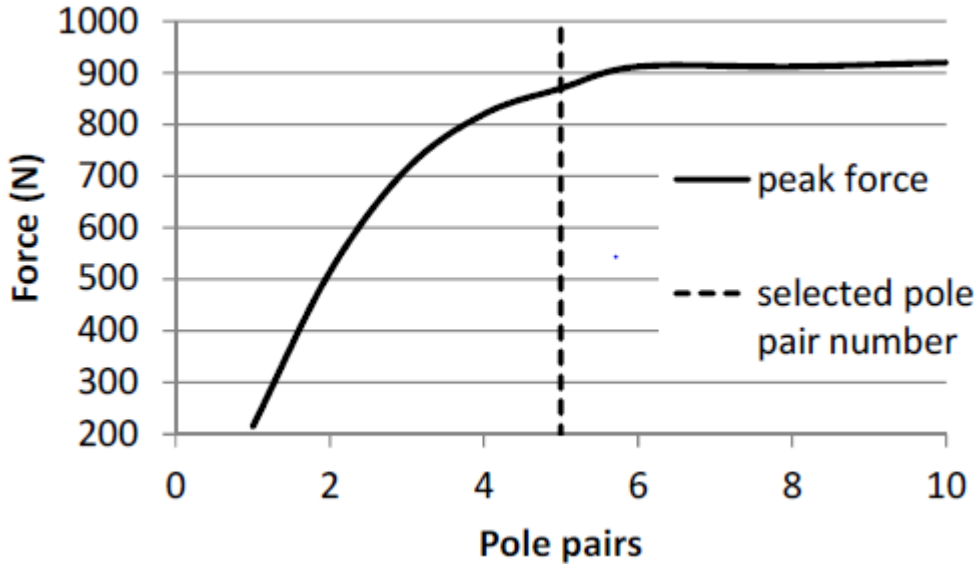

\

Figure 3.20 Effect of pole pairs on output force

3.6.2 Optimisation Results of MPM

From above optimised objectives and tooth shapes, there are four design options. Results are in table 3.11. Where design (a) corresponds to minimising electrical loading, design (b) corresponds to minimising magnet mass, design (c) and design (d) share the same optimisation strategy, but with a trapezoidal shape. Both rectangular tooth designs are compliant with the design constraints. The designer has a straight choice between a low magnet mass 88% efficiency design with a power factor of 0.17 (b), or a more sensible 96% efficient machine with power factor 0.67 using 85% more magnet (a). In this instance, optimising for minimum electric loading gives a better-looking design. Trapezoidal designs (c) can give an only slight increase in efficiency and improvement in the power factor compared to design (a), design (d) shows a similar minor improvement in performance compared to design (b), but is still dogged by a low power factor of 0.2. In practical situations, this is likely to exclude it from being taken forward. Design (c) is hence selected as the baseline machine design against which improvements can be measured.

Tooth shape	**Rectangular**		**Trapezoidal**		
	a	**b**	**c**	**d**	
Objectives by minimising	**Electrical loading**	**Magnet mass**	**Electric loading**	**Magnet mass**	**Unit**
MMF	2135	5894	1850	5894	A
Magnet mass	2.28	1.23	2.24	1.21	kg
Translator mass	5.29	5.76	5.72	5.68	kg
Stator mass	15.56	28.49	20.79	26.88	kg
Copper loss	117.8	325.2	89.3	325.5	W
Iron loss	39.9	125.4	35.1	107.1	W
Efficiency	95.9	88.2	96.7	88.6	%
Power factor	0.67	0.17	0.70	0.20	

Table 3.11 MPM optimising results

3.6.3 Optimisation Results of FS

Results of FS designs corresponding to optimisation options are shown in table 3.12. Where design (e) corresponds to minimising electrical loading with rectangular tooth shape, design (f) corresponds to minimising magnet mass with rectangular tooth shape, design (g) and design (h) share the same optimisation routine but another tooth shape (trapezoidal tooth). It can be

seen that the trapezoidal tooth shape gives an impressive improvement on translator mass, magnet mass and output performance. Compared to design (e), design (g) can reach the smallest translator mass (6.3 kg) which is ever achieved before. For design (h), it can achieve 2.5 kg magnet mass design (20% improvement) and 16.4kg translator mass (26% better). However from one aspect in minimising electrical loading optimisation (as comparing design (g) to (c)) the efficiency and the power factor are much lower; from another aspect in minimising magnet mass optimisation design (h) shows much larger magnet mass compared to design (d). In general, the low power factor, low efficiency and high material mass characteristics reflect that FS is not comparable to the performance of MPM.

Tooth shape	**Rectangular**		**Trapezoidal**		
	e	**f**	**g**	**h**	
Objectives by minimising	**Electrical loading**	**Magnet mass**	**Electric loading**	**Magnet mass**	**Unit**
MMF	6506	4305	4868	3675	A
Magnet mass	8.6	3.1	10.5	2.5	kg
Translator mass	8.2	22.2	6.3	16.4	kg
Stator mass	92.1	91.2	111.7	103.1	kg
Copper loss	359	238	269	203	W
Iron loss	43	66	55	98	W
Efficiency	87.7	92.0	91.5	92.1	%
Power factor	0.2	0.3	0.2	0.4	

Table 3.12 FS optimising results

3.6.4 Flux Leakage in FS

The poor performance of FS is primarily due to the flux leakage. The two flux paths, corresponding to the translator teeth aligning with alternate stator teeth are as shown in figure 3.21. The flux is gathered circumferentially on the upper and lower surfaces of the magnet before being channelled radially down stator teeth. There is an inherent leakage path circumferentially across adjacent teeth. To measure the leaked flux in this topology, two sets of auxiliary winding coils are placed which are enclosed by the two flux leakage paths. Thus flux profiles can be extracted along with displacement as main flux, flux leakage 1 and flux leakage 2. Taking design (f) as an example as shown in figure 3.22, it shows main flux linking

a single phase coil and leakage flux which calculated as linkage cutting dummy coils inserted on each leakage path. In the direct axis position at 0mm, 26% of the magnet driven flux is flowing in the main flux path, and 74% is split between the two leakage paths. Trapezoidal design (h) has a remarkable improvement on flux leakage effect with 35% of main flux and 65% of leaked flux. Even so, FS designs using trapezoidal teeth are still unable to produce sufficient force unless the translator mass constraint is removed. Even comparing design (h) with 2.53 kg of magnets still more than 2.24 kg of that in baseline MPM (c). Moreover, both the power factor and efficiency of (h) are well below those of the baseline design.

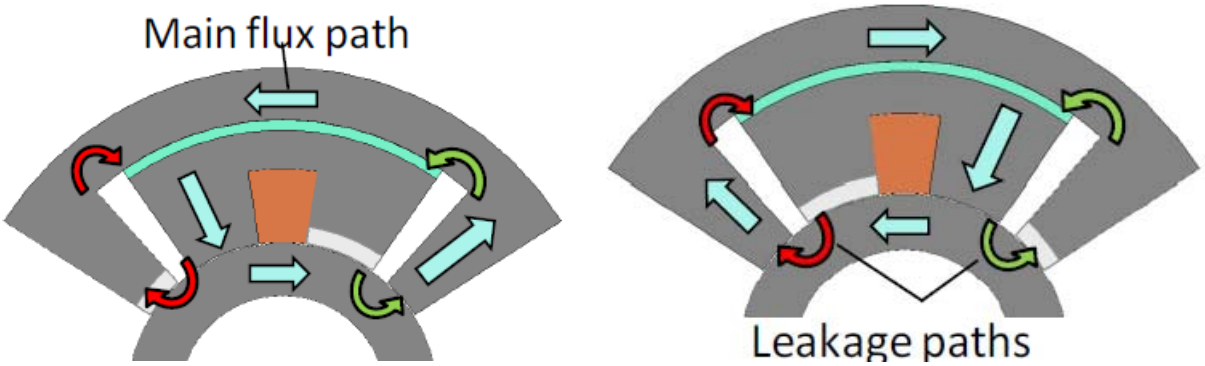

Figure 3.21 Flus path in FS

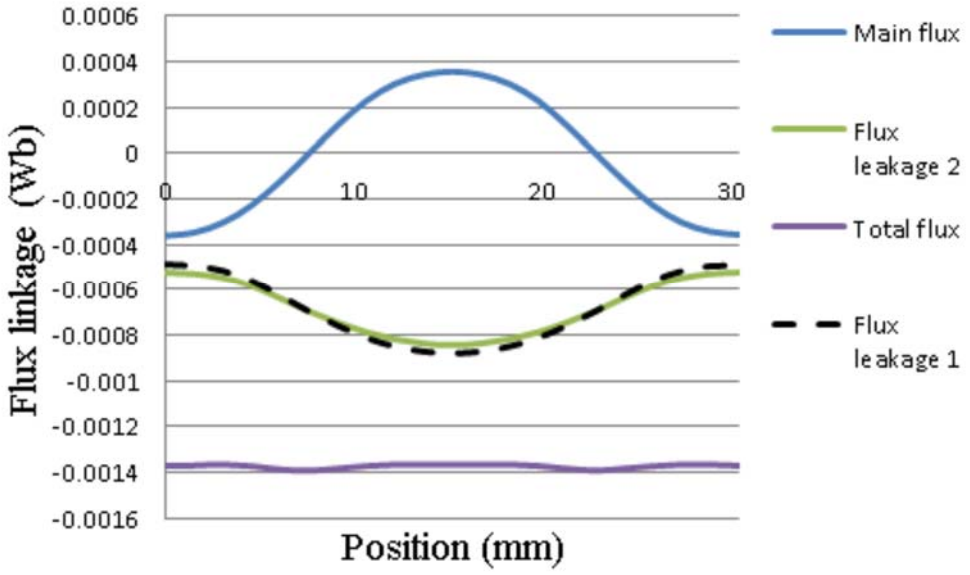

Figure 3.22 Main field flux leakage profile

To summarise, against the initial specification where the active length is equal to the stroke length, FS cannot save magnet mass compared to either of the MPM designs. FS with the lowest magnet mass performs poorly in all other metrics. The ‘best’ all round design (c) is

that with the second lowest magnet mass and is the MPM optimised for low electric loading- as this allows for a high power factor and a good efficiency. In reality, if the power factor is a concern, then this low loaded MPM must be used, and this work shows using the objective function of minimising electric loading is a good tool for lifting the power factor.

3.6.5 Effects of Different Stroke Length and Active Length

This section aims to assess if the FS topology could provide an alternative to design (c). The discussion is only relevant if power factor may be discounted from the selection process, as may be the case for a capacitor compensated system, thus all FS designs are based on trapezoidal tooth with minimising magnet mass optimisation. The broader conclusion about magnet mass is drawn from this work are specific to the case where the stroke length is equal to the active length. Figure 3.23 shows the magnet mass result extrapolated for increased stroke length with a fixed active length. It can be seen that when active length/ stroke is less than 0.714 (stroke length has seven pole pairs), then FS start to show a potential advantage on saving magnet usage.

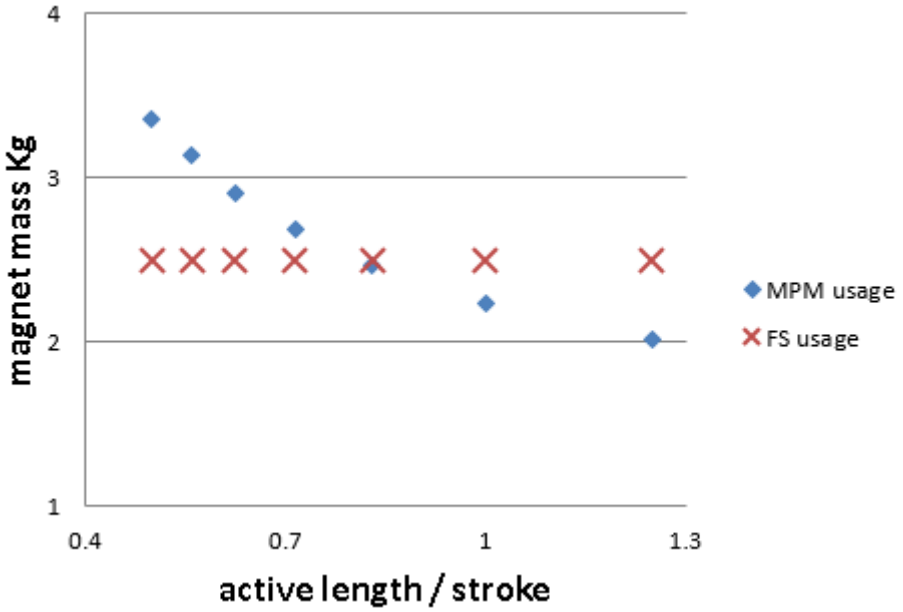

Figure 3.23 Effect of different stroke length topologies

To verify above conclusions, the optimisation routine for FS and MPM is repeated for a fixed stroke length and variable active lengths which aim to hit the force requirement. The active length is varied by changing the number of pole pairs on the stator, thus fixing mechanical frequency. Figure 3.24 shows the optimised results, where magnet mass of both machines increases for long active lengths. MPM has a minimum magnet mass of 2.0 kg at the ratio of 0.8. As long as active length/ stroke smaller than 0.6, FS start to offer reduced magnet mass

options compared to MPM. As in reality, active length is a variable thus the central conclusion is that the minimum magnet mass achievable from an MPM cannot be matched by an FS, as the best FS topology always requires more magnet mass. In fact, it again proved that the flux leakage in FS is massive which is hard to be offset by varying machine active length to stroke length ratio.

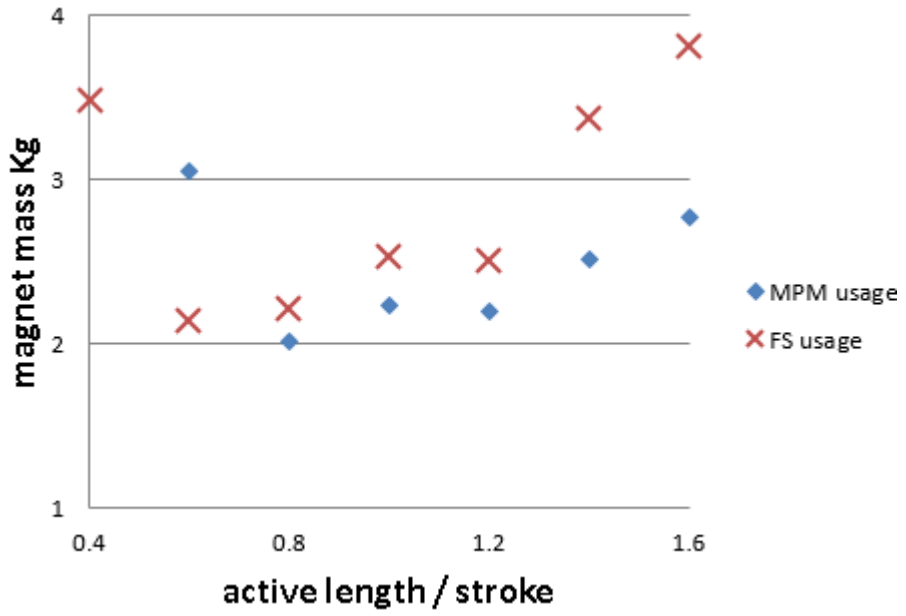

Figure 3.24 Effect of different active length topologies

3.7 Summary

From results above, MPM has the advantage of low copper loading thus low copper loss and high efficiency without using much more magnet material. The power factor of MPM is also comparable to conventional longitudinal flux topologies. Optimizing with low electric loading can effectively achieve better machine performance for all-around output performances. The trapezoidal tooth structure can effectively improve FS performances but due to the high flux leakage, it still not compatible to target Free-Piston Engine requirements. Different active to stroke length ratios are also investigated but show a failure to offset the inherent flux leakage effect of the FS. To sum up, MPM topology is taken forward for the later more detailed design and building process which will be presented in the next Chapter 4.

Chapter 4. Three Phase MPM Evolutionary Development

4.1 Introduction

Based on Chapter 3, this Chapter will present a detailed design of MPM include the stator tooth combination design, the single tooth winding design, machine resizing and the stator tooth dimension optimisation, stator laminations design and final topology performance investigation. By completing a detailed design of the MPM, the designer will achieve a more straightforward construction of the assembly and a cheaper cost on materials. Moreover, a more reasonable dimension that matches the machining precision should be determined to match the process technology.

4.2 The Stator Tooth Combination Design

The flux paths of two extreme positions of the designed MPM for a single phased topology are as shown in figure 4.1. For three-phased topology, flux paths can be regarded as a combination of three individual modules which separated by 120 electric degrees. In figure 3.2 is a three-phased topology. In this case, the stator contains at least three components (all using SMC materials) and require a stator housing to combine them. If using a combination of laminations and SMC then this stator topology will require housing to contain nine separated components for each pole pair pitch as shown in figure 4.2 (a). To simplify the above point, an idea of combining stator tooth is applied. In figure 4.3 is the combination sketch diagram of the stator along the translator circumference for a pole pair pitch. Where green blocks represent tooth positions of the separated tooth topology with full pitched structure (figure 4.2(b)), and red blocks represent those of the combined tooth topology (figure 4.2(c)). It shows that combining tooth can effectively reduce the stator components' number to four, where component 1 is SMC material which supplies flux paths at both radial and axial directions and components 2-4 are laminations which only supply radial flux paths. As a result, Flux paths for combined tooth topology is as shown in figure 4.4. Their static force results are as shown in figure 4.5, where it can be seen that by combing tooth of MPM the mean force can be maintained. Thus it can be concluded that the stator tooth combination design is feasible.

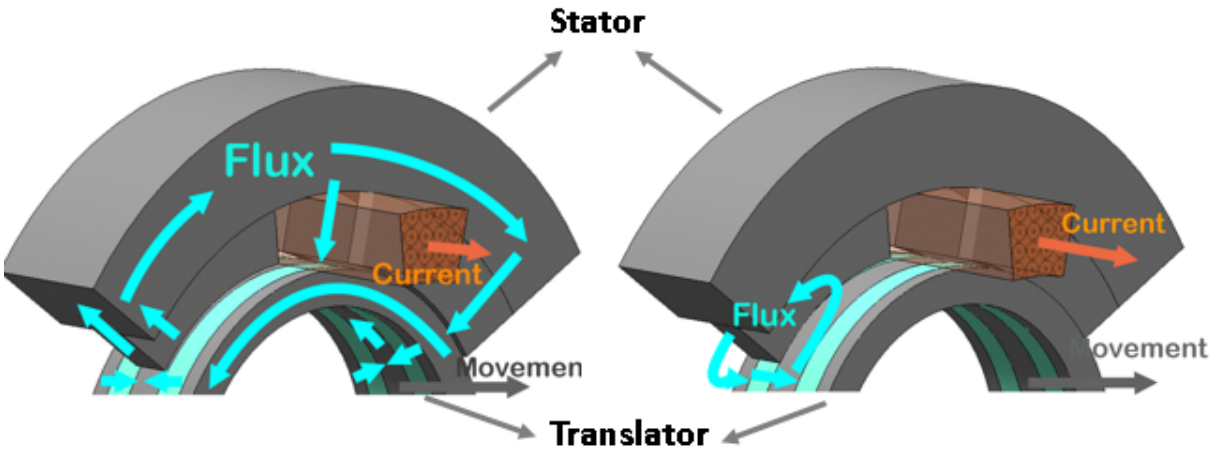

Figure 4.1 Two extreme position flux paths for MPM

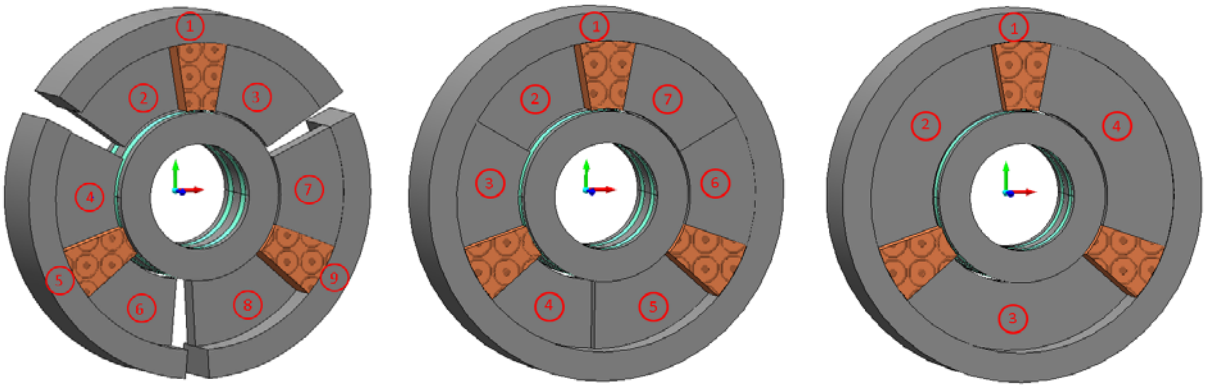

(a) (b) (c)

Figure 4.2 One pole pair pitch of a three-phased topology

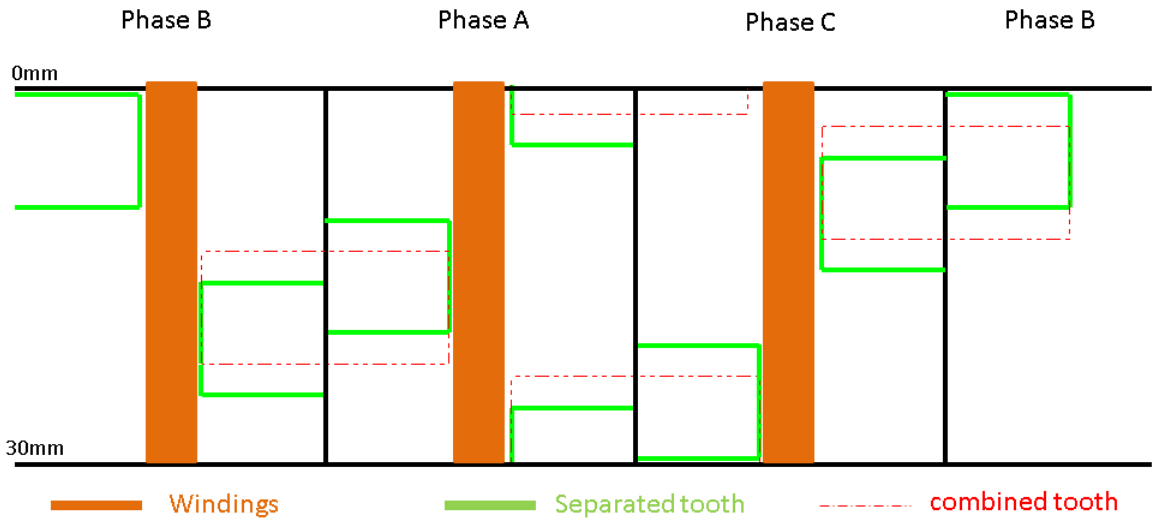

Figure 4.3 2D sketch diagram of the stator tooth combination process

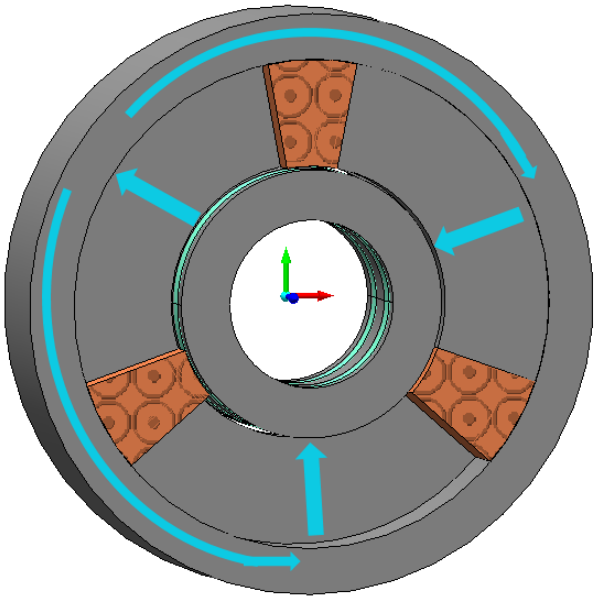

Figure 4.4 Combined tooth topology flux path

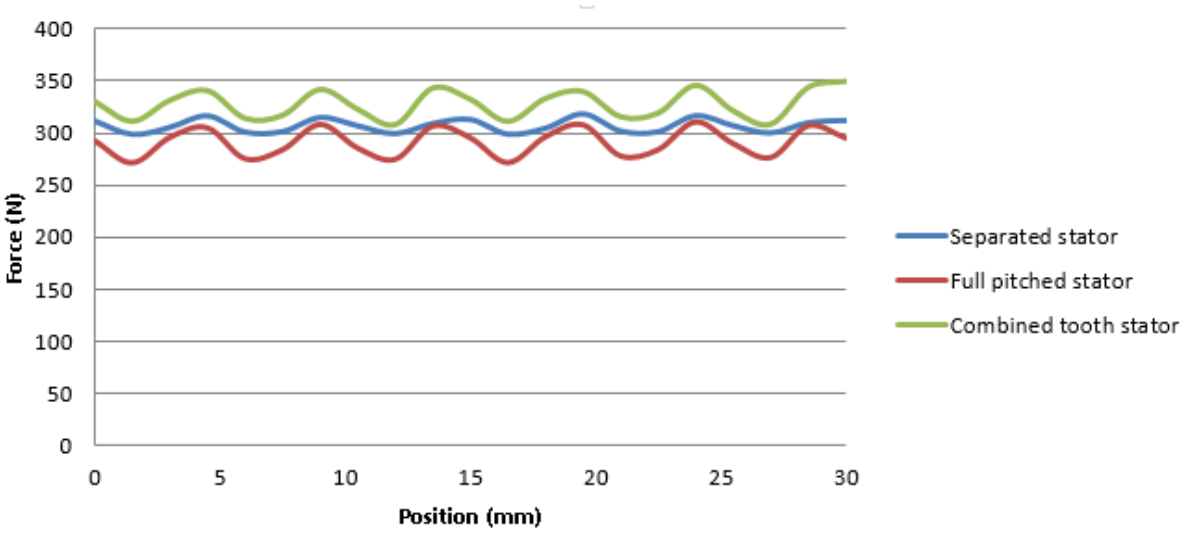

Figure 4.5 Force results for different tooth topologies

4.3 The Single Tooth Winding Design

Single tooth winding is generally used to reduce end windings and simplify the winding difficulty in conventional machines. For linear MPM, due to the return path of the coil contributes nothing to the machine force output and would increase the overall machine size. Thus the single tooth winding shows more potential to couple with the MPM topology. After combing teeth of the MPM, then it is possible to apply a single tooth winding as shown in figure 4.6. In theory, by applying such a winding topology, it can effectively reduce the copper usage to 50% if ignoring the end winding waste. However, a drawback of this is the force reduction due to the low winding factor. If maintain all machine dimensions and the slot current density unchanged then the phase MMF of the single tooth winding will reduce to half

of that in c-core winding meanwhile out and return coils are all contribute to the machine force output, as a result in figure 4.7 shows a 23% force reduction when the single tooth winding is applied. The reason behind this is due to the short pitch factor (k_p) between forward and backward coils. As the phasor diagram illustrates in figure 4.8, where arrow ab and bc represent magnetic loadings which affect both forward and backward windings surrounding the stator tooth and ac represents the equivalent magnetic loading. From calculation, k_p is 0.866 which matches the 23% force reduction very well.

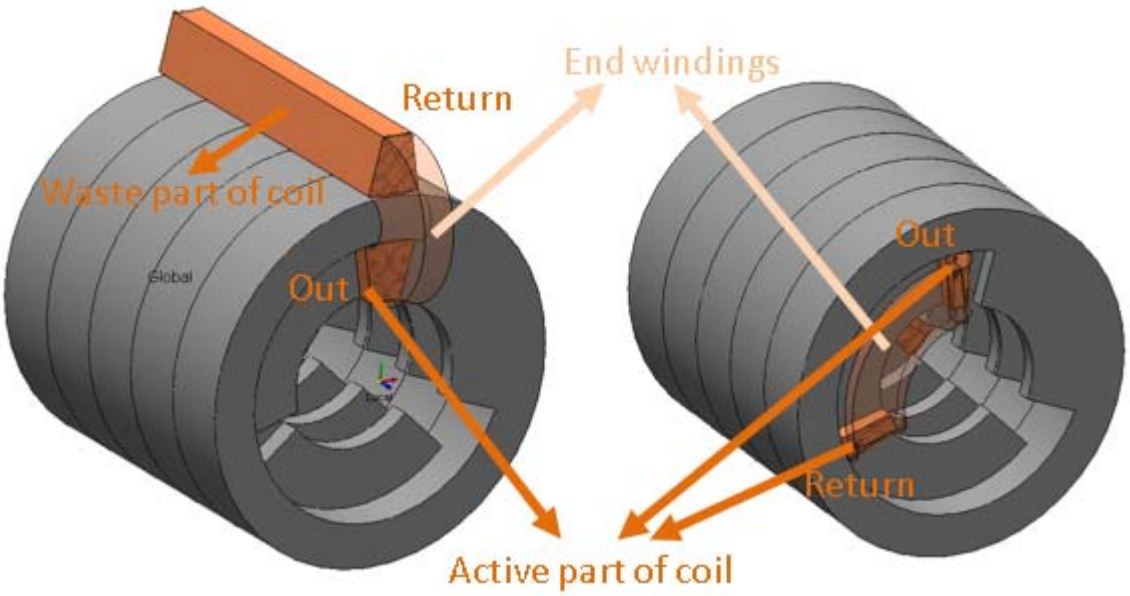

(a) C-core winding (b) Single tooth winding

Figure 4.6 Winding evolution sketches

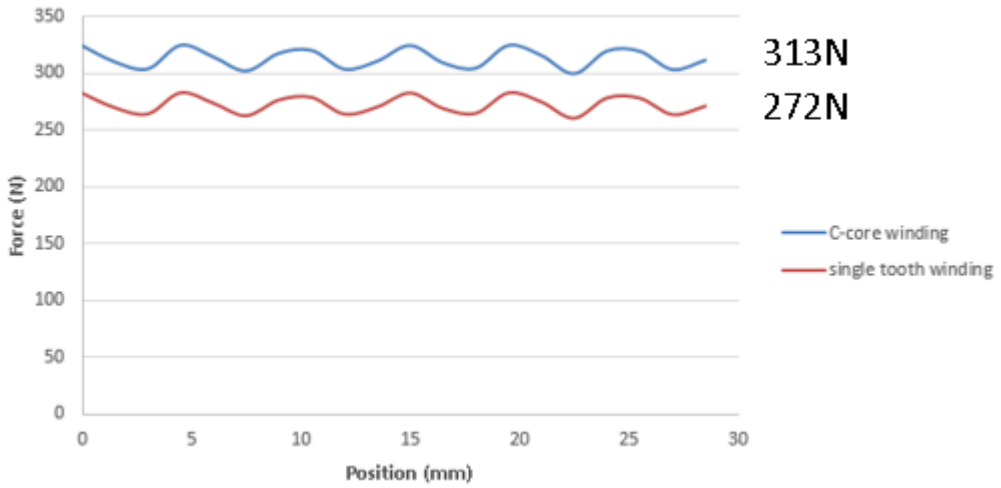

Figure 4.7 Force reduction of the single tooth winding

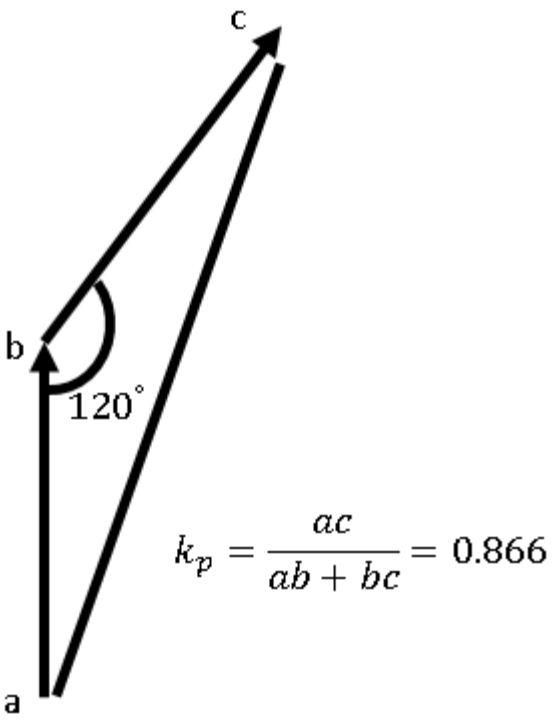

Figure 4.8 Phasor diagram of the winding factor

To counter the force reduction, the designer decides to increase the electrical loading or phase MMF. As shown in figure 4.9 the peak phase MMF of the single tooth winding is 1764A, which is increased by 27% compared to half of that in the C-core winding (1389A). Meanwhile the peak flux of the single tooth winding (0.000781Wb) is about 85% of that (0.00092Wb) in the C-core winding. It can be seen that the reduction factor (85%) of the flux in the single tooth winding is close to the analytical k_p (86.6%). However, by increasing the phase MMF to 1764A, the force can maintain unchanged as shown in figure 4.10. Considering the return coil in the C-core winding, the increased single tooth winding phase MMF is still only 63% of that in the C-core winding. If using the same the coil diameter with the same fill factor, then it can be concluded that the single tooth winding can use only 63% of the electrical loading in the C-core winding to offset the effect of the winding factor. In other words, the single tooth winding has an advantage on saving copper loss and simplifying machine windings.

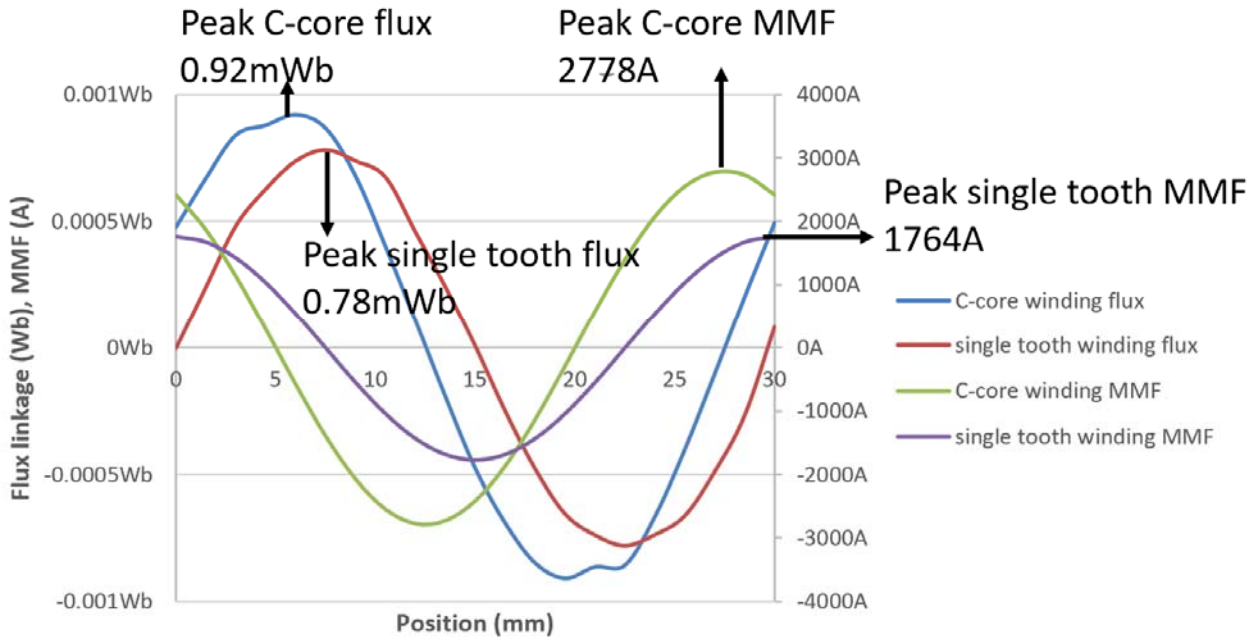

Figure 4.9 Flux and applied MMF waveforms

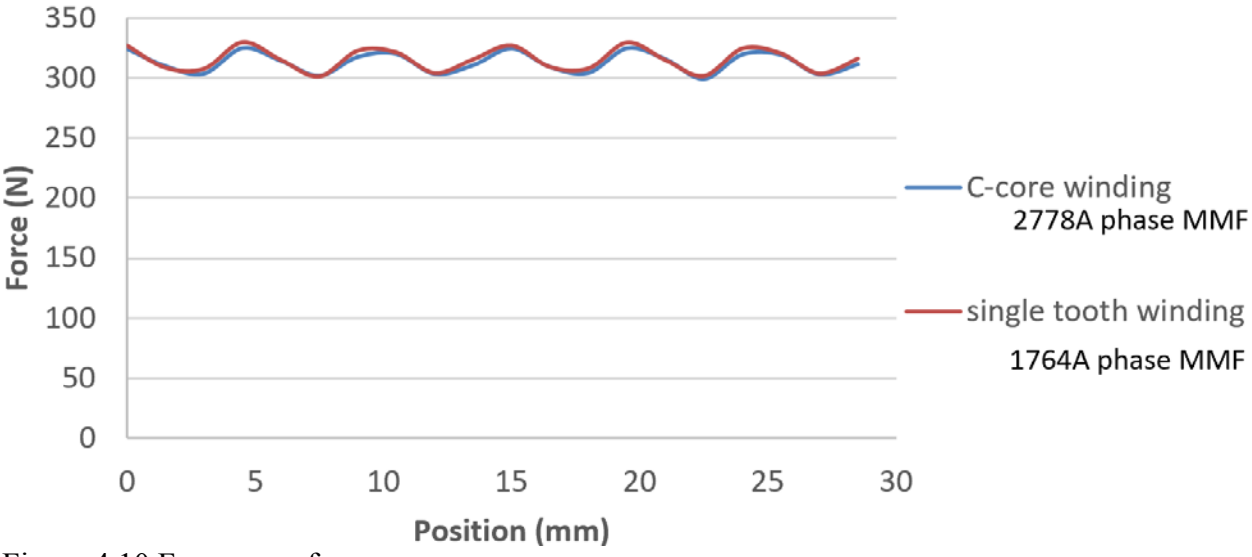

Figure 4.10 Force waveforms

4.4 Machine Resizing and Stator Tooth Dimension Optimisation

As a result of section 4.2 and 4.3, it is decided to take forward the combined tooth stator structure with a single toothed winding due to its simpler manufacture and higher efficiency. However, the implementation of such single tooth winding could be hard to achieve due to the small winding space and high bend ratio at the winding end. To minimise the winding difficulty when assembly, the next stage is to perform an optimisation on the overall size based on the strategy discussed in Chapter 3. This optimisation aims to reduce the translator size thus to save more space for the winding without significantly altering the machine outer

diameter. As concluded in Chapter 3 the best objective function is to minimise the phase MMF. However, the translator inner diameter constant (80mm) will be removed to allow a reduction in the current density to less than 3.5A/mm^2. The air gap is fixed at 1mm. Constraint 1 is to converge the translator mass to 6 kg, and constraint two is to maintain the force at 1500N. Instead of the trapezoidal tooth shape, the original rectangular tooth shape will be applied to the model so that the tooth can be laminated. The new optimised dimensions and results compared the previous topology are listed in table 4.1, and their overall sizes are shown in figure 4.11 in the same scale. It can be seen that after the new optimisation, the machine can have more winding space and smaller end winding bend ratio without significant change on the overall size.

ID	**Shaft_**	**sl_f**	**J**	**s_f**	**t_m**	**t_f**	**s_h**	**t_cb**	**Ob_1**	**Co_1**	**Co_2**
unit	mm				mm		mm		A	kg	N
Topology b	80	0.15	7	0.3	8.3	0.45	16.5	23.5	2135	5.29	1500
New topology	52	0.24	3	0.3	12.9	0.4	29	26	1833	5.59	1500

Table 4.1 Overall dimensions and results comparison

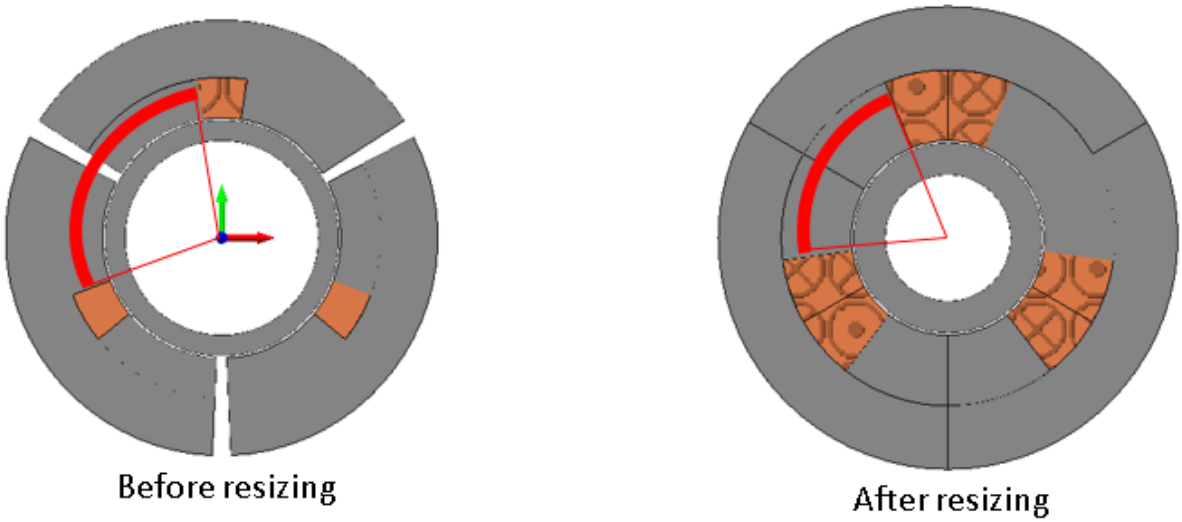

Figure 4.11 Overall sizes comparison in the same scale

The winding space and bend ratio can be further improved by varying the tooth root angle as shown in figure 4.12. Without changing the phase MMF but varying the tooth root angle the force profile is in figure 4.13. It shows that when the tooth root angle is at 51.6 degrees, the force can just hit required the 300N (one pole pair pitch model) with about 35% increasing on

winding space. Meanwhile, the average bend ratio of the windings can be further reduced due to the smaller tooth root angle.

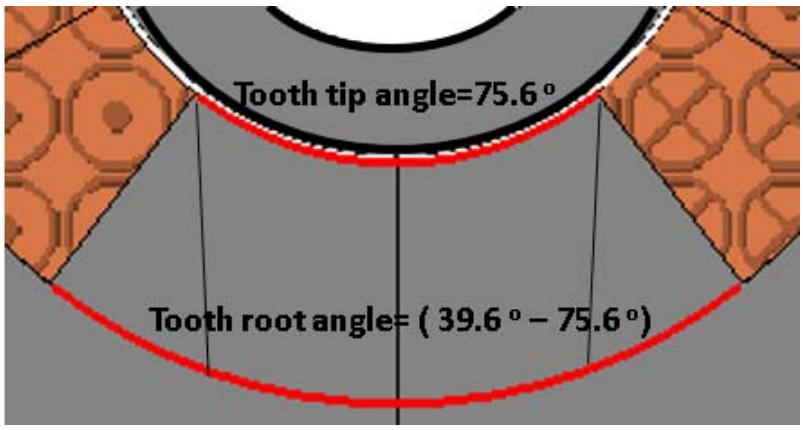

Figure 4.12 Sketch of varying tooth root angle

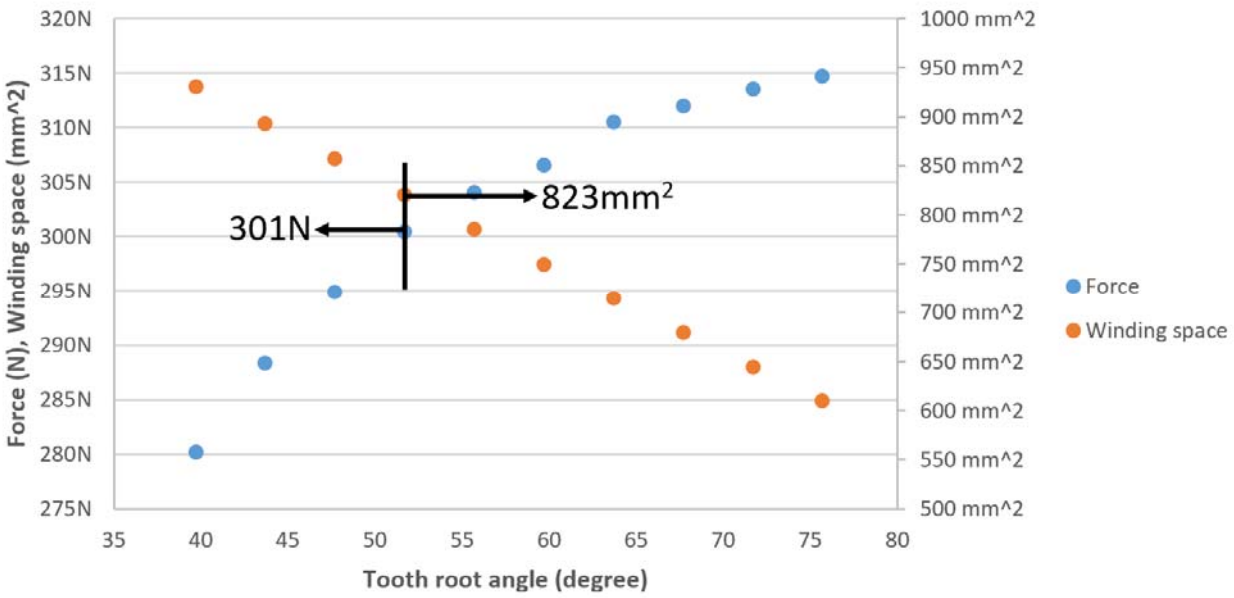

Figure 4.13 Force profile by varying tooth root angle

4.5 The Stator Laminations Design

So far the general machine dimension is confirmed, if all iron core components are using SMC material (fully 3D flux design), then it directly can be regarded as the final machine structure. However, due to the high cost and limited supply of SMC material, some alternative construction options are investigated for a low-cost prototype build, as shown in figure 4.14:

- In (a) stator teeth are composed of lamination steels where the flux is radially conducted and SMC core back ring is used to supply flux path along circumferential and axial directions.

- In (b) shows an option that can reduce the SMC usage by extending the tooth lamination area thus the SMC ring can be replaced by smaller SMC blocks.
- In (c) a further minimisation of the SMC block is shown, it shows that the Small SMC block is like a square shape.
- In (d) the square-shaped SMC block is replaced by a circumferentially laminated block. In this case along the circumferential direction, stator teeth can supply a flux path at the 2D plane (x, y) and circumferentially laminated block can supply another 2D plane flux path (x, z). Thus a 3D flux path can be formed.

Their performances are as shown in figure 4.15 where it shows that the SMC can be eliminated entirely by using option (d) with two types of lamination steels' combination. Meanwhile, the flux can maintain at 96% and force at 92%. It can conclude that such laminating strategy can effectively save the cost on the stator material. However, in practice, there could have small parasitic airgaps between separate stator segments which could weaken the flux thus the force, Chapter 7 will investigate this through testing.

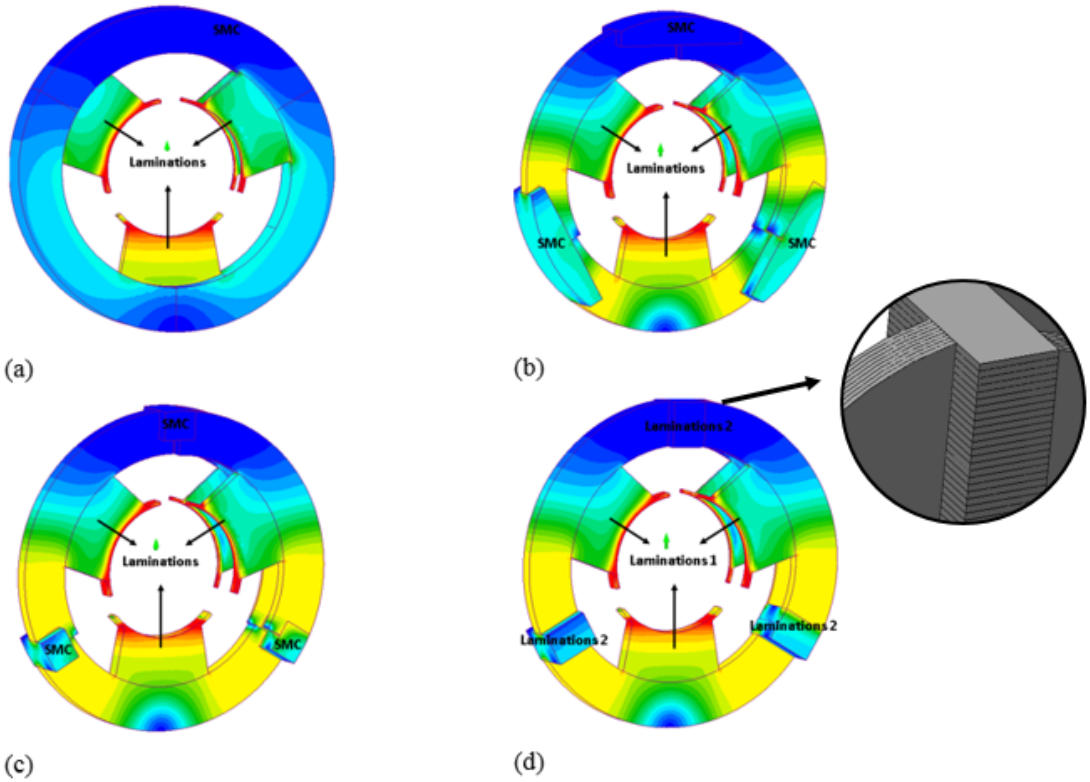

Figure 4.14 Lamination strategies

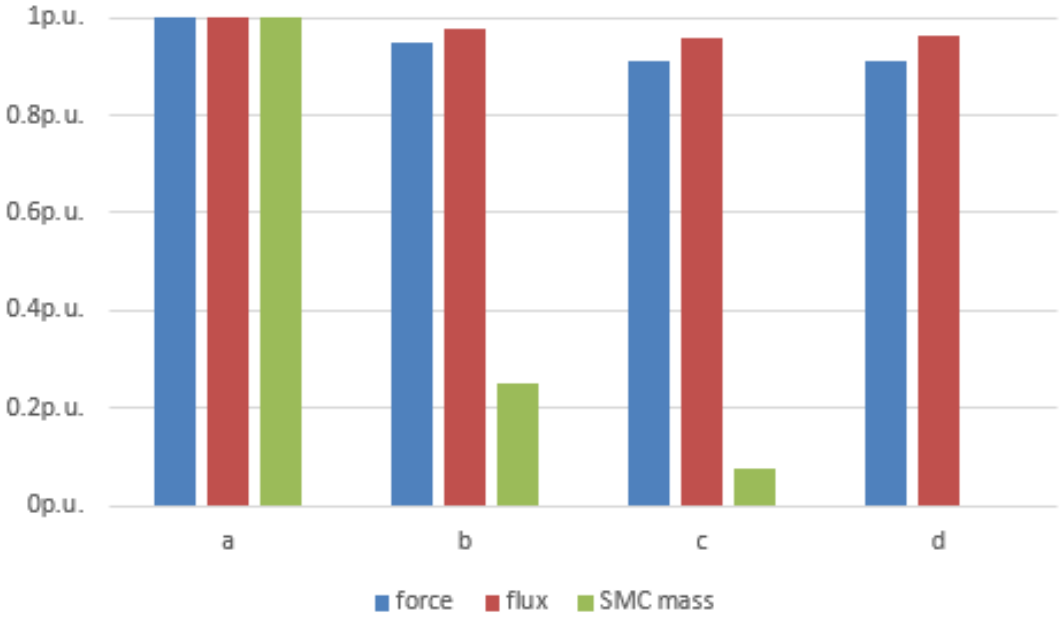

Figure 4.15 Performance comparison

4.6 Final Topology Performance Comparison and Summary

Figure 4.16 shows the final topology, performance comparison with the original topology is in table 4.2. From the electrical point of view the final design can achieve better efficiency and lower THD due to the applying of single tooth winding; from manufacture aspect, the final design takes advantages of fewer components and less material usage due to the tooth combination design and laminations design. Moreover, due to the machine resizing and detailed tooth shape design, the winding will be easier to assemble to the stator. What is more, when different current densities are applied the force profile is shown in figure 4.17. It shows that the armature current flux is saturated when the current density is at 3.5 A/mm^2, in other words, the machine is close to the maximum loaded condition which means the machine is designed to minimised size as well.

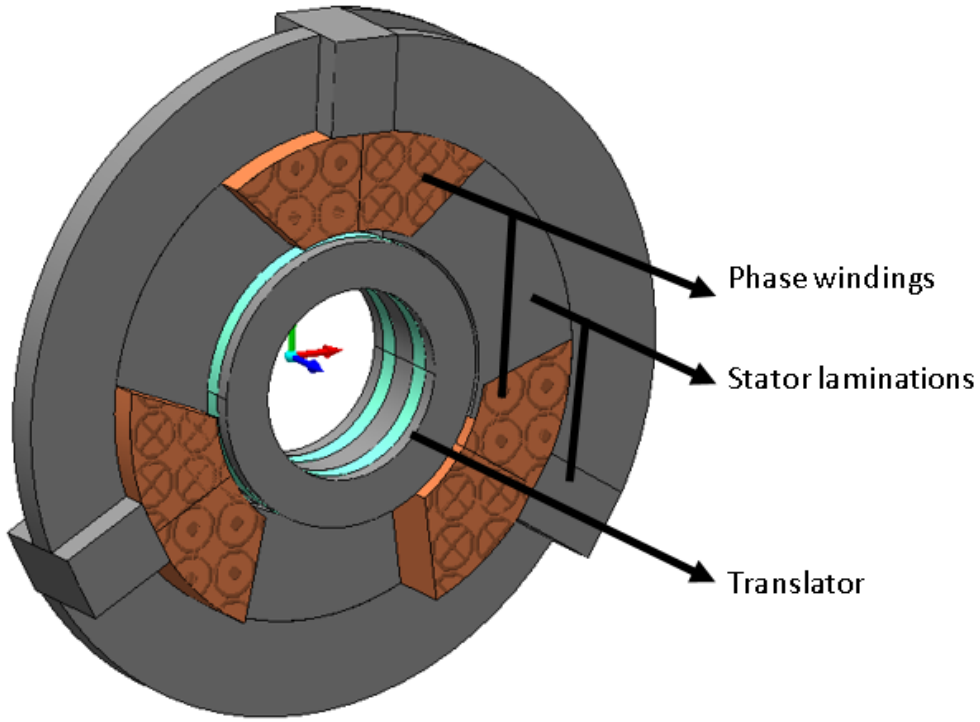

Figure 4.16 Final topology

Topology	Original	Final
MMF (A)	2135	1833
Magnet mass (kg)	2.28	2.33
Translator mass (kg)	5.29	5.96
Stator mass (kg)	15.56	13.8
Copper loss (W)	117.8	50.6
Iron loss (W)	63.0	78.8
Efficiency (%)	95.5	96.7
Power factor	0.67	0.62
THD	21.01	10.14

Table 4.2 Performance comparison after detailed design

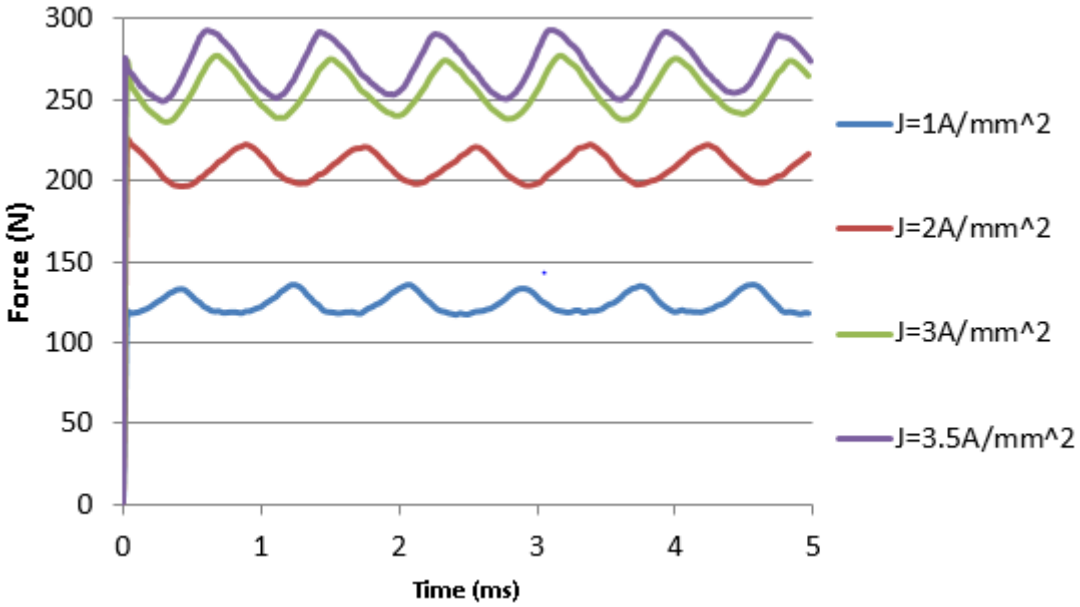

Figure 4.17 Force profile vs current density

In general, after the detailed design discussed in this chapter, the final MPM topology is confirmed. Simulated results show advantages of the final topology among both performance and building aspects. A numerical solution associated with this topology will be given in Chapter 5 to discover the insight of the transverse flux machine and Chapter 6 will present the detailed building process and mechanical design.

Chapter 5. The Insight Numerical Study for MPM

5.1 Introduction

Chapter 4 confirms the detailed design of the MPM. In this Chapter, a numerical study will be discussed to uncover the insight of the working principle of the MPM. Firstly, a swapped loading method based on Lorentz's law is used to calculate the thrust force. Then a numerical solution based on the reluctance network is formed to extract the effective air gap flux density profile which is also used to validate simulated results. The flux factor and flux linkage factor make central roles in thrust force production and machine power factor. Finally, two case studies are extended to discuss the influence of pole pair numbers on machine performances. Throughout this study, the insight of the MPM will be discovered, and better understandings on the transverse machine will be achieved.

5.2 Swapped Loading Method and Thrust Force Derivation

In Chapter 3 the force derivation of longitudinal flux machine has been discussed, since the radial main field flux is cutting the winding coils thus when armature current is applied the force can be calculated from three orthogonal components of Lorentz's law, the equation is as shown in equation. 2-6 where B and A are magnetic loading and electrical loading respectively. However, in transverse flux machine topology since the current flow is not directly cut by the main field thus a more complicate analysis method is required to evaluate the force.

5.2.1 Swapped Loading Method

In [80] [81] authors introduced an effective way to derive the thrust force for a transverse flux machine by swapping loadings (B and A), namely replacing the PMs with equivalent current sheets to give A and the armature current produces the air gap flux density B. Figure 5.1 gives a single phased circumferential view sketch for the final designed MPM, by using swapped loading method, magnets can be replaced by current sheets (dots and crosses). When the translator is at the peak thrust force position (magnets align to stator teeth), the peak armature current is applied to phase windings. At this point, the armature field flux can be classified into three components as main flux (ϕ_{po}), fringing flux (ϕ_{ne}) and leakage flux (ϕ_{leak}). The red line through the highly permeable steel tooth is the main flux which can produce a positive thrust force (F_{po}), the fringing flux is demoted by a red dashed field line through the low permeable 'air tooth' produces a negative thrust force (F_{ne}), the green line is the leakage flux which does not contribute to the thrust force. The net thrust force is the difference of F_{po} and

F_{ne}. Detailed derivations are formulated in equation. 5-1. *Area* is the effective area between armature tooth and translator equivalent current sheets, MMF_{eq} is the equivalent magnetic motive force of the magnet, L_{eq} is the effective current length, B_s is the radial flux density which producing thrust force, K_B is defined as the flux factor in [82] [83] and typically is only 32% or less in transverse flux machines [80], M is the magnetisation or coercivity of magnets and d_m is the magnet depth. In fact, not only K_B but also the flux linkage factor K_L contributes to the thrust force production and their combination also directly influences the power factor which will be discussed in later sections.

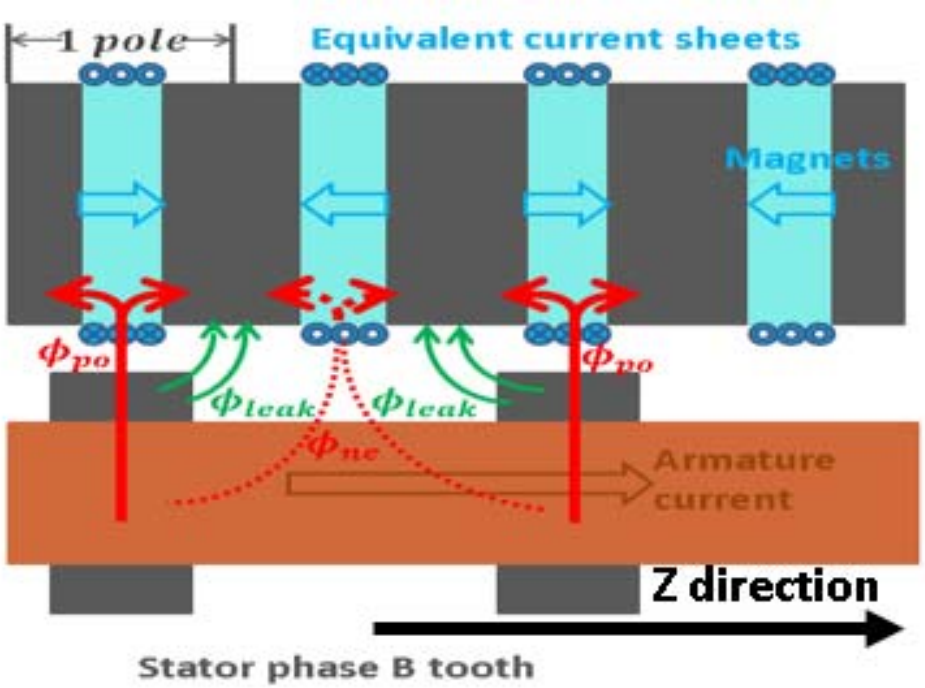

Figure 5.1 Swapped loading method sketch for the final designed MPM

$$F_{peak} = F_{po} - F_{ne} = \frac{\phi_{po} - \phi_{ne}}{Area} \times MMF_{eq} \times L_{eq}$$

$$= \frac{(\phi_{po}+\phi_{ne})}{Area} \times \frac{\phi_{po}-\phi_{ne}}{\phi_{po}+\phi_{ne}} \times MMF_{eq} \times L_{eq}$$

$$= \frac{(\phi_{po}+\phi_{ne})}{Area} \times \frac{B_{po}-B_{ne}}{B_{po}+B_{ne}} \times MMF_{eq} \times L_{eq}$$

$$= B_s \times K_B \times MMF_{eq} \times L_{eq}$$

$$MMF_{eq} = \mathrm{M} \times d_m \tag{5-1}$$

5.2.2 Flux Density Extraction and Force Calculation

The target MPM has a 3D flux path, so flux density varies in both radial and axial directions of the translator outer circumference, as shown in figure 5.2 (a single phased for example). The flux density is seen to be higher in the area close to the steel tooth and conversely the flux density for air tooth is weaker. Detailed simulated FEA data for both B_{po} and B_{ne} are shown in figure 5.3(a) and (b), where each linear represents flux density profile at different location. In reality the thrust force is generated all along the magnets' equivalent sheets, however due to the constancy of equivalent current sheets, the average flux density value can be taken into account without losing any generality. The designer chooses 7 points to gain average flux density for B_{po} and B_{ne} respectively (*z1* to *z7* and *z8* to *z14*) due to the consideration of simulation accuracy and computation time trade-off. In figure 5.3(c) is the average flux density profile along a single phase span, where the blue curve is the profile of the average B_{po} (average of those in figure 5.3(a)), the red curve is the average B_{ne} (average of those in figure 5.3(b)) and the green curve is the difference of B_{po} and B_{ne} (or effective flux density). The constancy of equivalent current sheets not only apply to the translator moving direction but also apply to the phase arc span. Thus when calculating the effective thrust force, mean values of average flux density profiles are required as B_{po}, B_{ne} and B_{po} - B_{ne} which equal to 0.59T, 0.11T and 0.48T respectively from figure 5.3(c). In this case since the steel tooth and air tooth share the same effective area thus the flux density factor can represent the flux factor as$\frac{0.48}{0.59+0.11} = 68.57\%$. However by observing figure 5.1 there is still considerable leakage flux which contributes nothing to the thrust force, the designer will consider this factor in the numerical solution section to extract B_{po}, B_{ne} and $B_{po} - B_{ne}$. By substituting mean values of flux density profiles from figure 5.3 and detailed MPM dimensions from table 5.1 into equation. 5-1 the thrust force for a single phase and single pole pair model at this position can be estimated as: $Thrust = B_s \times K_B \times \mathrm{M} \times d_m \times \frac{120}{360} \times 2\pi \times r = (0.59 + 0.11)T \times 68.57\% \times 827600 \times 0.006 \times \frac{120}{360} \times 2\pi \times 0.0394 = 197\mathrm{N}$. For three phased 5 pole paired topology the equivalent thrust force is about: $Thrust = 1.5 \times 5 \times 197 = 1477.5\mathrm{N}$ which is close to the final MPM simulated value (1354N).

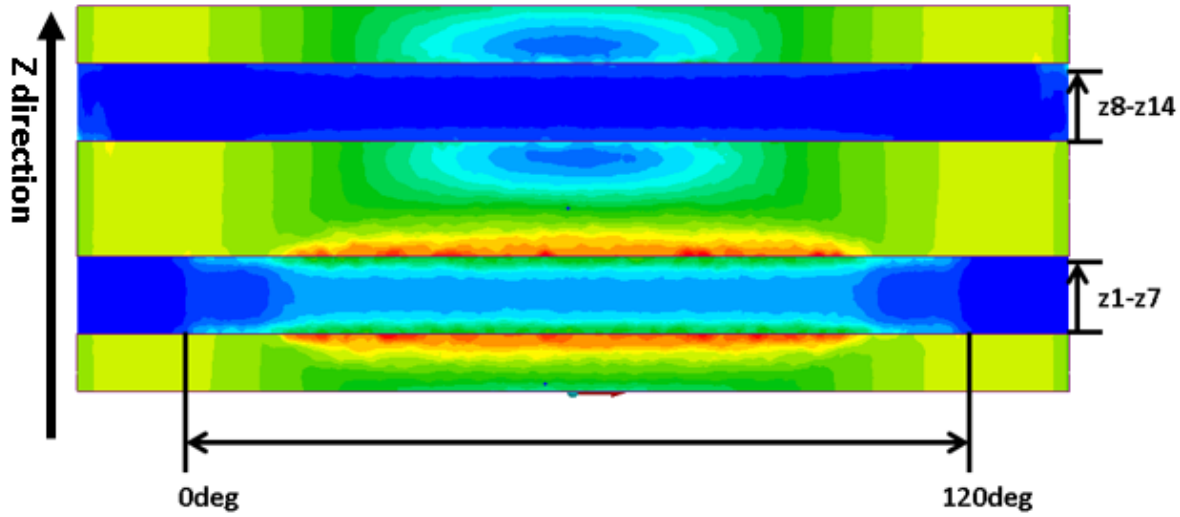

Figure 5.2 Flux density sketch map along the translator surface (single phased)

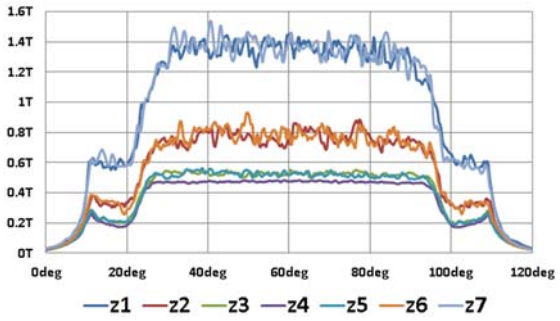

(a) B_{po} vs phase angle at different z axial position

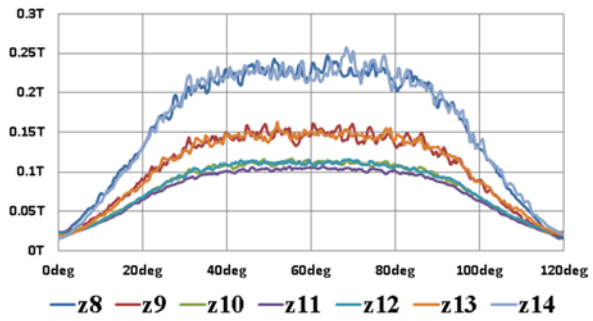

(b) B_{ne} vs phase angle at different z axial position

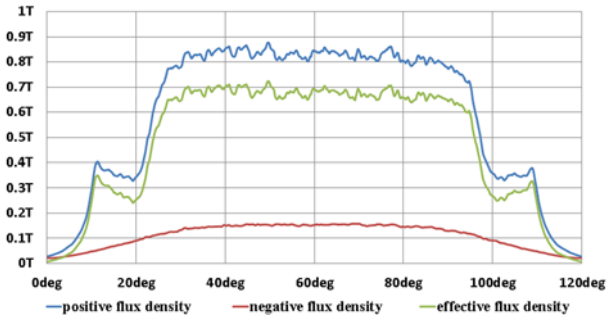

(c) Average flux density profile

Figure 5.3 Detailed flux density profile

Translator inner radius (mm)	26
Translator core back depth (mm)	12.9
Translator outer radius (mm)	38.9
AG (mm)	1
Tooth arc (degree)	60
Tooth height (mm)	29
Stator core back depth (mm)	26
Stator core back inner radius (mm)	68.9
Stator core back outer radius (mm)	94.9
Translator magnet depth (mm)	6
Translator steel depth (mm)	9
Pole pair pitch (mm)	9
Stator Tooth depth (mm)	30
Phase angle β	0
Max current density (A/mm^2)	3.5
Max single phase single pole pair peak thrust (N)	200
Power factor	0.62

Table 5.1 Machine detailed dimensions

5.2.3 Flux Density and Force Profiles

When the translator is moving, flux density profiles according to displacement are as shown in figure 5.4. Where six points are selected separated by 18 electric degrees, namely the translator is moving from aligning to the magnet position to aligning to the SMC core back position. It shows that both positive and negative flux densities are dropping while the translator is moving. However, the positive flux density drops more rapidly as a consequence the effective flux density, and flux factor converges to almost 0. In fact, such trend not only due to the translator displacement but also caused by the target phase armature current decreasing. Clearer data corresponding to the equation 5-1 is in figure 5.5, where the green curve illustrates B_s profile which reflects the armature current effect, the red curve illustrates the flux factor profile which reflects the translator displacement effect and the blue curve illustrate the effective flux density profile which will finally determine the thrust force profile. Comparison of the calculated thrust force profile and the simulation are in figure 5.6. Results show a peak error of less than 13% on force and 6.6% difference on THD for the moving case.

Displacement (degree) **Flux density profiles**

0

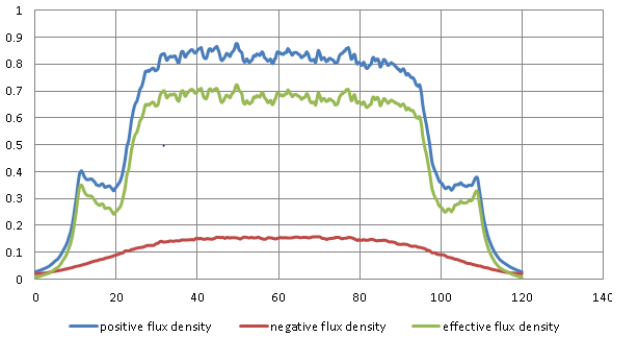

18

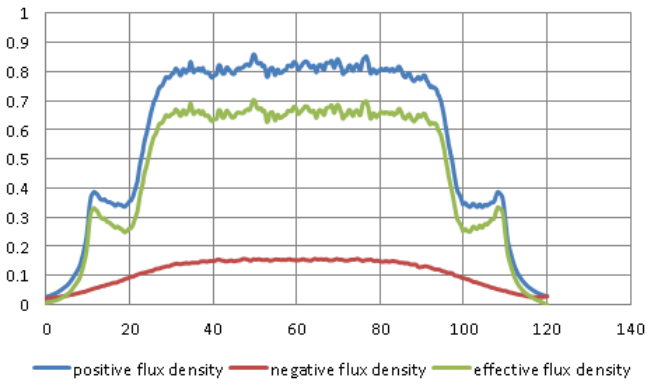

36

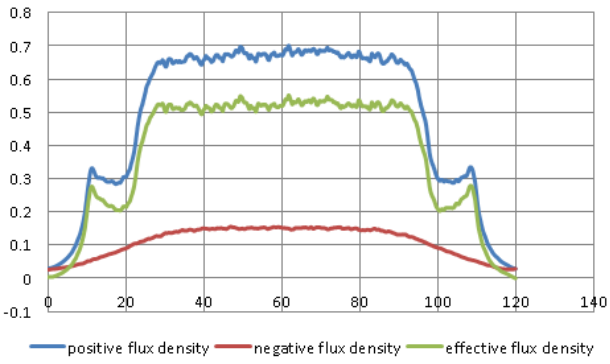

54

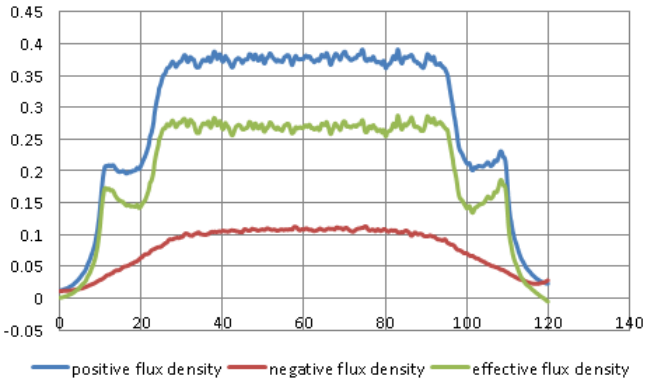

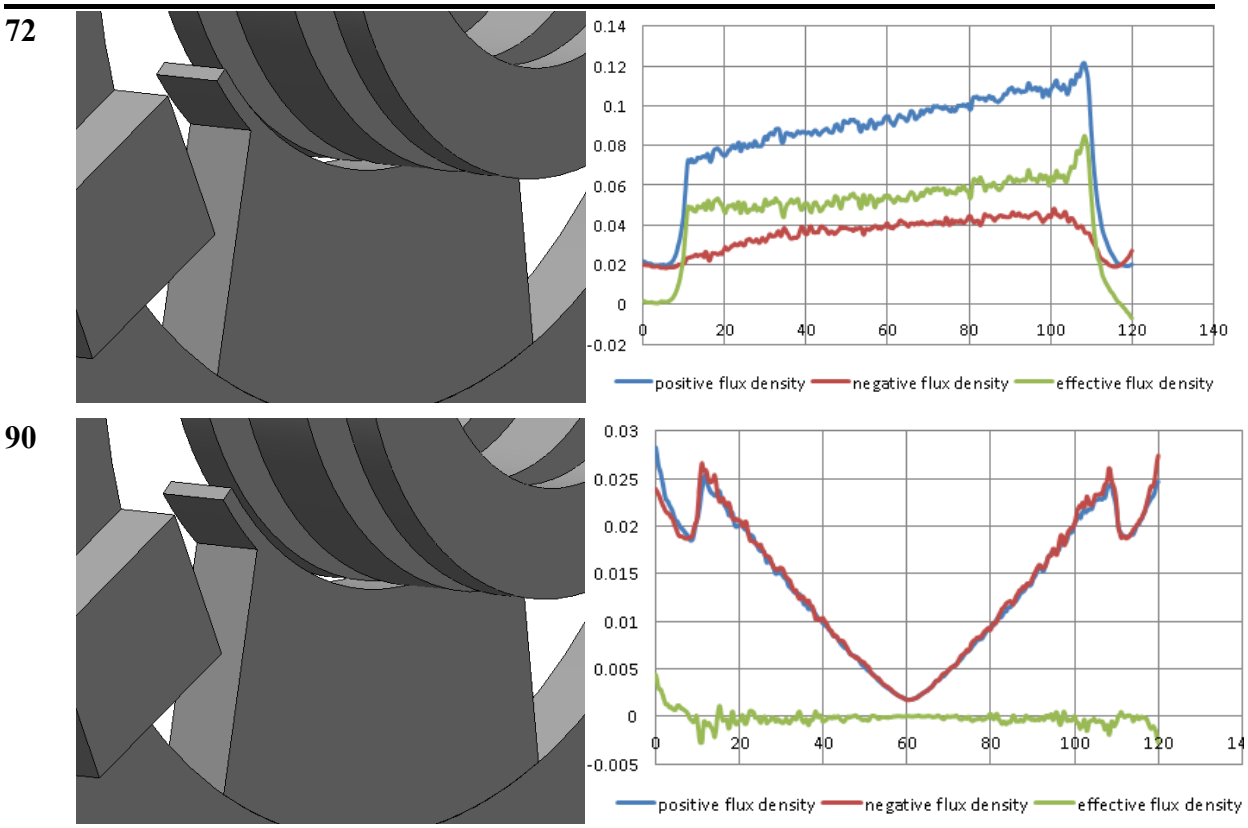

Figure 5.4 Detailed flux density profiles against translator positions

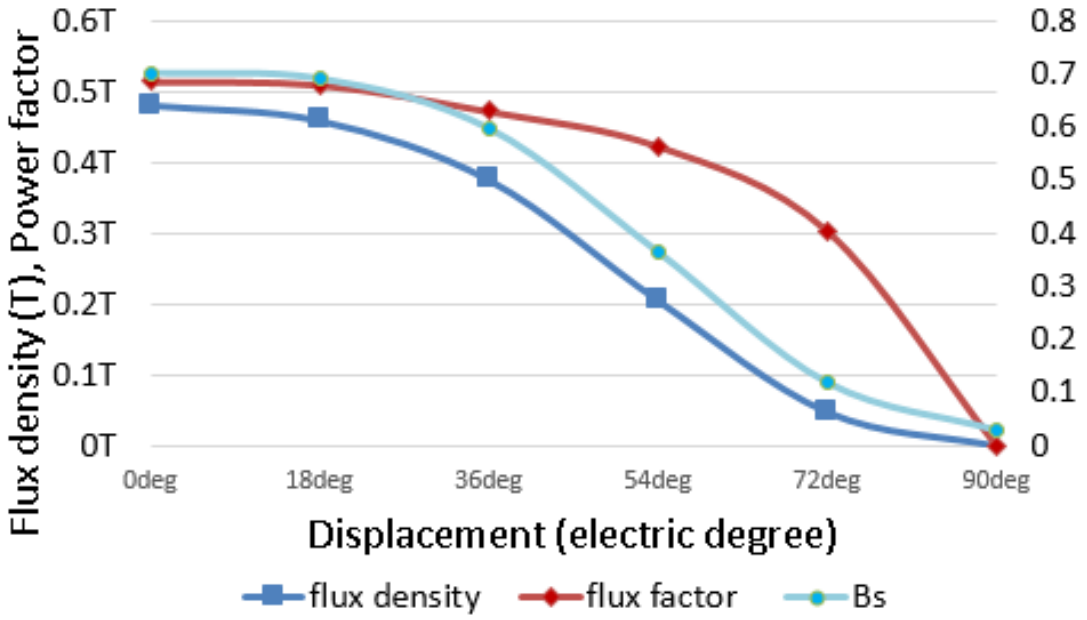

Figure 5.5 Clearer flux density profile based on displacement

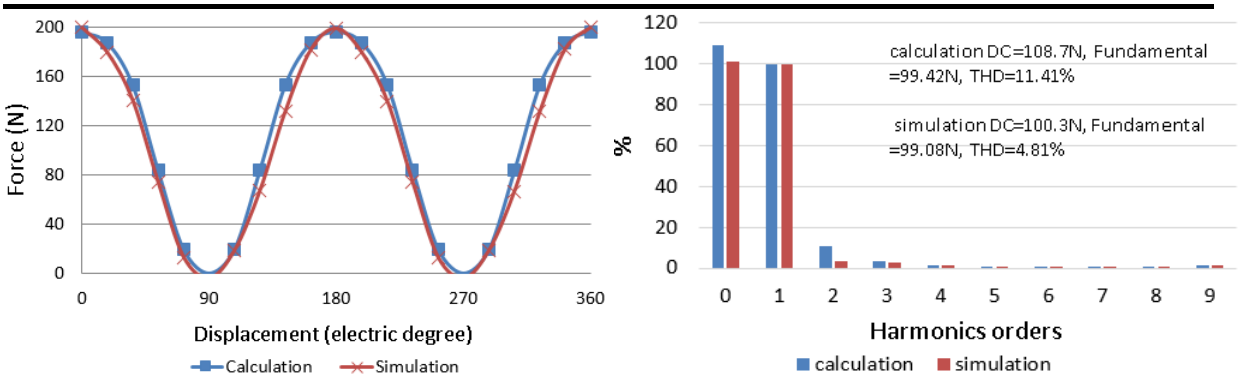

Figure 5.6 Comparison of calculating and simulating results on the thrust force

5.3 Flux Factor and Flux Linkage Factor

In above section, the designer uncovers the relation between the armature current flux density profile and the resultant thrust force. The conclusion is that the flux factor makes a vital role on the thrust force production, in other words, the flux factor indirectly reflects the use efficiency of the armature flux. The flux factor is a unique parameter of the transverse flux machine, and high flux factor can contribute to high force density, higher efficiency and high power factor, besides a more common factor that could affect the thrust force is the flux leakage.

The flux leakage normally takes place in the air gap, slots area for all types of machines include the main flux leakage and the armature flux leakage. For conventional longitudinal flux machines, if flux fields are not saturated then flux leakages for both main field and armature field could only take a small part of the total flux. As for transverse flux machines, due to the high complexity of the stator structure, the flux leakage of the armature field could be much higher than that of the longitudinal machine (even for low armature current). It is also the reason of low power factor property for the transverse flux machine. In figure 5.7 the flux sketch and the flowchart detailed explain the concept of the flux factor and flux linkage factor defined by the designer for the target MPM. Where the red block (marked as a) is the flux which produces positive thrust force, black block (as b) is the flux which produces negative thrust force, and green blocks (as c) are the leaked flux which contributes nothing to the thrust force. The sum of a, b and c is the total flux produced by the armature current. Thus the flux linkage factor (K_L) and the flux factor (K_B) are expressed in equation. 5-2 and equation. 5-3. For designed MPM, simulated results show the flux linkage factor K_L is 38%, and the flux factor K_B is 68.6%.

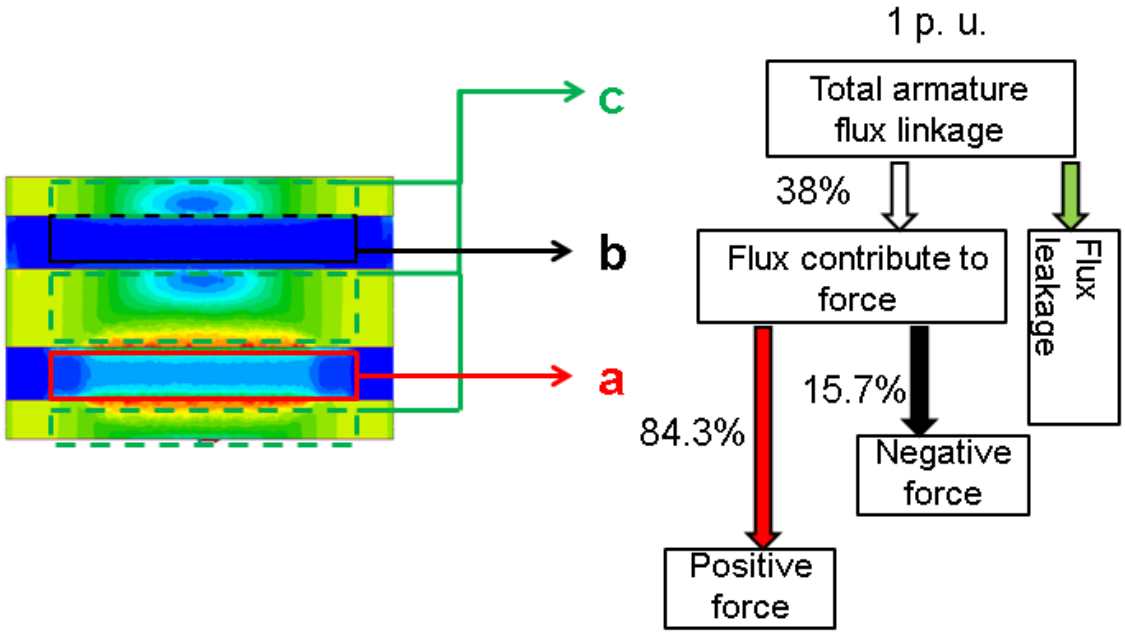

Figure 5.7Flux distribution sketch for designed MPM

$$K_L = \frac{a+b}{a+b+c} \tag{5-2}$$

$$K_B = \frac{a-b}{a+b} \tag{5-3}$$

5.4 Reluctance Network and Numerical Solution

For above sections, all results related to the flux profiles are from 3D FEA simulations. However, a drawback of this is the computation time cost (typically 3-4 hours for the static solver and 18-24 hours for the dynamic solver). In this section the designer like to try to calculate $B_{po} - B_{ne}$, flux factor and flux linkage factor by using a simplified reluctance network model based on the equivalent magnetic circuit as introduced in [84].

5.4.1 Reluctance Network

Two assumptions are made before the modelling. Firstly, all steel components share the same relative permeability at a fixed position (for other positions, the permeability requires to be recalculated based on the B-H curve of the material). Secondly, for each phase, the air gap flux density is circumferentially constant between 30-90 degrees and linearly drops to zero from 30-0 and 90-120 degrees respectively (this is an imitation of flux density profiles which aim to reduce the modelling complexity). The axial variation of the radial flux is of no concern as only the average flux is taken into account. Furthermore, the modelling segments for each phase along a pole pair pitch is set as minimum segments number eight due to the flux blocks distribution (a, b and c with two blocks) and symmetry to reduce the modelling complexity.

An example drawing of the reluctance network at zero electrical degree position is in figure 5.8. The modelling is mainly composed of three parts as the stator tooth part, the translator part and the stator core back part. Where the stator tooth part contains three separate phases with eight columns for each phase along a pole pair pitch, the translator part contains four columns and the stator core back part is a single unit which conducted flux between different phases. Rows for each phase include steel tooth reluctance and air tooth reluctance, air gap reluctance, air joint reluctance and steel joint reluctance. The general layout of the reluctance network is almost unaffected by the position, but according to different positions the reluctance components' material and values could be changed (for example the stator tooth part of phase A or C can be regarded as that of Phase B at another position).

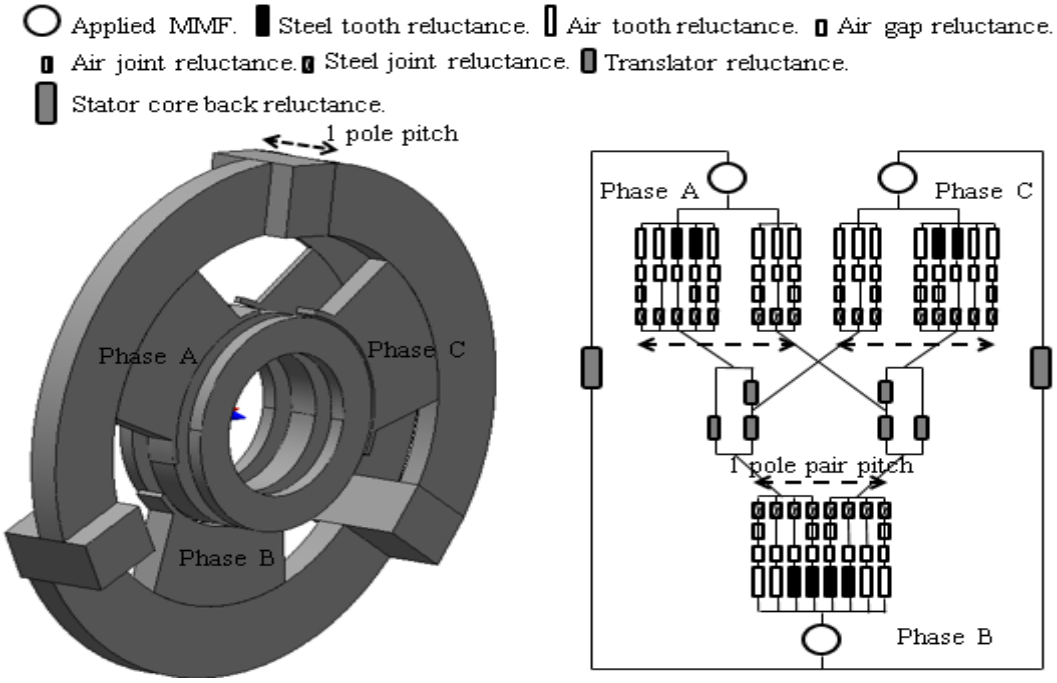

Figure 5.8 3D model and 2D reluctance network drawing

5.4.2 Flux Profile Calculation and Comparison

After confirming the reluctance network topology then it becomes possible to determine the reluctance value for each component according to the size specification given in table 5-1 and equation. 5-4, where R_{eq} is the equivalent reluctance for the component, L_{eq} is the equivalent component length, μ_r is the relative permeability, μ_0 is the permeability constant, and A_{eq} is the equivalent component cross-section area. The relative permeability is estimated by the flow chart shown in figure 5.9 and final located at 7676. The Simulink model of the reluctance network with detailed results is as shown in figure 5.10, where the display and display 1 denote half of the leaked flux, display 2 denotes half of the positive flux, display 3 denotes half of the negative flux and display 4 is the total flux value. As a result, ϕ_{leak} is

0.4164m Wb, ϕ_{po} is 0.1842m Wb, ϕ_{ne} is 0.03m Wb, and ϕ_{total} is 0.6306m Wb. Thus K_L is about 34.0%, and K_B is about 72.0% (38% and 68.6% from simulations). If taking effective cross-section area into account (30-90 degree of a phase span with 6mm magnet width) then peak B_{po} is 0.755T and peak B_{ne} is *0.123*T. Thus corresponding flux density profiles from calculations are as shown in figure 5.11, which mean values for B_{po}, B_{ne} and effective flux density are 0.566T, 0.092T and 0.474T respectively, compared to simulated results (0.59T, 0.11T and 0.48T) the numerical reluctance network method show a good agreement with an error less than 2% on the effective flux density.

$$R_{eq} = \frac{L_{eq}}{\mu_r \times \mu_0 \times A_{eq}} \tag{5-4}$$

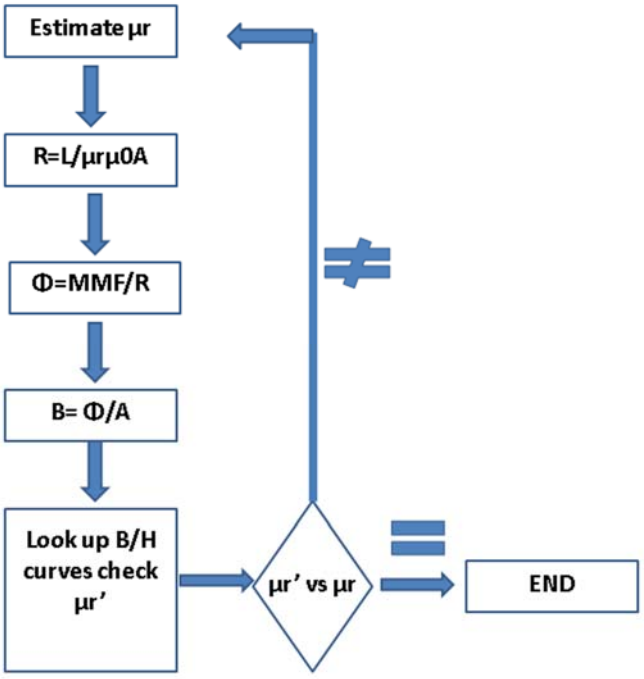

Figure 5.9 Flow chart for relative permeability estimation

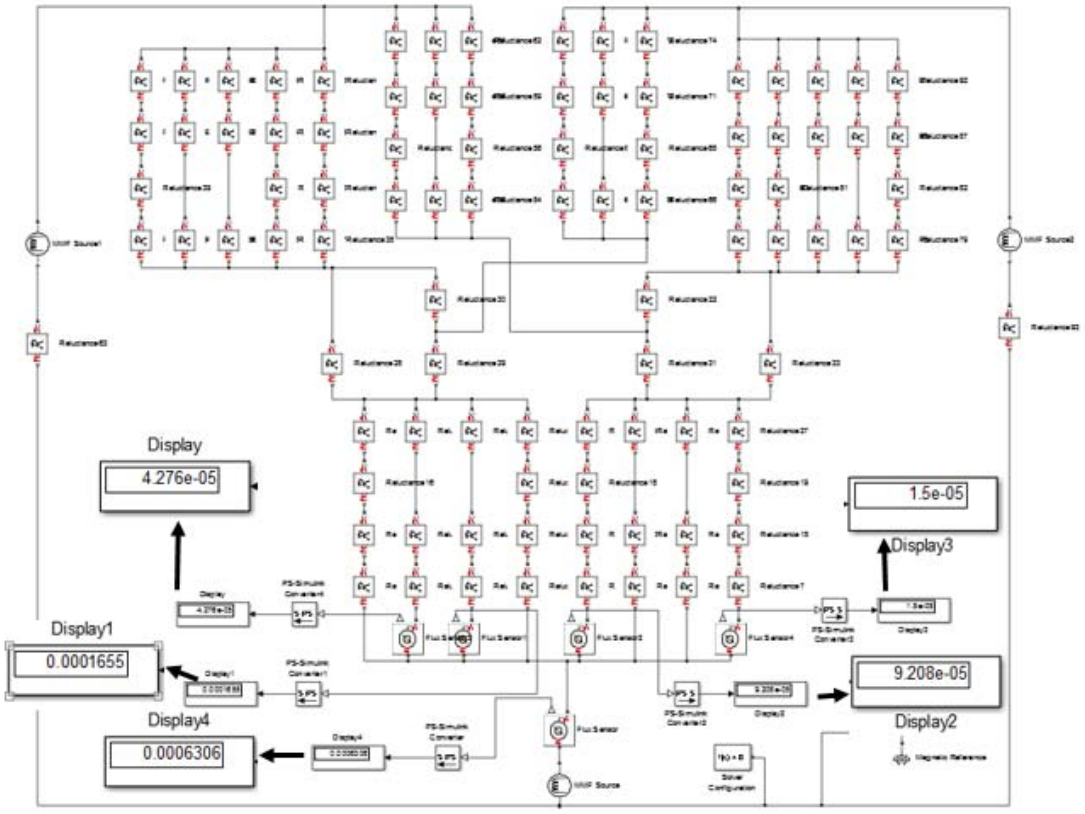

Figure 5.10 Reluctance network Simulink model

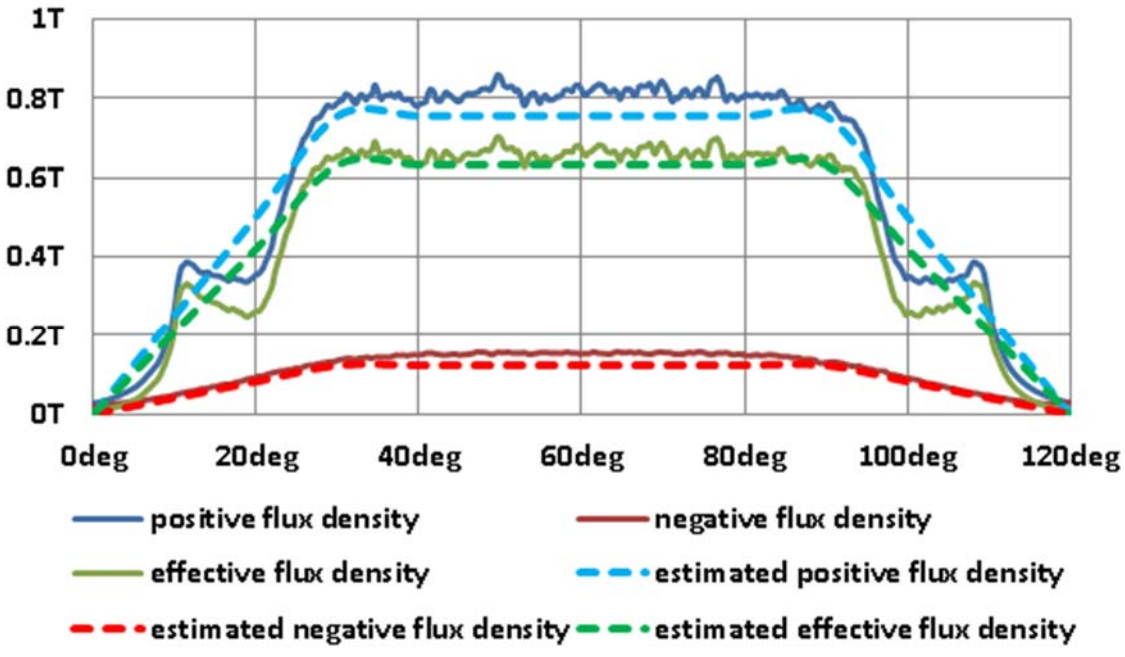

Figure 5.11 Numerical and simulated flux density profile comparison

5.5 Power Factor Deduction and Relation to Flux Factor and Flux Linkage Factor

5.5.1 Power Factor Derivation

The power factor is the cosine function of the phase angle θ between the armature current I_a and the armature terminal voltage V. When using a set of current sources the phasor diagram is as shown in figure 5.12(a). For the designed MPM, the peak fundamental EMF per turn (E_f) is 0.8681V as shown in figure 5.12(b). Since the phasor diagram is independent of the number of coil turns, thus the power factor can be deducted from 1 turn model, and details are as follows. In equation. 5-3 it denotes the relation between radial flux density B_s and armature current I_a (I_a equals to the phase MMF since turn number is set as 1). By combing equation. 5-1 to equation. 5-5 the armature current I_q can be expressed as a function of phase peak Fore F_{peak} as shown in equation. 5-6, it can be seen that for a specific thrust force requirement the higher K_L and K_B the less I_a could be required. Thus better efficiency can be achieved. Other two parameters related to the power factor are presented in equation. 5-7 and equation. 5-8, where v is the linear speed in m/s and p_τ is the pole pair pitch in m. As a result, it can be concluded from equation. 5-9 that the power factor is related to both flux linkage factor K_L and flux factor K_B ($E_{fconstant}=\frac{E_f}{\omega_e}$). In other words, since parameters $Area$, MMF_{eq}, L_{eq} and $E_{fconstant}$ are related to the final MPM topology dimensions and materials which can be regarded as constants, thus for a specific thrust force requirement, higher K_L and K_B also contribute to higher power factor.

$$B_s = \frac{\phi_{total} \times K_L}{Area} = \frac{I_a \times K_L}{R_{eqtotal} \times Area} \tag{5-5}$$

$$I_a = \frac{F_{peak} \times R_{eqtotal} \times Area}{K_L \times K_B \times MMF_{eq} \times L_{eq}} \tag{5-6}$$

$$L_q = \frac{1}{R_{eqtotal}} \tag{5-7}$$

$$\omega_e = \frac{2\pi \times v}{p_\tau} \tag{5-8}$$

$$PF = \cos\left(\tan^{-1}\frac{I_a \times L_q \times \omega_e}{E_f}\right)$$

$$= \cos\left(\tan^{-1}\frac{F_{peak} \times Area}{K_L \times K_B \times MMF_{eq} \times L_{eq} \times E_{fconstant}}\right) \tag{5-9}$$

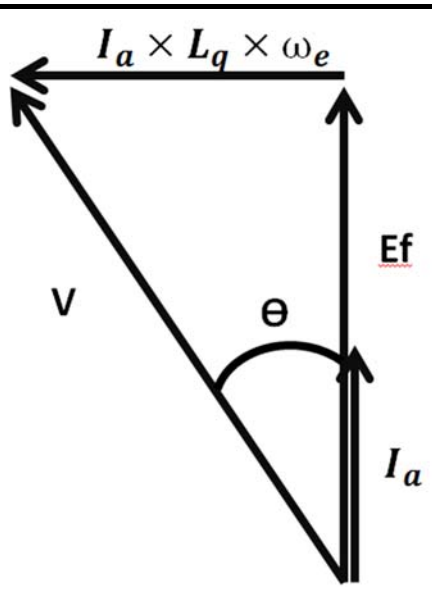

(a). Designed MPM phasor diagram

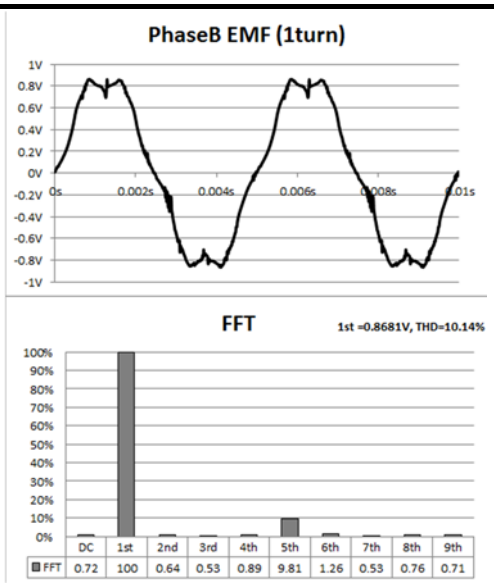

(b). Designed MPM peak EMF (1 turn)

Figure 5.12 Designed MPM power factor and EMF profiles

5.5.2 Power Factor against Electric Loading

For any machine topology the power factor is highly influenced by the electric loading saturation (i.e. the same topology can achieve varied power factor according to different I_a). If I_a is increased, the steel relative permeability drops and the equivalent reluctance increases. The resulting flux therefore doesn't increase linearly with the armature current. When the armature current increasing to a certain level, the saturation can cause the power factor as well as the flux produced by the current ($I_a \times L_q$) converges to a constant. The thrust force, the effective flux density, K_L, K_B and the power factor profiles with different armature current densities are as shown in figure 5.13 (Solid lines for calculations and dash lines for simulations). It can be observed that as the current density increases from 1 to 3.5A/mm^2, the thrust force profile shares the same trend as the effective flux density profile in per-unit form, K_L and K_B essentially keep constant and the power factor gradually drops from 0.8 and finally converge to 0.62. Thus it can be concluded that the power factor variation matches the regulation as mentioned in equation. 5-9 and the designed MPM topology can reach 0.62 power factor for the worst-case scenario. Compared to 0.35- 0.53 in [85], the deigned MPM shows better performance due to the better K_B. However due to intrinsic low K_L, the MPM still show a poor power factor feature compared to the conventional longitudinal flux machine. (As usual as the weak spot of the transverse flux machine).

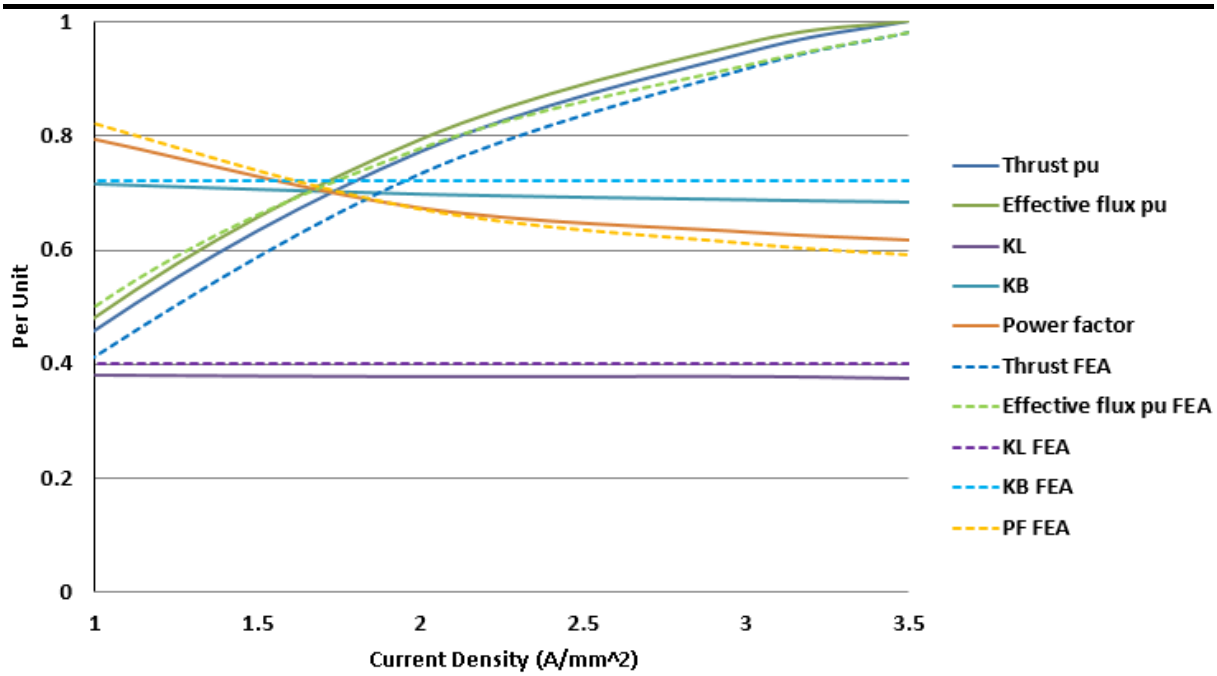

Figure 5.13 Performance vs current density

5.6 Two Case Studies of Pole Pair Influence on Machine Performances

The study performed in the previous section denotes the relation between the power factor and the thrust force (or armature electric loading). However the influence of K_L and K_B are basically not involved, in this section two case studies will be presented to highlight the importance of the pole pair number to K_L and K_B thus the machine performances (thrust force and power factor). Both calculations are based on the swapped loading method and the equivalent reluctance network and FEA results are shown for the agreement comparison.

5.6.1 Force against Pole Pairs Number

The first case study is about the investigation of machine performance with different pole pair numbers under a constant armature current condition. In figure 5.14 it shows that K_B remains relatively constant with an increase in pole pair number. However, K_L and the total flux show improvements while the pole pair number increased. These are due to the distance between adjacent translator iron cores (or air join reluctances) keep reducing as long as the pole pair numbers increasing while the other reluctance components remain constant. As a result when the armature current profile is set as a constant the total flux increases from 0.79 p.u. (one pole pair) to 1 p.u. (five pole pairs), and K_L is improved from 0.14 (one pole pair) to 0.38 (five pole pairs). By combing both the total flux and K_L profiles the effective flux density profile can be calculated and shows agreement to the thrust force profile in per-unit form. In general, the first study proofs that increasing pole pair number can effectively increase $K_L \times K_B$ thus contributes to higher thrust force.

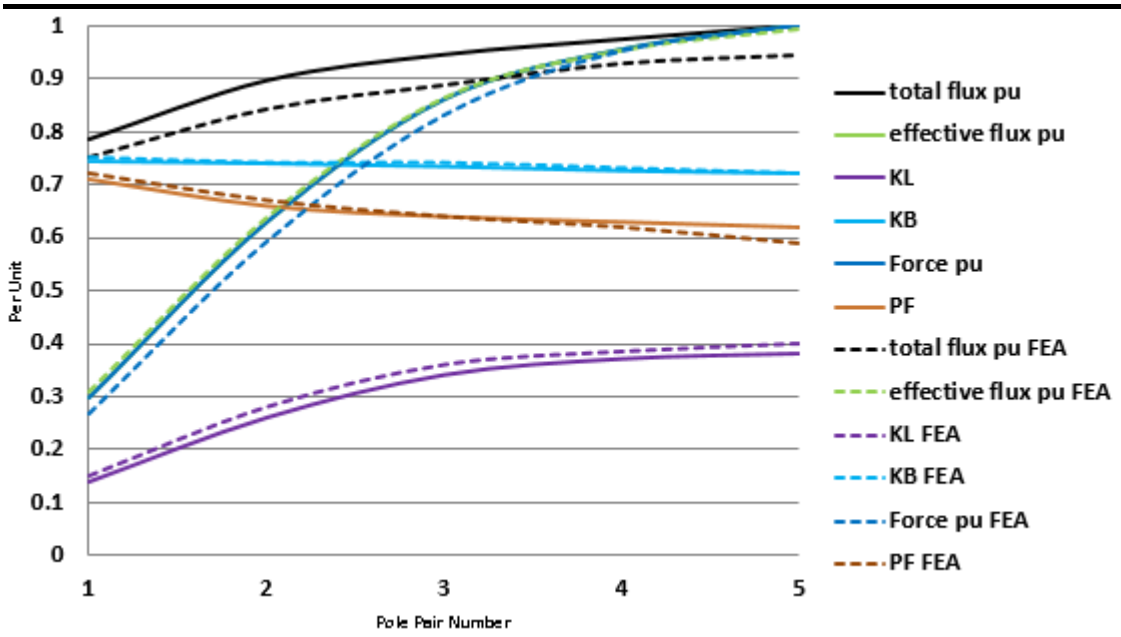

Figure 5.14 Performances of machine on different pole pair numbers with constant armature current profile

5.6.2 Power Factor against Pole Pairs Number

The second case study is a validation of the relations between K_B and K_L and the power factor when the same thrust force requirement (380N) is applied to the different pole pair number models. In figure 5.15 K_L and K_B show similar trends as those in figure 5.14. To achieve the same thrust force while pole pair number is increasing, the required armature current (or total flux) reduces from 1 p.u. (one pole pair) to 0.53 p.u. (five pole pairs), however due to K_L improves with increasing pole pair numbers, the effective flux and the thrust force can maintain at the same level. The resulting power factor improves from 0.71 (one pole pair) to 0.89 (five pole pairs), it again proofs the increasing $K_L \times K_B$ contributes to a higher power factor. Two case studies together demonstrate that the power factor and the thrust production are much more related to K_L as the pole pair number is varied, K_B remains relatively constant. It is believed that K_B is more related to the machine steel material and windings topology.

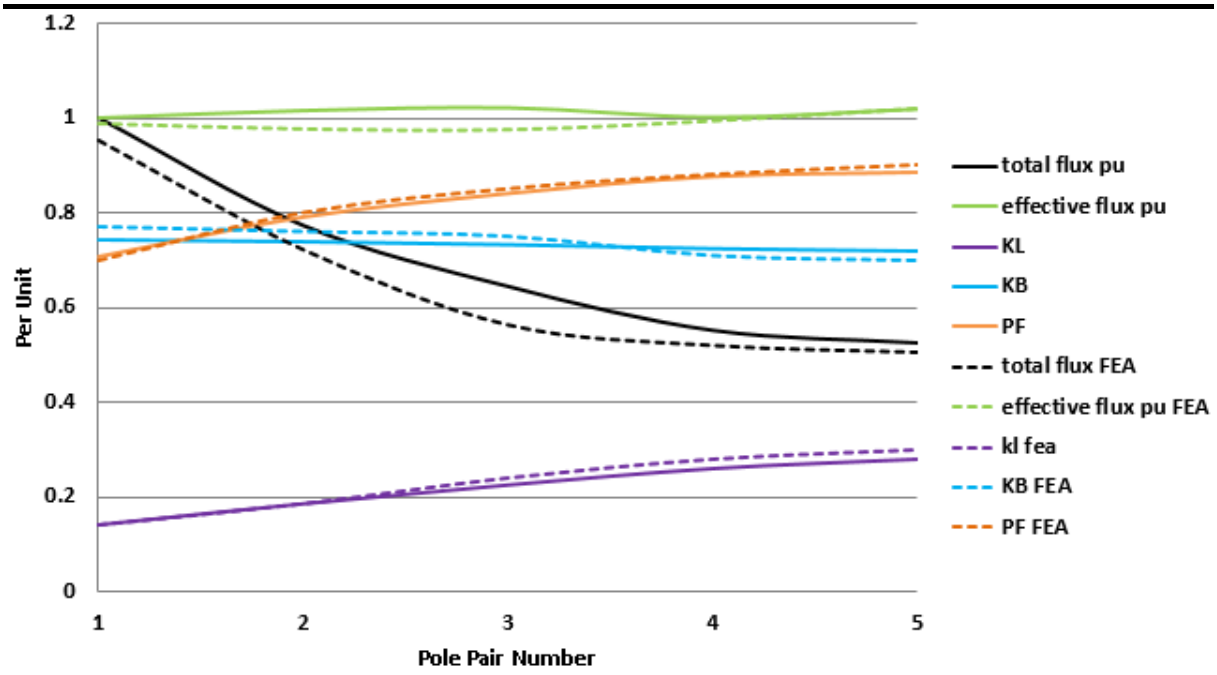

Figure 5.15 Performance of machine on different pole pair numbers with a constant thrust force production

5.7 Summary

In this Chapter, the insight of the working principle of the final designed MPM is investigated. An effective analysis method (swapped loading method) is presented which explains the thrust force production based on the armature current flux density profile and magnets equivalent current sheets. A numerical reluctance network solution based on the equivalent magnetic circuit and material relative permeability estimation is proposed and used to compared with FEA results. The flux linkage factor (K_L) and the flux factor (K_B) are defined by the designer and being found making central roles on the thrust force production and power factor determination (the higher K_L and K_B the higher thrust force and better power factor). It has been found that K_L is highly related to the machine pole pair number (the higher Pole pair number the higher K_L) and K_B relatively keep as constant. By further considering the influence of the saturation of the machine, for the worst-case scenario (maximum electric loading) the power factor can still achieve 0.62. Compared to conventional transverse flux machines in the literature, the final designed MPM appears to have better power factor due to good K_B. However, compared to conventional longitudinal flux machines this MPM still show disadvantage on the power factor due to the low K_L. Two case studies compare both FEA and numerical results and give validations of the equations analysis. So far, all electrical designs and insightful discussion about the final MPM topology are complete. In Chapter 6, mechanical designs will be discussed, and assemblies include the test bench arrangement will be presented.

Chapter 6. The Prototype Design of MPM

6.1 Introduction

After discussions in Chapter 4, the designer confirmed the final dimension of MPM topology to build. In Chapter 5, a numerical solution is performed to compare with the simulation result. In this Chapter, the designer will present the detailed building processes of the target MPM including the translator design, the stator design, the winding design, the linear actuator selection and the bench assembly. This chapter aims to better the rigidity of subassemblies and confirm the driving actuator's parameters through simulations which aim to ensure the reliability of the bench and the test environment.

6.2 The Translator Design and Assembly

6.2.1 The general layout

In terms of material, the translator is only composed of the SMC iron cores and axially magnetised magnets which are used to form a no-load magnetic flux path. From the mechanical aspect, the translator is also composed of the translator support, two end caps, two parts of shafts and two linear bearings as shown in figure 6.1. The translator support and end caps are made of aluminium; shafts are made of ground and polished stainless steel which are designed for low frictional coefficient. Aluminium and stainless steel are non-magnetic materials, with magnetic permeability close to that of the air, thus there is almost no effect on the machine flux distribution in the static performance. However the necessary existence of them would increase the total translator mass. In fact when designing a specific linear electric machine for use with the Free-Piston Engine the translator mass must remain within a limit (6 kg) to match the motion frequency requirement. Since the linear machine designed here will be tested as a prototype working with a linear actuator, the total translator mass increasing will not make a critical effect.

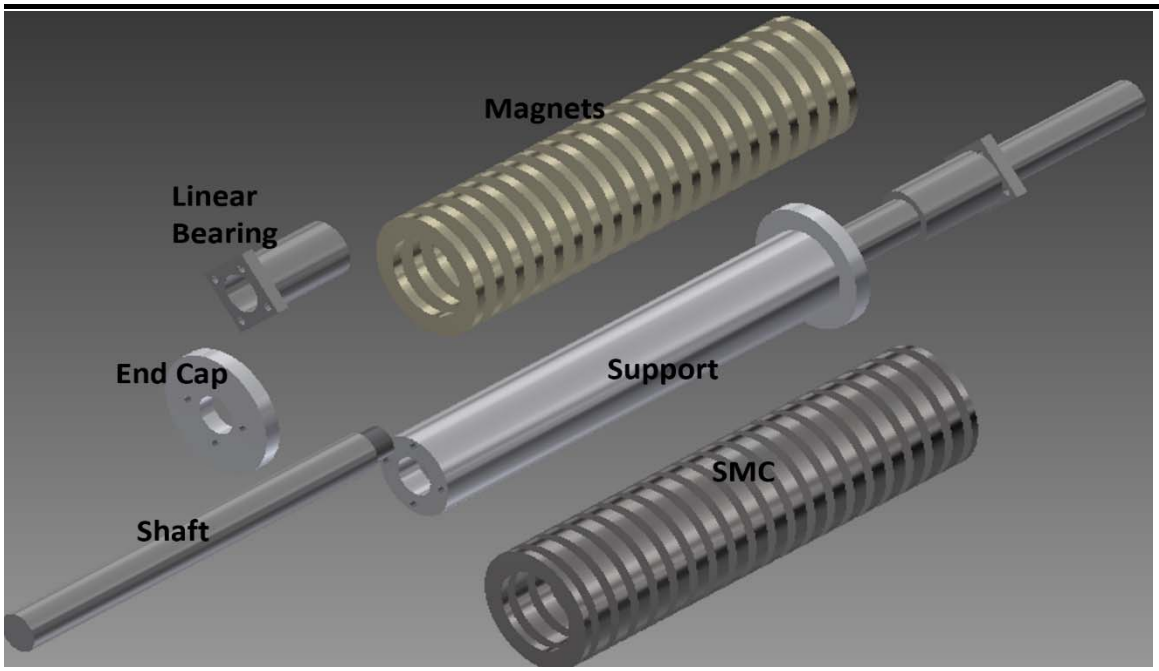

Figure 6.1 Translator assembly sketch

6.2.2 Mechanical Strength Analysis of the Translator Shaft

Before making mechanical parts of the translator, simulations are applied to estimate the shaft dimension required to counter the translator deformation. The deformation of the translator could not only influence the effective air gap length thus affect the machine performance but could also damage the magnet and thus destroy the machine. A large shaft can certainly protect the translator, but more cost on the material and higher requirement on the linear actuator would increase the test difficulty, thus there is a trade-off between the shaft strength and the shaft size. In addition to gravity, there are two bigger side loads that need to be taken into consideration: no load magnetic attraction and on load magnetic attraction, as illustrated in figure 6.2. The side load (or the magnetic attraction force) is produced due to the asymmetry property of the three-phase stator tooth structure, where the amplitude shows a ripple shape and the direction is rotating with the translator position. In other words, if it is assumed that the magnetic cogging and force are produced along the z-axis then the side load is produced at the plane along x and y-axis in a rotating form. Results from the simulation indicate that peak no-load side load is 500N and peak on load side load is about 1750N.

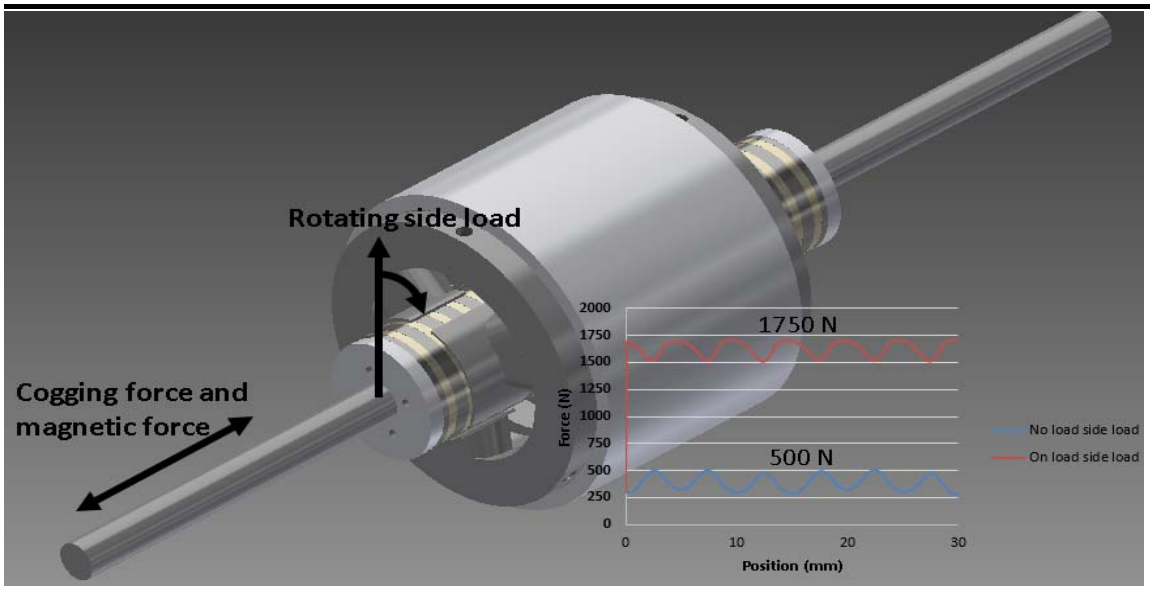

Figure 6.2 Side loads data with sketch

The worst case scenario, as shown in figure 6.3, is when the magnetic attraction is aligned to the gravity. Designed variables are illustrated in figure 6.4(a) where *d1* is the shaft diameter, *d2* is the shaft male thread diameter and *l3* is the shaft male thread length. Deformations are simulated in the software Autodesk\Inventor by using FEA method, where linear bearings are set as contact to the shaft and at fixed position. The worst case force is applied to the translator where it is enclosed by the stator. By setting an appropriate mesh, then the deformation, stress and safety factor profile can be extracted. An investigation of variable *l3* is illustrated in figure 6.4(b), it can be seen that the shaft deformation will start to converge to minimisation when thread length is at 40mm. More detailed shaft dimension variables (*d1* and *d2*) optimisation results are listed in table 6.1 as 1750N attraction and gravity are applied to the central of the translator. The designer wishes to minimise the deformation to less than 10% (less than 0.1mm) and safety factor no less than three to protect magnets and guarantee the machine performance. Safety factor is defined as the ratio of absolute strength (structural capacity) to actual applied load which immediately points out areas of potential yield. By this definition, a safety factor of one means the material is essentially at yield, any additional load will cause the structure to fail. A structure with safety factor of two will fail at twice of the actual applied load. Buildings commonly use a factor of safety of 2.0 for each structural member. Pressure vessels use 3.5 to 4.0, automobiles use 3.0, and aircraft and spacecraft use 1.2 to 3.0 depending on the application and materials [90]. The safety factor optimisation results corresponding to table 6.1 are listed in table 6.2. From both the deformation and the safety factor profile aspects, the designer intends to apply 25mm translator diameter, 20mm male thread diameter on the translator and 40mm thread length.

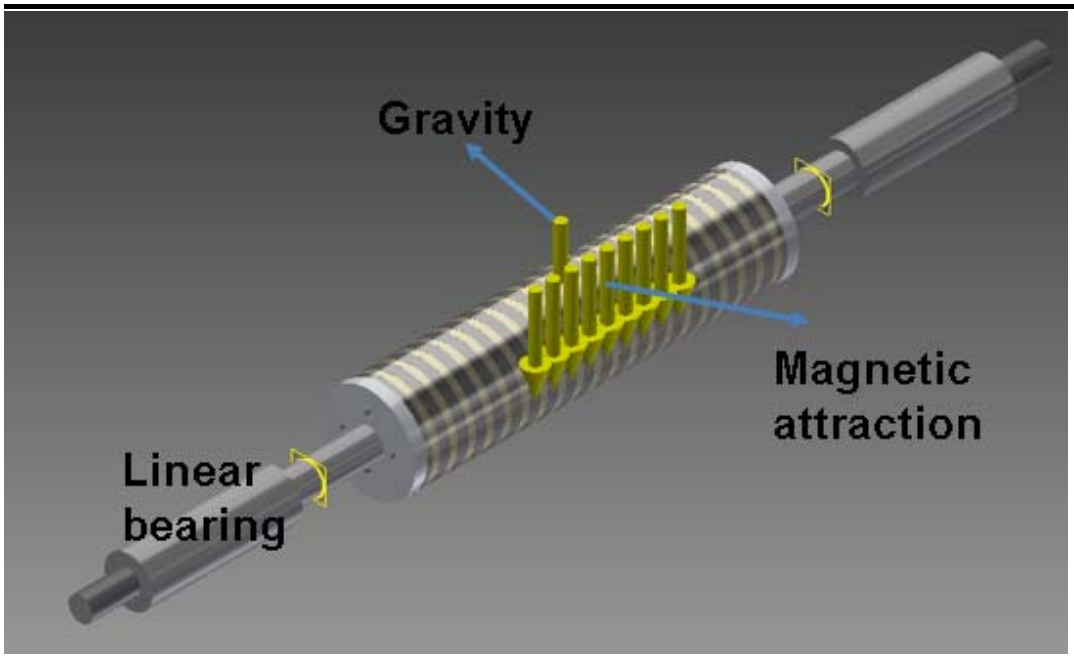

Figure 6.3 Worst case of force to deform the translator

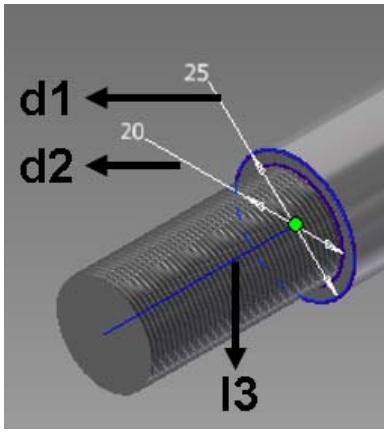

(a)

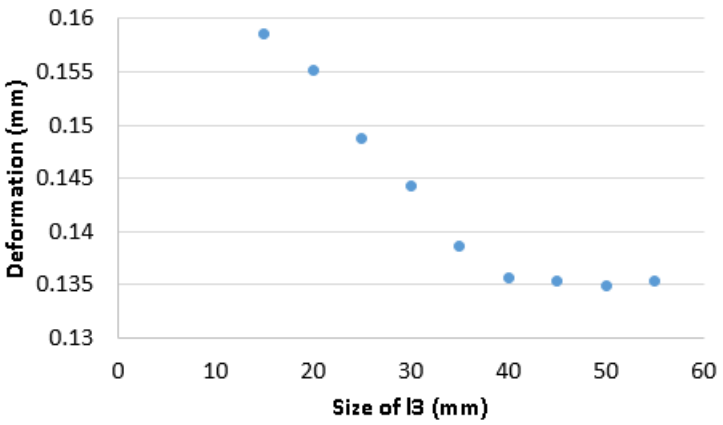

(b) Peak deformation vs l3

Figure 6.4 Design variables sketch and investigation on l3

Max Deformation(mm)		**d1(mm)**						
		10	15	20	25	30	35	40
d2(mm)	5	0.767	0.190	0.0773	0.0394	0.0235	0.0153	0.0109
	10		0.182	0.0732	0.0376	0.0223	0.0143	0.0100
	15			0.0669	0.0346	0.0211	0.0137	0.00961
	20				0.0314	0.0195	0.0130	0.00927
	25					0.0182	0.0124	0.00897
	30						0.0118	0.00871
	35							0.00845

Table 6.1 v1 and v2 optimisation on the translator deformation

Safety factor		d1(mm)						
		10	15	20	25	30	35	40
d2(mm)	5	0.341	0.934	1.87	2.14	2.37	2.19	2.11
	10		0.905	2.31	3.35	5.64	8.21	9.48
	15			2.34	4.55	5.72	8.91	8.39
	20				4.88	6.75	9.36	9.24
	25					6.93	8.73	10.3
	30						9.95	11.2
	35							14.2

Table 6.2 d1 and d2 optimisation on the safety factor

The deformation profile above is investigated with the worst case of a force applied to the centre of the translator. Moreover, investigation of different translator positions is in figure 6.5. It shows that the worst position is when the translator moved to one terminal of the stroke (contacted to the linear bearing). The corresponding deformation and safety factor results are in table 6.3. It shows that for the worst case of position and force, the deformation and safety factor are still meet demands (9.64% and 2.96).

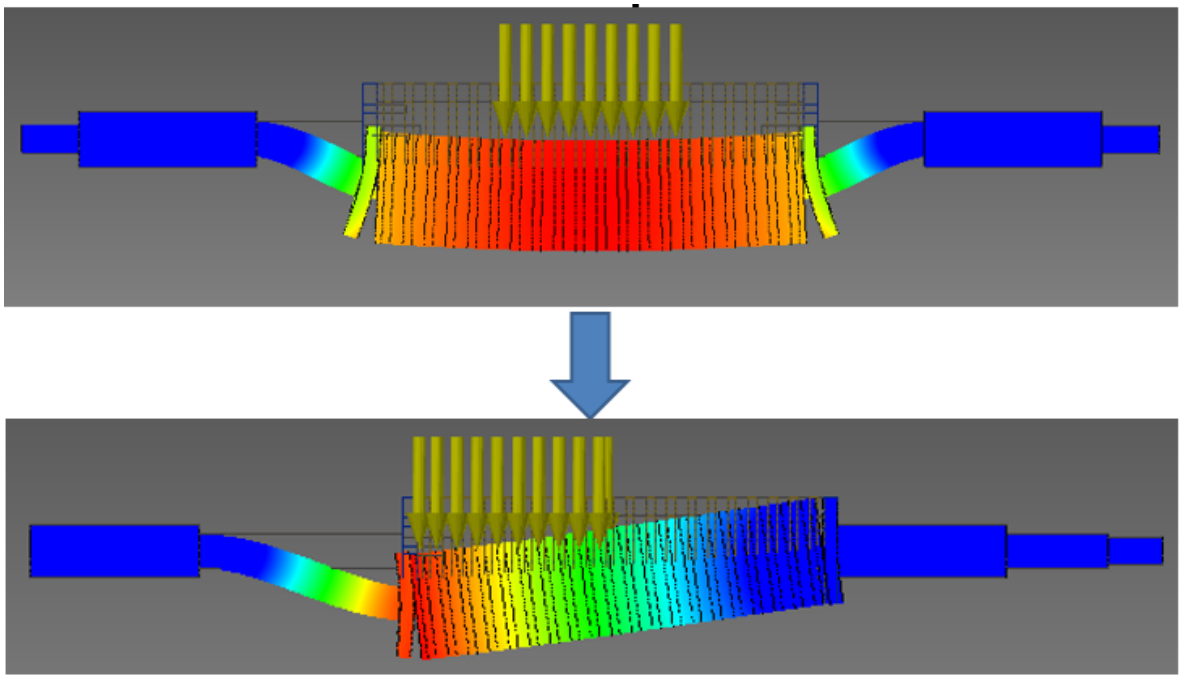

Figure 6.5 Simulation sketches for different translator positions

	Max deformation (mm)	Safety factor
Position (mm) on load		
75mm (central)	0.0314	4.88
150mm (terminal)	0.0964	2.96
Position (mm) no load		
75mm (central)	0.0100	15
150mm (terminal)	0.0297	9.63

Table 6.3 Deformation and safety factor results for different positions

6.2.3 Building of the Translator

In practice the assembled translator is as shown in figure 6.6 wherein (a) assembled stainless steel shaft and aluminium support, in (b) is the fully assembled translator with magnets, SMCs and end caps. What is more, the surface is glued to enhance the mechanical strength.

(a) Shaft and support

(b) Full translator

Figure 6.6 Assembled translator

6.3 The Stator Design and Assembly

6.3.1 The General Layout

The overall assembly of the stator is shown in figure 6.7, components including: laminations, the support, the stator housing, stroke housings, stator end caps, stator bases. Where the support is used to hold laminations; the stator housing is used to stabilise laminations in the support to against the attraction from translator magnets; stroke housings combined with bases are working as fixtures to hold the support and laminations, also offering the moving space for the translator; stator end caps are designed to embed in two stroke housings which work with linear bearings to hold the translator. All these components are made of solid aluminium which can simultaneously offer high stiffness and low flux permeability.

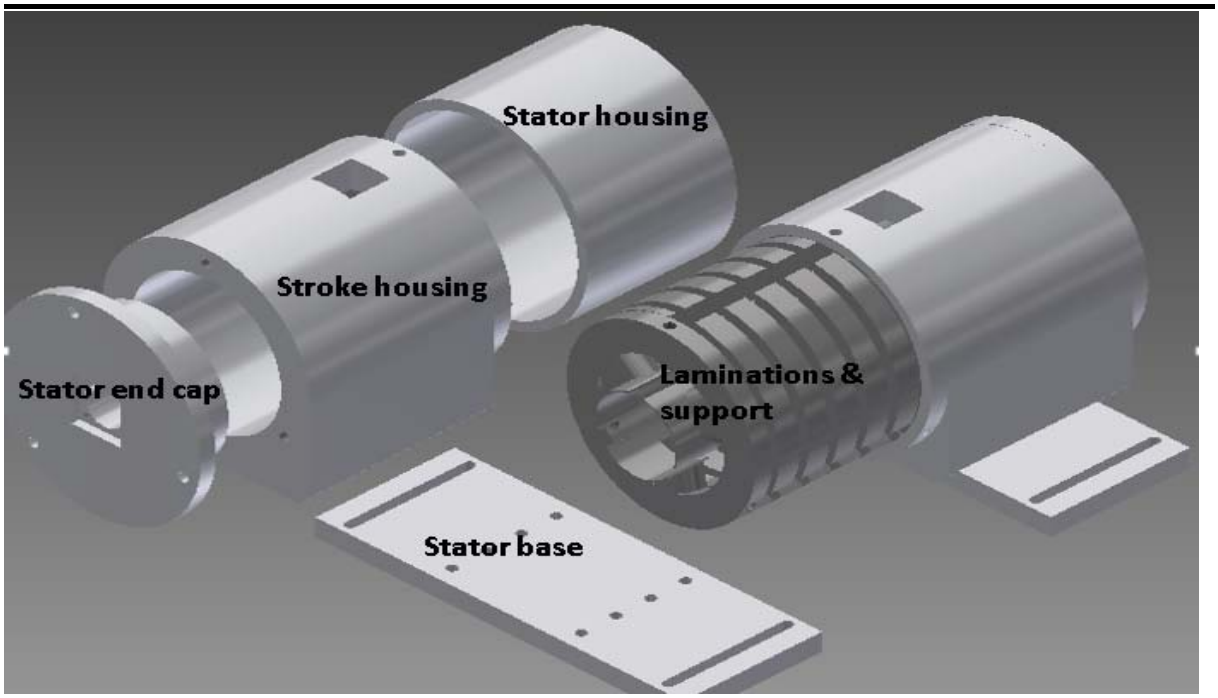

Figure 6.7 Overall assemble strategy of the stator

6.3.2 Non-Magnetic Laminations Support

6.3.2.1 Design of the Lamination Support

As aforementioned in Chapter 4, the active part of the stator is composed of two types of laminations as illustrated in figure 6.8 (a). Since they are separate components, it is essential to use a non-magnetic material support to mechanically combine them. Instead of using stainless steel or aluminium material which are extremely difficult to process for complicate structure, the designer decides to use lighter plastic material with rapid prototyping 3D printing technology to form a support which can firmly contain lamination components as shown in figure 6.8 (b). In fact the designer estimated that there must have some small gaps between laminations which could affect the equivalent air gap of the machine thus the output performance. This factor will be the main reason of the difference of simulation and measurement which will be discussed in Chapter 7. Another potential risk is the high temperature when armature current is applied to the stator windings, by which the plastic support could be melted if the temperature exceed the melting point for too long time. However this will be countered by using thermocouples which are connected to windings and laminations, in this case the temperature can be monitored to ensure the safety of the support. This will be discussed in the next section and tested in Chapter 7.

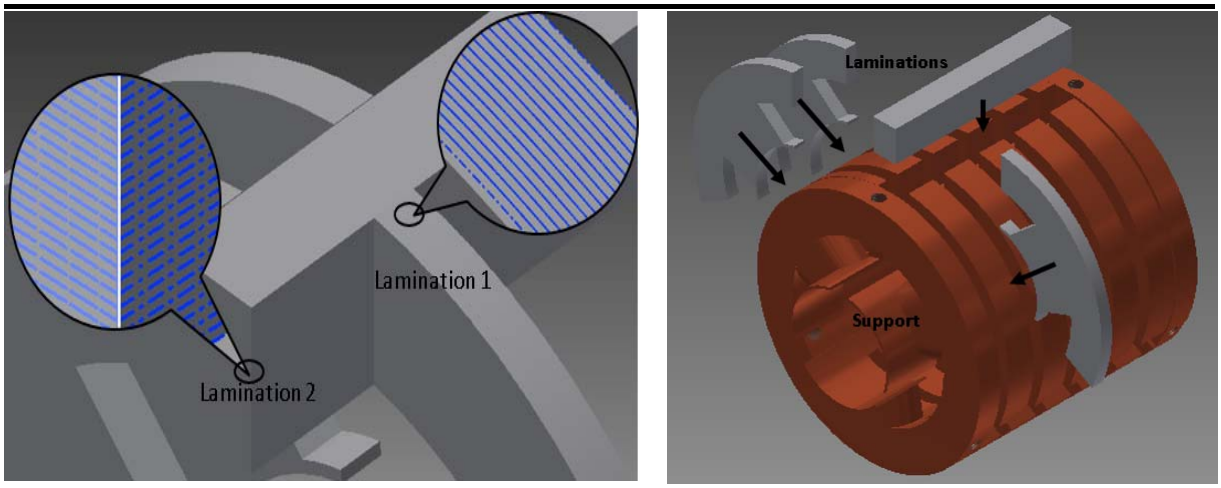

(a) Laminations sketch (b) 3D printing support and laminations

Figure 6.8 Lamination and Support Design

6.3.2.2 Building of the Lamination Support

When the laminations are inserted into the support structure, since the support is printed without any tolerance designed, a sanding process was required. However, such process can ideally assemble laminations into the support firmly. The assembled support and laminations are as shown in figure 6.10 in 2 different views. In fact, the designer believes there should still have some parasitic airgaps between these lamination components at joint positions that could affect the equivalent armature reluctance thus influence the magnetic force. The designer will check the parasitic airgaps in the test process in Chapter 7.

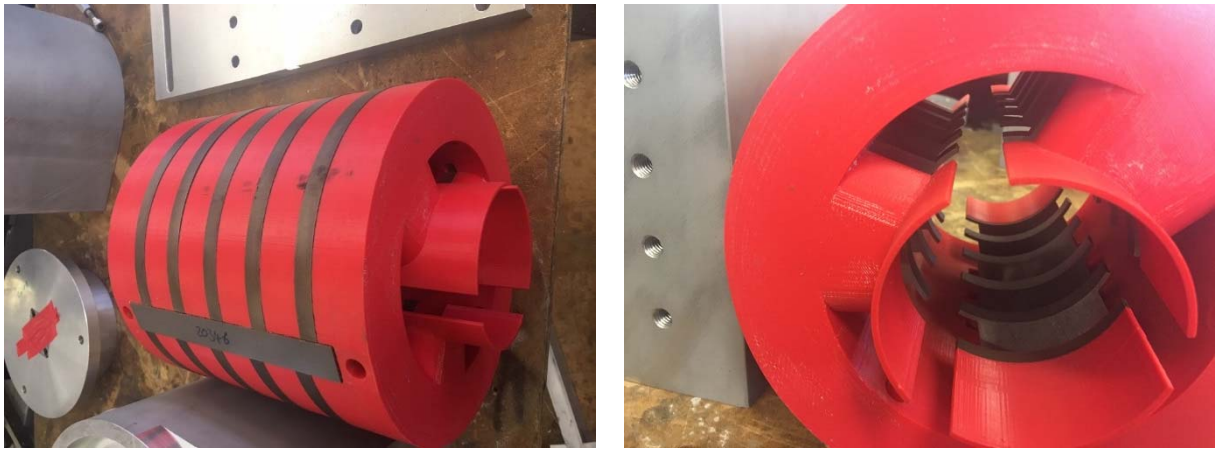

(a). Outer view (b). Inner view

Figure 6.9 Assembled laminations and the support from 2 views

6.3.3 Stroke Housing and End Caps

Machined structures of the stroke housing and the stator end cups are in figure 6.10. In (a) the slotted structure is used to hold the lamination support, and the bottom tooth is used to fit the

machine on the stator base. In (b) is the end cup which used to fit the linear bearing. All precise dimensions of components above are in the appendix.

(a). A slotted feature of the stroke housing

(b). End cap with the linear bearing

Figure 6.10 Machined stroke housing and the end cap

6.4 The Winding Design and Assembly

6.4.1 The Winding Assembly Strategy

The designer decides to use single toothed windings on the stator due to the potential of saving copper material and the assemble simplicity as discussed in Chapter 4. However, in practice, manual winding is found to only achieve an inferior fill factor (about 0.3) due to the bend ratio of end windings and the manual operation accuracy. To achieve a higher fill factor, the designer uses an elongated 3D printed bobbin and winder machine to form the winding. In figure 6.11 (a) is the bobbin model which is made by two separate parts, Windings are initially wound and fixed on the bobbin by the winder as shown in figure 6.11 (b) and then took out from the bobbin as shown in figure 6.12 (a), finally relocated to the laminations assembled stator support as shown in figure 6.12.

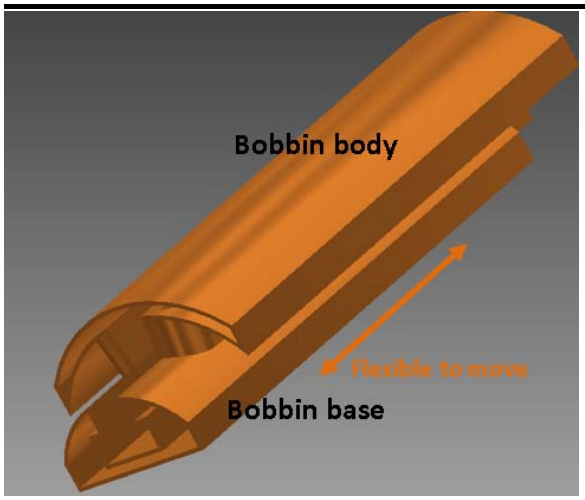

(a). Bobbin unit model

(b). Winder machine

Figure 6.11 Bobbin and winder

(a). Windings removed from the bobbin

(b). Windings relocated to the stator support

Figure 6.12 Windings relocation

6.4.2 The Winding Dimension Selection

The total slot area for each phase is 823 mm^2 as detected by the simulation (in figure 4.13). For easy assembly, the designer intends to only use half of this area for the winding (around 412 mm^2). The designer also decides to use 1.1 mm diameter coils to form the winding by referring American wire gauge based on the 700 circular mils per amp rule [86]. From table 6.4 below (part of the AWG), the maximum current applied is about 19A. In table 4.2 the required phase MMF for the final topology is 1833A. Thus about 100 turns are required. In other words, the minimum fill factor required is $2\times100\times0.55^2\pi \div412= 0.46$. By several attempts, as shown in figure 6.13(b), it is found that by using bobbin and winder machine the

winding turns can easily achieve 120 turn (corresponding to 0.55 fill factor), each turn only need to carry about 15A peak current.

AWG gauge	Conductor Diameter Inches	Conductor Diameter mm	Ohms per 1000 ft.	Ohms per km	Maximum ampacity
14	0.06410	1.62814	2.5250	8.282000	32.000
15	0.05710	1.45034	3.1840	10.443520	28.000
16	0.05080	1.29032	4.0160	13.172480	22.000
17	**0.04530**	**1.15062**	**5.0640**	**16.609920**	**19.000**
18	0.04030	1.02362	6.3850	20.942800	16.000
19	0.03590	0.91186	8.0510	26.407280	14.000
20	0.03200	0.81280	10.1500	33.292000	11.000

Table 6.4 Part of American wire gauge (AWG) [86]

6.5 The Linear Actuator Selection

6.5.1 Introduction

In this project, to test a linear machine, a linear actuator is used to perform both static and dynamic tests. Thus it is essential to choose a compatible linear actuator. For the static test, there is no speed requirement on the linear actuator, but it must be able to maintain the translator at any position. For the dynamic test, the worst case peak force and speed must be considered.

6.5.2 Dynamic analysis

A simplified dynamic equation (equation. 6-1) is as follows, where F_{drive} is the force required to be supplied by the linear actuator, $F_{generator}$ is the force need to be against from the test generator, m is the translator mass, v is the translator velocity, and k_e is the viscous friction coefficient.

$$F_{drive} - F_{generator} = m\frac{dv}{dt} + k_e v \tag{6-1}$$

In fact, $F_{generator}$ can be estimated when the machine is simulated as a generator. Assuming a pure resistive loading in figure 6.13, when 5 Hz sinusoidal motion profile is applied to the FEA simulation model, the generator force against resistance value profile is shown in figure 6.14(a). It shows that the maximum peak force can be achieved when 70 Ohm resistors are applied and the force profile is about in phase with the speed profile as shown in figure 6.14(b). When different frequency motions are applied, the same peak generator force can be

obtained by linearly increasing the resistance value. In other words, the generator force profile can be approximated as shown in equation. 6-2, where 700 is the peak generator force, and f is mechanical frequency (Hz) of the translator. The corresponding velocity is expressed as shown in equation. 6-3, where l_s is the stroke length and k_e is assumed as zero.

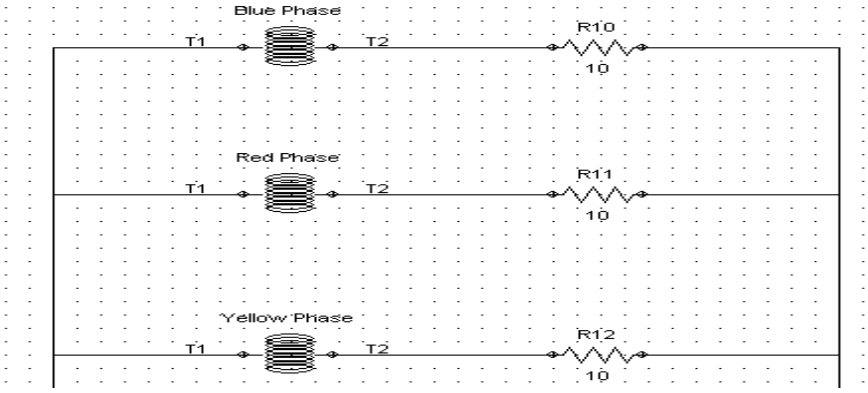

Figure 6.13 Generator circuit

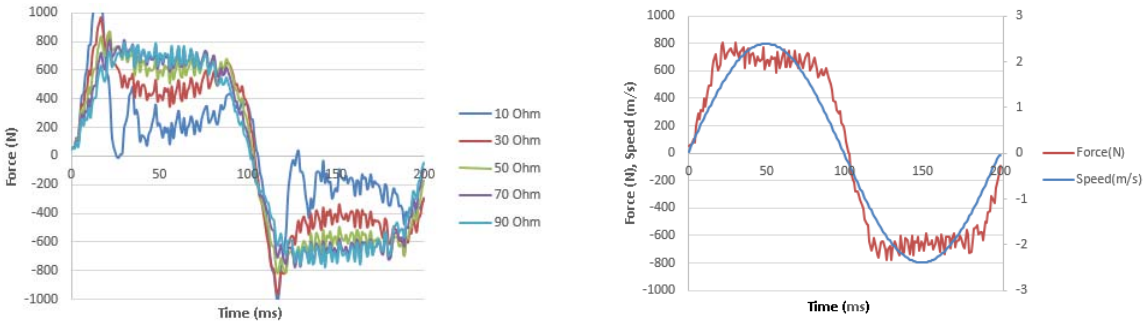

(a). Force profile based on different resistors (b). Force profile with speed profile

Figure 6.14 Generator force and speed profile

$$F_{generator} = 700\sin(2\pi ft) \tag{6-2}$$

$$v = 2\sqrt{2} \times l_s f \sin(2\pi ft) \tag{6-3}$$

6.5.3 SIMULINK

Figure 6.15 shows the simulated model of equation. 6-1in Matlab SIMULINK. Results of the peak drive force requirement against increasing motion frequencies are as shown in figure 6.16, where almost no change of the peak drive force can be observed when the mechanical frequency is less than 4 Hz. Above this point, the peak drive force starts to increase more and more rapidly. As for the mechanical strength of the ball screw of the linear actuator must next be considered. As reported by the supplier [87], to obtain a relatively small motor volume and safe ball screw working condition a 4.6 kg linear actuator is selected.

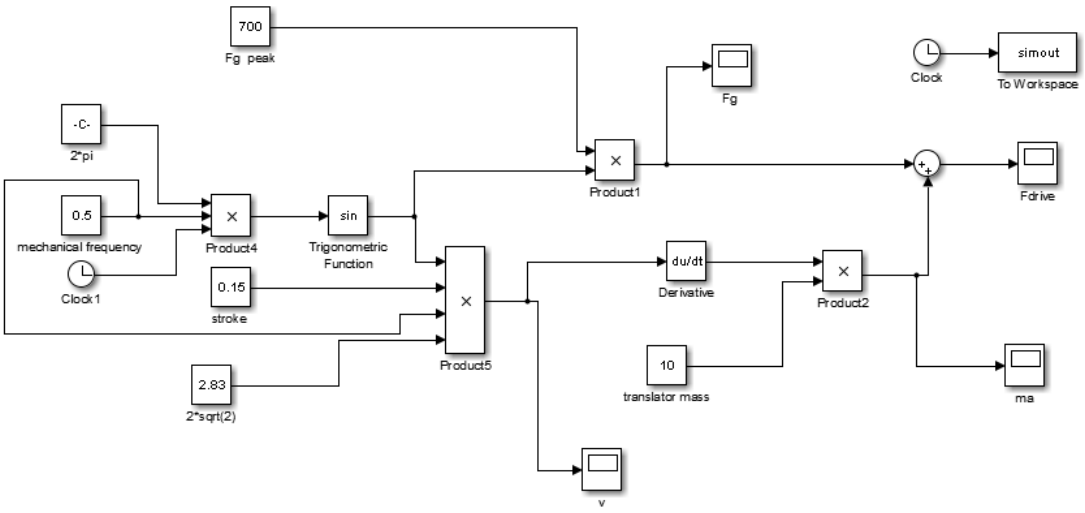

Figure 6.15 Simulated model of the linear actuator force profile

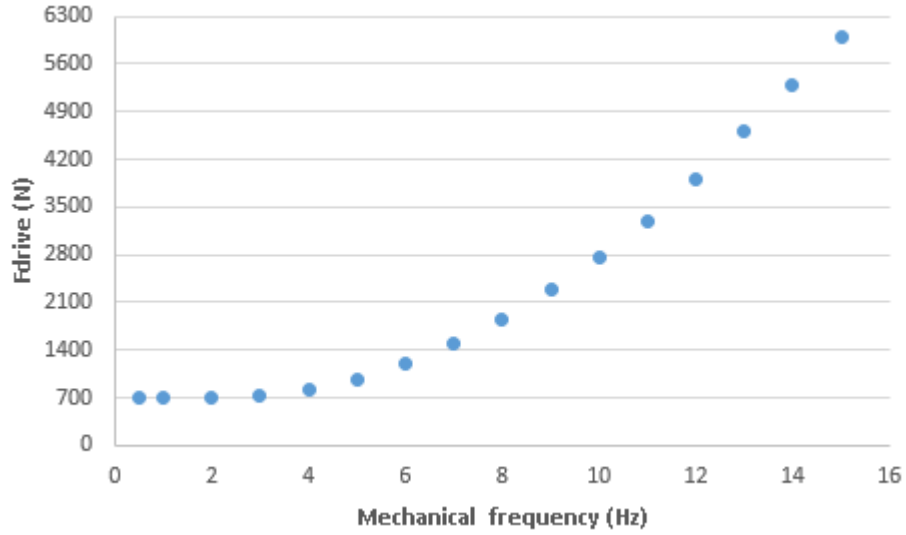

Figure 6.16 Peak F drive against the mechanical frequency

6.6 Other Components Selection and Bench Assembly

In figure 6.17 is the overall view of the test bench. Where component 1 is the linear machine prototype which is mechanically connected component 2 is the load cell. Two sets of load cells are separately applied when measuring cogging force and static DC force (smaller scaled used in cogging force test, and the bigger one is aiming to detect the static DC force and the dynamic generator force). Component 3 which connected to the load cell is the linear actuator, two sets of linear actuators are used to complete static tests and dynamic tests respectively (low powered used in static test to measure cogging and static DC force and high powered is aiming to detect the EMF); component 4 is the displacement transducer which used to detect the translator position for both static and dynamic tests. Components 5 are the DC power source units which used in static force test. Component 6 is oscilloscope which used along the

whole test process for data collecting. Other components including LRC, voltage and current meters are initially used to measure armature winding resistance inductance, EMF, phase current. More detailed test results and comparisons will be expanded and discussed in the next Chapter 7.

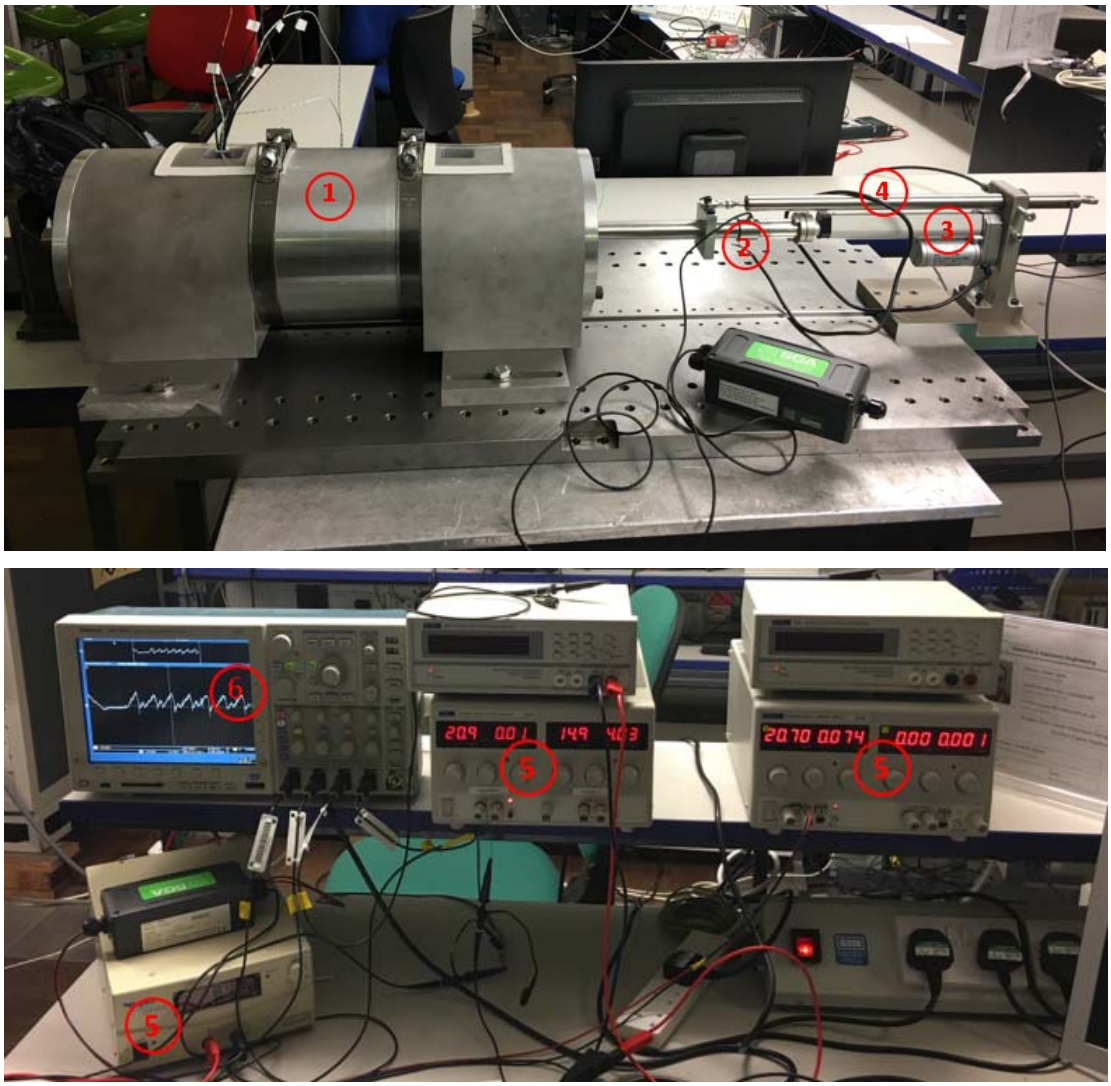

Figure 6.17 Overall test bench and equipment

6.7 Summary

To sum up, in this Chapter the mechanical strength estimation and the detailed assemble strategy is discussed. The assembly result shows the feasibility of the design strategy, the linear actuator and other measuring tools are selected. After the final bench assembly, the experimental test is ready to start, and Chapter 7 will present tests and compare to simulations.

Chapter 7. The Prototype Test and Validation

7.1 Introduction

This chapter aims to investigate some machine outputs including both static and dynamic performances by experimental measurements. All measurements are compared to corresponding simulations aim for the validation. Static tests include the cogging force test, static DC force test and fixed position test. Dynamic tests discover the EMF test at different speeds. Parasitic gaps and translator offset will be investigated to evaluate the assembly error.

7.2 Winding Resistance and Winding Inductance Measuring

Before any of the tests, the armature winding resistance and inductance are individually measured by LRC meter. A successful resistance check can guarantee the wound safety of the winding. The winding inductance measurement can illustrate the machine saliency and check the winding turns.

A single phase winding resistance can be measured by merely connect two terminals of a single-phase winding to the LRC meter in the resistance model. Each phase has 120 turns which are preassembled on the elongated bobbin. The resistance can be estimated by referring dimensions listed in table 6.4 and bobbin dimensions as illustrated in figure 7.1. Table 7.1 shows the estimated and measured resistance values. The difference could be the caused by the end winding but not dramatic for the prototype.

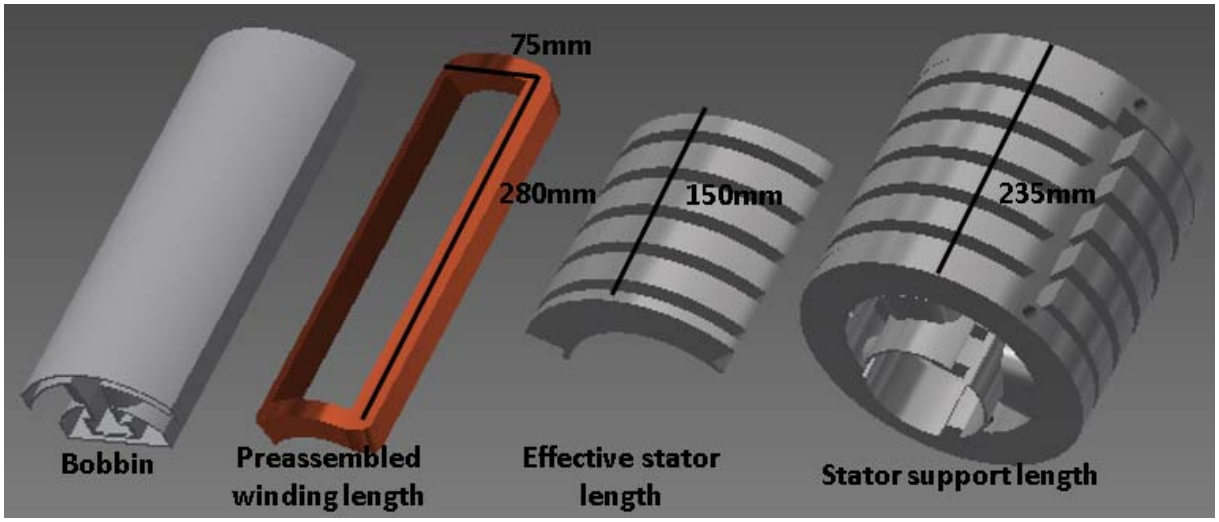

Figure 7.1 An overview of the winding related components dimensions

A single phased inductance profile along a pole pair pitch is measured by using LRC meter in the inductance model. A comparison of the inductance profile from both the simulation and the measurement is illustrated in figure 7.2 and with their mean values listed in table 7.1. The

mean value of the measurement is about 84% of that in the simulation. The phase inductance is a reciprocal function of the equivalent reluctance of the magnetic circuit of the machine. The error of measured inductance could also inherent to the armature field flux thus the produced force in measurement. Reasons for this error could be complicated including measuring accuracy, end winding effect, and assembly aspect. The designer believes that the primary reason is due to parasitic airgaps between different stator segments which could drag down the phase inductance (detailed analysed is in later section 7.5.2), but the end winding effect could also offset part of the parasitic airgaps influence on the phase inductance. In figure 7.2, there are four ripples within a pole pair pitch which indicate d and q positions of the translator. Where q is the position when the teeth is aligned to the magnet, if applying peak armature current at this position then a peak magnetic force can be achieved. As for d is the position when the tooth is aligned to the SMC core back, at this position, the main flux is at peak value. The trough of the waveform indicates a minimum inductance where is when the tooth is aligned to the joint between magnets and SMC core back. A corresponding reluctance force profile is produced when current filed is passing the tooth as illustrated in figure 7.3 (with 4A DC applied to a single phase winding), where it can be seen that the reluctance force produced while the translator is at d or q axis position is zero. In theory, this type of reluctance force is one of the force components in the static DC test with a constant current. However, due to the amplitude of this reluctance force is very small which can be neglected in both static force tests.

Phase winding	**Calculation or simulation**	**Measurement**
Resistance (Ohm)	1.42	1.55
Mean inductance (H)	0.045	0.038

Table 7.1 Summary of phase resistance and inductance

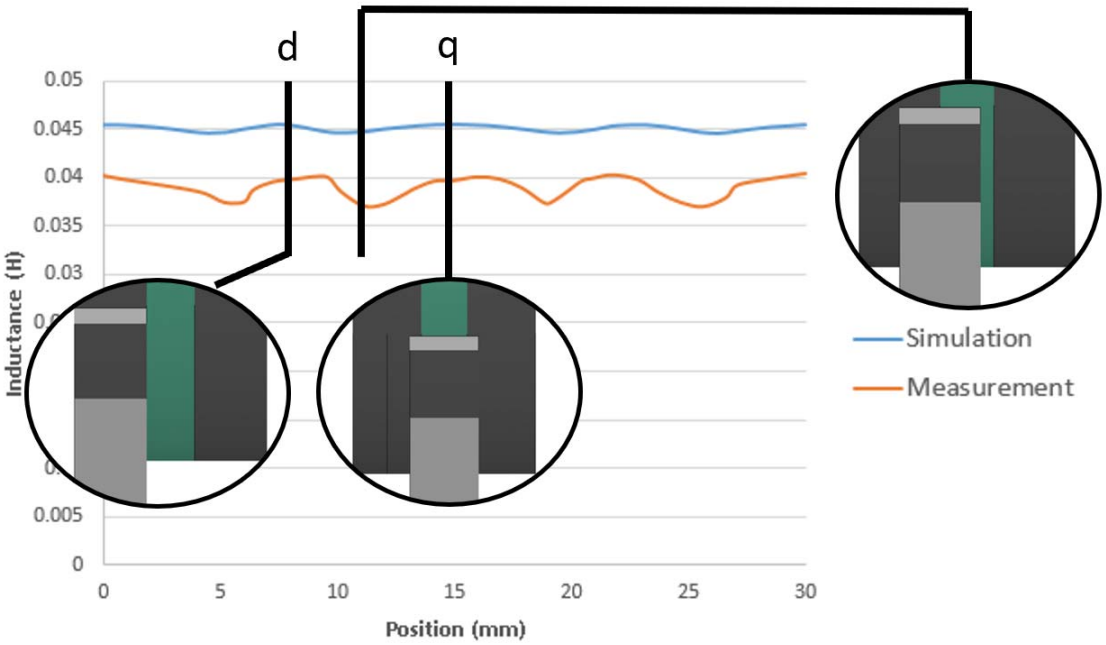

Figure 7.2 Phase winding inductance profile comparison

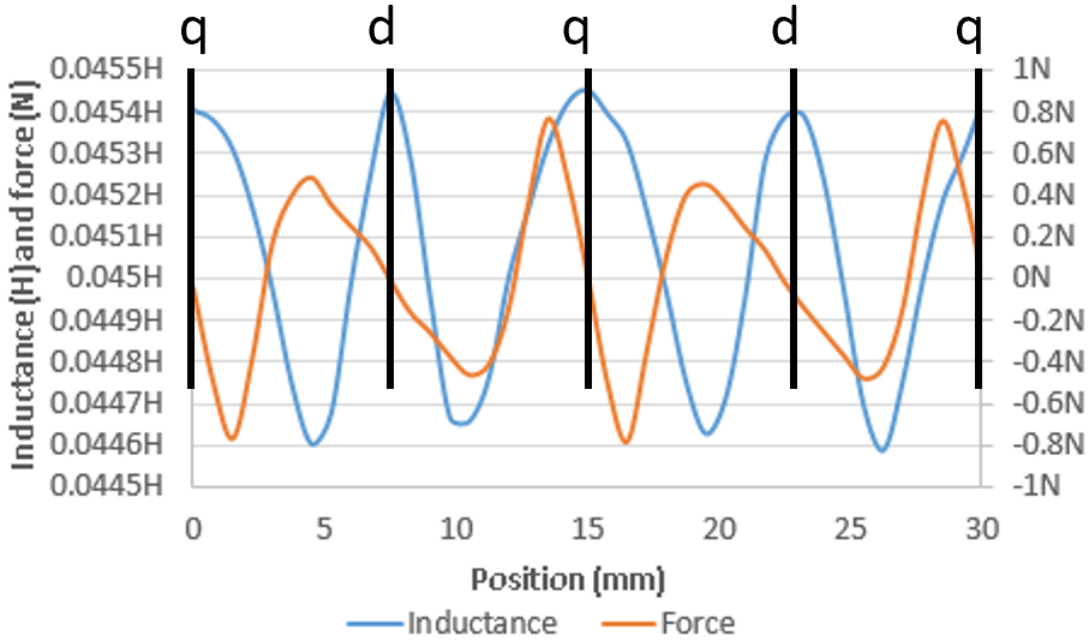

Figure 7.3 Simulated reluctance force profile

7.3 Cogging Force Test

In this test, to achieve a continuous cogging force profile, it allows the linear actuator to supply a slow motion on the translator. Thus the force profile can be detected by the load cell and recorded by the oscilloscope. When measuring the cogging force, a DC offset force is observed in figure 7.4, this offset force is the mechanical friction component, if applying this force to the original forward profile then the cogging force stars to be symmetric to the horizontal axis. Figure 7.5 shows detailed cogging force profiles along one pole pair pitch from both the measurement and the simulation. There are six ripples in the cogging force waveform due to there are three teeth (one for each phase) distributed along a pole pair pitch with two pole magnets. The simulated waveform shows a decent cogging force waveform, whereas that in measurement shows more realistic due to the measuring error (which could be caused by the linear actuator internal mechanical error).

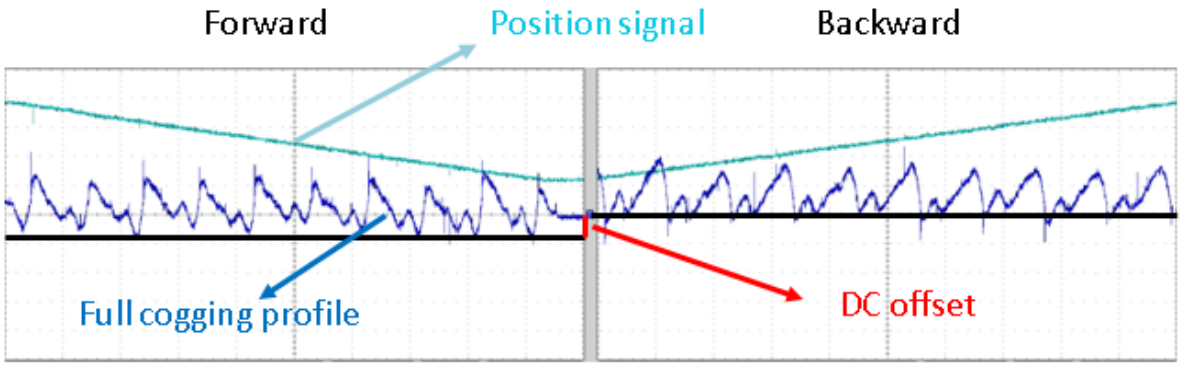

Figure 7.4 Cogging force measurement with DC offset

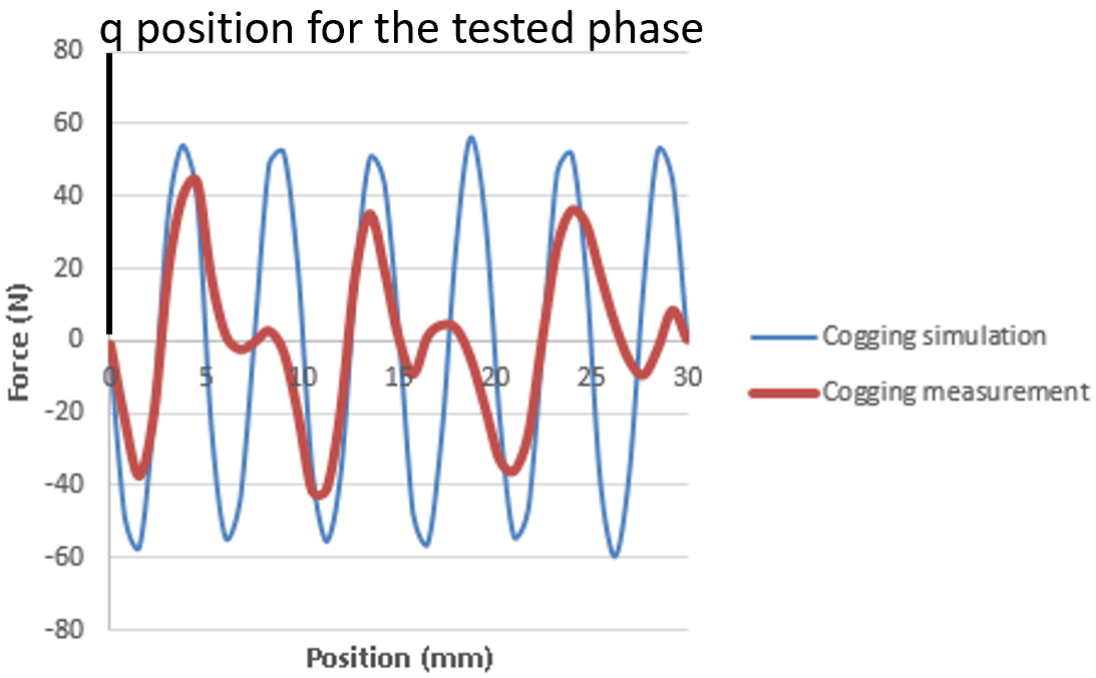

Figure 7.5 Cogging force comparison

7.4 Static DC Force Test

There are two types of static DC force tests: constant DC source with displacement and fixed position with AC source. All these two tests only apply current to a single phase. Where the first test is to investigate the combination of force profiles including magnetic force, reluctance force and cogging force, whereas the second test is to investigate the pure magnetic force profile. Both tests' measurements will compare with simulations.

7.4.1 Force with Constant Current Test

In the first test, A slow constant motion is applied to the translator that starting from the q axis position of the measured phase. In the meantime, a DC source is applied to the phase winding. Figure 7.6 shows the simulated force profiles with incremental phase currents applied to the phase winding. It shows that the cogging force is integrated to all force profiles. Meanwhile, the peak force increases with the current. In fact, the reluctance force profile shown in figure 7.3 is also part of the force components, but due to the small amplitude, thus the cogging force can be regarded as the only inherited force without losing any generality. Figure 7.7 presents measurement results with a summary of key data in table 7.2. Similar shapes can be observed, but with peak force only about 74.5%, 78% and 73% of those in simulations, this is generally due to the parasitic airgaps between different stator segments, which could weaken the total flux through the core (increasing core equivalent reluctance). In fact, even with 12A phase current (the maximum current can achieve in the laboratory), the resultant force profile is still not starting to saturate. The designer believes that even apply current more than 15A, the measured force will not start to saturate due to the low phase inductance caused by the parasitic airgaps.

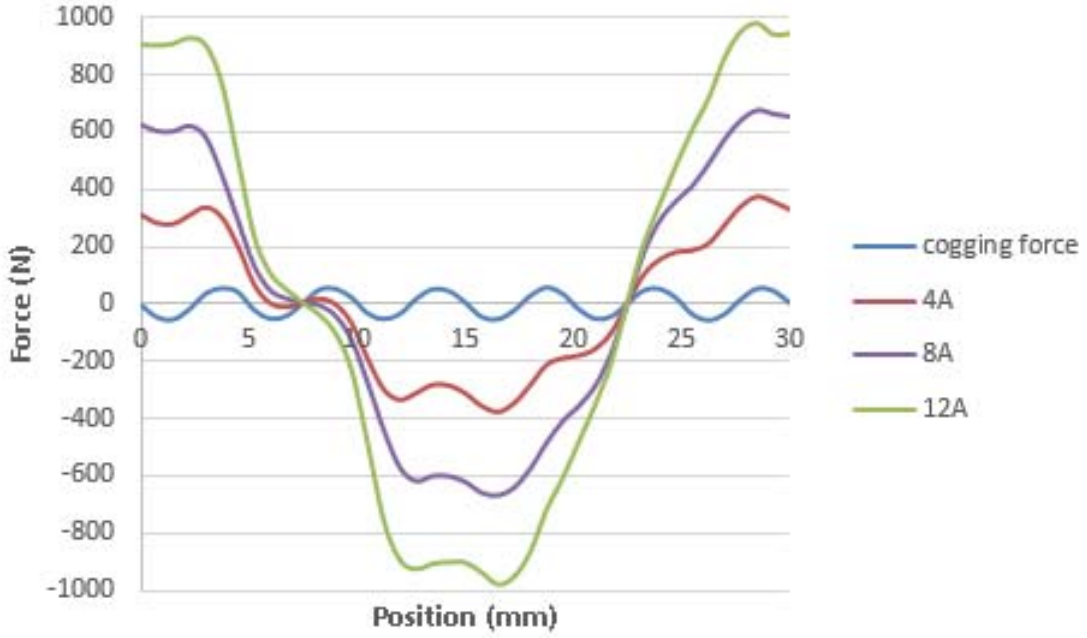

Figure 7.6 DC force with displacement from simulation

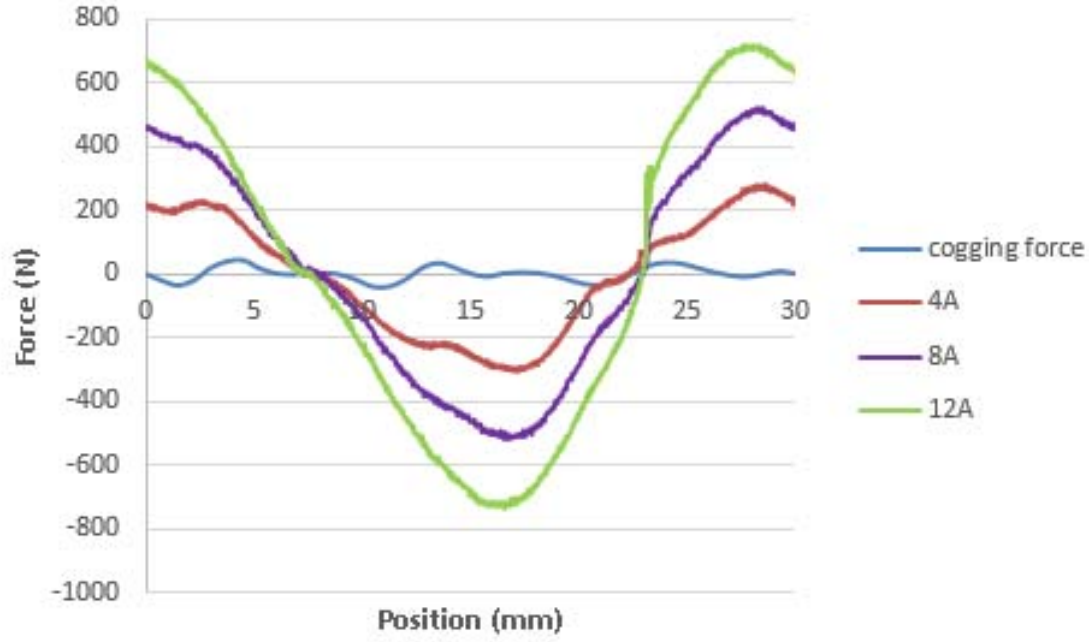

Figure 7.7 DC force with displacement from the measurement

Peak force (N)	**Simulation**	**Measurement**	**Ratio**
4A	376	280	74.5%
8A	672	524	78.0%
12A	975	715	73.0%

Table 7.2 Summary of simulation and measurement

7.4.2 Force with Fixed Position Test

For the second static DC test, since the position is fixed at zero cogging force and zero reluctance force position. Thus it is more like to investigate the pure magnetic force. In both simulations and measurements, the translator is fixed at q axis position for the measured phase. Whereas in the simulation, the cosine of current waveforms with peak current at 4A, 8A and 12A are applied to the phase winding. While in the measurement, 11 points along a cycle are selected to apply current. Results are in figure 7.8 with peak force data listed in table 7.3. It shows that all force profiles show good agreements to the current characteristic. Ratios of peak force are between 70% to 75%, which are close to those in the constant current test. Also, the force is not starting to saturate even with 12A peak current.

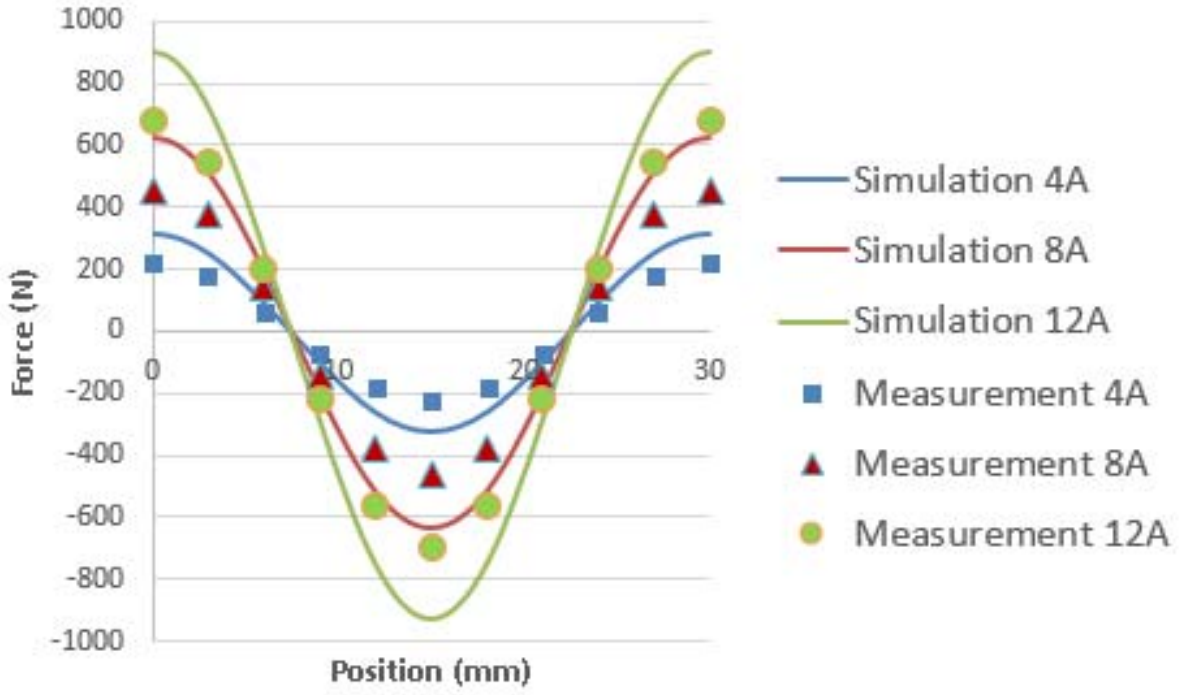

Figure 7.8 Comparison of simulation and measurement of the magnetic force profile

Peak force	Simulation	Measurement	Ratio
4A	313	220	70.3%
8A	623	455	73.0%
12A	902	678	75.2%

Table 7.3 Summary of simulation and measurement

7.5 Dynamic Test

The dynamic test primarily uses the same test bench but replace the low-speed linear actuator to a more advanced one that can supply much higher speed. Thus EMF can be measured with varied speed options.

7.5.1 Dynamic EMF Test

EMF is the open circuit induced voltage. Namely, when a motion is applied to the translator, then a corresponding voltage could be measured from the two terminals of the phase winding. For the target prototype, the only variable that dominates the EMF is the translator instant speed. Figure 7.9 (a) shows EMF predictions of the ideal machine for oscillation of 100 mm with a peak velocity of 50 mm/s. EMF induced in all three coils is identical with a peak of 0.6 V per phase during peak translator velocity. Figure 7.9 (b) shows the equivalent experimental results, with the peak EMF being between 0.43 V and 0.4 V in different phases. The discrepancy is close to 28%, which is attributed to parasitic airgaps within the machine. In-balance between phases is assumed to be as a result of translator eccentricity. Both these effects are investigated below.

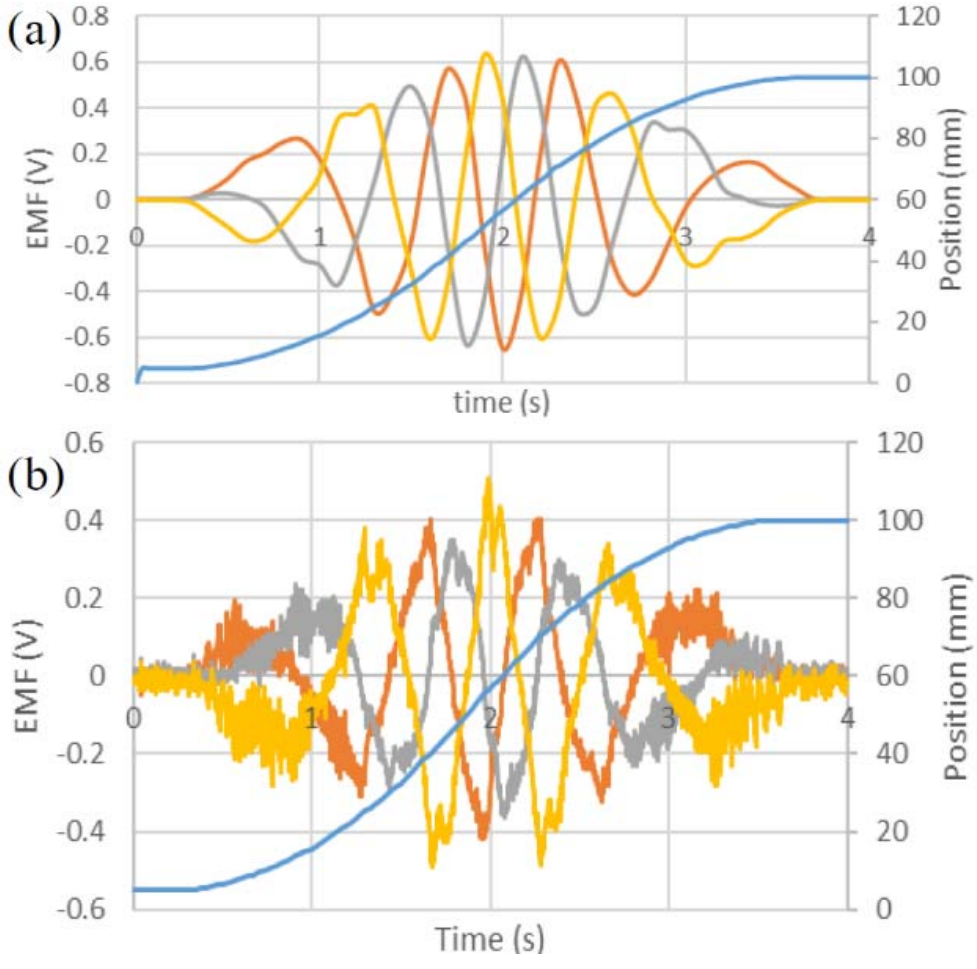

Figure 7.9 Simulated (a) and experimental (b) low-speed test back EMF

7.5.2 Parasitic Airgaps Investigation

The separate components of the stator are slotted together and held in a 3D printed plastic holder. It is found to give rise to parasitic airgaps between the laminated teeth and bars. To account for this, the FEA model was adapted as shown in figure 7.10 to include airgaps between 0.1 and 0.3 mm. Figure 7.11 shows simulation results and RMS values are in Table 7.4. From this study, it appears an average gap of 0.2 mm exists between laminated stator components.

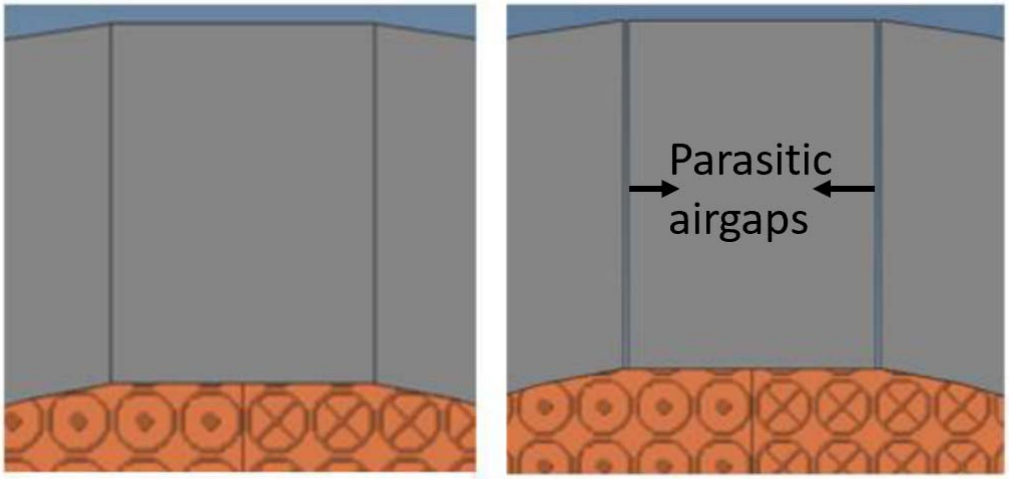

Figure 7.10 Parasitic air gaps between components

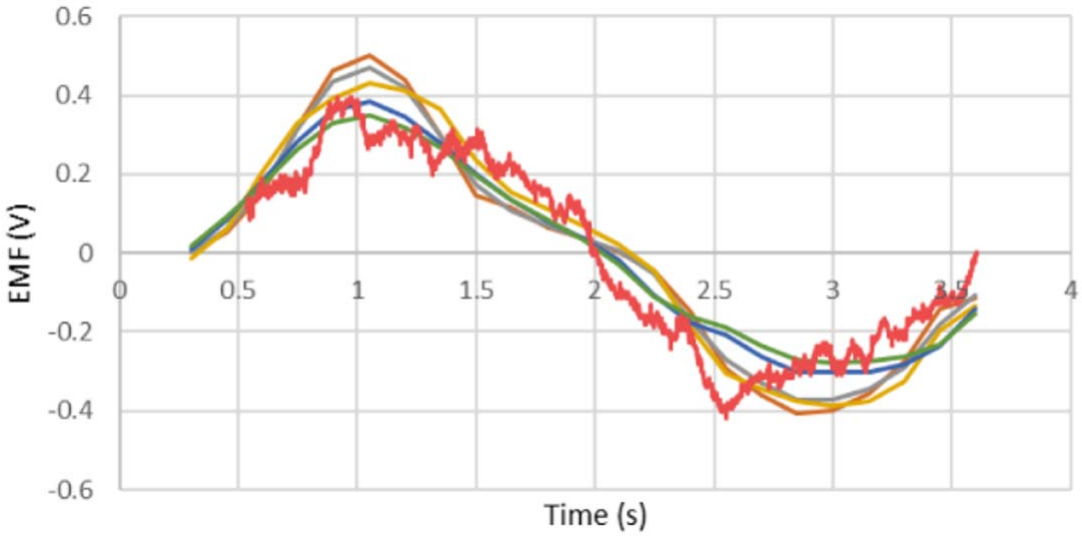

Figure 7.11 Parasitic airgap comparison to real topology performance

	Simulations					Experiment
Airgap size (mm)	0	0.1	0.15	0.2	0.3	
Emf (Vrms)	0.273	0.263	0.255	0.233	0.217	0.233

Table 7.4 RMS EMF values over the positive cycle

7.5.3 Translator Offset Investigation

When the machine is finished assembling, the stator casing prevents measurement of the physical air gap. Although tolerance on the magnets and SMC components is good and predicted shaft deflection is less than 0.1 mm, the results imply the translator is not concentric with the stator. To understand how translator offset affects machine performance, the dynamic simulation was run with a translator offset, assuming a shift equally towards one of the coils and equally away from the other two. RMS values of flux linkage vary less than 2% across the three coils in the perfectly centred machine, whereas an offset of 0.5 mm gave a difference of 16% between phases.

A set of experimental results is used to validate the modified FEA model which includes 0.2 mm parasitic airgaps and 0.1mm offset. The rig is run with a maximum velocity of 300 mm/s, and experimental and simulated results are in figure 7.12. The maximum simulated peak EMF across the three phases is 3.13 V, 2.8 V and 2.3 V. The equivalent experimental results are 2.95 V, 2.5 V and 2.0 V, implying a simulation error of 6-15%.

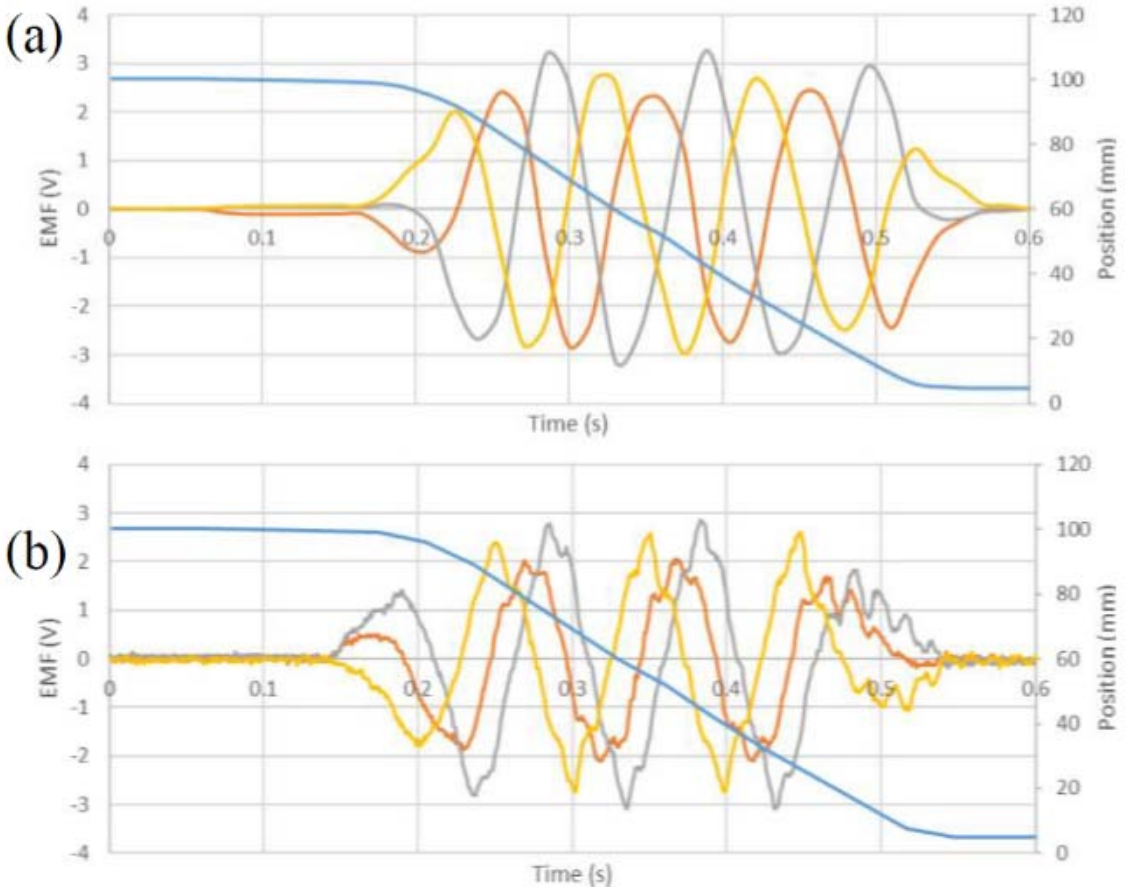

Figure 7.12 Simulated (a) and experimental (b) high-speed test back EMF, using modified FEA model to account for airgaps and offset translator

7.6 Summary

In this chapter, some necessary tests are completed to compare with the simulation result. Experimental measurements have been presented including static force tests and dynamic EMF tests on parasitic airgaps and the translator offset. It is estimated that a total 0.2mm gap and 0.1mm translator offset exists in the assembled prototype. These assembly error caused a 25% error on the force, a 28% error on the EMF and 16% error on the machine self-inductance. This consequence matches the designer's prediction while redesigning the machine topology in Chapter 4 and designing the assembly strategy in Chapter 6. However such error's value is considered high and would push the designer to think about other assembly and building strategies to improve the machine performance in the future work.

Chapter 8. Conclusions and Future Works

The aim of this thesis is to select the best topology among candidate topologies to work with a target Free-Piston Engine. Comparison of performances for different topologies is based on the simulation work. The selected topology (MPM) is built and tested to validate simulation results. The insight of MPM is unfolded by using numerical solution based on the magnetic reluctance network to explain the low power factor property of the transverse flux machine. A novel building and assembly strategy are applied to the MPM to save the cost of the final designed topology. Detailed conclusions are expanded later and based on these conclusions some future works are portrayed.

8.1 Published Material

Below are relevant published and peer-reviewed material relating to this research.

1) Wang, J. and Baker, N.J., 2015, May. Comparison of flux switching and modulated pole linear machines for use with a free piston. In *Electric Machines & Drives Conference (IEMDC), 2015 IEEE International* (pp. 642-648). IEEE.
2) Baker, N.J., Wang, J. and Atkinson, G.J., 2016, September. Optimization and comparison of linear transverse flux and flux switching machines. In *Electrical Machines (ICEM), 2016 XXII International Conference on* (pp. 2471-2477). IEEE.
3) Wang, J. and Baker, N.J., 2016, April. A comparison of alternative linear machines for use with a direct drive free piston engine. In *Power Electronics, Machines and Drives (PEMD 2016), 8th IET International Conference on* (pp. 1-6). IET.
4) Baker NJ, Raihan MAH, Almoraya AA, Wang J, 2017. Electric Machine Design for Wave Energy Converters. *In European Wave and Tidal Energy Conference* (EWTEC 2017), Cork, Ireland

Abstracts submitted to PEMD 2018

1) Experimental comparison of two linear machines developed for the free piston engine. N.J.Baker, A. Sa. Jalal, J. Wang
2) A Study of Assembly Building and Testing Design on Transverse Flux Machine J. Wang, N.J. Baker

Potential journal papers

1) Based on chapter 3 and is the development of a TFM for free piston engines, plus the death of the flux switching machine, whatever the mass. This is similar to the journal paper rejected 18 months ago, but I think if you include some results we can submit it

to IEEE Industrial Applications, and say it is an updated version of the paper you presented last September in Switzerland.

2) based on chapters 4 and 5, perhaps submitted to IEEE energy conversion on IET power applications (as we have tried previously) including development of the design, single tooth verses c core winding, development of the reluctance network, and the work on power factor versus pole number plus some work on the build and results. This is a really novel machine you have built so we should be able to publish that

8.2 Conclusions

8.2.1 Exclusion of Flux Switching Machine Topology

The first important conclusion is obtained by comparing static simulation results, that with the specified mechanical constraints the nominated flus switching topology cannot fulfil the target Free-Piston Engine's requirement. Namely if the translator mass must be limited at 6 kg the force can only reach 525N (about 1/3 of the required force). If lift the translator mass constraint and optimise to minimum magnet mass, then the other parameters including the phase MMF, the translator mass and total mass are much higher the other four topologies (as shown in figure 8.1). What is more, even allowing FS to have a higher electric loading and much heavier mass the usage of magnets still shows disadvantage. The reason behind this scene is due to the higher main field flux leakage (74%). To counter this leakage a trapezoidal tooth structure is used and offset to flux leakage to 65%. Even though as illustrated in figure 8.2 is full results comparison between the 'worst' MPM (maximum magnetic loaded topology) and the 'best' FS (maximum electric loaded topology), it shows that FS still cannot save any magnet usage. What is more, the other performances of FS including the translator mass, the stator mass, efficiency and power factor are show disadvantage. Thus it can be proved FS selected in this thesis is not compatible with the target Free-Piston Engine.

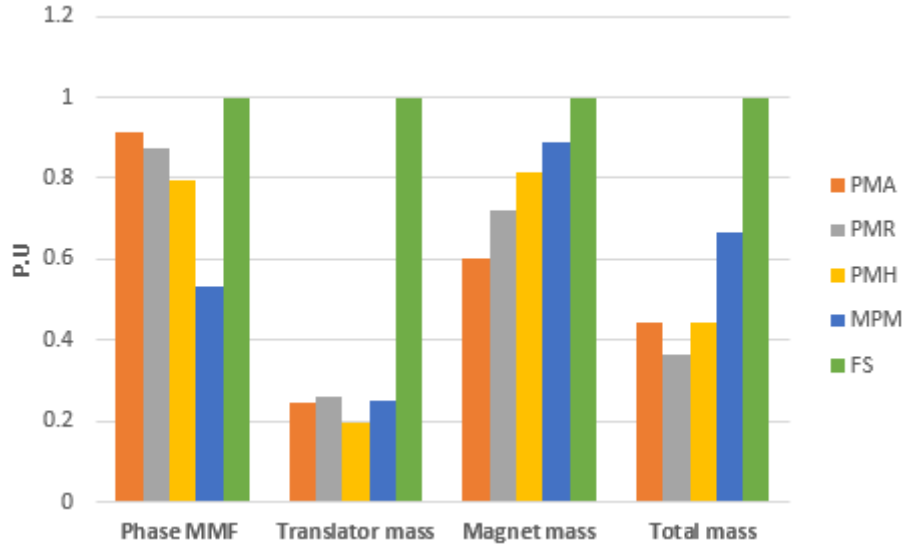

Figure 8.1Static results comparison for all nominated topologies

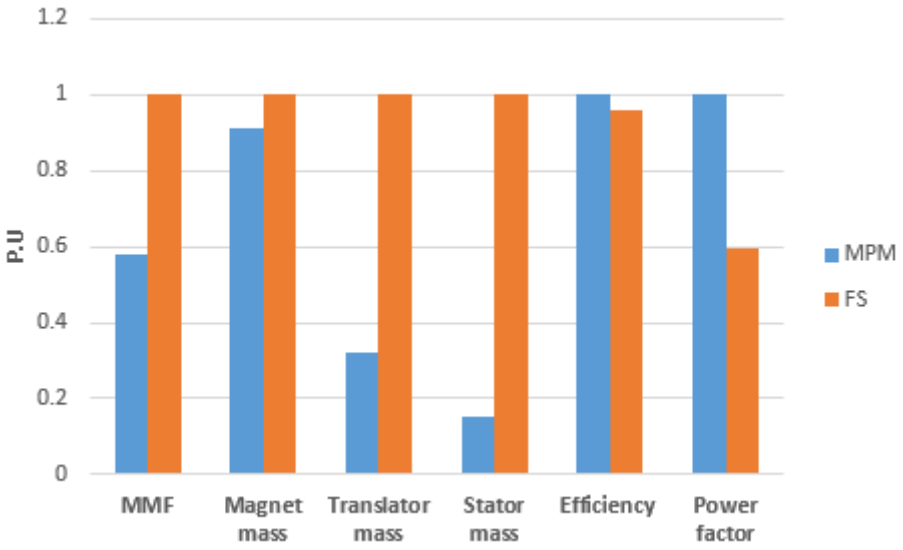

Figure 8.2 Full results comparison between the 'worst' MPM and the 'best' FS

8.2.2 Optimisation Routine Feasibility

The second conclusion from this thesis shows that the optimisation strategy used in Chapter 3 is feasible. Rather than manually optimise all topologies with different effort, easy optimisation objectives are used. Where minimising the magnet mass is equivalent to minimising the magnetic loading (A) and minimising the phase MMF is equivalent to minimising the electric loading (B). Based on mechanical constraints (the translator mass and magnetic force requirement) an optimisation example for MPM with triangular tooth shape is as shown in figure 8.3, where it can be observed that minimising the electric loading (A) shows advantages on both efficiency and power factor. Thus it can be proved that optimising by minimising the electric loading can surely achieve better dynamic results.

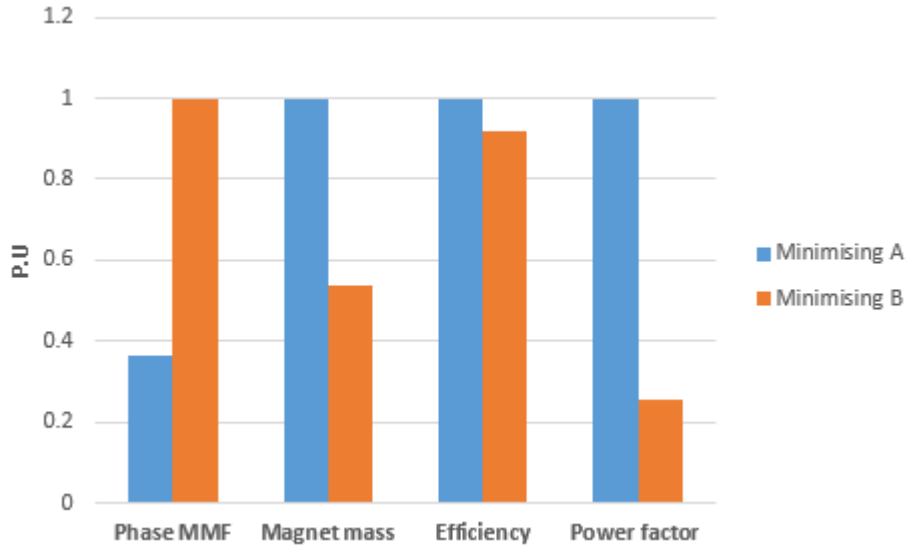

Figure 8.3 An example of optimisation of MPM with different objectives

8.2.3 Single Tooth Winding and C-Core Winding Comparison

The third conclusion is the advantage of using single tooth winding in the linear modulated pole machine topology (MPM). This is due to both the mechanical and electric aspects, where from mechanical point of view, a passive return coil must be used to form a closed loop for the current but without any contribution to the thrust force; as for the electric aspect a single toot winding originally produces a short pitch factor (0.866), which could influence the output force. As presented in figure 8.4, a single tooth winding topology theoretically can save 50% of the copper loss with the same active phase MMF, however the resultant force could be dragged to 86.6%. By increasing phase MMF in single tooth winding with the same sized coils, the force can be offset to the original required force with only 63% copper usage of that in the C-core winding. Besides, the single tooth winding can also improve the harmonics THD from 20% to 10%. Thus it can be proved that using single tooth winding is a better option in the linear MPM.

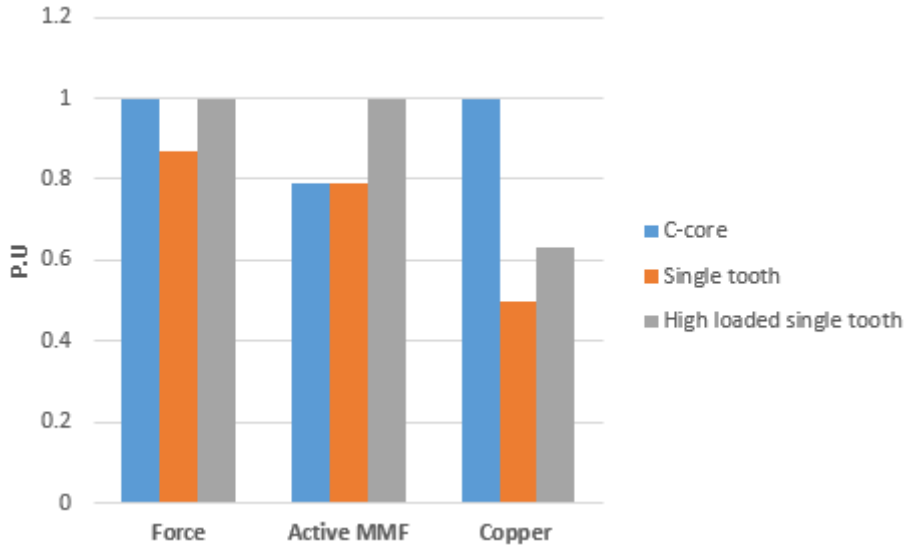

Figure 8.4 Comparison between C-core winding and single tooth winding on copper usage

8.2.4 Insight of Transverse Flux Machines' Low Power Factor Property

The fourth conclusion is the finding of the flux linkage factor (K_L) and flux factor (K_B) when discussing the working insight (the force production and the power factor derivation) of the MPM (transverse flux machine). Simulations and numerical solutions are both used to validate each other as shown in table 8.1, the designer announces that the better power factor of the final designed MPM is due to the high K_B. However due to the intrinsic low K_L, the power factor of transverse flux machines still shows poor compared to that of conventional longitudinal flux machines.

Parameters	**Simulations**	**Numerical solutions**
Flux linkage factor (K_L)	0.38	0.34
Flux factor (K_B)	0.69	0.72

Table 8.1Comparison of simulations and numerical solutions on two key factors

8.2.5 Feasibility of the Building and Assemble Strategies

The fifth conclusion is from the experimental test. There is a 16% error found in the self-inductance and EMF profiles compared to simulation results, whereas a 28% error is found in force profiles. These two errors and the later comparison illustrate that there must have some parasitic airgaps between different segments. However, this could be resolved by applying more refined stator support structure, other stiff material or higher printing accuracy.

8.3 Future Works

8.3.1 Flux Switching Types of Longitudinal Flux Topology

In this thesis, the flux switching (FS) topology shows unsatisfactory (low force produce and low power factor) due to both the main flux and armature current flux have a high flux leakage. Where the main flux leakage is the property of the flux switching structure and the armature flux leakage is the property of the transverse flux structure. So for the next stage, the designer would like to try more conventional flux switching topologies with longitudinal flux feature. As shown in figure 8.5 is one of such topologies, where at this position, the red phase main flux linkage is at maximum condition. An indication of the flux distribution for the red phase is in figure 8.6, where two leakage flux paths show a similar characteristic with that of the FS discussed in Chapter 3. It is believed that such topology could perform better capability on force production and power factor, but still stay puzzled if it can save magnet usage compared to the MPM.

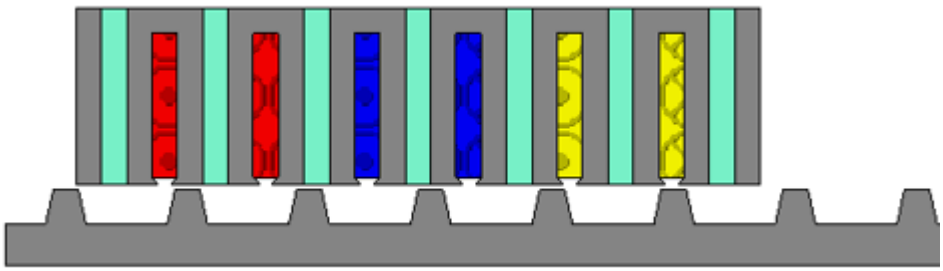

Figure 8.5 One of the flux switching topology with longitudinal flux feature

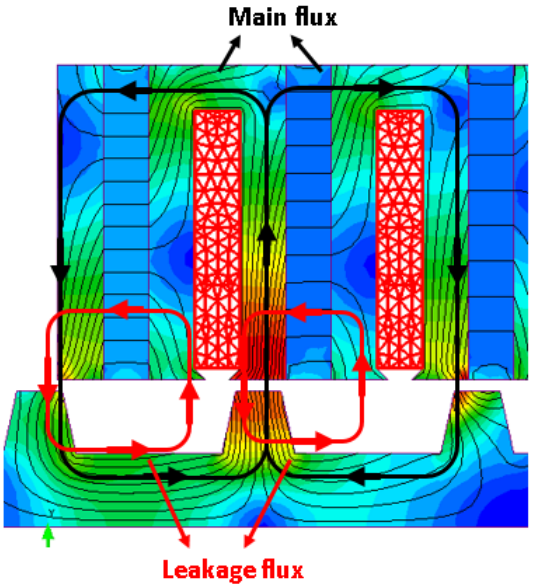

Figure 8.6 The flux distribution of the red phase

8.3.2 Advance Optimisation Routine Trade-Off

In this thesis, two objectives are used in the optimisation routine as either minimising the magnet mass or minimising the phase MMF. In other words, the optimisation only takes two extreme conditions to discuss. However, a more comprehensive optimisation can be achieved if quantifying the electrical loading (A) and the magnetic loading (B) by referring their peak flux values respectively. As shown in figure 8.7 below is the sketch of the optimisation concept, if more combinations can be extracted from the optimisation routine based on mechanical constraints, then more options' results can be compared, and more comprehensive design can be achieved.

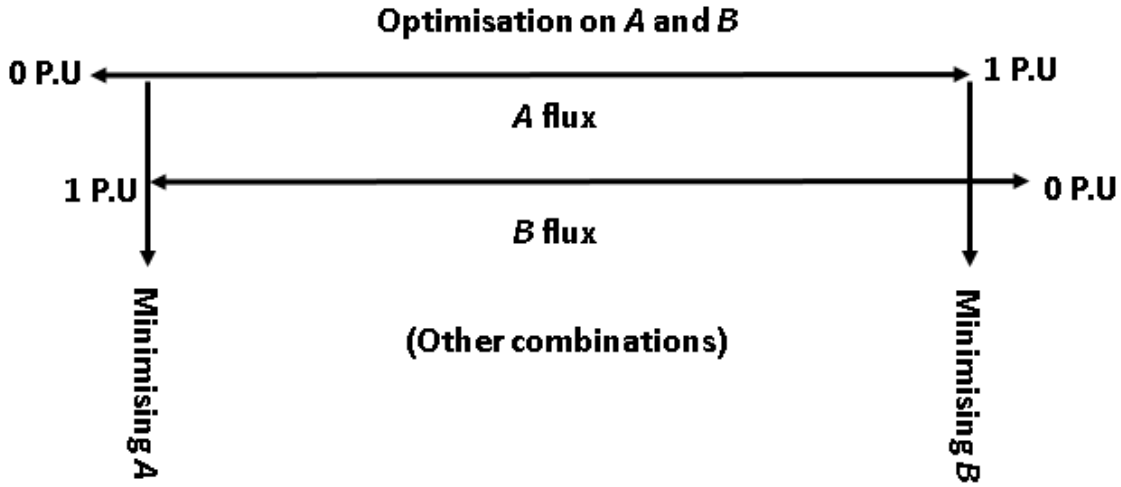

Figure 8.7 Advance optimisation concept

8.3.3 Single Cell Winding Topology Investigation

Based on the third and the forth conclusions, another winding topology is nominated as a future work which is called the single cell winding design. As shown in figure 8.8, for the single tooth winding, the armature current produced flux is conducted by both high permeable steel tooth and low permeable 'air' tooth. However, applying illustrated singe cell winding then the armature current flux could be concentrated through only high permeable steel tooth. In this case, a higher flux factor (K_B) even higher flux linkage factor (K_L) could be able to achieve, thus contribute to higher force production and better power factor.

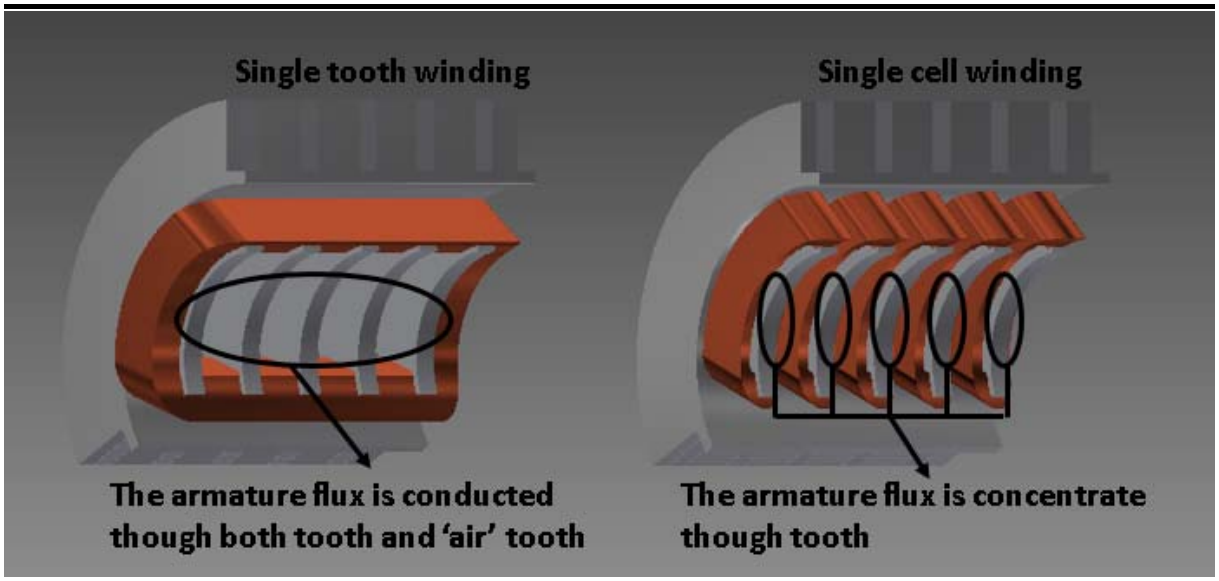

Figure 8.8 Single tooth winding and single cell winding

8.3.4 Control of Linear Electric Machine

The most important work needs to be investigated is the control aspect of the linear electric machine. As mentioned at the beginning of this thesis, the designer intends to simulate the machine in the motor model with a set of current sources. The reason is due to the start-up for the Free-Piston Engine, namely the linear electric machine is initially required to work as a motor to start the Free-Piston Engine. A typical start-up procedure waveform is in figure 8.9 [88], where the motion frequency needs to several cycles to accelerate to the rated frequency, in the meantime the linear motor is required to supply a constant force to drive the piston. In this case, instead of simple PMW control, a more complicate vector control method is required to supply the star-up variable motion frequency, where the three phase stator currents are identified as two visualised orthogonal components (d, q axis). It is believed that by completing the control design, the MPM prototype will become available to integrate into the Free-Piston Engine system.

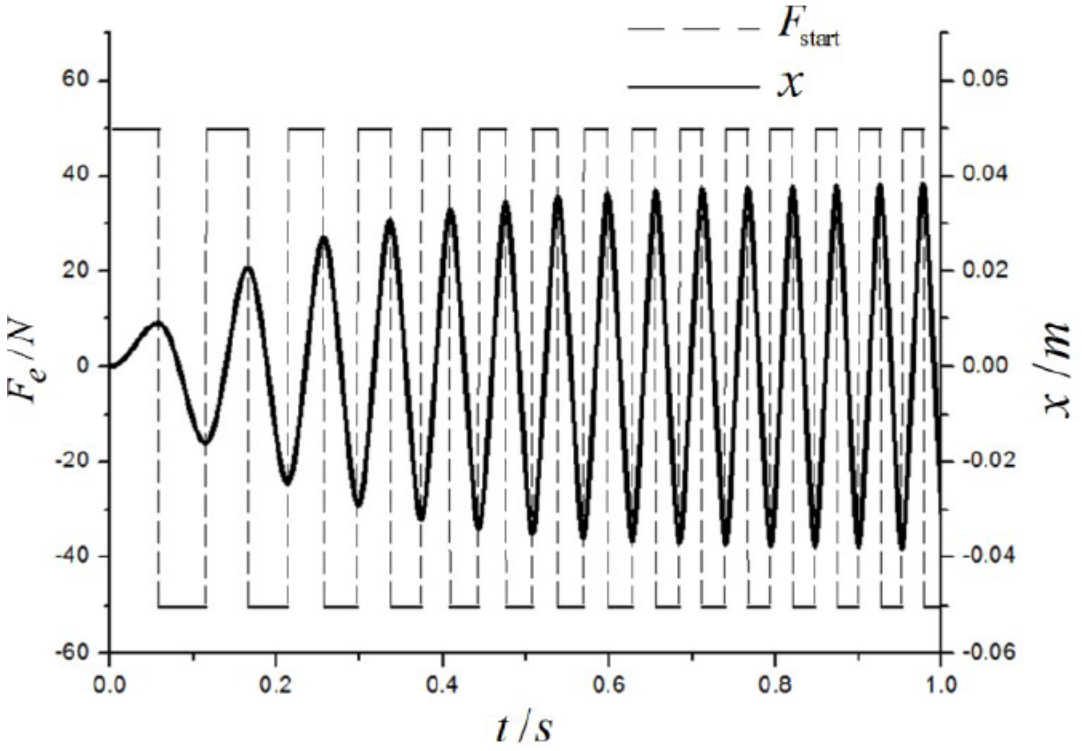

Figure 8.9 A typical Start-up procedure for the Free-Piston Engine [88]

Reference

[1] Mao, J., Zuo, Z. and Feng, H., 2011. Parameters coupling designation of diesel free-piston linear alternator. *Applied Energy*, *88*(12), pp.4577-4589.

[2] Mikalsen, R. and Roskilly, A.P., 2008. Performance simulation of a spark ignited free-piston engine generator. *Applied Thermal Engineering*, *28*(14), pp.1726-1733.

[3] Pateras, P.R., Pescara & Raymond Corp, 1928. *Motor-compressor apparatus*. U.S. Patent 1,657,641.

[4] Farmer, H.O., 1947. Free-piston compressor-engines. *Proceedings of the Institution of Mechanical Engineers*, *156*(1), pp.253-271.

[5] Mikalsen, R. and Roskilly, A.P., 2007. A review of free-piston engine history and applications. *Applied Thermal Engineering*, *27*(14), pp.2339-2352.

[6] Prados, M.A., 2002. *Towards a linear engine* (Doctoral dissertation, Ph. D. thesis, Stanford University, Stanford, CA).

[7] Mohamed, N.N., Ariffin, A.K. and Fonna, S., 2006. Simulation of a two-stroke spark ignition free piston linear engine motion. *Jurnal Teknologi*, *44*(A), pp.27-40.

[8] Fredriksson, J., 2006. *Modelling of a free piston energy converter*. Chalmers University of Technology.

[9] Golovitchev, V.I., Bergman, M. and Montorsi, L., 2007. CFD modelling of diesel oil and DME performance in a two-stroke free piston engine. *Combustion science and technology*, *179*(1-2), pp.417-436.

[10] Kosaka, H., Akita, T., Moriya, K., Goto, S., Hotta, Y., Umeno, T. and Nakakita, K., 2014. *Development of free piston engine linear generator system Part 1-investigation of fundamental characteristics* (No. 2014-01-1203). SAE Technical Paper.

[11] Goto, S., Moriya, K., Kosaka, H., Akita, T., Hotta, Y., Umeno, T. and Nakakita, K., 2014. *Development of free piston engine linear generator system part 2-investigation of control system for generator* (No. 2014-01-1193). SAE Technical Paper.

[12] Wang, J. and Howe, D., 2004. Design optimization of radially magnetized, iron-cored, tubular permanent-magnet machines and drive systems. *IEEE Transactions on Magnetics*, *40*(5), pp.3262-3277.

[13] Cawthorne, W.R., Famouri, P., Chen, J., Clark, N.N., McDaniel, T.I., Atkinson, R.J., Nandkumar, S., Atkinson, C.M. and Petreanu, S., 1999. Development of a linear alternator-engine for hybrid electric vehicle applications. *IEEE transactions on vehicular technology*, *48*(6), pp.1797-1802.

[14] Arshad, W.M., Thelin, P., Bäckström, T. and Sadarangani, C., 2003, May. Alternative electrical machine solutions for a free piston generator. In *The Sixth Intl Power Engineering Conference (IPEC2003), Singapore*.

[15] Mao, J., Zuo, Z. and Feng, H., 2011. Parameters coupling designation of diesel free-piston linear alternator. *Applied Energy*, *88*(12), pp.4577-4589.

[16] Salman, M., 2012. Analysis, design and control aspects of linear machines using co-simulation.

[17] Niu, X., 2013. *Modeling and Design Analysis of a Permanent Magnet Linear Synchronous Generator*.

[18] Rozman, G.I., Markunas, A.L., Hanson, M.J. and Weber, L.E., Sundstrand Corporation, 1996. *Method and apparatus for starting a synchronous machine*. U.S. Patent 5,488,286.

[19] Nasar, S.A. and Boldea, I., 1976. Linear motion electric machines.

[20] Wang, J., Howe, D. and Jewell, G.W., 2003. Fringing in tubular permanent-magnet machines: Part I. Magnetic field distribution, flux linkage, and thrust force. *IEEE Transactions on Magnetics*, *39*(6), pp.3507-3516.

[21] Hasanien, H.M., Abd-Rabou, A.S. and Sakr, S.M., 2010. Design optimization of transverse flux linear motor for weight reduction and performance improvement using response surface methodology and genetic algorithms. *IEEE Transactions on Energy Conversion*, *25*(3), pp.598-605.

[22] Harris, M.R., Pajooman, G.H. and Sharkh, S.A., 1997. The problem of power factor in VRPM (transverse-flux) machines.

[23] Wang, J., Jewell, G.W. and Howe, D., 1999. A general framework for the analysis and design of tubular linear permanent magnet machines. *IEEE Transactions on Magnetics*, *35*(3), pp.1986-2000.

[24] Hsu, Y.S. and Tsai, M.C., 2011. Development of a novel transverse flux wheel motor. *IEEE Transactions on Magnetics*, *47*(10), pp.3677-3680.

[25] Baker, N.J., Atkinson, G.J., Washington, J.G., Mecrow, B.C., Nord, G. and Sjoberg, L., 2012, March. Design of high torque traction motors for automotive applications using modulated pole SMC machines. In *Power Electronics, Machines and Drives (PEMD 2012), 6th IET International Conference on* (pp. 1-6). IET.

[26] Polinder, H., Mecrow, B.C., Jack, A.G., Dickinson, P.G. and Mueller, M.A., 2005. Conventional and TFPM linear generators for direct-drive wave energy conversion. *IEEE Transactions on Energy Conversion*, *20*(2), pp.260-267.

[27] Zheng, P., Tong, C., Chen, G., Liu, R., Sui, Y., Shi, W. and Cheng, S., 2011. Research on the magnetic characteristic of a novel transverse-flux PM linear machine used for free-piston energy converter. *IEEE Transactions on Magnetics*, *47*(5), pp.1082-1085.

[28] Lei, G., Liu, C., Guo, Y. and Zhu, J., 2015. Multidisciplinary design analysis and optimization of a PM transverse flux machine with soft magnetic composite core. *IEEE Transactions on Magnetics*, *51*(11), pp.1-4.

[29] Cullity, B.D. and Graham, C.D., 2011. *Introduction to magnetic materials*. John Wiley & Sons.

[30] Shokrollahi, H. and Janghorban, K., 2007. Soft magnetic composite materials (SMCs). *Journal of Materials Processing Technology*, *189*(1), pp.1-12.

[31] Wohlfarth, E.P., 1959. Hard magnetic materials. *Advances in physics*, *8*(30), pp.87-224.

[32] Laithwaite, E.R., 1975. Linear electric machines—A personal view. *Proceedings of the IEEE*, *63*(2), pp.250-290.

[33] Eastham, J.F., 1990, January. IEE Power Division: Chairman's address. Novel synchronous machines: linear and disc. In *IEE Proceedings B (Electric Power Applications)* (Vol. 137, No. 1, pp. 49-58). IET Digital Library.

[34] Zehden, A., 1905. *Electric traction apparatus*. U.S. Patent 782,312.

[35] Laithwaite, E.R., 1957. Linear induction motors. *Proceedings of the IEE-Part A: Power Engineering*, *104*(18), pp.461-470.

[36] Laithwaite, E.R., 1987. The high-speed transport game. In *A History of Linear Electric Motors* (pp. 125-168). Macmillan Education UK.

[37] Gieras, J.F., Piech, Z.J. and Tomczuk, B., 2016. *Linear synchronous motors: transportation and automation systems*. CRC press.

[38] Kosten, M. and Piotrovsky, L., 1974. *Electrical Machines, Vol. 2: Alternating Current Machines*. Mir Publihers, Moscow.

[39] Manual, L.D., 1999. Sulzer Electronics. *Ltd, Zürich, Switzerland*.

[40] Smith, A.C., 1990. Magnetic forces on a misaligned rotor of a PM linear actuator. In *Proc. of the 1990 Int. Conf. on Electrical Machines* (pp. 1076-1081).

[41] Jahns, T.M., 1994. Motion control with permanent-magnet AC machines. *Proceedings of the IEEE*, *82*(8), pp.1241-1252.

[42] Covic, G.A., Boys, J.T., Kissin, M.L. and Lu, H.G., 2007. A three-phase inductive power transfer system for roadway-powered vehicles. *IEEE Transactions on Industrial Electronics*, *54*(6), pp.3370-3378.

[43] Liu, C.T. and Kuo, J.L., 1994. Experimental investigation and 3-D modelling of linear variable-reluctance machine with magnetic-flux decoupled windings. *IEEE Transactions on Magnetics*, *30*(6), pp.4737-4739.

[44] Hinds, W.E. and Nocito, B., 1973, April. The Sawyer linear motor. In *Proceedings of the Second Symposium on Incremental Motion Control Systems and Devices* (pp. W1-W10).

[45] Adamiak, K., Barlow, D., Choudhury, C.P., Cusack, P.M., Dawson, G.E., Eastham, A.R., Grady, B., Ho, E., Hongping, Y., Pattison, L. and Welch, J., 1987, May. The switched reluctance motor as a low-speed linear drive. In *Intl. Conf. on Maglev and Linear Drives* (pp. 39-43).

[46] Wang, J., Jewell, G.W. and Howe, D., 1999. A general framework for the analysis and design of tubular linear permanent magnet machines. *IEEE Transactions on Magnetics*, *35*(3), pp.1986-2000.

[47] Wang, J., Howe, D. and Amara, Y., 2005. Armature reaction field and inductances of tubular modular permanent magnet machines. *Journal of applied physics*, *97*(10), p.10Q504.

[48] Wang, J. and Howe, D., 2004. Design optimization of radially magnetized, iron-cored, tubular permanent-magnet machines and drive systems. *IEEE Transactions on Magnetics*, *40*(5), pp.3262-3277.

[49] Qishan, G. and Hongzhan, G., 1985. Effect of slotting in PM electric machines. *Electric machines and power systems*, *10*(4), pp.273-284.

[50] Wang, J., Howe, D. and Jewell, G.W., 2003. Fringing in tubular permanent-magnet machines: Part II. Cogging force and its minimization. *IEEE Transactions on Magnetics*, *39*(6), pp.3517-3522.

[51] Wang, J., Inoue, M., Amara, Y. and Howe, D., 2005. Cogging-force-reduction techniques for linear permanent-magnet machines. *IEE Proceedings-Electric Power Applications*, *152*(3), pp.731-738.

[52] Wang, J., West, M., Howe, D., Zelaya-De La Parra, H. and Arshad, W.M., 2007. Design and experimental verification of a linear permanent magnet generator for a free-piston energy converter. *IEEE Transactions on Energy Conversion*, *22*(2), pp.299-306.

[53] Weh, H. and May, H., 1986, September. Achievable force densities for permanent magnet excited machines in new configurations. In *Proc. Int. Conf. Electrical Machines* (Vol. 3, pp. 1107-1111).

[54] 苏士斌, 史仪凯, 袁小庆, 韩康, 崔田田 and 马艳, 2013. 横向磁通电机研究综述. *电子学报*, *41*(11), pp.2290-2296.

[55] cWang Qian, Zou Jibin, et al. "Overview of high torque density transverse flux machines [J]." *Chinese High Technology Letters* 7 (2010): 021.

[56] Arshad, W.M., Thelin, P., Backstrom, T. and Sadarangani, C., 2004. Use of transverse-flux machines in a free-piston generator. *IEEE transactions on industry applications*, *40*(4), pp.1092-1100.

[57] Cosic, A., Chandur, S. and Fredrik, C., 2005. A novel concept of a transverse flux linear free-piston generator.

[58] Cosic, A., Sadarangani, C. and Timmerman, J., 2008, October. Design and manufacturing of a linear transverse flux permanent magnet machines. In *Industry Applications Society Annual Meeting, 2008. IAS'08. IEEE* (pp. 1-5). IEEE.

[59] Hasanien, H.M., Abd-Rabou, A.S. and Sakr, S.M., 2010. Design optimization of transverse flux linear motor for weight reduction and performance improvement using response surface methodology and genetic algorithms. *IEEE Transactions on Energy Conversion*, *25*(3), pp.598-605.

[60] Washington, J.G., Atkinson, G.J., Baker, N.J., Jack, A.G., Mecrow, B.C., Jensen, B.B., Pennander, L.O., Nord, G.L. and Sjöberg, L., 2012. Three-phase modulated pole machine topologies utilizing mutual flux paths. *IEEE Transactions on Energy Conversion*, *27*(2), pp.507-515.

[61] Pinguey, E., 2010. On the design and construction of modulated pole machines.

[62] Mecrow, B.C., Jack, A.G., Atkinson, D.J., Dickinson, P.G. and Swaddle, S., 2002. High torque machines for power hand tool applications.

[63] Wang, F., Zong, M., Zheng, W. and Guan, E., 2003, November. Design features of high speed PM machines. In *Electrical Machines and Systems, 2003. ICEMS 2003. Sixth International Conference on* (Vol. 1, pp. 66-70). IEEE.

[64] Rauch, S.E. and Johnson, L.J., 1955. Design principles of flux-switch alternators. *Transactions of the American Institute of Electrical Engineers. Part III: Power Apparatus and Systems*, *74*(3), pp.1261-1268.

[65] Hoang, E., Ahmed, H.B. and Lucidarme, J., 1997, September. Switching flux permanent magnet polyphased synchronous machines. In *EPE 97*.

[66] Zhu, Z.Q., Pang, Y., Howe, D., Iwasaki, S., Deodhar, R. and Pride, A., 2005. Analysis of electromagnetic performance of flux-switching permanent-magnet machines by nonlinear adaptive lumped parameter magnetic circuit model. *IEEE Transactions on magnetics*, *41*(11), pp.4277-4287.

[67] Fang, Z.X., Wang, Y., Shen, J.X. and Huang, Z.W., 2008, April. Design and analysis of a novel flux-switching permanent magnet integrated-starter-generator. In *Power Electronics, Machines and Drives, 2008. PEMD 2008. 4th IET Conference on* (pp. 106-110). IET.

[68] Chen, J.T., Zhu, Z.Q., Thomas, A.S. and Howe, D., 2008, October. Optimal combination of stator and rotor pole numbers in flux-switching PM brushless AC machines. In *Electrical Machines and Systems, 2008. ICEMS 2008. International Conference on* (pp. 2905-2910). IEEE.

[69] Amara, Y., Barakat, G., Paulides, J.J.H. and Lomonova, E.A., 2013. Overload capability of linear flux switching permanent magnet machines. In *Applied Mechanics and Materials* (Vol. 416, pp. 345-352). Trans Tech Publications.

[70] Xu, W., Zhu, J., Zhang, Y., Wang, Y., Li, Y. and Hu, J., 2010, December. Flux-switching permanent magnet machine drive system for plug-in hybrid electrical vehicle. In *Universities Power Engineering Conference (AUPEC), 2010 20th Australasian* (pp. 1-6). IEEE.

[71] Zhu, Z.Q., Chen, X., Chen, J.T., Howe, D. and Dai, J.S., 2008, October. Novel linear flux-switching permanent magnet machines. In *Electrical Machines and Systems, 2008. ICEMS 2008. International Conference on* (pp. 2948-2953). IEEE.

[72] Du, Y., Cheng, M., Chau, K.T., Liu, X., Xiao, F., Zhao, W., Shi, K. and Mo, L., 2014. Comparison of linear primary permanent magnet vernier machine and linear vernier hybrid machine. *IEEE Transactions on Magnetics*, *50*(11), pp.1-4.

[73] Ahmed, N., Atkinson, G.J., Baker, N.J., Sjöberg, L. and Stannard, N., 2013, May. Flux Switching Modulated Pole Machine topologies which offer greater mechanical simplicity. In *Electric Machines & Drives Conference (IEMDC), 2013 IEEE International* (pp. 354-358). IEEE.

[74] Guarnieri, M., 2015. Two Millennia of Light: The Long Path to Maxwell? s Waves [Historical] The United Nations Educational, Scientific, and Cultural Organization (UNESCO) has desi. *IEEE Industrial Electronics Magazine*, *9*(2), pp.54-60.

[75] Wang, J., West, M., Howe, D., Zelaya-De La Parra, H. and Arshad, W.M., 2007. Design and experimental verification of a linear permanent magnet generator for a free-piston energy converter. *IEEE Transactions on Energy Conversion*, *22*(2), pp.299-306.

[76] Wang, J. and Baker, N.J., 2015, May. Comparison of flux switching and modulated pole linear machines for use with a free piston. In *Electric Machines & Drives Conference (IEMDC), 2015 IEEE International* (pp. 642-648). IEEE.

[77] Ahmed, Nabeel, et al. "Flux Switching Modulated Pole Machine topologies which offer greater mechanical simplicity." *Electric Machines & Drives Conference (IEMDC), 2013 IEEE International*. IEEE, 2013.

[78] Baker, N.J., Wang, J. and Atkinson, G.J., 2016, September. Optimization and comparison of linear transverse flux and flux switching machines. In *Electrical Machines (ICEM), 2016 XXII International Conference on* (pp. 2471-2477). IEEE.

[79] Wang, J. and Baker, N.J., 2016, April. A comparison of alternative linear machines for use with a direct drive free piston engine. In *Power Electronics, Machines and Drives (PEMD 2016), 8th IET International Conference on* (pp. 1-6). IET.

[80] Anglada, J.R. and Sharkh, S., 2017. An insight into torque production and power factor in transverse-flux machines. *IEEE Transactions on Industry Applications*.

[81] Baker, N.J., Atkinson, G.J., Washington, J.G., Mecrow, B.C., Nord, G. and Sjoberg, L., 2012, March. Design of high torque traction motors for automotive applications using modulated pole SMC machines. In *Power Electronics, Machines and Drives (PEMD 2012), 6th IET International Conference on* (pp. 1-6). IET.

[82] Harris, M.R. and Mecrow, B.C., 1993, September. Variable reluctance permanent magnet motors for high specific output. In *Electrical Machines and Drives, 1993. Sixth International Conference on* (pp. 437-442). IET.

[83] Harris, M.R., Pajooman, G.H. and Sharkh, S.A., 1996. Performance and design optimisation of electric motors with heteropolar surface magnets and homopolar windings. *IEE Proceedings-Electric Power Applications*, *143*(6), pp.429-436.

[84] Cosic, A., Sadarangani, C. and Leksell, M., 2008, September. 3D analyses of a novel Transverse Flux machine for a free piston energy converter. In *Electrical Machines, 2008. ICEM 2008. 18th International Conference on* (pp. 1-6). IEEE.

[85] Harris, M.R., Pajooman, G.H. and Sharkh, S.A., 1997. The problem of power factor in VRPM (transverse-flux) machines.

[86] Cable, M.V.C., sizes are designated by American Wire Gauge (AWG) and Thousand Circular Mils (Kcmil). *Conductor and conduit sizes indicated are for copper conductors unless otherwise noted. Insulated conductors shall have the date of manufacture and other identification imprinted on the outer surface of each cable at regular intervals throughout cable length. Wires and cables manufactured more than*, *12*.

[87] Electric Linear Actuator Sizing Report available at http://sizeit.tolomatic.com/project/load/OTA2Mjc=

[88] Li, Y.X., Zuo, Z.X., Feng, H.H. and Jia, B.R., 2015. Parameters matching requirements for diesel free piston linear alternator start-up. *Advances in Mechanical Engineering*, *7*(3), p.1687814015574408.

[89] Nick. J.B, 2017. Design of Machine and Drives 2: Permanent Magnet Machine Design. *School of Electrical and Electronic Engineering, EEE8015/EEE8102 Handout 2*, pp. 2

[90] Burr, A and Cheatham, J: Mechanical Design and Analysis, 2nd edition, section 5.2. Prentice-Hall, 1995.

Appendix

The dimensions' specification for the final assembled MPM is listed in the table below and along with drawings for all components.

Parameters	Specifications
Translator	
Pole pair number	10
Outer diameter (mm)	77.8
Axial length (mm)	320
Shaft diameter (mm)	25
Shaft length (mm)	476
Weight (kg)	10.27
Stator	
Pole pair number	5
Phase number	3
Number of turns	120
Outer diameter (mm)	189.8
Axial length (mm)	185
Stator housing	
Outer diameter (mm)	210
Inner diameter (mm)	189.8
Stroke housing	
Outer diameter (mm)	210
Inner diameter (mm)	150

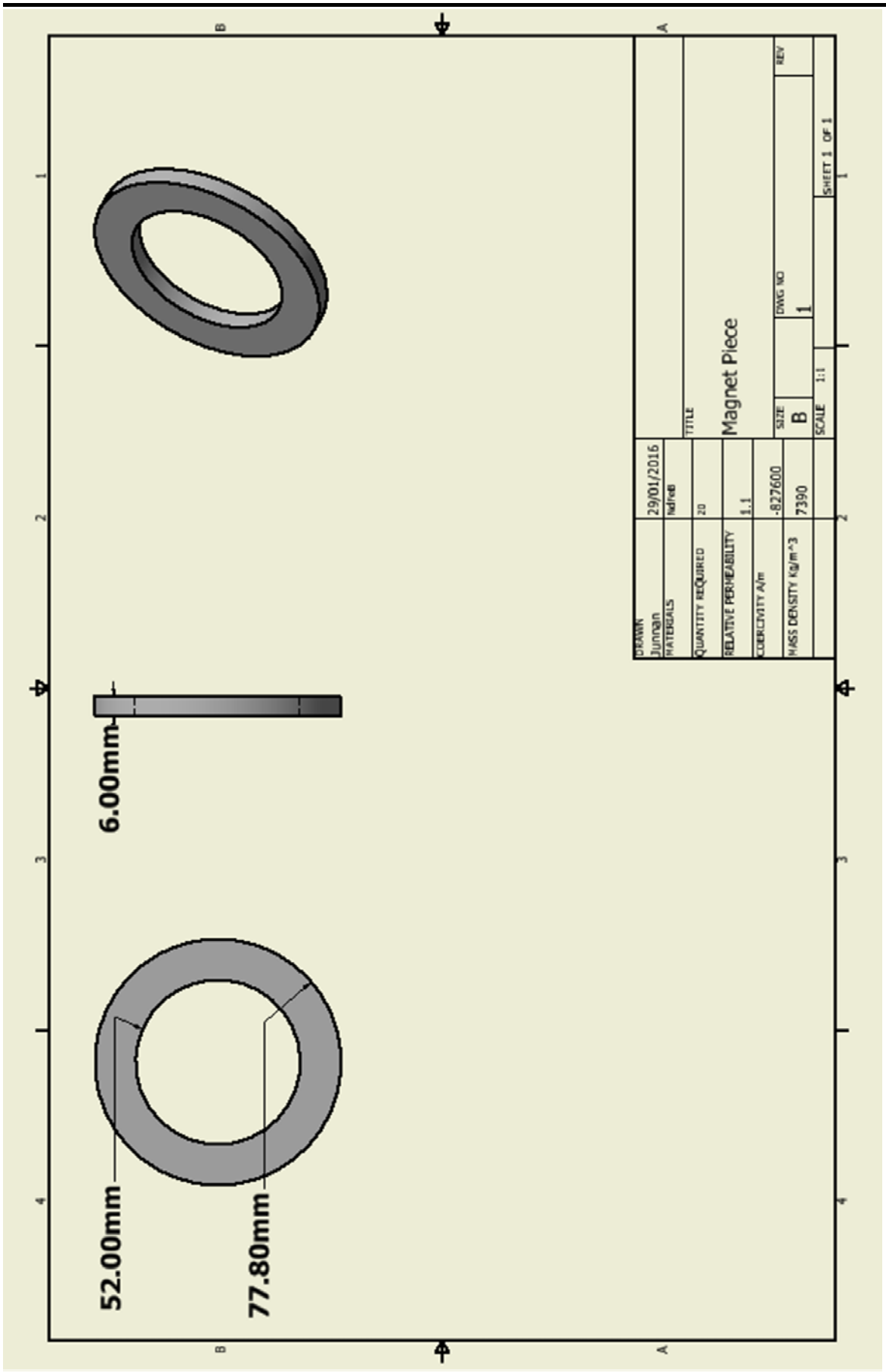
6.00mm
52.00mm
77.80mm
DRAWN
Junnan
29/01/2016
MATERIALS
Ndfe0
QUANTITY REQUIRED
20
RELATIVE PERMEABILITY
1.1
COERCIVITY A/m
-827600
MASS DENSITY Kg/m^3
7390
TITLE
Magnet Piece
SIZE
B
DWG NO
1
REV
SCALE 1:1
SHEET 1 OF 1

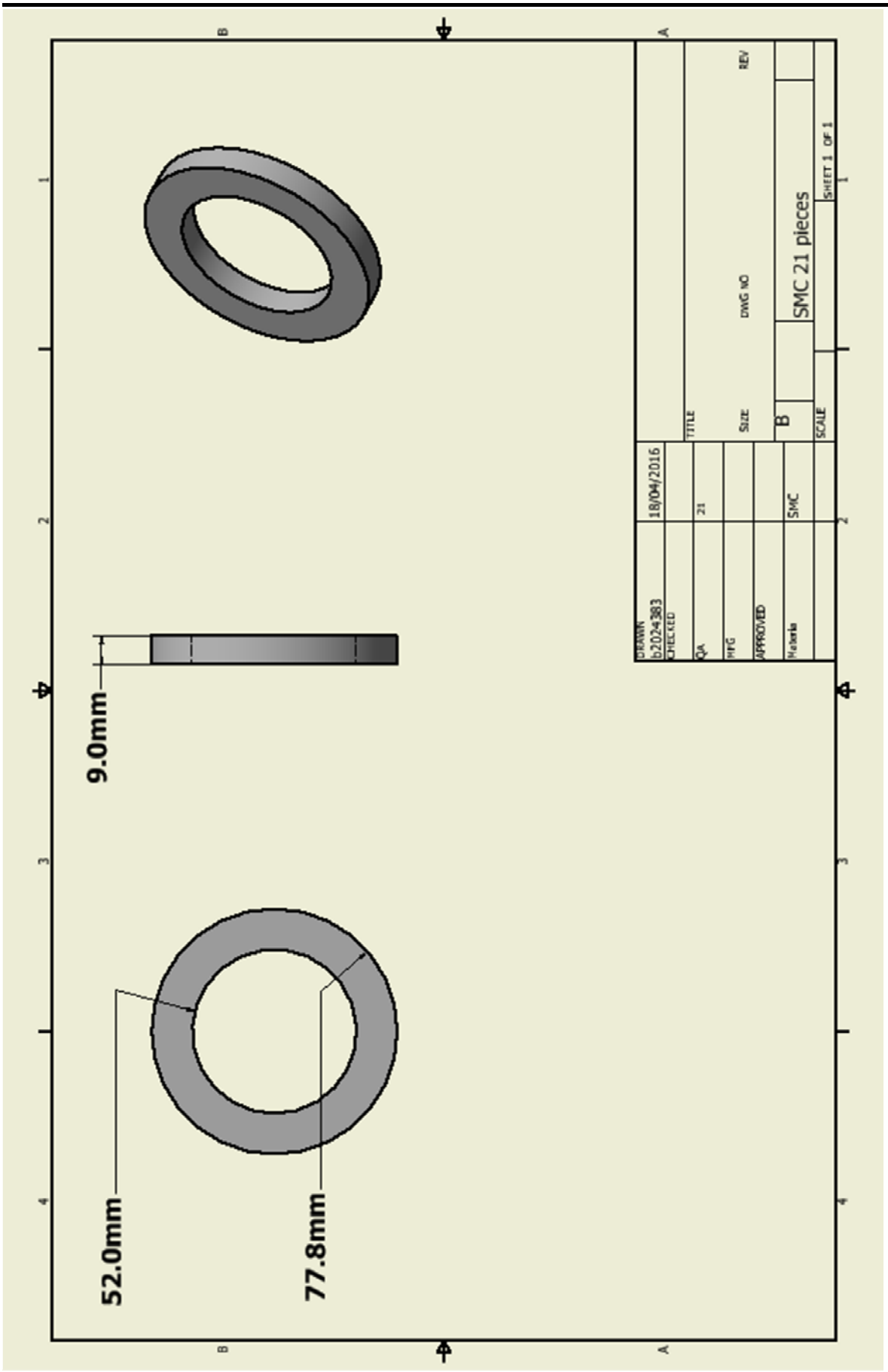
9.0mm
52.0mm
77.8mm
DRAWN
b2024383
18/04/2016
CHECKED
QA
21
MFG
APPROVED
Helena
SMC
TITLE
SIZE
B
DWG NO
REV
SMC 21 pieces
SCALE
SHEET 1 OF 1

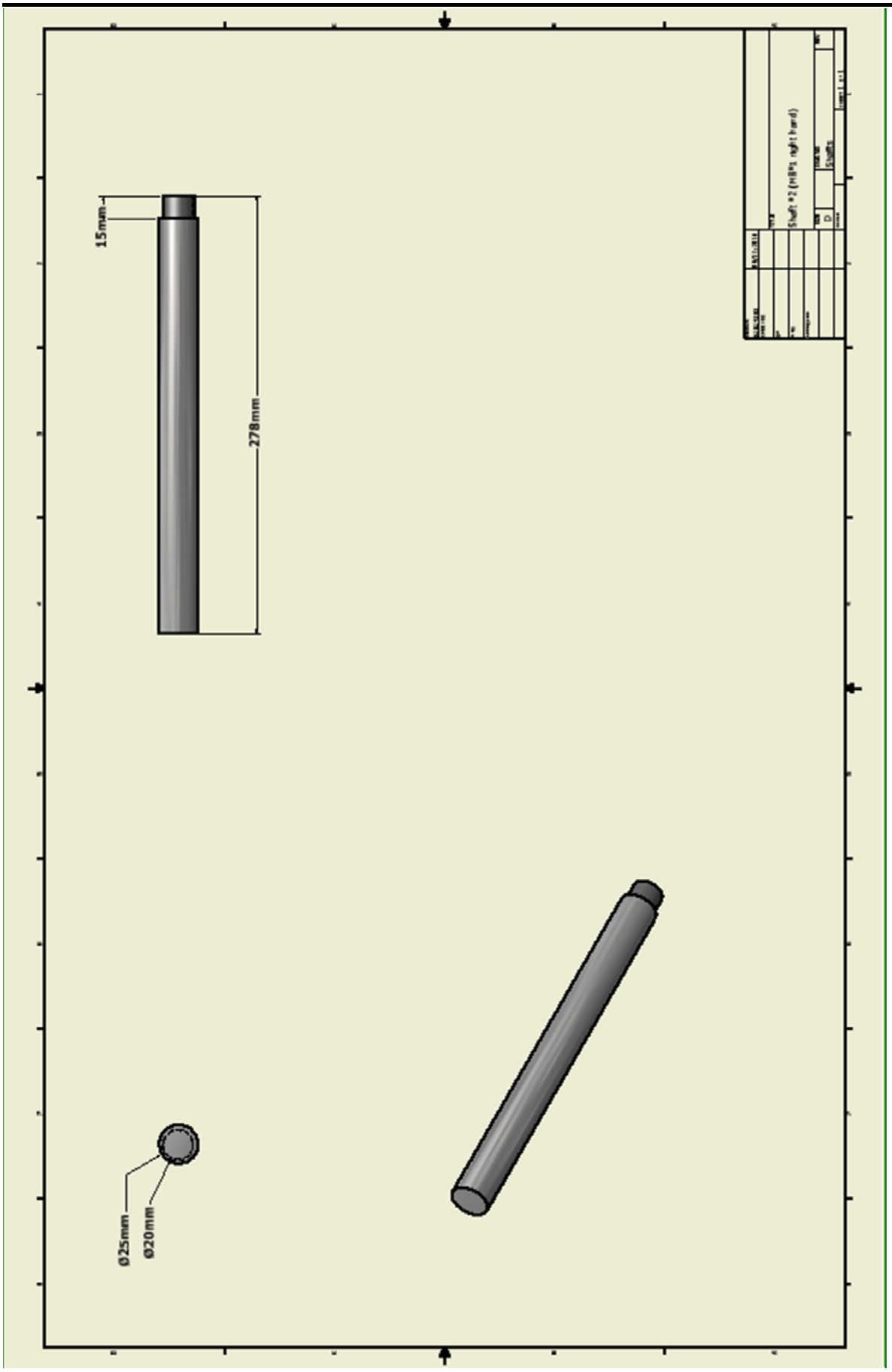
15mm
278mm
Ø25mm
Ø20mm

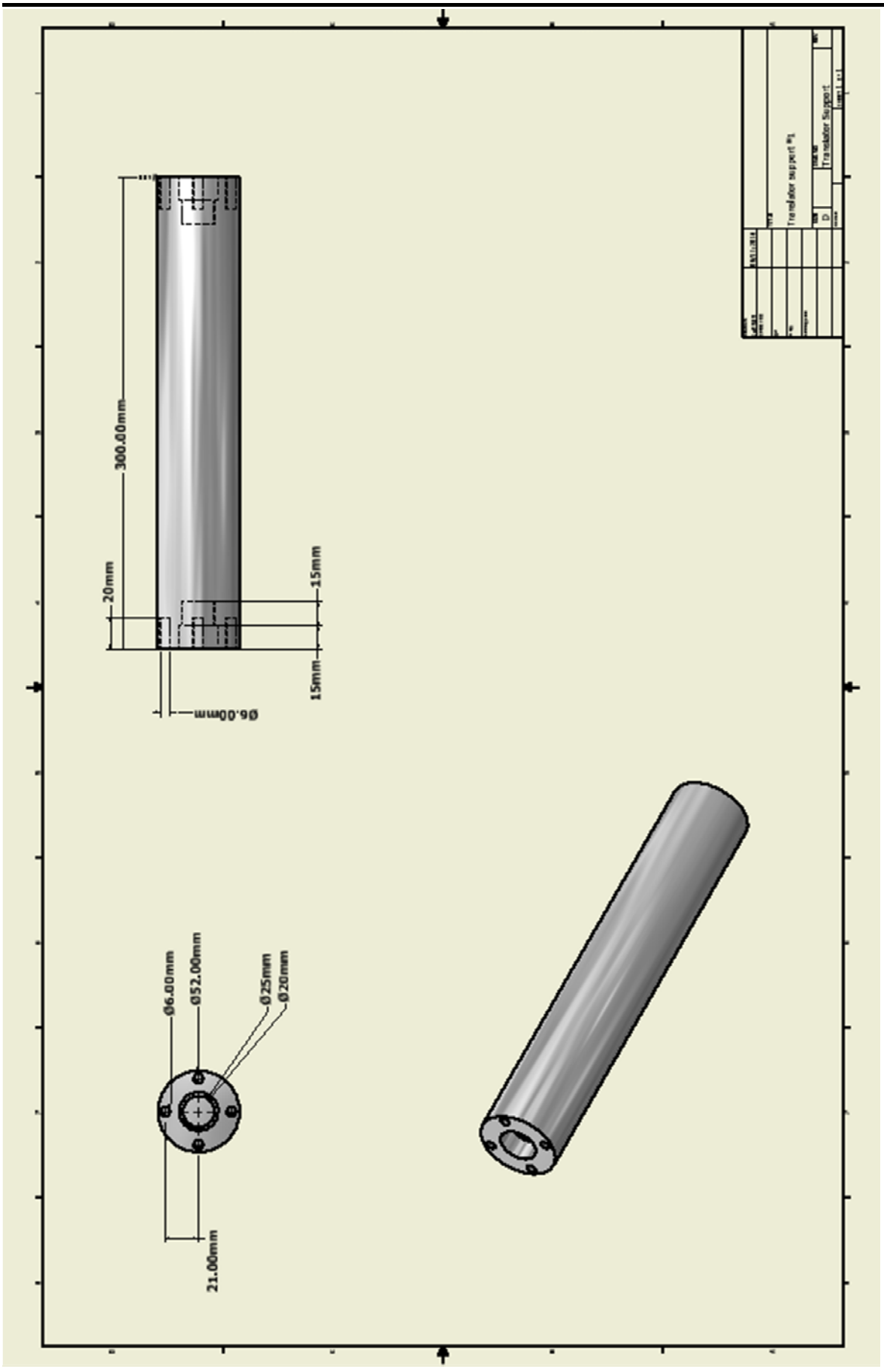
300.00mm
20mm
15mm
15mm
Ø6.00mm
Ø6.00mm
Ø52.00mm
Ø25mm
Ø20mm
21.00mm
Translator support
Translator Support

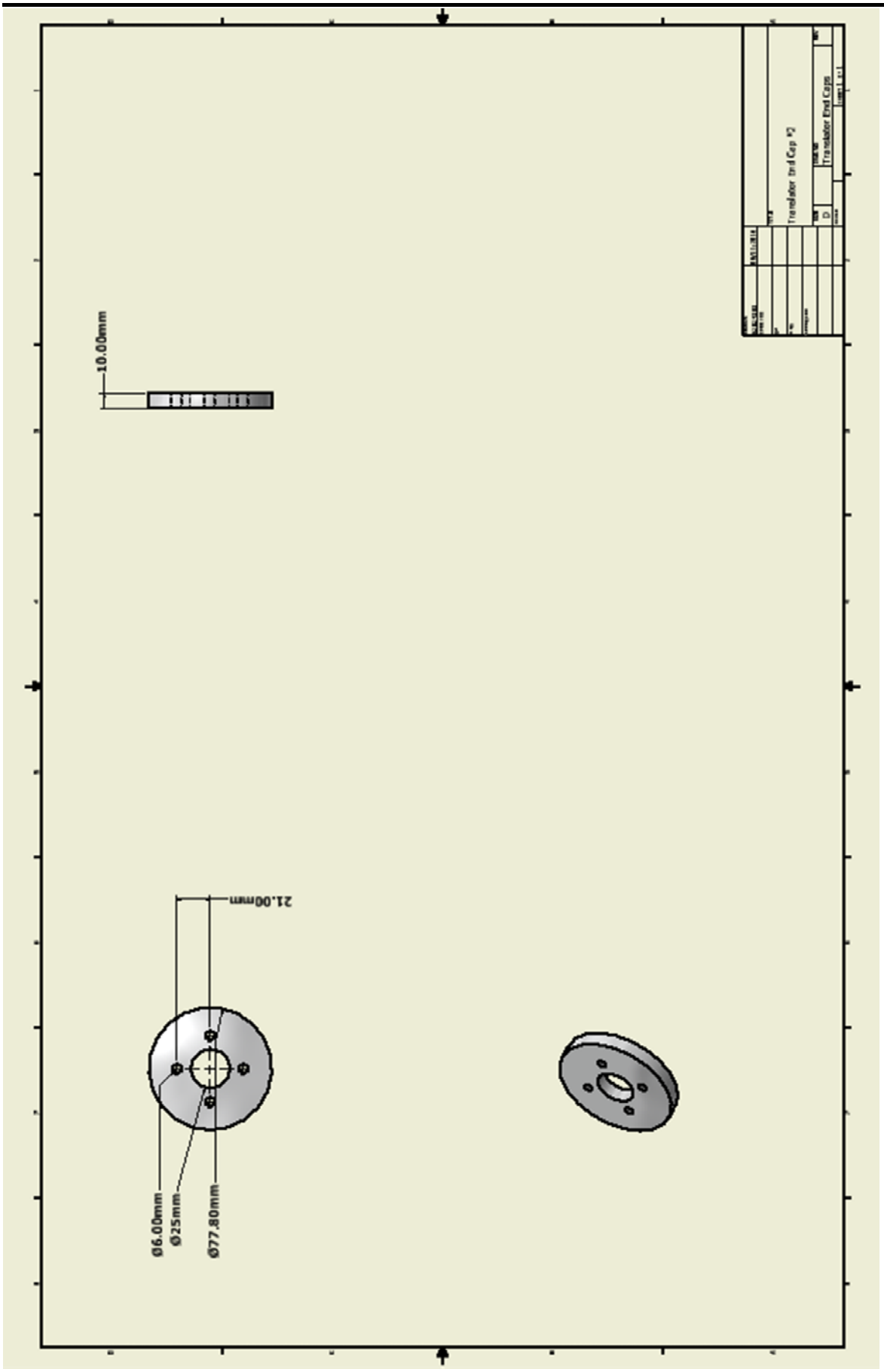
10.00mm
21.00mm
Ø6.00mm
Ø25mm
Ø77.80mm

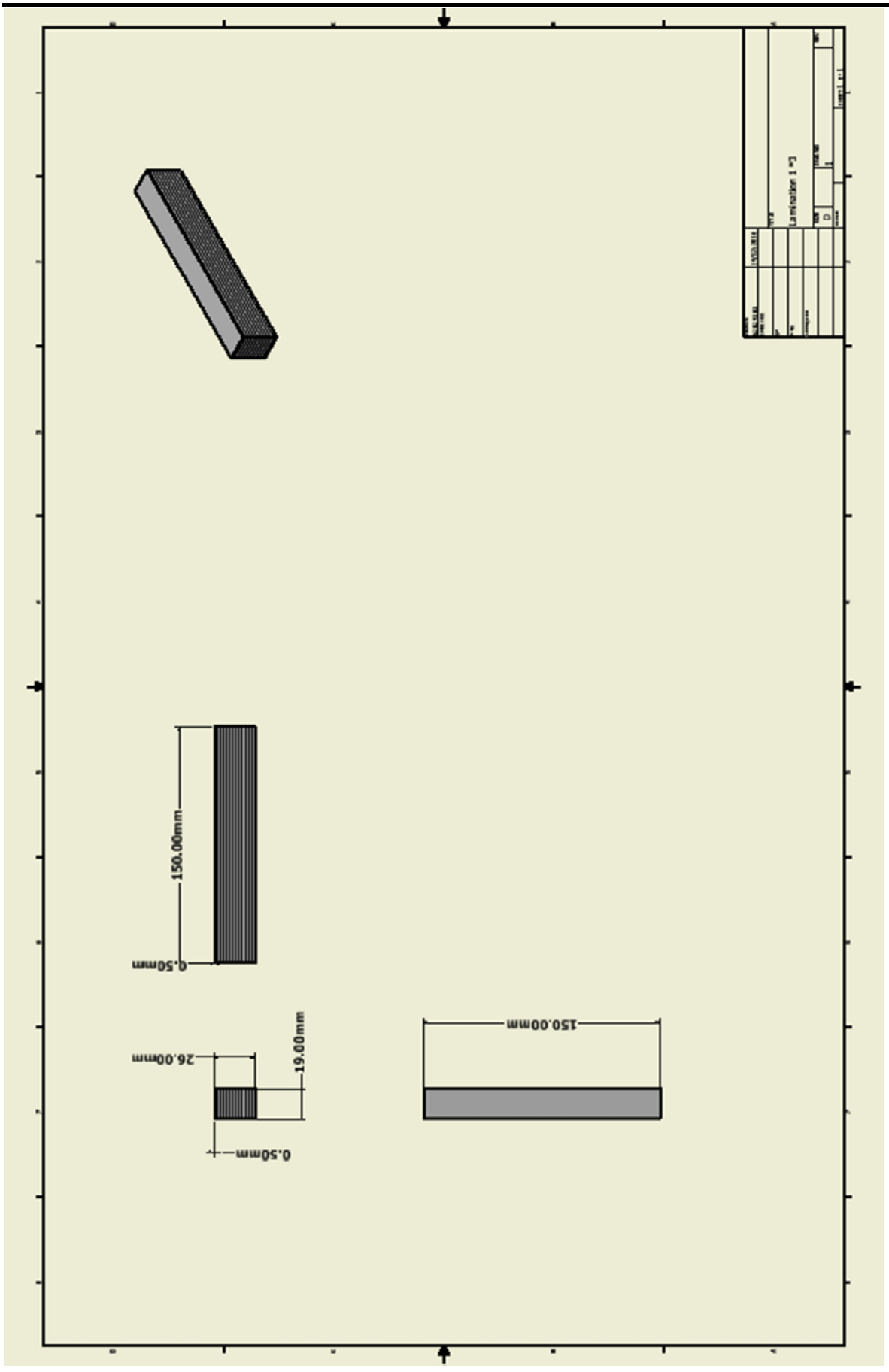
150.00mm
0.50mm
26.00mm
19.00mm
0.50mm
150.00mm

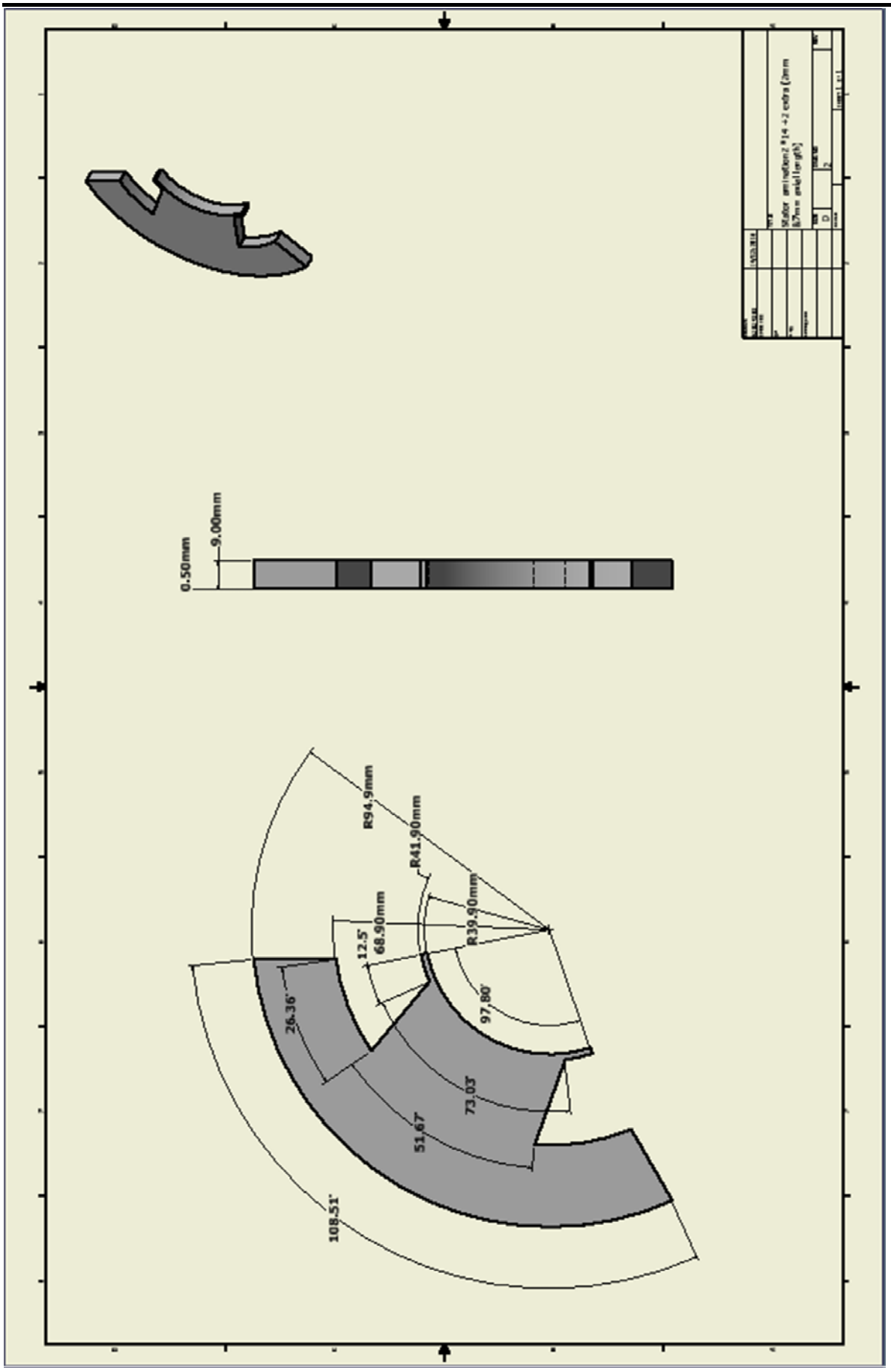
0.50mm
9.00mm
R94.9mm
R41.90mm
R39.90mm
68.90mm
12.5°
26.36°
97,80°
73.03°
51.67°
108.51°

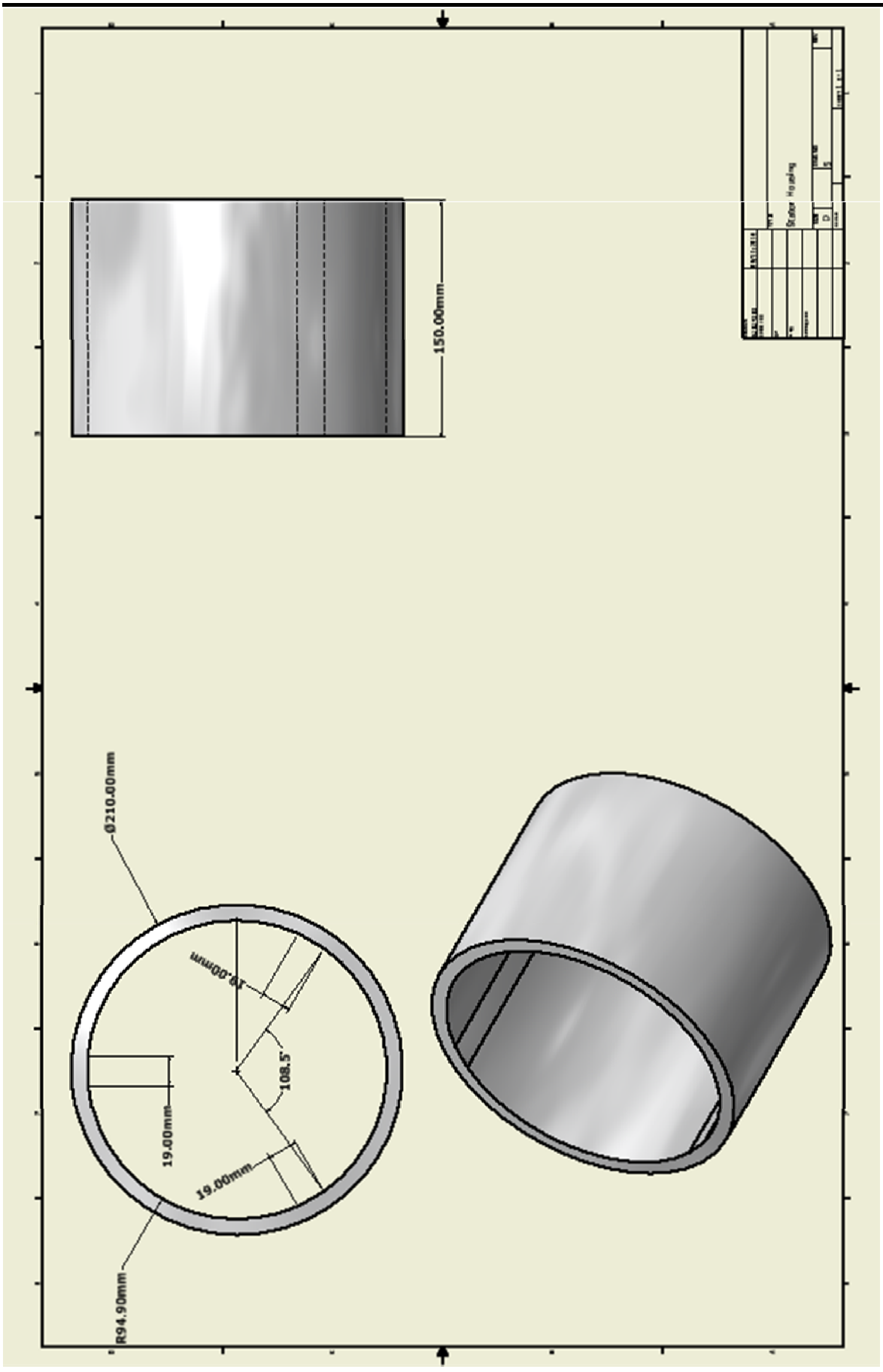
150.00mm
Ø210.00mm
19.00mm
108.5°
19.00mm
19.00mm
R94.90mm

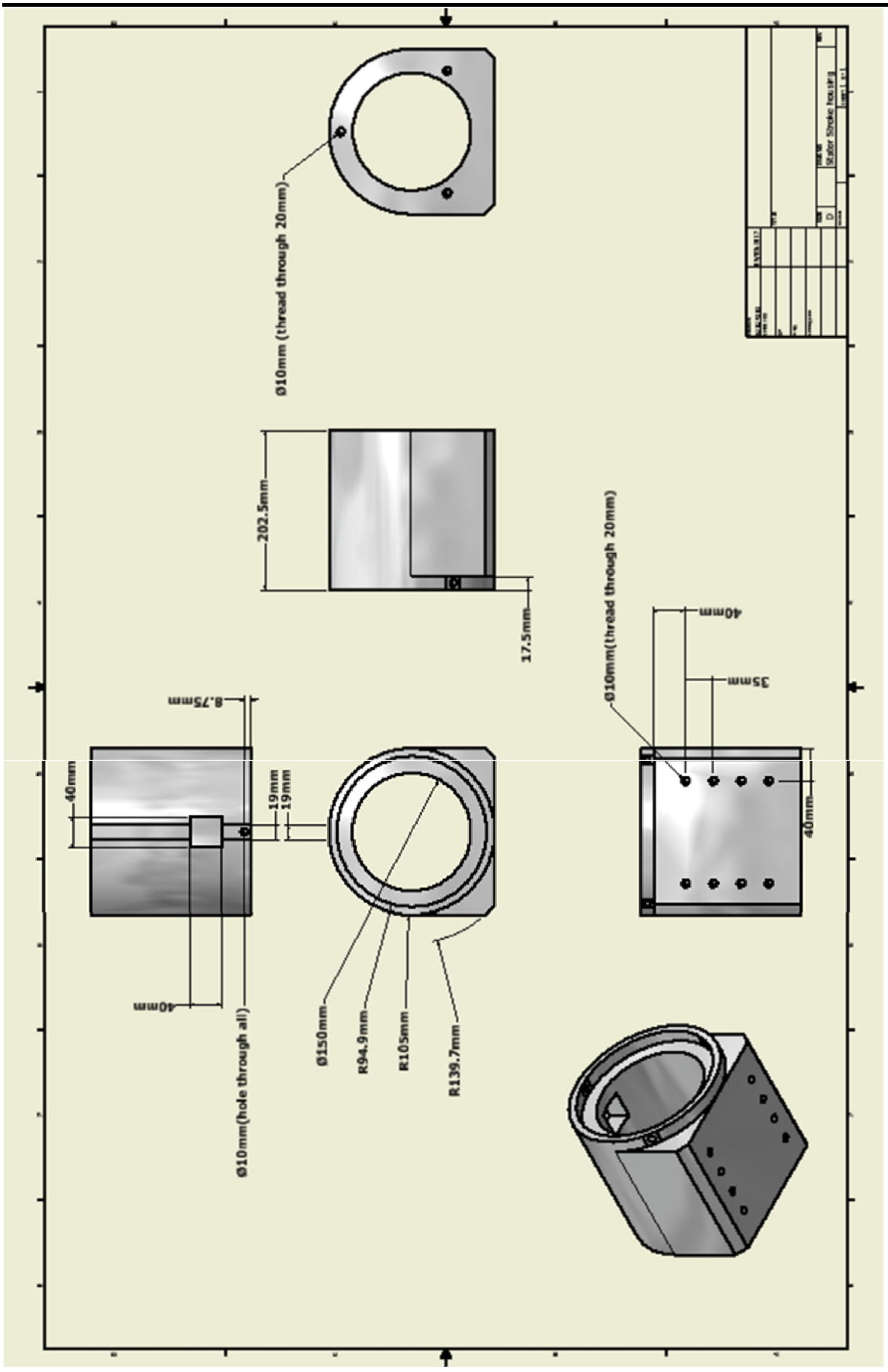
Ø10mm (thread through 20mm)
202.5mm
17.5mm
Ø10mm(thread through 20mm)
40mm
35mm
40mm
8.75mm
40mm
19mm
19mm
40mm
Ø10mm(hole through all)
Ø150mm
R94.9mm
R105mm
R139.7mm

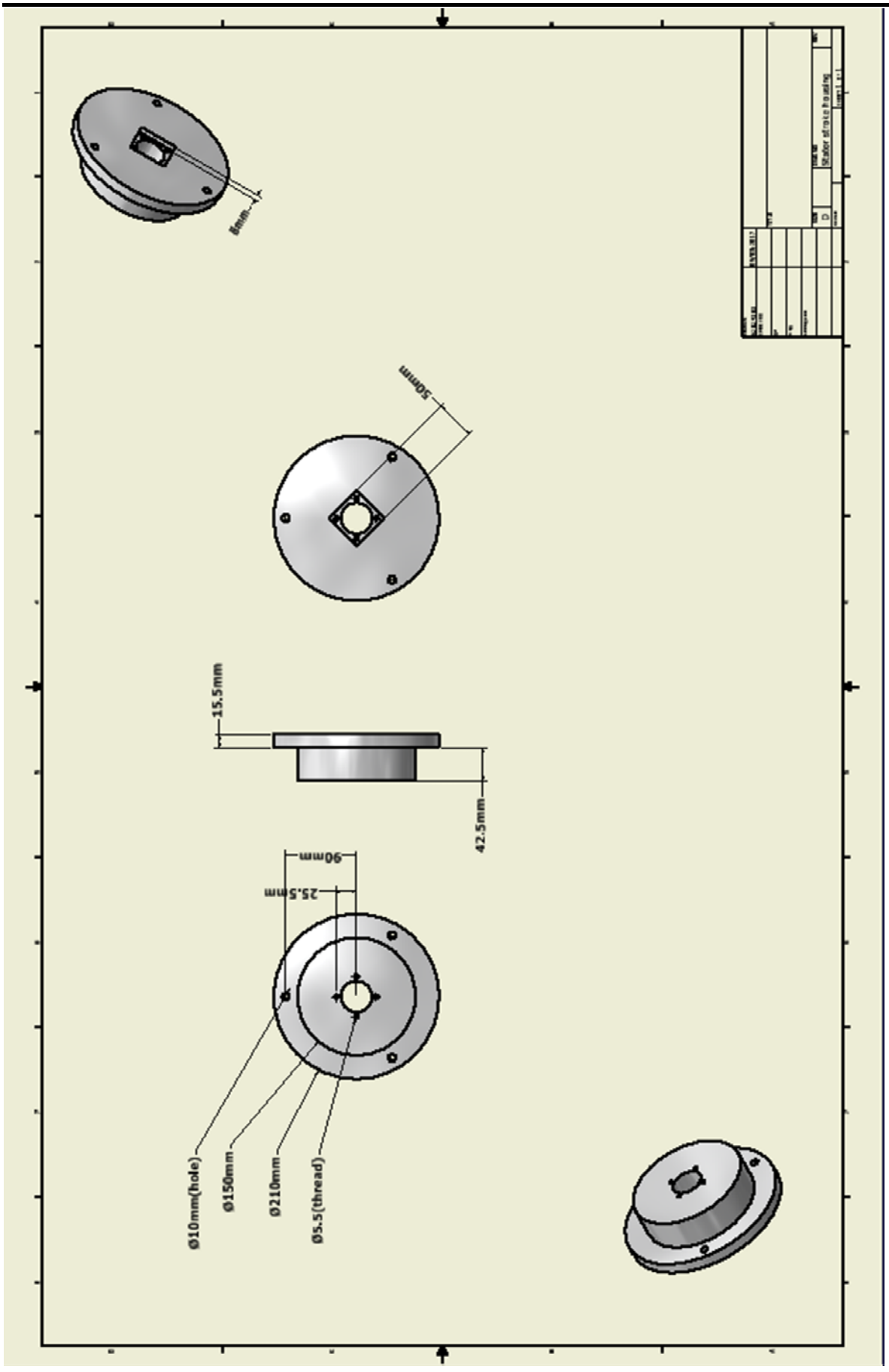
8mm
50mm
15.5mm
42.5mm
90mm
25.5mm
Ø10mm(hole)
Ø150mm
Ø210mm
Ø5.5(thread)